9-1-2015

Enhancement of Nucleate Boiling on Rough and Dimpled Surfaces with Application to Composite Spreaders for Microprocessors Immersion Cooling

Arthur Suszko

Recommended Citation

Suszko, Arthur. "Enhancement of Nucleate Boiling on Rough and Dimpled Surfaces with Application to Composite Spreaders for Microprocessors Immersion Cooling." (2015). https://digitalrepository.unm.edu/me_etds/25

Arthur Suszko

Candidate

Mechanical Engineering

Department

This dissertation is approved, and it is acceptable in quality and form for publication:

Approved by the Dissertation Committee:

Mohamed S. El-Genk, Chairperson

Yu-Lin Shen

Mehran Tehrani

Mahmoud Taha

ENHANCEMENT OF NUCLEATE BOILING ON ROUGH AND DIMPLED SURFACES WITH APPLICATION TO COMPOSITE SPREADERS FOR MICROPROCESSORS IMMERSION COOLING

by

ARTHUR SUSZKO

B.S., Mechanical Engineering, Rutgers University, 2009

DISSERTATION

Submitted in Partial Fulfilment of the
Requirements for the Degree of
Doctor of Philosophy

Engineering

The University of New Mexico
Albuquerque, New Mexico

July, 2015

ACKNOWLEDGEMENTS

I thank the Institute for Space and Nuclear Power Studies, which funded my education to completion at The University of New Mexico. I thank my research and academic advisor and chair of the dissertation committee, Dr. Mohamed S. El-Genk, Regents' Professor of Nuclear and Mechanical Engineering, and Founding Director of the Institute for Space and Nuclear Power Studies, for his assistance and help throughout the duration of this research. He has helped me become and effective and efficient scientist. Many thanks to the other members of my committee, Dr. Yu-Lin Shen, Professor and Associate Chair of Mechanical Engineering, Dr. Mehran Tehrani, Assistant Professor of Mechanical Engineering, and Dr. Mahmoud Taha, Professor and Department Chair of Civil Engineering, for their valuable feedback and suggestions to the content of this dissertation.

I value the help and mentorship I received early on from Dr. Amir F. Ali, whose experience helped me get me going quickly, as well as his direct help and contribution in my early research. Not only was he a valuable mentor, but he is also a good friend. I would also like to thank undergraduate student Aaron Tyson, for his help in running experiments, analyzing and organizing data.

I acknowledge the valuable contributions by Professor Krishna Kota and Mr. Stephen Wootton of the Mechanical and Aerospace Engineering Department at the New Mexico State University (NMSU), Las Cruses, NM, for preparing the drawing and machining and polishing the dimpled Cu surfaces used in the present dissertation.

Last but not least, a special thanks to my family and friends for their support of my goals and achievements.

Enhancement of Nucleate Boiling on Rough and Dimpled Surfaces with Application to Composite Spreaders for Microprocessors Immersion Cooling

by

Arthur Suszko
B.S., Mechanical Engineering, Rutgers University, 2009
Ph.D., Mechanical Engineering, University of New Mexico, 2015

EXECUTIVE SUMMARY

Microprocessors have substantially increased total power dissipation and transistors density over the past two decades, owing to the growth in complexity, performance, and parallelism of computational systems. To continue to effectively and safely dissipate larger amounts of power, advanced methods of cooling such as immersion cooling by nucleate boiling of dielectric liquids are being considered. For electronic cooling applications, dielectric liquids are chemically inert, environmentally friendly, and have low saturation temperatures (34 – 56^{o}C at 0.1 MPa) advantageous for keeping the chip's junction temperature below that recommended by the manufacturer (85 – 115 ^{o}C), depending on the application.

This research experimentally investigated the enhancement of pool nucleate boiling of PF-5060 dielectric liquid on uniformly heated, 10 x 10 x 1.6 mm rough and dimpled Cu surfaces. Fabricating these surfaces is cost effective and scalable, making them suitable for immersion nucleate boiling cooling of high powered microprocessors requiring heat spreaders of different sizes. The PF-5060 has a saturation temperature of 51.4^{o}C at ~0.085MPa – the local pressure in Albuquerque NM, where the experiments were carried out. Because various circuit board orientations and the perpendicular mounting of add-in cards such as graphics processing units results in chip orientations that vary from 0^{o} – 180^{o} with respect to gravity, the effects of these surface inclinations on nucleate boiling of saturated and subcooled PF-5060, are thoroughly investigated for

both the rough and dimpled Cu surfaces. In the experiments, liquid subcooling was varied up to 30 K. Experimental nucleate boiling heat transfer coefficient curves for rough Cu surfaces were used to computationally investigate the performance of composite spreaders. These spreaders removed the thermal power dissipated by a 20 x 20 mm microprocessor with and without hot spots, by saturation nucleate boiling of PF-5060.

To ensure the consistency of the experimental results, all pool boiling experiments reported in this dissertation are for degassed PF-5060 liquid and uniformly heated 10 x 10 x 1.6 mm Cu surfaces. Multiple experiments performed for the same conditions, separated by at least 2 hours, and sometimes a few days, verified the reproducibility of the results. The absence of boiling hysteresis confirmed no influence by the thermal inertia of the heated Cu surface, but rather the thermophysical properties of the PF-5060 dielectric liquid and surface characteristics solely influenced the nucleate boiling results.

Results on the effect of the average surface roughness, (Ra = 0.039 – 1.79μm), inclination angle ($\theta = 0^o – 180^o$), and liquid subcooling (ΔT_{sub} = 0 – 30 K) on nucleate boiling enhancement and CHF on plain Cu surfaces are presented and discussed throughout the dissertation, along with several developed correlations and comparisons with prior work. In the upward facing surface inclination ($\theta = 0^o$), increasing surface roughness, Ra, from 0.039 to 1.79 μm, increased the maximum nucleate boiling heat transfer coefficient, h_{MNB}, by as much as ~150%, and the Critical Heat Flux (CHF) by ~39%. The h_{MNB}, increased proportional to Ra to the power ~0.23, from ~0.67 W/cm^{2}K for Ra = 0.039 μm, to ~1.65 W/cm^{2}K for Ra = 1.79 μm. The corresponding values of CHF increased proportionally to Ra to the power ~0.08, from ~15.5 W/cm^2 to ~21.5 W/cm^2, respectively. The data of the nucleate boiling heat transfer coefficient, h_{NB}, was correlated as: $h_{NB} = Aq^B$. The coefficients “A” and exponent “B” are both functions of Ra. As Ra increases from 0.039 to 1.79 μm, the coefficient “A” increases from 0.09 – 0.23, while the exponent “B” decreases from 0.81 – 0.69 which is consistent with results reported by others.

The effect of the inclination angle on the nucleate boiling of PF-5060 on rough Cu surfaces is independent of surface roughness. The values of both h_{MNB} and CHF decreased as θ increased. Their lowest values in the downward facing orientation (θ = 180^o) are ~40% and ~31% of their upward facing ($\theta = 0^o$) values, respectively. For the upward facing orientation ($\theta = 0^o$), the CHF increased with increased liquid subcooling, ΔT_{sub} at a rate of 2.2%/K. This rate of increase is independent of the Ra, but depends on the surface inclination angle. It increases as θ increases, to a maximum rate of 4.0%/K in the downward facing orientation ($\theta = 180^o$).

The developed correlations for h_{NB}, h_{MNB}, and CHF, as a functions of Ra, θ, and ΔT_{sub}, are in good agreement with the experimental data to within $\pm$ 12%, $\pm$ 12%, and + 12%, respectively. The present correlation for h_{NB} for the upward facing orientation ($\theta = 0^o$), as a function of Ra, falls within the middle of the range of predictions by other established correlations.

High speed videos of saturation nucleate boiling at low applied heat flux (~0.5 W/cm^2) on rough Cu surfaces were captured at 210 fps, and analyzed for the transient growth of the discrete vapor bubbles. From the transient growth measurements, the bubble departure diameter and detachment frequency were determined, and used to estimate the surface average density of nucleation sites on the smooth and rough Cu surfaces. For the smooth Cu (Ra = 0.039 μm), the determined departure bubble diameter, D_d, and detachment frequency, f_d, are 655 $\pm$ 53 μm and 31 $\pm$ 4 Hz, respectively. On the rough Cu surfaces (Ra $\geq$ 0.21 μm), the measured values are 438 $\pm$ 36 μm and 38 $\pm$ 3 Hz, respectively, and independent of surface roughness. The present values D_d fall within a broad range of values reported by others for similar dielectric liquids. The obtained values of the f_d are generally lower than those reported by others.

The determined D_d and f_d were used in conjunction with the experimental nucleate boiling curves, along with the estimated total wetted surface areas of the Cu surfaces, to estimate the surface average density of active nucleation sites, N, per footprint area, as a function of wall superheat. For smooth Cu, the active sites density ranges from 100 to 2000 cm^{-2}, compared to 650 to 10,000 cm^{-2} for the rough Cu surfaces. For all Cu surfaces, N increases with increasing wall superheat and / or surface roughness.

The performed pool boiling experiments also investigated nucleate boiling of PF-5060 on uniformly heated 10 x 10 x 1.6 mm dimpled Cu surfaces. The dimples with diameters Φ_d = 300, 400, and 500 μm, are arranged in a triangular lattice with a fixed pitch-to-diameter ratio of 2.0. The dimples enhance nucleate boiling compared to the smooth polished Cu surface (Ra = 0.039 µm), but not as much as some of the rougher Cu surfaces with Ra $\geq$ 0.58 µm. In the upward facing orientation, the surfaces with Φ_d = 300, 400, and 500 µm have h_{MNB} of ~1.04 – 1.08, ~0.98 – 1.01, and 0.65 – 0.72 $\mathrm{W/cm^2K}$, respectively, and CHFs of ~19.2 – 19.5, ~18.3 – 18.7, and ~17.7 – 18 $\mathrm{W/cm^2}$, respectively.

The effect of the inclination angle on the nucleate boiling of PF-5060 on dimple Cu surfaces is similar to that obtained for the rough Cu surfaces. The values of h_{MNB} and CHF decreased as θ increased, to their lowest values in the downward facing orientation ($\theta = 180^{\circ}$). These values are ~40% and ~33% of their upward facing ($\theta = 0^{\circ}$) values, respectively. In the upward facing orientation, the CHF increased linearly with the liquid subcooling at a rate of 1.8%/K. This rate is 20% lower than that obtained for smooth and rough Cu surfaces for the same dielectric liquid.

High speed videos of nucleate boiling on the dimple surfaces at a heat flux of ~0.5 $\mathrm{W/cm^2}$, revealed dimpled surfaces to have a different type of boiling than on the rough Cu surfaces. As opposed to the randomly distributed sites for bubbles nucleation on the rough Cu surfaces, the growing bubbles were almost entirely associated with the surface dimples. The larger dimples promoted more evaporation, leading to higher bubble growth rates. The bubble volumetric growth rate is highest on the dimpled surface with Φ_d = 500 µm, and lowest on the surface with Φ_d = 300 µm. The measured bubble departure diameter on the surfaces with Φ_d = 300, 400, and 500 µm are 738 $\pm$ 61 µm, 962 $\pm$ 75 µm, and 1051 $\pm$ 73 µm, respectively. The corresponding bubble detachment frequencies are 8.6 $\pm$ 0.7 Hz, 10.2 $\pm$ 1.0 Hz, and 13.5 $\pm$ 1.8 Hz, respectively. These departure diameters depended largely on the surface tension forces holding the bubble down along the rim of the dimple, determined by the circumference of the dimple and thermophysical properties of the PF-5060 dielectric liquid. These values of the bubble departure diameter and detachment frequency are much larger and lower, respectively, than on smooth rough Cu surfaces at the same applied heat flux.

The pool boiling experimental results on rough Cu with Ra = 1.79 µm were used in 3-D computational thermal analyses investigating the performance of advanced composite spreaders, for immersion cooling of high powered microprocessors. The spreaders are comprised of two thin ~0.5 mm thick Cu laments that protectively encase a

layer of thermally anisotropic material such as highly ordered pyrolytic graphite (HOPG). The exposed surface of the top Cu filament is cooled by saturation nucleate boiling of PF-5060. The analyses varied the in-plane (k_x = 325 – 2000 W/mK) and through-plane (k_z = 5 – 20 W/mK) thermal conductivities, and thickness of the thermally anisotropic material layer (δ = 0 – 1 mm), and the spreader surface area. The impacts of each were determined on the total power removed, and maximum chip temperature, of a 20 x 20 x 0.25 mm underlying microprocessor dissipating uniform power, as well as with central and multiple hot spots with heat flux ratios up to 10.

In the computations, the surface of the spreader was limited to 90% CHF, and minimum surface temperature of 1^{o}C above that for boiling incipience in the experiments. These constraints ensure safe operation and nucleate boiling over the entire spreader surface. The total power removed by the composite spreader ranges from 6 – 400% more than that possible by an all Cu spreader of the same thickness. The enhancement in total power removed depends on the ratio of the axial to lateral absolute resistances, R_z/R_x, and the size of the spreader, w. Increasing R_z / R_x increases the total power removed by composite spreader. The R_z and R_x depend on the thickness of the anisotropic layer, δ, and thermal conductivities k_x and k_z. Correlations were developed to relate the impacts of k_x, k_z, δ, and w on the total power removed, Q, and maximum chip temperature, $T_{chip,max}$. These correlations are in good agreement with the computed data, to within ± 1 – 7%.

The total thermal resistance, R_{TOT}, which the summation of the resistances from the thermal interface material, composite spreader, and that of nucleate boiling at the spreader surface, ranges from 0.16 – 0.4 ^{o}C/W, depending on the k_x, k_z, and δ of the thermally anisotropic layer, and w of the spreader.

For industrial applications involving nucleate boiling of PF-5060 or other similar dielectric liquids such as FC-72, and specifically immersion cooling of high performance microprocessors, the presented results and developed correlations are useful design tools. Additionally, results demonstrated that composite heat spreaders with scalable surface modifications, such as surface roughening and dimples machining, are very promising for the immersion cooling of high powered microprocessors.

TABLE OF CONTENTS

List of Figures

List of Tables

Nomenclature

A	Area, footprint area (cm^2), Correlation coefficient (Eq. (4.2))
a	Semi-major axis (mm)
A_r	Fraction increase in surface area
B	Correlation coefficient (Eq. (4.3))
b	Semi-minor axis (mm)
Bo	Bond number
C	Thermal Conductance ($W/cm^{2o}C$)
CHF	Critical Heat Flux (W/cm^2)
CHS	Central hot spot
c_p	Specific heat capacity (J/kgK)
CPU	Central processing unit
Cu	Copper
D	Bubble diameter (mm, μm)
f	Bubble detachment frequency (Hz)
F	Nucleate boiling angular dependence coefficient
F_{PF}	Correlation constant (Eq. (2.5))
FOM	Figure-of-Merit (mm^2) (Eq. (6.1))
g	Gravitational acceleration (cm/s^2)
G	Emery paper grit count, General function
GPU	Graphics processing unit
h	Heat transfer coefficient (W/cm^2K)
h_{fg}	Latent heat of vaporization (kJ/kg)
HOPG	Highly Ordered Pyrolytic Graphite
HFR	Heat Flux Ratio
I	Current (A)
Ja	Jakob Number
k	Thermal conductivity (W/mK)
K_1	Thermophysical constant
M	Molecular weight (g/mol)
MPC	Microporous Copper

n	Summation number
nf	Correlation constant (Eq. (2.4))
N	Active nucleation sites density (#/cm^2)
P	Power (W), Pressure (Pa)
P_r	Prandlt number
PG	Porous graphite, pyrolytic graphite
q	Heat flux (W/cm^2)
Q	Total power removed / dissipated (W)
r	Distance along the diagonal (mm)
R	Thermal Resistance (^{o}C/W), CHF angular dependence coefficient
Ra	Surface average roughness (µm)
SEM	Scanning Electronic Microscope
t	Time (s, ms)
t_0	Arbitrary initial recording time (ms)
t_b	Bubble growth time, ($t - t_0$), (ms)
T	Temperature (^{o}C, K)
T	Average Temperature (^{o}C, K)
TDP	Thermal design power (W)
TIM	Thermal interface material
V	Bubble volume, Voltage measurement (V)
W	Uncertainty estimate
w	Width of the spreader (mm)
z	Roughness height (µm)

Greek Symbols

Δ	Difference, Uncertainty estimate
δ	Thickness (mm)
μ	Viscosity (kg/ms)
Φ	Dimple diameter (µm)
ϕ	Contact angle (^{o})
ρ	Density (kg/m^3)
σ	Surface tension (N/m)
θ	Inclination Angle (^{o})

Subscripts

b	Bulk or pool, Bubble
boil	Nucleate boiling
CHF	Critical Heat Flux
chip	Computer chip or microprocessor
d	Departure, detachment, dimple
hs	Hotspot
incip	Nucleate boiling incipience
l	liquid
max	Maximum
min	Minimum
MNB	Maximum nucleate boiling
NB	Nucleate boiling
NC	Natural convection
o	Reference value
rand	Random
s	Surface
sat	At saturation conditions
sp	Heat spreader
sub	Subcooled temperature
sys	Systematic
TIM	Thermal interface material
TOT	Total
v	Vapor
w	Wall or surface
x, y, z	Relative to Cartesian coordinates

Superscripts

*	Dimpled surface, limit maximum for 90% CHF and $T_{\mathrm{s,min}} = +1^{\mathrm{o}}\mathrm{C}$

1. Introduction

The rapid growth of microprocessors performance, complexity, and increasing parallelism during the last two decades, have led to exponential increases of chip total power dissipation and transistors density. The NV40 performance graphics processing unit (GPU), released in 2005 by Nvidia, contains 222 million transistors within a 288 mm^2 chip die (Nvidia, 2015). The Smithfield performance central processing unit (CPU), released by Intel in the same year, contains 230 million transistors within a 206 mm^2 die (Intel, 2015). The most recent release of the Maxwell architecture flagship GPU, by Nvidia, contains a staggering 8 billion transistors within a 601 mm^2 chip die (Nvidia, 2015), while the Haswell-EP architecture workstation CPUs, released by Intel in 2014, contain up to 5.56 billion transistors within a 661 mm^2 die (Intel, 2015). These numbers represent ~24x – 27x increases in the total transistors count, and ~8x – 17x increases in the transistors density, for the high performance CPUs and GPUs over the past decade alone. The continuous increases of transistor density and count, and the processing speed of chips, presents ongoing challenges for the thermal management of high performance microprocessors.

Microprocessors have an assigned thermal design power (TDP) rating, which is the total amount of power a heat sink remove safely from a chip during regular operation. However, in short duration peak operation, the chip may exhibit power dissipation as much as 50% higher than the rated TDP. Over the past decade alone, the TDP requirements for CPUs increased over 100%, and over 500% for GPUs (Figure 1.1a). Conversely, the chip die average surface heat flux has fluctuated around ~50 W/cm^2 (Figure 1.1b). This power dissipation heat flux has been considered the upper limit for dedicated air cooling solutions, by some researchers in the years prior (Zhang et al. 2003; Xu et al. 2004; Lasance, 2005).

Localized power densities, or hot spots, have reached on the order of ~100W/cm^2. At the hot spots, local heat fluxes could reach 3 – 8x higher than that of the chip average (Wei, 2008). Hot spots create temperature differentials across the chip, inducing thermal stresses that could markedly reduce the serviceable life.

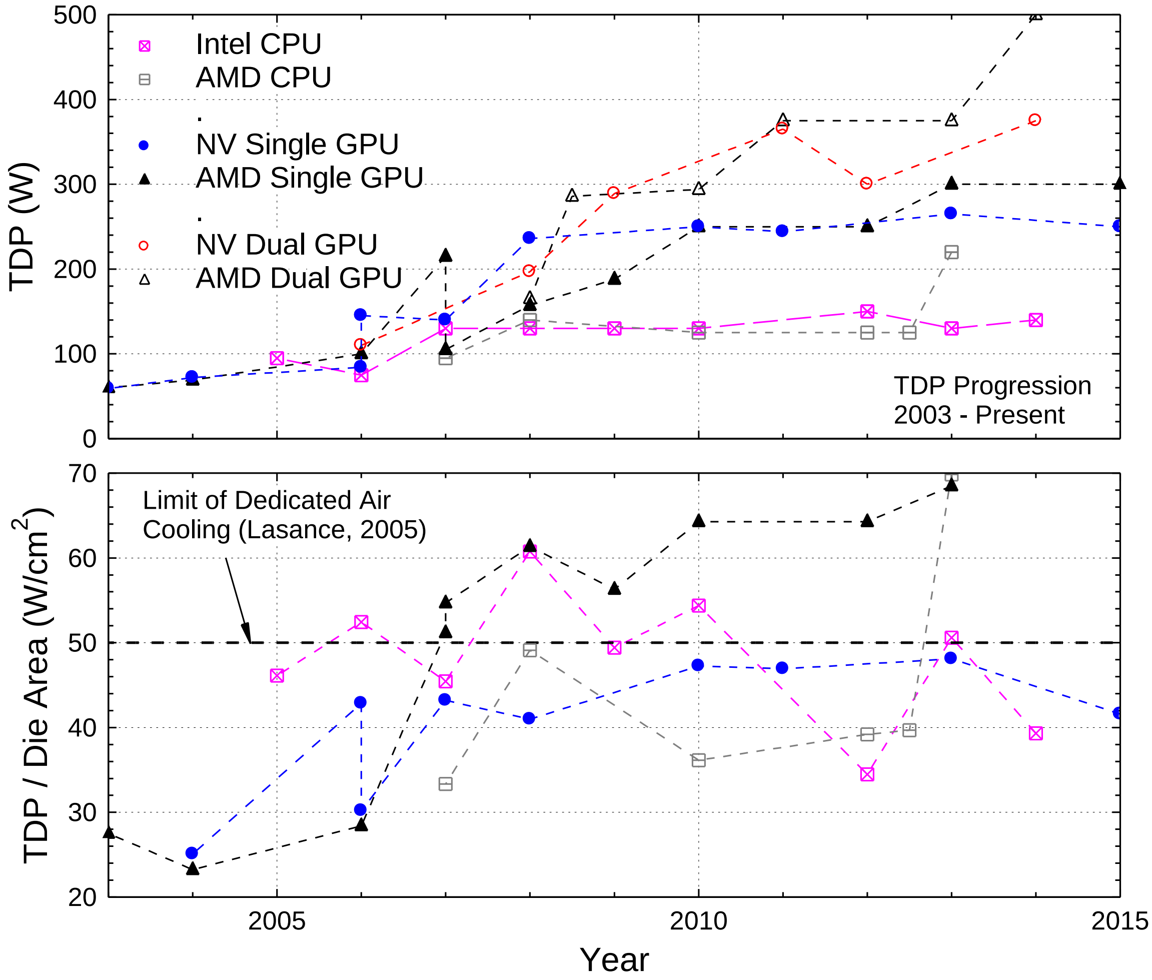

Figure 1.1 The increase of the thermal design power and mean power density of high performance microprocessors over the last 12 years.

The rapid increases in the total power dissipation (Figure 1.1a) and transistors density of microprocessors have stimulated an evolution in cooling techniques capable of keeping the high powered microprocessors below the recommended maximum junction temperature, $T_{j,max}$, typically 85 – 115^{o}C (ITRS, 2013), depending on the application. As the total power dissipation and density of microprocessors continues to increase, advanced methods of cooling such as forced liquid convection in microchannels, immersion pool and flow nucleate boiling, jet impingement, and spray cooling will have to be considered (Estes and Mudawar, 1995; Katsuta, 1977; Monde, 1978; Bar-Cohen and Wang, 2009; Mudawar, 1992; Hall and Mudawar, 1999; Rainey and You, 2000; Pavlova and Amitay, 2006; Arik et al. 2007; Kandlikar and Bapat, 2007; Kim, 2007;

Khan et al. 2008; Anandan and Ramalngam, 2008; El-Genk and Ali, 2009, 2010a,b ; Ali and El-Genk, 2012a). Recently, Advanced Micro Devices (AMD) has begun using coolers that use forced liquid convection in microchannels, for its highest power chips dissipating upwards of 200 W (AMD, 2015). Two phase based cooling methods, such as nucleate boiling, liquid jet impingement, and spray cooling, offer even better cooling performances.

Immersion cooling by nucleate boiling offers many advantages that make it desirable for cooling high powered microprocessors. These advantages include an almost uniform surface temperature, large scale cooling capability, mitigation of chip hot spots (El-Genk and Ali, 2013), low thermal resistances (El-Genk and Saber, 2008; El-Genk and Ali, 2013), and no pumping requirement. Additionally, the low saturation temperatures of dielectric liquids, such as the Fluorinert FC-72 (56°C at 0.1 MPa), the Performance Fluid PF-5060 (56°C at 0.1 MPa), and Novec HFE-7000 (34°C at 0.1 MPa) (3M, 2015), help keep high power density chips below the maximum junction temperature, $T_{j,max}$, or within the recommended range by manufacturers (85 – 115°C (ITRS, 2013)). El-Genk and Saber (2008), and El-Genk and Ali (2013), have numerically demonstrated that nucleate boiling of heat spreaders with enhanced surfaces are capable of cooling spreaders for underlying chips with power dissipation fluxes from 70 – 85 W/cm^2. This range of power density is much higher than the limit of air cooling (~50 W/cm^2) depicted in Figure 1.1b. Dielectric liquids are also environmentally friendly, chemically combatable with most standard electronic materials, and have no handling concern (3M, 2015).

Other studies have reported that two phase cooling of large datacenters could potentially reduce energy consumption by as much as ~50% (Olivier et al. 2010, 2011; Marcinichen et al. 2012), compared to refrigerated air. Additionally, with immersion nucleate boiling cooling, the heat dissipated by the microprocessors may be recaptured for even greater energy savings (Tuma, 2010), and floor space, requiring less infrastructure than refrigerated air. However, the highly wetting dielectric liquids, with low surface tensions, tend to flood and reduce the amount of trapped air within the surface micro for bubble nucleation. This delays the incipience of boiling, until a high enough surface temperature is reached in order to stimulate the formation of large enough vapor embryos for subsequent bubbles growth. This, known as the temperature excursion prior to boiling incipience, could reach as much as 35 K for dielectric liquids on plain Copper (Cu) and Silicon (Si) surfaces (Rainey and You, 2000; b; El-Genk and Bostanci, 2003a, b; McNiel, 1992; Chang, You, and Haji-Sheikh, 1998). Temperature excursion is undesirable for microprocessors and a concern in immersion nucleate boiling cooling using dielectric liquids, because it increases the microprocessor operating temperature at very low power dissipation levels, typically in the standby or idle mode of operation.

Nucleate boiling is also limited by the critical heat flux (CHF). The CHF, or departure from nucleate boiling, is associated with a surface dryout and surge in temperature, which could melt or damage the spreader surfaces and underlying chips. Therefore, the CHF, which depends on the properties of the boiling liquid and heated surface, surface microstructure, and operating pressure, must be known with good confidence. For immersion nucleate boiling cooling of microprocessors, the design heat flux should be kept within an adequate margin from CHF. In general, the maximum design heat flux is typically kept at ~30 – 70% below CHF.

Many investigations to enhance nucleate boiling heat transfer, reduce or eliminate the temperature excursion prior to boiling incipience, and increase CHF of dielectric liquids have been reported (Nakayama et al.1980; Anderson and Mudawa, 1989; Miller and Wright; 1990, Ramilison, Sadasivan, and Lienhard, 1992; Chang and You; 1996; Misale et al. 1999; Rainey and You, 2000; Honda et al. 2002; Ramaswamy et al., 2003; Wei and Honda, 2003; El-Genk and Bostanci, 2003; Jabardo and Ribatski, 2003; Xu et al., 2004; Pioro et al. 2005; Vemuri and Kim, 2005; Jung and Kawk, 2006; Nimkar et al., 2006; Yu et al., 2006; Arik et al., 2007; Kim et al., 2007; El-Genk and Parker, 2008; Parker and El-Genk, 2009; Wu et al. 2008; McHale and Garimella, 2008, 2010, 2013; Jones et al. 2009; Hosseini et al. 2011; El-Genk and Ali, 2009, 2010, 2012, 2013;).. The experimental results demonstrated enhancements in nucleate boiling on modified surfaces which include but are not limited to: rough and microstructured surfaces, nano- and microparticle coatings, porous surfaces, fabricated pores, cavities, dimples or microfins, and surfaces of modified hydrophobicity.

Other parameters that have been reported to affect nucleate boiling and CHF include the surface orientation and the liquid subcooling (Mudawar, Howard, and Gersey, 1997; Chang and You, 1996; Howard and Mudawar, 1999; Rainey and You, 2001; El-

Genk and Bostanci, 2003a,b; Priarone, 2005; Parker and El-Genk, 2006a,b; Parker and El-Genk, 2008; El-Genk and Ali, 2012; Ali and El-Genk, 2013). The effect of the surface orientation is of primary interest for the immersion nucleate boiling cooling of microprocessors, as the printed circuit board that holds the chips may be mounted upward facing, vertically, or downward facing. A more detailed review on the methods employed to enhance nucleate boiling heat transfer and CHF, as well as the effect of the surface orientation and liquid subcooling, is provided in the next chapter.

1.1 Scalable Surfaces for the Enhancement of Nucleate Boiling

Many studies have investigated the effects of surface roughness, microstructure, and material properties on nucleate boiling of different liquids (Danilova and Bel'skii, 1965; Kozitskii, 1971; Nishikawa et al. 1982; Cooper, 1984; Wang and Dhir, 1993; Luke, 1997, 2006; Ribatski and Jabardo, 2003; Klausner and Mei, 2004; Gorenflo et al. 2004; Pioro et al. 2004; Jones et al. 2009; Jabardo, 2010; Hosseini et al. 2011; McHale and Garimella, 2013). Using rough surfaces to enhance nucleate boiling has attracted the interest of numerous investigators for many decades. The emerged consensus is that the micro features of rough surfaces increase the density active of sites for bubbles nucleation, and thus enhance nucleate boiling. It has also been reported that the enhancement in nucleate boiling increases with increased surface roughness up to a point, beyond which little improvement occurs (Kozitskii, 1971; Jabardo, 2010). Reported results of saturation nucleate boiling on rough surfaces showed the heat transfer coefficient, h_{NB}, to increase proportional to the average surface roughness, Ra, to the power 0.1 – 0.2 (Jones, 2009).

Other studies have reported that increasing the surface roughness makes it more hydrophobic (Wenzel, 1949), which decreases the bubble departure diameter and detachment frequency, thus enhancing nucleate boiling and CHF (Wang and Dhir, 1993; Hong et al. 1994; Nakae et al. 1998; Klausner and Mei, 2004; Takata et al. 2005; Wu et al. 2010; Ahn et al. 2012, Hsu and Chen, 2012). The average surface roughness is directly related to the radius of curvature of the liquid miscues at the interface with the trapped air pockets in surface crevices (Nakae et al. 1998; Klausner and Mei, 2004), as well as the surface average density of active sites for bubbles nucleation (Nimkar et al. 2006; McHale and Garimella, 2010)

Other surfaces that enhance nucleate boiling are those with increased total wetted area. Increasing the wetted or geometrical surface area enhances the total rate of heat removal by nucleate boiling, and has been demonstrated using surfaces with micro-fins and macro- and micro-pins of different heights and cross-sectional areas (Rainey and You 2000; Ramasway et al. 2000, 2003; Honda et al. 2002, Wei and Honda 2003, and Wei et al. 2005; Yu and Lu 2006; Parker and El-Genk 2009). These studies reported increases in the total rate of heat removal with increasing pin or micro-fin height, but at the expense of increasing the footprint surface temperature. The nucleate boiling heat transfer coefficient, h_{NB}, based on the geometrical or the wetted surface area, is lower than that based on the footprint area of the heated surface. In general, surfaces with micro-spaced micro-fins or pins decrease CHF with little enhancement in nucleate boiling (Wei and Honda 2003; Ujereh et al. 2007; Jung and Kwak 2006; Vemuri and Kim 2005; El-Genk 2012). On the other hand, surfaces with macro-pins or fins with large spacing of several millimeters, enhance both CHF and h_{NB}, based on the footprint area, but their values, based on the actual wetted surface area, are lower (Parker and El-Genk 2009; El-Genk 2012).

1.2 Research Needs

Despite the large body of published work on the enhancement of nucleate boiling and CHF on rough surfaces, there are large variances in the reported data. In addition, the predictions of developed correlations for the nucleate boiling heat transfer coefficient on roughened surfaces vary widely (Rohsenow, 1952; Zuber 1959; Mikic and Rohsenow, 1970; Judd and Hawng, 1976; Kutatelatze and Gogonin 1980; Nishikawa et al. 1982; Cooper 1984; Gorenflo et al. 2004; Jabardo, 2010). Reasons often cited are the different methods used for surface preparation, roughness measurements techniques, and the properties of the surface materials (Gorenflo et al. 2004; Luke, 1997, 2006; Nikmar et al. 2006; Jabardo 2010; Hosseini et al. 2011) and lack of data for various liquids. Additionally, reported studies investigating the effect of surface roughness on nucleate boiling of the highly wetting dielectric liquids are relatively limited, compared with other non-dielectric liquids. Therefore, there is a need to systematically investigate the effect of surface roughness on nucleate boiling and CHF of dielectric liquids.

Although extended surfaces with arrays of micro-pins or micro-fins for enhancing nucleate boiling are boiling have been shown to be effective, their performance is limited by the fin effect (Rainey and You, 2000; Ujereh et al. 2007; Parker and El-Genk 2009). The decrease in surface temperature along the fins decreases the local nucleate boiling heat transfer coefficient. The additional thermal resistance of the pins increases the temperature of the footprint surface. Therefore there is a need to investigate surfaces with manufactured dimples, rather than micro-fins or pins, for enhancing h_{NB} and CHF for dielectric liquids.

Dimples surfaces, like micro-pinned or micro-finned surfaces, increase the wetted surface area, but without the fin effect. Dimpled surfaces are relatively easy to scale up for industrial applications including boilers, refrigeration, and immersion cooling of electronics. In addition to increased wetted surface area, the base of dimples should operate hotter than the flat portion between the dimples, which could enhance h_{NB}. However, more is needed to understand the effect of the size and density of dimples on the enhancement of nucleate boiling and CHF. Very little has been reported on the nucleate boiling of dielectric liquids and other liquids on dimpled surfaces. Additionally, reported work on the nucleate boiling of dielectric liquids on dimpled or similar surfaces with micro cavities, has been for saturation boiling in the upward facing orientation (Miller et al. 1990; Yu et al. 2006; Hutter et al. 2010). Because of packaging requirements, the circuit board with attached micro-fins or pins may be mounted in different orientations, thus the effects of the surface orientation of dimpled surfaces on both h_{NB} and CHF of dielectric liquids are worthy of investigation.

Immersion cooling of high powered microprocessors by nucleate boiling of dielectric liquids uses traditionally flat Cu heat spreaders. The center of the spreaders directly above the underlying microprocessors, may operate close to the maximum nucleate boiling heat transfer coefficient, $h_{\mathrm{MNB.}}$ However, the surface temperature and h_{NB} drops with distance away from the heat source. This decrease in the nucleate boiling heat transfer coefficient limits the spreader size and total thermal power dissipated by the underlying chip. As a result, the traditional flat Cu spreaders are too small to remove the high powers generated by today’s high powered microprocessors that may reach or exceed 150W (AMD, Intel, Nvidia, 2015). The primary limitation on increasing the thermal power dissipated by the underlying chip, is the ability to increase the lateral spreading of the generated heat, and hence the spreader surface area cooled by nucleate boiling. Thus, there is a need to design and investigate heat spreaders that are thermally anisotropic and quantify their performance for immersion cooling high powered microprocessors, while keeping the maximum junction temperatures below or within the range recommended by manufacturers.

1.3 Objectives

The objectives of the research performed in this dissertation are to address the needs identified earlier, for enhancing nucleate boiling and CHF of PF-5060 dielectric liquid, on rough and dimpled Cu surfaces, and assessing the performance of thermally anisotropic heat spreaders for high powered chips. The specific objectives are:

1. Perform pool boiling experiments to investigate the effects of surface roughness, Ra, inclination angle, θ, and liquid subcooling, ΔT_{sub} on nucleate boiling and CHF of PF-5060 dielectric liquid on uniformly heated 10 x 10 mm Cu surfaces. The test matrix for the performed pool boiling experiments includes 13 Cu surfaces with Ra ranging from 0.039 to 1.79 μm, θ from 0^{o} to 180^{o}, and ΔT_{sub} of 0 – 30 K (Table 1.1). Correlations are developed that account for the effects of surface roughness, inclination angle, and liquid subcooling on the nucleate boiling heat transfer coefficient and CHF of PF-5060. The developed CHF and h_{NB} correlations are compared with others reported in the literature. To help interpret the obtained results, high speed visualization of nucleate boiling is used to determine the surface roughness on the dynamic growth of discrete bubbles, at an applied heat flux of ~0.5W/cm^{2}. Measurements of the discrete bubble growth are used to determine the bubble departure diameter and frequency. These results are used in conjunction with the experimental pool boiling curves to estimate the number of active nucleation sites density on the Cu surfaces of different roughness, and are compared with the estimates for others on microstructured and porous surfaces in dielectric liquids.

Table 1.1 The experimental matrix investigating the effects of surface roughness, inclination angle, and liquid subcooling on nucleate boiling of PF-5060 dielectric liquid on uniformly heated 10 x 10 mm Cu surfaces.

# of Cu Surfaces	Surface Roughness (μm)	Surface Inclination (^{o})	Liquid Subcooling (K)	# of Unique Experiments
13	0.039 – 1.79	0, 60, 90, 120,150, 160, 170, 180	0, 5, 10, 20, 30	300+

2. Perform pool boiling experiments to investigate the effects of the dimple diameter, Φ_d, the inclination angle, θ, and the liquid subcooling, ΔT_{sub} on the nucleate boiling and CHF of PF-5060 dielectric liquid on uniformly heated 10 x 10 mm Cu surfaces. The test matrix for the pool boiling experiments includes 3 dimpled Cu surfaces, with Φ_d of 300, 400, and 500 μm, and depths of 200 μm, spaced in a triangular lattice with a pitch to diameter ratio of 2.0. (Table 1.1). The results from these experiments are compared to those of the same dielectric liquid on rough Cu surfaces. To further interpret the obtained results, high speed visualization of nucleate boiling is used to determine if the dimple affects the discrete bubble transient growth, and hence the enhancement of nucleate boiling heat transfer.

Table 1.2 The experimental matrix investigating the effects of dimple size, inclination angle, and liquid subcooling on nucleate boiling of PF-5060 dielectric liquid on uniformly heated 10 x 10 mm dimpled Cu surfaces.

# of Dimpled Cu Surfaces	Dimple Diameter (μm)	Surface Inclination (^{o})	Liquid Subcooling (K)	# of Unique Experiments
3	300, 400, 500	0, 60, 90, 120,150,180	0, 10, 20, 30	~50

3. Conduct 3-D numerical analyses to investigate the performance of composite spreaders with a rough Cu surface cooled by saturation nucleate boiling of PF-5060 dielectric liquid, for thermal management of a 20x20 mm high performance microprocessor chip. The spreaders are comprised of two 0.5 mm-thick Cu laments separated by a thin layer ($\leq$ 1.0 mm) of thermally anisotropic material, such as graphite or highly oriented pyrolytic graphite (HOPG) (Figure 1.2). The analyses are

to quantify the effects of the thickness and thermal conductivities (k_x = 325 – 2000 W/mK, and k_z = 5 – 20 W/mK) (Table 1.3) of the anisotropic layer on the total thermal power removed by nucleate boiling from the spreader surface, the spreader total thermal resistance, and the maximum temperature of underlying chip. The performed analyses investigated the cooling of 20 x 20 x 0.25 mm underlying microprocessors with uniform heat dissipation, as well as 0.5 x 0.5 mm and 1.0 x 1.0 mm hot spots with heat flux ratios up to 10, as well as of a chip with multiple 1.0 x 1.0 mm hot spots. In addition, the performance results for a thermally anisotropic spreader with an oxidized (or aged) Cu surface are compared to those with a non-oxidized Cu surface, to assess long term performance.

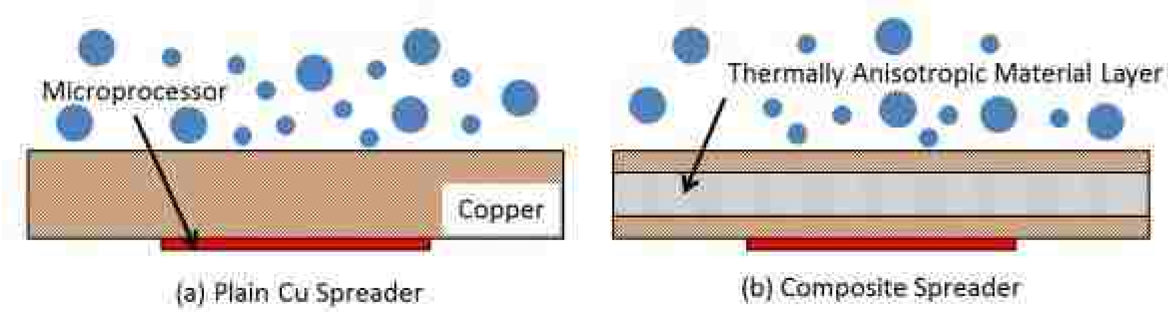

(a) Plain Cu Spreader (b) Composite Spreader

Figure 1.2. Schematic of and all Cu and thermally anisotropic composite spreader investigated for immersion cooling of high powered microprocessors by nucleate boiling of PF-5060 dielectric liquid.

Table 1.3. Computational matrix investigating the effects of the thermally anisotropic layer thickness, thermal conductivities, and spreader size, on the performance of composite spreader cooled by nucleate boiling of PF-5060 dielectric liquid.

Spreader Size (mm)	Layer Thickness (mm)	Layer k_x (W/mK)	Layer k_z (W/mK)	# of Unique Cases
20 – 70	0, 0.25, 0.5, 0.75, 1.0	325, 500, 1000, 1800, 2000	5, 8, 10, 20	250+

1.4 Summary

The next chapter reviews the advanced methods for cooling high powered microprocessors and fundamentals of pool nucleate boiling of dielectric liquids. A review of the literature on relevant and related work is also presented. Chapter 3 describes the experimental pool boiling facility, as well as the approach and experimental procedures taken to ensure sound and reproducible results. Chapter 4 presents and discusses the experimental results for saturation and subcooled nucleate boiling PF-5060 on rough Cu surfaces at different orientations. The results of the visualization study of the dynamic growth of the discrete vapor bubbles on the rough Cu surfaces are also presented in this chapter. Chapter 5 presents the experimental results for saturation and subcooled nucleate boiling PF-5060 on the dimpled Cu surfaces at different orientations. The visualization study of discrete bubbles and the measured transient growth on the dimpled Cu surfaces is also presented in this chapter. Chapter 6 details the performed 3-D numerical analyses of the thermally anisotropic heat spreaders. The approach, methodologies, and the verification of the codes used for compute the performance of the thermally anisotropic spreaders, are presented with the results of the analyses in Chapter 6. Summaries and conclusions based on the obtained research results are provided in Chapter 7. This chapter also provides some suggestions for future related work.

2. Background

This chapter begins by briefly summarizing the different methods of cooling high powered microprocessors, with the focus shifting to immersion cooling by pool nucleate boiling. The generalized pool boiling curve is then introduced as the basis for the discussion on the fundamentals of pool boiling and discrete vapor bubble growth. The fundamentals of nucleate boiling are broken up into sub-sections that discuss the unique behaviors and qualities of the specific regions and points of interest on the pool boiling curve. A literature review conducted for the enhancement of nucleate boiling, the effect of surface roughening and surface inclination angle on nucleate boiling heat transfer, bubble visualization studies, reports on estimations of active nucleation sites density, and other related topics to the work conducted in this dissertation are covered in this chapter.

2.1 Methods for Cooling Microprocessors

Methods for cooling microprocessors are categorized as passive or active. Over the past decades, the cooling of high powered microprocessors has evolved from passive cooling by the natural convection of air, to active microchannel liquid cooled heat sinks. Active cooling requires mechanical devices such as fans or pumps to drive the working fluid that absorbs and moves the heat dissipated by the chip, and is typically rated by how much cubic feet per minute of air, or gallons per minute of liquid, can be pushed through the system. Methods of active cooling include the forced convection of air, forced convection of liquid in microchannels, immersion cooling by flow boiling, jet impingement, and spray cooling. When the mechanical element of the cooling system is removed, the mode of cooling becomes passive, and includes the natural convection of air or liquid, and immersion cooling by pool nucleate boiling.

2.1.1 Natural Convection Cooling

Figure 2.1 compares the local heat transfer coefficients of the different methods of cooling microprocessors. Natural convection is a passive method of cooling that may utilize any working fluid, requires no maintenance (and thus may be considered free performance), and has been reported to adequately cool small electronics dissipating up to 5 W of thermal power (Cengel, 2002). However, due to its local low heat transfer coefficient range, the natural convection of air has not been suitable for cooling high performance microprocessors for many decades now. Bahadur and Bar-Cohen (2005) conducted a study on the natural convection cooling of pinned heat sinks composed of a high thermal conductivity polymer, and reported the base of the heat sink temperature rose from 10 to 70 oC above ambient, as the applied power increased from 1.2 – 7.2W. Therefore, cooling by natural convection only serves as a mean to cool lower power devices (< 10 W). When natural convection is not adequate, the forced convection of air, by means of fans, is often utilized.

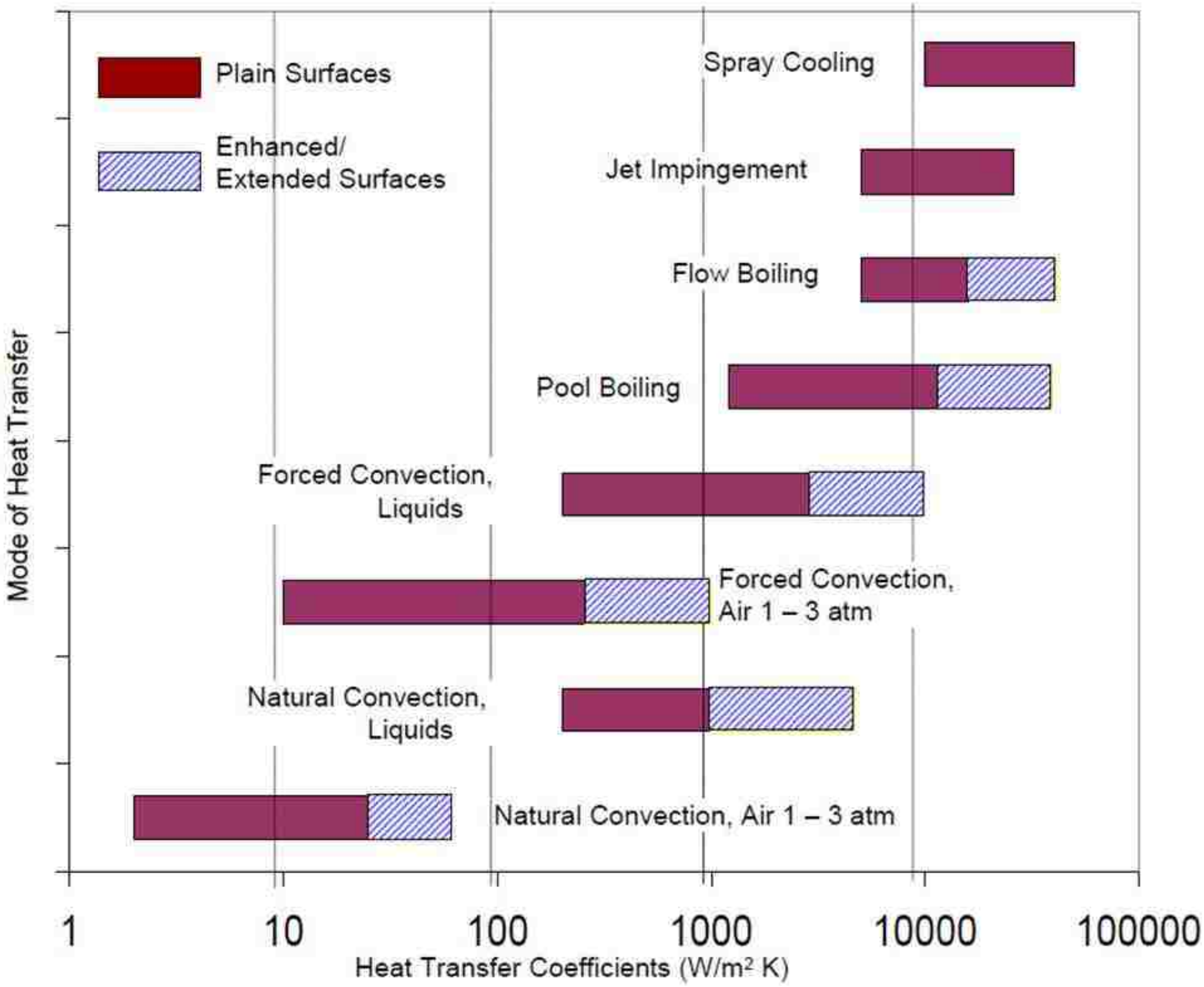

Figure 2.1 The range of capability of the different methods for microprocessors cooling (Simmons, 1996; Ali, 2013)

2.1.2 Forced Convection of Air Cooling

The forced convection of air provides heat transfer coefficients one order of magnitude greater than of natural convection (Figure 2.1). It has also uses to its advantage, very large surface areas by extended fin arrays to increase the total surface area it acts upon. This has been the most common method of cooling high powered microprocessors over the past two decades. Advances in heat pipe and vapor chamber technologies have proven effective in moving the heat away from the source, to nearby large area fins that greatly increase the surface area the forced convection of air operates on, thus greatly increasing the total heat removal capability of the heat sink. The thermal resistances of advances air cooled heat sinks have been reported to range from 0.5 – 4 ^{o}C/W (Kim et al. 2003; Pastukhov et al. 2003; Zhang et al. 2003).

The drawback of this method of cooling is the large physical occupancy that increases the overall materials cost, as well as weight of the heat sink. For example, air coolers for high performance GPUs extend outward and occupy two and sometimes three motherboard PCI-Express slots that could otherwise be used for additional GPUs and subsequent compute power, or other add-in cards. Additionally, rack mount server chasses do not have the physical space to accommodate very large tower styled air coolers.

Shortly after the turn of the millennium, researchers who investigated thermal management of high powered microprocessors, suggested an upper limit to the cooling capability by the forced convection of air to ~50 W/cm^2 mean dissipated power density (Zhang et al. 2003; Lasance, 2005) and ~250W maximum power dissipation (Xu et al. 2004). While advances in forced convection of air cooling technology have allowed microprocessors to slightly exceed these value (Figure 1.1), the trend still shows roughly ~50 $\underline{+}$ 10 W/cm^2 mean power density after ~2006, for high powered CPUs and GPUs, as well as ~250W maximum power dissipation for a single chip die, with very little movement upward, making the predictions by (Zhang et al. 2003; Xu et al. 2004; Lasance, 2005) in previous years accurate. AMD, who has pushed beyond 60 W/cm^2, has begun to use new technologies for the thermal management of the highly power dense microprocessors. Closed loop liquid coolers (CLCs) (Figure 2.2) that operate on the forced convection of liquid, have been implemented on recent high powered CPUs and

GPUs manufactured by AMD (AMD Corporation, 2015). The next section discusses cooling by the forced convection of liquid in microchannels.

Figure 2.2. The closed loop liquid cooler is a high performance microprocessor cooling alternative to high end air cooling.

2.1.3 Forced Convection of Liquid in Microchannels Cooling

Forced convection of liquids in microchannel heat sinks have slowly become introduced for the cooling of high performance microprocessors. This method of cooling has been reported to achieve thermal resistances as low as ~0.1 ^{o}C/W (Schmidt 2004; Kou et. al, 2008). Forced convection of liquids require the proper selection of parameters such as operating pressure, coolant, flow rate (Anandan and Ramalingam, 2008), microchannel specifications, radiator fins per inch, and long term operation reliability. The packages come in many sizes, with CLCs being amongst the smallest. As the long term reliability of closed loop liquid coolers (CLCs) becomes realized, these coolers will replace air coolers that have are very near their maximum cooling potential (Zhang et al. 2003; Xu et al. 2004; Lasance, 2005; Figure 1.1) for higher powered microprocessors. As mentioned previously, the chipmaker Advanced Micro Devices has already started commercially using CLCs on their high performance CPUs and GPUs (AMD Corporation, 2015). However, the drawback of this method of cooling is that in the event of a pump failure, the cooling capability of the entire loop is entirely lost, as not even natural convection can operate within the confined spaces of microchannels. This technology will still likely become popular for the individual desktop workstations that contain just one or two high powered microprocessors, as the reliability and zero maintenance goal of the CLC is feasible. However, for large server farms and datacenters which contain hundreds and sometimes thousands of microprocessors, other cooling techniques, and preferably ones that lend themselves well to scale up, must be considered.

2.1.4 Jet Impingement and Spray Cooling

Micro-channels heat sinks cooled by forced convection of liquid, along with spray cooling and impinging jets, are methods of cooling that require circulating pumps and special arrangements to supply, distribute, and recollect the cooling liquid (Figure 2.3a) Jet impingement cooling offers the highest cooling capability for extremely high localized heat fluxes. However, it has inherent limitations that include the induced thermal stress caused by non-uniform surface and temporal distribution. Spray cooling provides uniform surface cooling, with much less impact on the integrity of the chip surface. However, a high pressure is required to break up the liquid into a spray or stream of very small liquid droplets, and a specially designed nozzle is required to ensure repeatable and long term cooling, while avoiding clogging (Figure 2.3b)(Hall and Mudawar, 1999; Tilton and Tilton 1993; Estes and Mudawar, 1995; Abbasi and Kim, 2010). The long term reliability of spray cooling has yet to be proven, and the constant replenishment of liquid also means the method of cooling is of high maintenance.

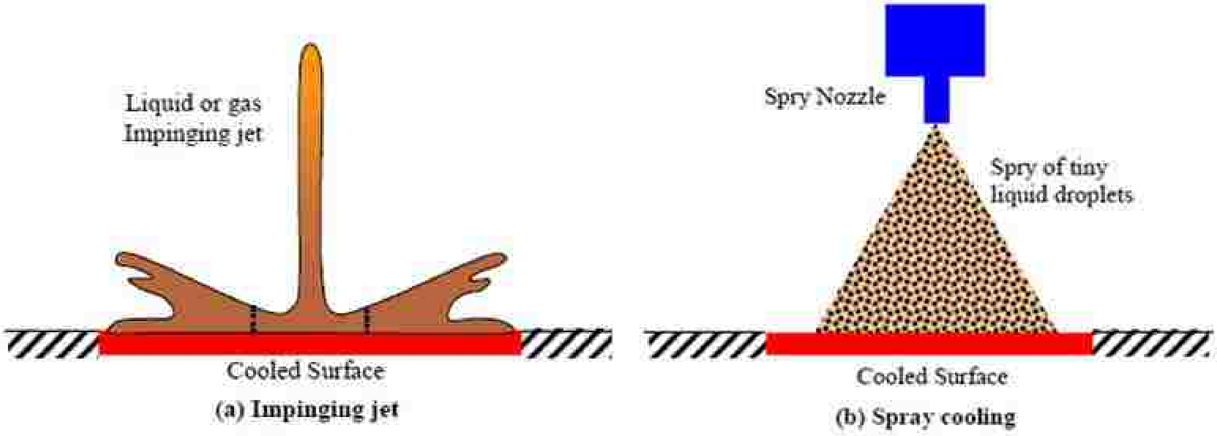

(a) Impinging jet

(b) Spray cooling

Figure 2.3. Schematics of cooling by (a) jet impingement and (b) spray cooling. (Ali, 2013)

2.1.5 Immersion Cooling by Pool Boiling

Immersion cooling by pool nucleate boiling (Figure 2.4) offers many advantages for the cooling of high power microprocessors. These include uniform surface temperatures, large scale cooling capability, an effective mitigation of chip hot spots (El-Genk and Ali; 2013) and low thermal resistance (El-Genk and Saber; 2008; El-Genk and Ali; 2013). Additionally, using low saturation temperature dielectric liquids, such as the Fluorinert FC-72 ($56^{o}C$ at ~ 0.1 MPa), the performance Fluid PF-5060 ($56^{o}C$ at ~0.1 MPa), or the Novec HFE-7000 (34 ^{o}C at 0.1 MPa), (3M Corporation, 2015) help keep $T_{j,max}$ below recommend values by the manufacturers (ITRS, 2013).

Other studies have also reported that two-phase cooling has the potential to reduce the energy consumption for large datacenters as much as 45% (Olivier et al. 2010; Oliver et al. 2011; Marcinichen et al. 2012) compared to using refrigerated air, and that even more savings can be realized by recycling the dissipated energy of the chips into the facility water and heating systems. One company that specializes in immersion cooling (Allied Control, 2015) claims 95% energy savings on cooling as one selling point. It can also simplify facility construction by reducing floor space requirements, by eliminating the need for air cooling infrastructure (Tuma, 2010). Figure 2.5 show images of some immersion cooled datacenters. For the cooling of high powered microprocessors, this is where immersion cooling has a lot of potential, as not only does it provide better performing, and simple thermal management of great numbers of microprocessors, but it also saves energy and floor space.

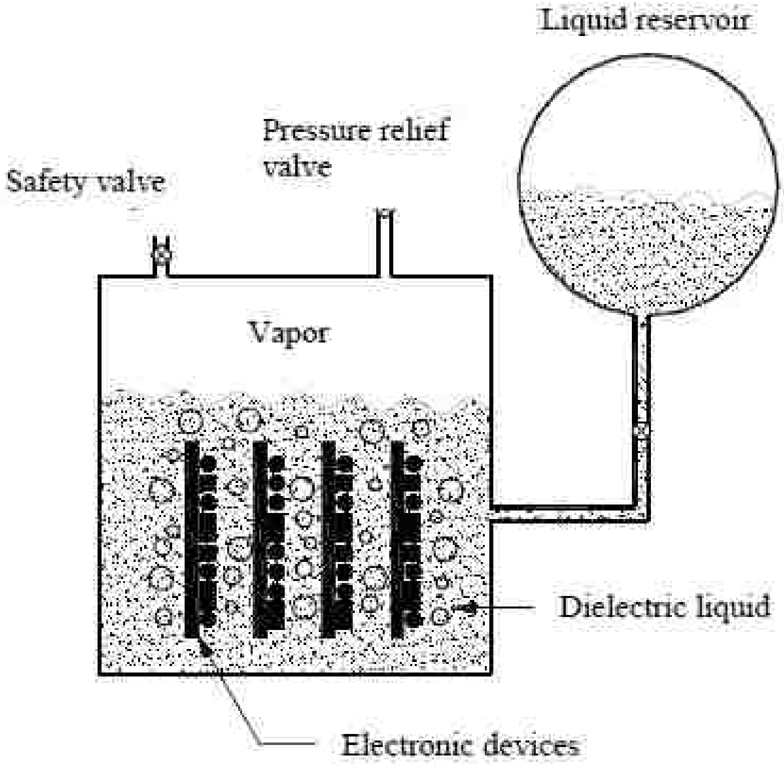

Figure 2.4. Schematic of an immersion cooling system (Abbasi and Kim, 2011).

Figure 2.5. Immersion cooling - CGG Datacenter, Houston TX.

2.2 Dielectric Liquids

Immersion cooling of microprocessors by nucleate boiling necessitates the use of dielectric liquids. Dielectric liquids have low dielectric constants (Table 2.1), are chemically compatible with electronics components, and environmentally friendly (3M Corporation, 2015). Additionally, the low saturation temperature dielectric liquids, such as the Fluorinert FC-72 (56^{o}C at ~ 0.1 MPa), the performance Fluid PF-5060 (56^{o}C at ~0.1 MPa), or the Novec HFE-7000 (34 ^{o}C at 0.1 MPa), (Table 2.1), help keep $T_{j,max}$ below recommend values by the manufacturer. Dielectric liquids also have low liquid surface tension (Table 2.1), which enhance nucleate boiling heat transfer through smaller bubble departure diameter and higher departure frequency.

Table 2.1. The Thermophysical properties of dielectric liquids PF-5060, HFE-7100, and HFE-7000 compared to Water (3M, 2015).

Physical Properties at T_{sat}.	PF-5060 (0.1 MPa)	HFE-7100 (0.1 MPa)	HFE-7000 (0.1 MPa)	Water (0.1 MPa)
Boiling point (^{o}C)	56.8	60	34	100
Freezing point (^{o}C)	-90	-135	-122.5	0
Molecular weight (g/mole)	338	250	200	18
Liquid density (kg/m^3)	1601	1372	1400	958
Vapor Density (kg/m^3)	13.127	9.7	8.17	0.6
Liquid viscosity (kg/m·s)	$4.6x10^{-4}$	$3.7x10^{-4}$	$3.2x10^{-4}$	$2.8x10^{-4}$
Liquid specific heat (J/kg·K)	1102	1253	1300	4220
Latent heat of vaporization (kJ/kg)	95.03	111.5	142	2256.7
Liquid thermal conductivity (W/m·K)	0.0537	0.062	0.075	0.68
Liquid surface tension (mN/m)	7.93	10	12.4	59
Dielectric constant	1.8	7.52	7.4	80

The highly wetting liquids cause large excursions in surface temperature prior to boiling incipience that could match or exceed 40^{o}C (Rainey and You, 2000; El-Genk and Bostanci, 2003a, b; El-Genk and Parker, 2004a, b;). However, the use of enhanced surfaces has allowed this obstacle can be overcome (Chang and You, 1996, Rainey and You, 2001; Sriraman and Banerjee, 2007, Im et al., 2012; El-Genk and Parker, 2008; El-Genk and Ali, 2010; Ali and El-Genk, 2013). In a study by Andersen and Mudawar (1989), the boiling incipience was found to be highly dependent on waiting between experiments, and increased as wait time increased. This suggested that the incipience of boiling was dependent on the vapor embryo size, rather than cavity size for highly wetting fluids such as dielectric liquids. They also reported that increased surface roughness promoted earlier boiling incipience.

For immersion cooling of microprocessors by pool nucleate boiling is a viable option for thermal management. The next section presents the fundamentals of pool nucleate boiling.

2.3 The Fundamentals of Pool Boiling and Bubble Growth

Figure 2.6 is the generalized pool boiling curve. The pool boiling curve is constructed experimentally by plotting the known surface heat flux to the measured wall superheat. In Figure 2.6, the regions of the boiling curve are labeled and are presented in the following sub-section by order of: (a) natural convection, (b) discrete bubbles region, (c) fully developed nucleate boiling and (d) lateral coalescence region. Also labeled are the points of nucleate boiling incipience, the maximum nucleate boiling heat transfer coefficient, h_{MNB}, and the critical heat flux (CHF). These points separate the different regions of the pool boiling curve, as well as mark the end of nucleate boiling at the CHF.

2.3.1 Natural Convection and Temperature Excursion

Prior to the boiling incipience, cooling by natural convection occurs (Figure 2.6). The temperature difference between the surface and bulk liquid causes a density gradient in a thin film of liquid along the heated surface. The resulting buoyant force pushes the heated liquid upward and away from the surface, and the replacement heavier bulk liquid drops down toward the heated surface. This circulatory process will continue indefinitely as long as the heated wall is warmer than the bulk liquid it is submerged in. The total heat transfer flux removed by natural convection from uniformly heated surfaces is

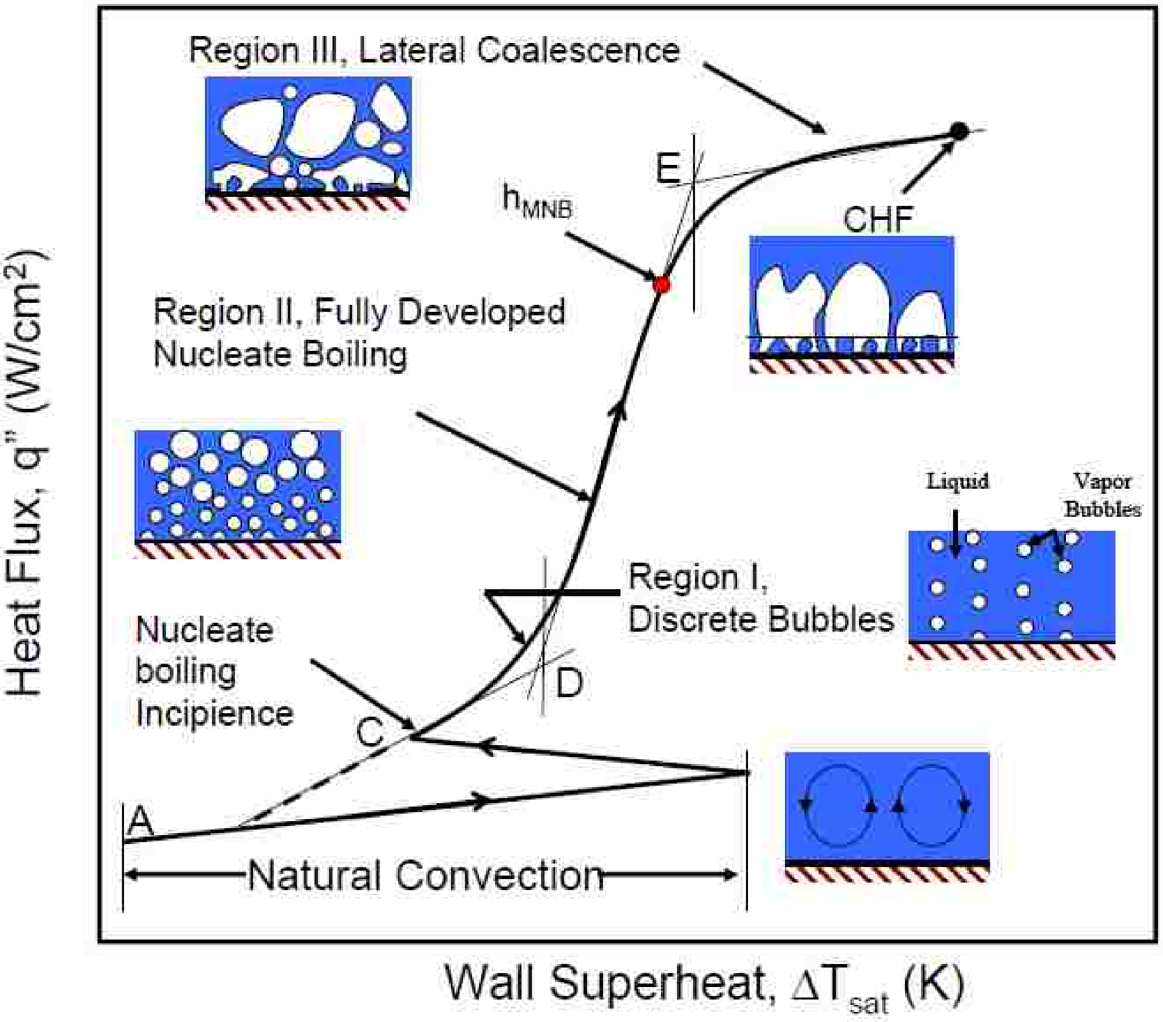

Figure 2.6. The general pool nucleate boiling curve with of dielectric liquids with labeled regions and points of interest (El-Genk and Ali, 2010).

proportional to the temperature difference between the surface and bulk liquid to the power 1.2 (Chang and You, 1996; Rainey and You, 2001; Ali and El-Genk, 2013).

$$q_{NC} \propto (T_w - T_{sat})^{1.2} \tag{2.1}$$

Highly dielectric liquids are subject to the temperature excursion prior to boiling incipience, and is when wall temperatures well in the excess of the saturation temperature are required to initiate nucleate boiling (Rainey and You, 2000; El-Genk and Bostanci, 2003a, 2003b). The highly wetting liquids deeply flood cracks, crevices, and grooves along the surface that may serve as active nucleate sites for bubbles nucleation. The smaller trapped pockets of air must first expand to sufficient size (Figure 2.7) before bubbles nucleation may begin. Temperature excursion is undesirable for the microprocessor cooling application, as temperature excursions as high as 25-40K for dielectric liquids have been reported (Rainey and You, 2000; El-Genk and Parker, 2004a, 2004b; El-Genk and Bostanci, 2003a, 2003b), and cause concern for the chip junction's maximum temperature. The sudden change in temperature at the incipience boiling after a large temperature excursion may also cause concern from a materials stress standpoint. Surfaces for the enhancement of nucleate boiling have been reported to reduce or remove entirely the temperature excursion of dielectric liquids. (Chang and You, 1996; Rainey and You, 2001; Sriraman and Banerjee, 2007; El-Genk and Parker, 2008; El-Genk and Ali, 2010; Im et al., 2012; Ali and El-Genk, 2013)

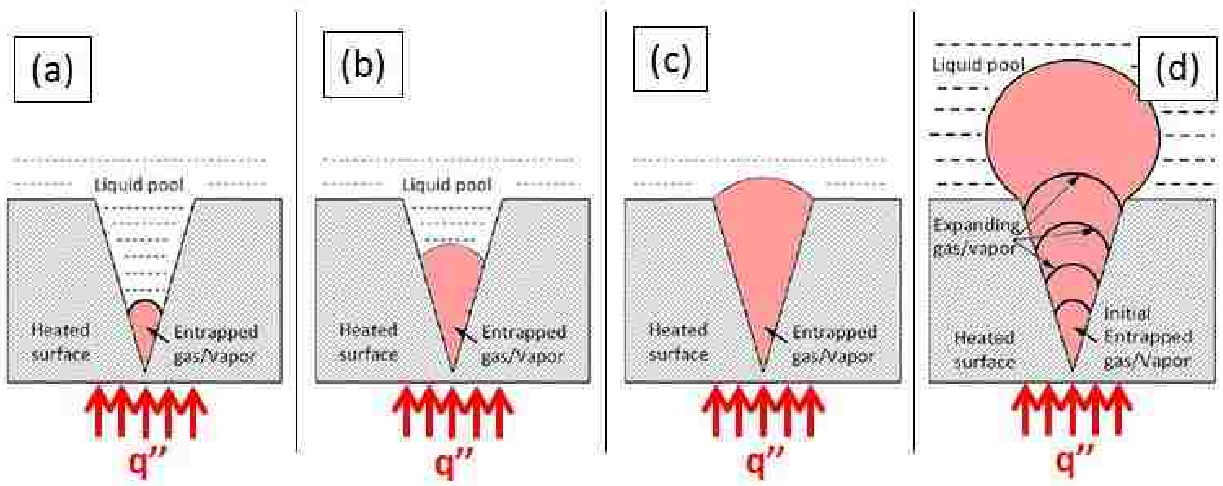

Figure 2.7. Growth of entrapped gas to bubble nucleation during temperature excursion.

2.3.2 Discrete Bubbles Region and Vapor Bubble Growth

After the incipience of nucleate boiling, marked by location "C" in Figure 2.6, the discrete bubbles region lasts for a short duration before the fully develop nucleate boiling region. For poorly wetting liquids, the incipience of boiling begins at lower surface heats, and follows the path marked by the dashed line in Figure 2.6. In the discrete bubbles region, few of all potential sites for bubbles nucleation are active. Many bubble visualization studies have been conducted in the discrete bubbles region, as the ebullition cycle of a single bubble may be captured in full detail without disturbance from neighboring sites (section 2.6). The bubble dynamics captured in the discrete vapor bubbles region have been used to determine the nucleate boiling characteristics of enhanced surfaces, as well as calculate the active nucleation sites density of the surface. Figure 2.8 is a schematic of the general ebullition cycle of a discrete vapor bubble. When the vapor bubble first begins to grow, it is inertially driven. This phase of growth is much faster than the thermally driven growth phase that follows, and lasts only on the order of ~1ms. The thermal growth is a much more stable growth, where typically the diameter of the bubble D_b, increases proportionally to the square root of the growth time. After the bubble has reached a sufficient size where the buoyant, viscous, and drag forces are able to overcome to surface tension force, the bubble departs, carrying the superheated vapor away from the surface, completing the ebullition cycle. This cycle then repeats itself indefinitely. The growth of the bubble is the means of heat removal from the surface, as liquid is vaporized. The detachment of the bubble moves the removed heat far away from the surface, and so the process may continue.

2.3.3 Fully Developed Nucleate Boiling and Bubbles Coalescence Regions

When enough heat is supplied to the surface such that all potential sites for bubbles nucleation are active, the surface undergoes fully developed nucleate boiling (Figure 2.6). As a result, the nucleate boiling heat transfer coefficients are highest, as indicated by the steepest slope of the boiling curve (Figure 2.6). As the heat flux is increased, the vapor bubbles grow and depart more quickly, enhancing the nucleate boiling heat transfer coefficient until reaching the maximum nucleate boiling heat transfer coefficient, $h_{MNB.}$ The h_{MNB} marks the end of the fully developed region, and is followed by the bubbles coalescence region with the further increase of applied heat flux.

In the bubbles coalescence region, the heat transfer coefficient decreases with increases in the input power, and results in larger increases of the surface temperature. This is caused by the added resistance to heat transfer by the coalescence of the growing and rising bubbles at and near the heated surface (El-Genk and Bostanci, 2003; Parker and El-Genk 2005). At the end of this region, failure to sufficiently replenish the surface with liquid, triggers critical heat flux (CHF), and surface dryout. The CHF is a limit not to exceed in electronics cooling application, and it is preferable to operate near and to the left of the h_{MNB} where heat transfer is higher and wall superheats are lower.

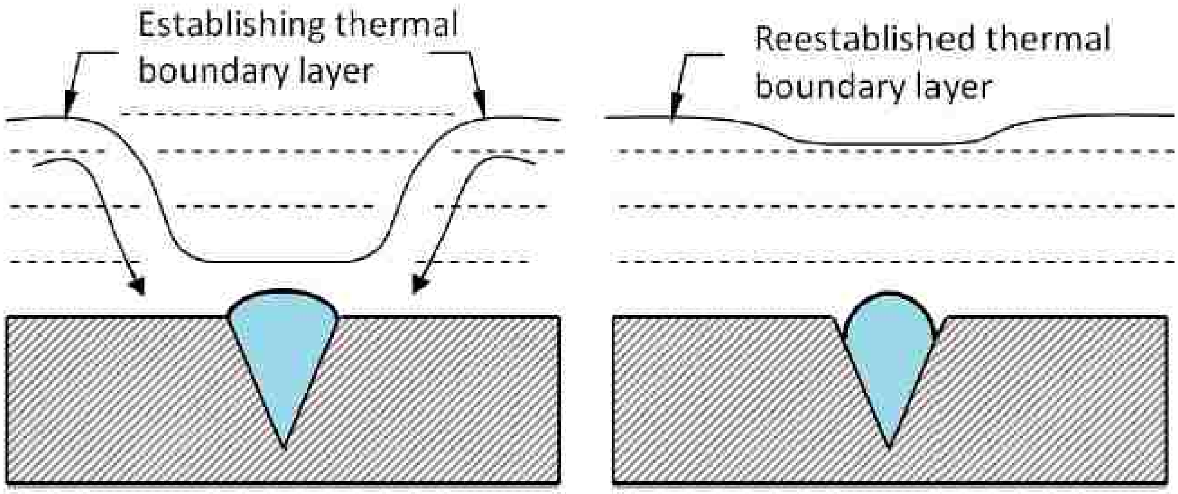

(a) Re-establishing thermal boundary layer after bubble departure, t = 0

(b) Re-established thermal boundary layer after bubble departure, , $t=t_{wait}$

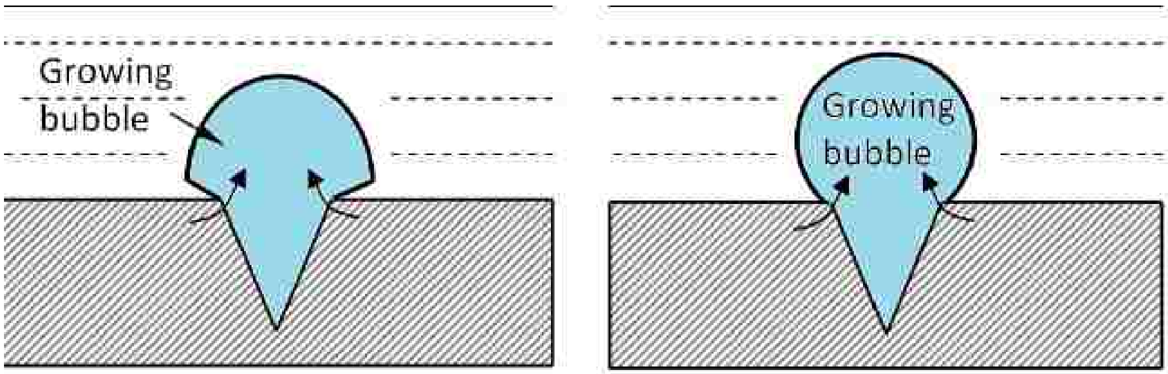

(c) Inertia driven bubble growth

(d) Thermally driven bubble growth

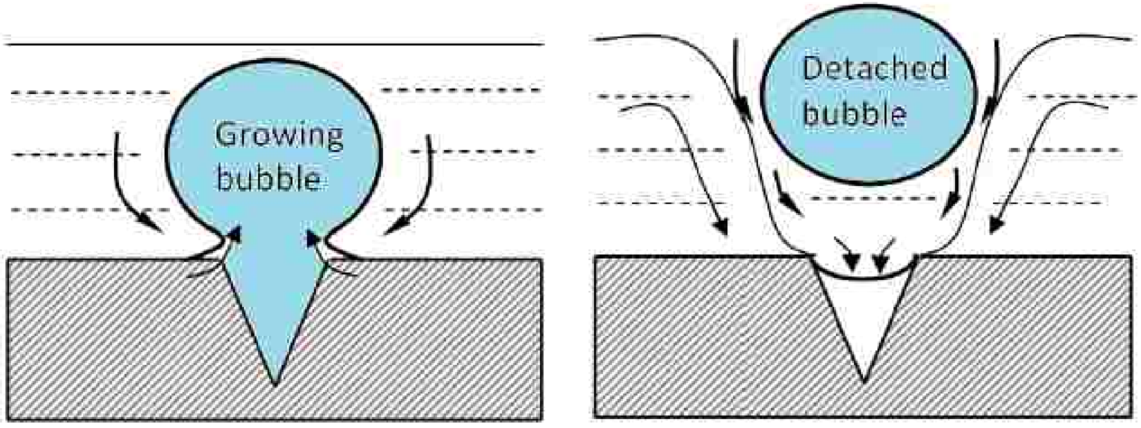

(e) Pinching of a detaching

(f) Rise of detached bubble, t = 0

Figure 2.8. Illustration of bubble Ebullition cycle in nucleate boiling (Ali, 2013)

2.3.4 Critical Heat Flux

The CHF occurs when surface heat fluxes high enough cause the departure from nucleate boiling. When this happens, individual bubbles no longer form and break away from the surface, but instead film vapor bubbles form and blanket the boiling surface from the bulk liquid. This results in a critical situation where a significant temperature spike at the surface can melt out the surface material or burnout the underlying hardware. Thus CHF imposes a limit on the design and operation of boiling heat transfer equipment. Boiling water reactors, for example, will operate at only about ~1/3 surface heat flux of the estimated CHF.

2.4 Critical Heat Flux

Models describing the mechanism responsible for CHF have been proposed (Kutateladze, 1952; Griffith, 1957; Zuber, 1959; Haramura and Katto, 1983). The microlayer model, proposed by Haramura and Katto (1983), describes the existence of a liquid microlayer beneath large vapor slugs or vapor mushrooms on the heated surface in the bubbles coalescence region. Coalescing bubbles at a number of adjacent sites isolate thin layers of liquid beneath the vapor slugs (Figure 2.9b). These vapor stems still feed the growing vapor bubble through evaporation. The large vapor slugs hover over the surface until enough vapor has been accumulated to detach. If the vapor stem evaporates before the vapor slug detaches, a local surface dryout has occurred (Figure 2.9c). This greatly increases the local thermal resistance, and forces the local heat flux to move to adjacent vapor slugs (Figure 2.9d), causing subsequent local dryout that very rapidly spread to full surface dryout, and CHF (Figure 2.9e) and the departure from nucleate boiling to film boiling (Figure 2.9f) ensures.

Zuber (1959) and Kutateladze (1952 and 1961), independently arrived at a similar relationship to predict the CHF for saturation pool boiling at the upward facing orientation as:

$$CHF_{sat}(\theta = 0^{o}) = C_{CHF,sat}(\theta = 0^{o}) h_{fg}\sqrt{\rho_g}[\sigma(\rho_l - \rho_g)]^{0.25} \tag{2.2}$$

The coefficient $C_{CHF,sat}$ was fixed to $\pi/24$ (~0.131) by Zuber (1959). Kutateladze (1952 and 1961) varied the value of coefficient from 0.13 to 0.19 for water and organic liquids boiling on graphite disks, chrome plated disks, and wires of different composition. The value of the coefficient, $C_{CHF,sat}$, for dielectric liquids has been reported to be dependent on the boiling surface characteristics, (El-Genk and Parker, 2008; El-Genk and Bostanci, 2003; Priarone, 2005; Ali and El-Genk, 2012, 2013) and have been reported to be anywhere from 0.26 to 0.96 for FC-72 and HFE-7100 liquids on porous graphite, microporous coated, and micro-finned surfaces (Mudawar, Howard, and Gersey, 1997; Arik, Bar-Cohen, and You 2007; Parker and El- Genk, 2006a,b; Parker and El-Genk, 2008; El-Genk and Parker, 2008; El-Genk and Ali, 2010; Ali and El-Genk, 2013;).

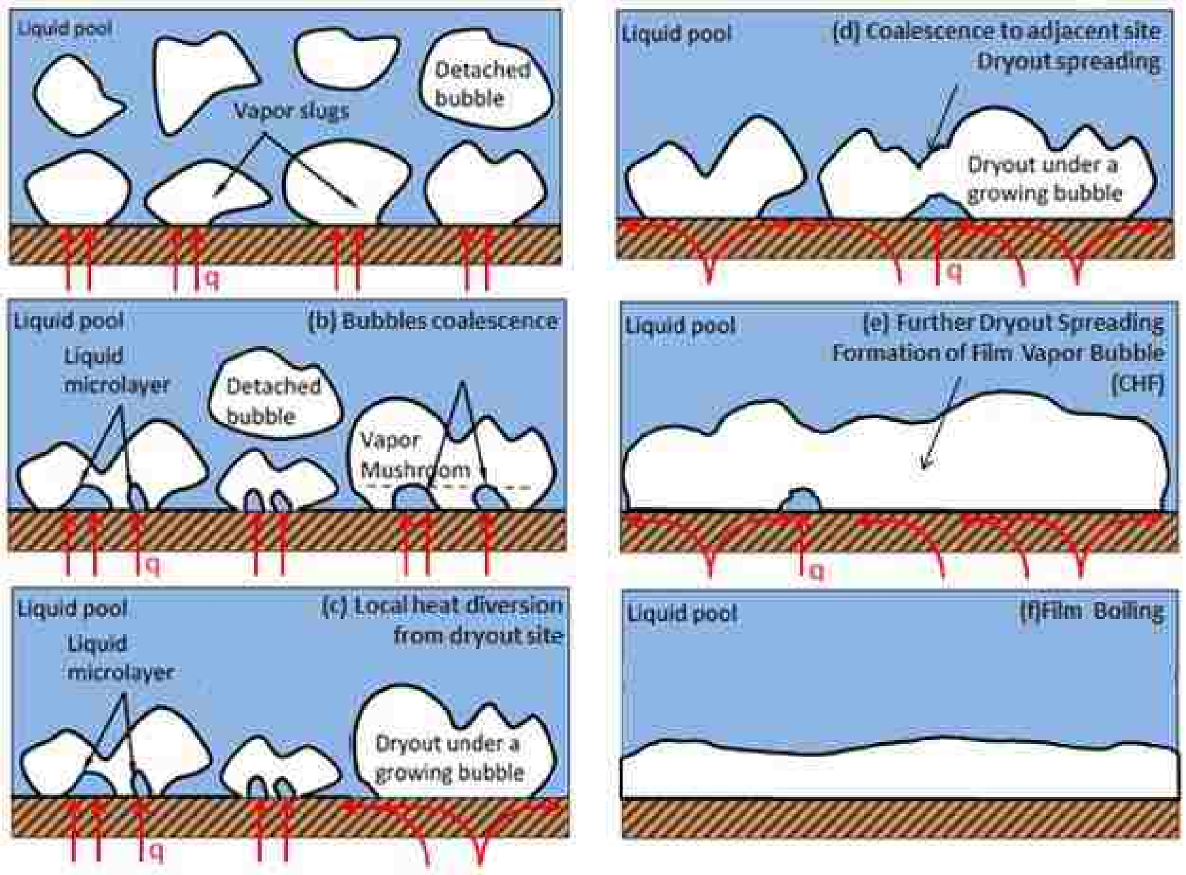

Figure 2.9. Vapor bubble and surface dynamics for triggering the critical heat flux.

2.5 Active Nucleation Sites Density

Active sites densities for bubble nucleation of dielectric liquids of FC-72 and FC-77 on smooth and roughened surfaces, and micro structured surfaces have been reported (Ramswamy et al., 2002; McHale and Garimella, 2008, 2010). The active nucleation site density has been estimated using proposed mathematical models, or with the aid of high speed visualization that captured high speed images of nucleate boiling (Section 2.6). For example, Ramswamy et al. (2002) observed a number of FC-72 bubble active sites on their interconnected micro-channels structured surface from high speed captured images, and was able to calculate the active site density. McHale and Garimella (2010) measured the mean bubble departure diameter and frequency of FC-77 on aluminum surfaces, and used the measurements to estimate the number of active sites.

Mathematical models for determining the active nucleation site density are generally based on the thermophysical properties of the liquid and surface characteristics (Lorenz, 1971; Yang and Kim, 1988; Benjamin and Balakrishnan, 1997; Kocamustafaogullari and Ishii, 1983; Hibiki and Ishii, 2003). Surface characteristics including the size of the cavity mouth, and the angle (assuming a conical shape) (Lorenz, 1971; Yang and Kim, 1988), and surface roughness (Benjamin and Balakrishnan, 1997) have all been used to construct the models to determine the active nucleation site density.

Kocamustafaogullari and Ishii (1983) assumed the active nucleation site density in pool boiling was influenced by fluid properties. A correlation was introduced as a function of liquid and vapor properties, and bubble departure diameter. They compared the correlation with existing experimental data and concluded that the developed correlation gave reasonable predictions. Benjamin and Balakrishnan (1997) introduced a correlation for the active nucleation site density in pool boiling of different pure liquids at low and moderate heat fluxes on stainless steel and aluminum surfaces with different surface finishes. The average surface roughness of the surfaces ranged from 0.2 – 1.2 μm. The correlation derived, as a function of Ra and a new coefficient similar to that proposed by Rohsenow (1952), accounted for the surface liquid interaction. A similar study carried out by Benjamin and Balakrishnan (1997) obtained an additional parameter that accounted for the surface physical properties, and variation of the physical properties of binary mixtures was introduced.

Hibiki and Ishii (2003) introduced a mathematical model to predict the active nucleation sites density in pool and flow boiling, in fully developed nucleate boiling. The model accounts for the effect of contact angle (or surface wettability), ϕ, the critical cavity radius, and surface superheat on the active nucleation sites density. The devolved correlation covered a wide range of static contact angles, ranging from 5^o to 90^o. and was validated using by predicts of other models and experimental data for different liquids, with deviation of ± 50%.

More general approaches equate the total rate of the thermal heat removed from the surface and the volume of the generated bubbles on the surface. The total rate of the heat removed is then simply a function of the bubble departure diameter, detachment frequency and the surface density of active nucleation sites.

2.6 Bubble Visualization Studies

2.6.1 Bubble departure diameter and detachment frequency

Investigators determined that increasing the surface roughness enhances surface hydrophobicity (Wenzel, 1949; Hong et al. 1994; Bico et al. 2002; Hosseini et al. 2011). For hydrophilic surfaces, this in turn decreases the bubble departure diameter, increases detachment frequency, and may thus enhance nucleate boiling. Images provided by investigators who mixed hydrophobicity along the same surface showed hydrophilic zones to contain small rapidly departing bubbles, whereas hydrophobic zones contained large slowly departing bubbles (Hsu et al. 2012a; Hsu et al. 2012b). The bubble dynamics have been shown to play a large role in observed nucleate boiling performance.

Bubble visualization studies have been performed to examine the effects of surface characteristics and heat flux on the bubble departure diameter and detachment frequency in saturation boiling of dielectric liquids. Rinni et al. (2001) measured bubble departure diameter of FC-72 on a synthetic diamond transparent plate, and reported the mean departure diameter of 400 – 500 µm was not strongly affected by the applied heat flux, which was varied from 4 – 10 W/cm^2. Ramswamy et al. (2002) reported bubble departure diameters between 500 – 700 µm and corresponding detachment frequencies of 170 – 200 Hz for nucleate boiling of FC-72 on Si surfaces with interconnected microchannels. They indicated that the pore diameter was most influential on the bubble departure diameter, with wall superheat also affecting bubble departure diameter. However, at lower surface superheats (4 – 6K), the bubble detachment frequency was independent of surface characteristics and superheat.

El-Genk and Bostanci (2003) reported a bubble departure diameter of 550 µm ± 70 µm and corresponding detachment frequency of 100Hz in saturation nucleate boiling of HFE-7100 on smooth Cu at a heat flux of ~0.5W/cm^2. Demiray and Kim (2004) measured the bubble departure diameter in FC-72 on a quartz wafer, and reported values of ~500 µm at low subcooling. Nikmar et al. (2006) reported bubble departure diameters in saturation boiling of FC-72 on Si surfaces that ranged from 260 – 450µm and detachment frequencies of 55 – 68 Hz. Both the bubble departure diameter and detachment frequency were found to increase with increasing heat flux, which was varied from 1 – 9 W/cm^2. In another work by Nikmar et al. (2006) on nucleate boiling of FC-72 on aluminum, brass, and copper, performance differences were attributed to the bubble growth rates, which were higher on the surfaces with higher thermal conductivity.

McHale and Garimella (2008) reported that the bubble departure diameters in saturated boiling of FC-72 on Indium Tin Oxide surfaces with average roughness 0.263 – 7.51 µm, ranged from 400 – 600 µm, and showed surface roughness to have a small effect on bubble departure diameter and detachment frequency. In another study by McHale and Garimella (2010) of saturated boiling of FC-77 liquid on smooth and rough aluminum surfaces, they reported the smooth surface to have a bubble departure diameter that increased from 600 – 2000 µm, and corresponding detachment frequency of 40 – 150 Hz, as the applied heat flux increased from 2 – 11 W/cm^2. For the rough aluminum surface, the bubble departure diameters were 400 – 500 µm and detachment frequencies of 80 – 200Hz. These results showed roughened surfaces to have less effect on bubble departure diameter with increasing heat flux.

Hutter et al. (2010) measured the bubble departure diameter and detachment frequency in saturation nucleate boiling of FC – 72 on silicon surfaces with artificial cavities. They reported bubble departure diameters of 200 – 500 µm and detachment frequencies of 10 – 40 Hz depending on the wall superheat. McHale and Garimella (2013) reported bubble visualization results for saturation nucleate boiling of FC-72 on borosilicate float glass roughened by diamond abrasion paste. The reported a mean bubble departure diameter of 400 – 500 µm and corresponding detachment frequency of 100 – 200Hz appeared to be independent of surface roughness. Table 2.2 provides a summary of these reported studies. Reported correlations to predict the bubble departure diameter and detachment frequency are discussed next.

2.6.2 Bubble departure diameter and detachment frequency correlations

Fritz (1935) introduced the earliest correlation to predict the bubble departure diameter. It is a function of the static contact angle, and was derived from balancing the surface tension and buoyant forces for water and Hydrogen bubbles at low heat flux. Zuber (1959) introduced a relationship for the product of the bubble departure diameter and detachment frequency, and is dependent on buoyant and surface tension forces. In a similar analysis from the balance of forces on the bubble at the moment of departure, Ruckenstein (1961) obtained an expression for the departure diameter, but considered the buoyant and drag forces only. The drag and acceleration forces were added in a correlation introduced by Roll and Myers (1964).

Zuber's relationship states that the product of the departure diameter and detachment frequency should equate to a constant along the same or similar surfaces. Ivey (1967) modified Zuber's relationship to be dependent on whether the departing bubble is inertially or thermally growth driven. Mikic and Rohsenhow (1969) introduced a correlation to predict bubble departure diameter that is dependent on surface, buoyant forces, as well as the Jacob Number which introduces the effect of surface superheat.

Kutateladze and Gogonin (1979) developed a correlation to predict the bubble departure diameter that introduced the Prandtl number, P_r, and presented it in terms of the Bond number, *Bo*. Little information was provided as to how this correlation was developed, though Jensen and Memmel (1986) modified the constants of this correlation. Kim et al. (2006) developed a correlation using a wide set of data across many fluids to predict the bubble departure diameter. Phan et al. (2010) developed a correlation to predict bubble departure diameter from numerical analyses, and used a wide range of experimental data to validate it. The list of correlations discussed is provided in Table 2.3.

The wide range of bubble departure diameters and detachment frequencies reported for dielectric liquids warrants more experimental bubble departure diameter and detachment frequency data – and preferably for liquids such as PF-5060 which have little data available, and is the focus of the bubble visualization chapter in this dissertation.

Table 2.2. Reported bubble departure diameter and detachment frequency for various dielectric liquids.

Surface	Liquid	Parameter(s)	D_d (µm)	f (Hz)	ref
Synthetic diamond plate	FC-72	Heat Flux 4-10 W/cm^2	400 – 500	~	(1)
Microchannel Si	FC-72	Pore diameter Heat Flux	500 – 700	170 – 200	(2)
Smooth Cu	HFE-7100	Heat Flux = 0.5 W/cm^2	550 µm ± 70	100	(3)
Quartz Wafer	FC-72	Subcooling	350 – 500	~	(4)
Smooth Si	FC-72	Heat Flux 1-9 W/cm^2	260 – 450	55 – 68	(5,6)
Rough ITO	FC-72	Surface roughness	400 – 600	~	(7)
Smooth Al	FC-77	Heat Flux 2-11 W/cm^2	600 – 2000	40 – 150	(8)
Rough Al	FC-77	Heat Flux 2-11 W/cm^2	400 – 500	80 – 200	(8)
Si w/ artificial cavities	FC-72	Wall superheat	200 – 500	10 – 40	(9)
Rough borosilicate float glass	FC-72	Surface roughness	400 – 500	100 – 200	(10)
Microporous Copper	PF-5060	Heat Flux = 0.5 W/cm^2 MPC layer thickness	431 µm ± 7	36 ± 2	(11)

(1)Rinni et al. (2001), (2)Ramswamy et al. (2002), (3)El-Genk and Bostanci (2003), (4)Demiray and Kim (2004) (5,6), Nikmar et al. (2006), (7,8)McHale and Garimella (2008, 2010), (9)Hutter et al. (2010), (10)McHale and Garimella (2013), (11)El-Genk and Ali (2013)

Table 2.3. Available correlations to predict bubble departure diameter and detachment frequency.

Correlation	Liquids	Ref
$D_d = 0.0208\emptyset\sqrt{\frac{2\sigma}{g(\rho_l - \rho_v)}}$	Water, Hydrogen	Fritz (1935)
$f_d D_d = 0.59(\frac{\sigma g(\rho_l - \rho_v)}{\rho_l^2})^{0.25}$	Water	Zuber (1963)
$f_d^2 D_d = constant\ for\ intertial\ driven\ growth$ $f_d^{0.5} D_d = constant\ for\ thermal\ driven\ growth$		Ivey (1967)
$D_d = 1.5 * 10^{-4}\sqrt{\frac{2\sigma}{g(\rho_l - \rho_v)}}(Ja\,*)^{\frac{5}{4}}\ for\ water$ $D_d = 4.65 * 10^{-4}\sqrt{\frac{2\sigma}{g(\rho_l - \rho_v)}}(Ja\,*)^{\frac{5}{4}} for\ others$	Water, HFE-7100, R11, R113	Rohsenhow (1969)
$B_o = 0.25(1.0 + 10^5 K_1)^{1/2}$ $K_1 = Ja/\mathrm{Pr}\{(\frac{g\rho_l(\rho_l - \rho_v)}{\mu_l^2})(\frac{\sigma}{g(\rho_l - \rho_v)})^{3/2}\}^{-1}$ $B_o = gD_b^2(\rho_l - \rho_v)/\sigma$		Kutateladze and Gogonin (1979)
$B_o = 0.19(1.8 + 10^5 K_1)^{\frac{2}{3}}$		Jensen and Memmel (1986)
$D_d = 2(25\sqrt{\frac{27}{2}}\,Ja\,\alpha\sqrt{\rho_l/\sigma})^2$	Water, n-Pentane, R11, R113, FC-72, Methanol	Kim and Kim (2006)
$D_d = (6\sqrt{\frac{3}{2}})^{\frac{1}{3}}(\frac{\rho_l}{\rho_v})^{-\frac{1}{2}}(\frac{\rho_l}{\rho_v} - 1)^{\frac{1}{3}} tan\Phi^{-\frac{1}{6}}(\frac{\sigma}{g(\rho_l - \rho_v)})^{\frac{1}{2}}$	Numerical: Water, FC-72, HFE-7100, n-Pentane, R11, R113	Phan et al. (2010)

2.7 Enhancement of Nucleate Boiling on Rough Surfaces

2.7.1 Early Studies

Surface roughening has been known to effect nucleate boiling as far back as 1935, when Jakob and Fritz (1931) photographically studied the bubble behavior of water on different heated surfaces, and noted roughened surfaces to generate more bubbles than smooth surfaces. Corty and Foust (1953) realized the influence of surface roughness and its effect on the required ΔT_{sat} to sustain nucleate boiling of Freon 113 at any given heat flux. This ΔT_{sat} decreased for rougher surfaces. Clark et. al (1959) discovered the pits and scratches (common features of a roughened surface) served as active nucleation sites for bubbles growth in nucleate boiling of Ether Pentane. Berenson (1962) reported an increase of up to 600% in nucleate boiling heat transfer of n-pentane on roughened surfaces, compared to smooth surfaces. Berenson (1962) also reported and agreed with Zuber (1959) that the critical heat flux (CHF) was not effected by roughness. Kurihara and Myers (1962) found surface roughness to effect the slope of the boiling curve, and stressed the importance of surface preparation to have an impact on the results. Hsu (1962) developed a theoretical model that predicts the size range of active nucleation cavities. This model has been by others to interpret the increase of active nucleation sites density caused by surface roughening. The results reported by Kozitskii (1971) on saturation boiling of n-butane on stainless steel tubes with an average surface roughness of 0.03 lm–1.3 μm, showed the h_{NB} increased as the surface roughness did up to 0.95 μm. At higher surface roughness, the enhancement in h_{NB} diminished with increased roughness up to 1.31 μm. The results also indicated that the h_{NB} increases proportionally to the applied surface heat flux, q, with an exponent "m" that varied from 0.72 to 0.8 for the range of Ra investigated. Sauer et al. (1975) reported sand paper treated surfaces had 20% higher heat transfer coefficients than of polished surfaces in the boiling of refrigerants.

2.7.2 Correlations to Predict Nucleate Boiling Heat Transfer

Mikic and Rosenhow (1969, 1970), developed an empirical correlation for nucleate boiling heat transfer that predicted the relationship between the applied heat flux, q, and surface superheat, ΔT_{sat}, if the active nucleation site density and bubble departure diameter was known. While the correlation claimed to be inclusive of surface characteristics such as surface roughening, experimental data is required beforehand to make use of the correlation. Copper (1984) proposed a reduced pressure form of a pool boiling correlation that included the surface roughness as a variable given as:

$$h_{NB} = 55p_r^{0.12-0.4343\, lnR_p}(-0.4343lnp_r)^{-0.55}M^{-0.5}q^{0.67} \tag{2.3}$$

where M is the molecular wright of the fluid, and R_p is the surface roughness in μm. This correlation also became the basis for predicting the nucleate boiling heat transfer coefficient in the form of: h_{NB} α Aq^B. The Copper correlation covers a range of reduced pressures from 0.001 ~0.9 and molecular weights of 2 to 200 (Cooper, 1984).

Gorenflo (1993) introduced a fluid specific reduced pressure correlation to predict nucleate boiling heat transfer, and included the effect of surface roughness. Gorenflo's correlation predicts the h_{NB} when a reference heat transfer coefficient, $h_{NB,0}$, is known at the reference conditions of reduced pressure, $p_{r0} = 0.1$, $Ra_0 = 0.4$ μm, and $q_0 = 2$ W/cm^2. Gorenflo (1993) provided values of the $h_{NB,0}$ for many alcohols and refrigerants, however if one was not known, it had to be obtained experimentally first to make use of the correlation. Gorenflo's correlation to predict the nucleate boiling heat transfer coefficient, h_{NB}, at a specified pressure, heat flux, and surface roughness, relative to the reference conditions is calculated using the following expression:

$$h_{NB} = h_{NB,0}F_{PF}(\frac{q}{q_0})^{nf}(\frac{R_a}{0.4})^{0.133} \tag{2.4}$$

$$nf = 0.9 - 0.3p_r^{0.3}$$

$$F_{PF} = 1.2p_r^{0.27} + 2.5p_r + \frac{p_r}{1-p_r} \tag{2.5}$$

This correlation is for a range of reduced pressure from ~0.001 to ~0.95, and is inclusive of very many boiling fluids as well as surface materials.

Ribatski and Jabardo (2003) introduced a modified form of the Cooper (1984) correlation for nucleate boiling of halocarbon refrigerants. The correlation expressed the nucleate boiling heat transfer coefficient, h_{NB}, as a function of surface roughness, Ra, reduced pressure p_r, heat flux q, and molecular weight M, as:

$$h_{NB} = B(q^{0.9-0.3p_r^{0.2}})p_r^{0.45}(-lnp_r)^{-0.8}{R_a}^{0.2}\sqrt{M} \tag{2.6}$$

The empirical constant B was given the following values : B = 85 for stainless steel (SS), B = 100 for Cu, and B = 110 for brass. The covered ranges of variables in this correlation were: $p_r = 0.008 – 0.26$, $q = 2.3 – 120$ W/cm^2, Ra = 0.02 – 3.3 μm, and surface materials of brass, Cu and SS.

2.7.3 More Recent Studies

As more boiling liquids became available, such as dielectric liquids, and experimental methods were improved, the study on the effect of surface roughness on nucleate boiling heat transfer picked up during in the past decade. Rainey and You (2000) reported experimental results on saturation boiling of FC-72 on a machine roughened Cu and compared the results to that of a polished Cu surface (Chang and You, 1996). The temperature excursion at the boiling incipience on the polished Cu was ~40 K, and for the machine-roughened Cu surfaces, the temperature excursions were 27 K and 10 K, respectively. The heat transfer coefficient on the roughened surface was about ~5 times higher, and the CHF increased by ~40%. These enhancements were attributed to the trapped air in small surface features. Kang (2000) reported surface increase to increase nucleate boiling heat transfer and CHF on vertical tubes by as much as 230%. He also reported surface roughness to have more of an impact at the vertical orientation due to increased liquid agitation, as the impact of surface roughness was greater as length to diameter of the tubes increased. Ribatski and Jabardo (2003) sandblasted brass, Cu, and SS surfaces and varied Ra from 0.07 μm to 2.6 μm, for the nucleate boiling of refrigerants. They reported an improvement in nucleate boiling heat transfer, and found the correlation developed by Gorenflo (1993) to predict best against their experiments.

Nimkar et al. (2006) conducted saturation pool boiling experiments of FC-72 on Aluminum (Al), Cu, and brass surfaces. They reported the Cu surfaces to perform best, despite the same Ra across the different surface, and attributed the performance to the surface material thermal conductivity. Jones (2007) reported surface roughness to improve nucleate boiling heat transfer of water at low Ra, however found little improvement at higher Ra. Jabardo et. al (2008) performed saturation pool boiling experiments of R-134a and R-123 on brass, Cu, and SS test sections that varied Ra from 0.03 – 10.5 μm. They reported surface roughness to initially increase the nucleate boiling heat transfer performance, and decrease at high Ra. They also reported the Cooper correlation (Equation (2.3)) to significantly over predict the experimental results for higher surface roughness.

Jones et al. (2009) performed saturation nucleate boiling of FC-77 on an aluminum test block that had Ra varied from 0.027 – 10 μm. They reported inconstancies in the effect of surface roughness on the nucleate boiling heat transfer, and that no correlations were available to accurately predict the experimental data. The rough surface (Ra = 10 μm) showed a 200% improvement in heat transfer compared to the smooth (Ra = 0.027μm) in saturation nucleate boiling of FC-77. They attributed performance gains of the rough surfaces to smaller cavities to be favorable for highly wetting liquids. The CHF of the FC-77 increased 40% as Ra increased. An overshoot nearly identical in magnitude was observed for the surfaces of Ra = 0.027 μm and 1.08 μm.

Jabardo (2010) presented a review on the effects of surface roughness in nucleate boiling heat transfer, and concluded that various preparation methods have maximum nucleate boiling heat transfer. Hosseini et al. (2011) reported results on saturation nucleate boiling of R113 on Al, Cu, and brass surfaces. The results showed the Cu surface performed best despite having the lowest surface roughness. At a q of 16.8 W/cm^2, the Cu surface had a 23% higher heat transfer coefficient than the aluminum, and 18% higher than the brass. They reported a maximum improvement of 38.5% in the nucleate boiling heat transfer coefficient from surface roughening. The Cooper correlation (Equation (2.3)) predicted their experimental data well for the rough surfaces, but over-predicted for the smooth surface.

Bon and Klausner (2011) reported surface roughness to improve the saturation nucleate boiling heat transfer of Hexane on Al, Cu, Si, Nickel (Ni), and Titanium (Ti) surfaces. Ahmad et al. (2011) reported the surface roughness to enhance the nucleate boiling heat transfer of saturated R-123 on metallic surfaces. McHale and Garimella (2012) reported the methodology used to obtain the surface roughness, had a large impacted the interpretation of the experimental data of nucleate boiling of FC-72 on Indium Tin Oxide (ITO) coated borosilicate float glass. They reported the necessity of using a filtering technique capable of picking up the fine scale surface features normally missed.

2.7.4 Variances in the Reported Results

In general, there has been a large variance in the reported results for the effect of surface roughness on nucleate boiling heat transfer. Researchers have attributed variances to the surface materials (Nimkar et al. 2006, Hosseini et al. 2011), the methods used to prepare rough surfaces (Kang 2000; Luke; 2006, Jabardo; 2010), as well as the methods used to measure the rough surfaces (McHale and Garimella; 2012). Roy Chowdhury and Winterton (1985) mentioned comparisons should only be made among surfaces of the same treatment, since the procedure used to treat the surfaces could significantly affect the experimental results. They demonstrated that surfaces with the same root mean square roughness could result in different data due to preparation techniques. Luke (2006) suggested empirical correlations such as Gorenflo (1993; Equations (2.4 – 2.5)) and Cooper (1984; Equation (2.3)) are no longer sufficient for design of a boiling heat exchanger, because of the wide scatter within the experimental data, which may be explained by large differences between the surface structures of varying heating elements. Pioro et al. (2004) reported surface roughness may only affect nucleate boiling heat transfer if the scale of the roughness is within range of the size of the cavities the bubbles nucleate from. Jabardo (2010) suggested the method preparation effects the cavity size distribution. He suggested rougher surfaces contained less differences in the distribution of minimum cavity sizes, resulting in less nucleate boiling performance differences at high heat flux, and that larger cavities were beneficial for nucleate boiling performance at low heat fluxes.

The developed correlations that predict the effect of surface roughness on nucleate boiling heat transfer (Equations (2.3) – (2.6)) have been shown to sparingly predict accurately against the more recent experimental data (Ribatski and Jabardo 2003; Jabardo et al. 2008; Jones et al. 2009). Therefore there is a need for more experimental and correlations that predict the effect of surface roughness on nucleate boiling transfer, which is the focus of Chapter 4 in this dissertation.

2.8 Surface Modifications for Nucleate Boiling Enhancement

Many different surface modifications for the enhancement of nucleate boiling on other scalable surfaces have been investigated. Scalable surface modifications mainly focus on (a) surface roughening (discussed in the previous section) (b) extended surfaces that increase the wetted area per foot print area for nucleate boiling either through material extensions of pins or fins (Anderson and Mudawar 1989; Rainey and You 2000 ; Ramasway et al. 2000, 2003; Honda et al. 2002; Wei and Honda 2003; and Wei et al. 2005; Yu and Lu 2006; Ujereh et al. 2007; Parker and El-Genk 2009), or material removal through the drilling of small cavities, pores, or dimples (Wright and Gebhart 1989; Miller et al. 1990; Yu et al. 2006).

Also briefly reviewed are the surface modifications that change the surface hydrophobicity to enhance nucleate boiling heat transfer as well as increase the CHF (Takata et al. 2005; Kim et al. 2007; Phan et al. 2009; Wu et al. 2010; Hendricks et al. 2011; Ahn et al. 2012; Hsu et al. 2012a; O'Hanley et al. 2012; Saeidi and Alemrajabi 2013). Over the past few years, researchers have begun to determine that the surface roughness parameter, and surface wettability parameter, should be separated to help avoid further reported variances on the effect of surface roughness on nucleate boiling heat transfer. This related work is still in the very early stages, and as such not yet generally conclusive.

2.8.1 Extended Surfaces

Anderson and Mudawar (1989) investigated several different micro-finned, micro-grooved, and micro-studded surfaces in saturation pool boiling of FC-72. The results showed the micro-finned surfaces to greatly enhance the nucleate boiling heat transfer, however a temperature excursion was present for each and varied from 10 K – 20 K. They reported CHF increases of ~75%, 50%, and 155% over plain surfaces for the micro-finned, micro-grooves, and micro-studded surfaces, respectively. They concluded the increase of CHF was due to the increase of wetted surface area. Micro-fins etched into silicon were investigated in saturation and subcooled pool boiling of FC-72 by Honda et al. (2002), Wei and Honda (2003), and Wei et al. (2005). The measured CHF for all micro-finned surfaces increased over a plain Si surface, and increased monotonically with fin height. Ramasway et al. (2000, 2003) conducted saturation pool boiling experiments of FC-72 on micro-machined surfaces. They reported large enhancements in nucleate boiling heat transfer. Their data displayed high heat transfer with increased pore size in the range of 90 – 320 μm and decreased pore pitch. Ujereh et al. (2007) performed saturation boiling experiments in FC-72 on plain Cu and surfaces with micro-pins that measured 0.25 x 0.25 x 0.25 mm. They reported a diminished nucleate boiling heat transfer coefficient on the micro-pinned surfaces, but an increase of 75% in the CHF. The temperature increase was caused by the added thermal resistance, known as the fin effect, due to axial conduction from the base surface through the micro-pins or micro-fins. The taller the pins, the lower the fin efficiency, and hence the increase in the total heat removal rate.

Rainey and You (2000) investigated saturation nucleate boiling of FC-72 on a Cu surface with a 5x5 array of small pins. The total rate of heat removal increased with the height of the pins up to ~4 mm, but beyond that, no further enhancement in nucleate boiling occurred. This was due the fin effect, which decreased the surface temperature for the taller pins to initiate bubbles nucleation. Yu and Lu (2006) investigated saturation nucleate boiling of FC-72 on surfaces with arrays of square pins that were 1 mm wide, 0.5 – 4.0 mm tall, and spaced 0.5 – 2.0 mm apart. The CHF based on the footprint areas increased with the height of the pins, and decreasing with the spacing of the pins. The wetted-surface average CHF and h_{NB} decreased due to the fin effect and the resistance to bubble detachment, because the spacing between the pins is smaller than the typical bubble departure diameter.

Parker and El-Genk (2009) investigated saturation boiling of HFE–7100 dielectric liquid on Cu surfaces with 2x2 mm corner pins of varying height from 2 – 5 mm. They also investigated the effect of surface inclination angle, from 0^{o} (upward facing) to180^{o} (downward facing) on the CHF. Compared to smooth plain Cu, the rate of heat transfer by natural convection and CHF increased 68% and as much as 157%, respectively. The ~4 mm spacing between the pins was much larger than the typical bubble departure diameter (~0.5 mm), and resulted in the smallest boiling resistance for the surface with the ~5 mm tall pins. The CHF values, based on the actual wetted or geometrical surface area, were lower than that on plain Cu. This difference increased with the height of the corner pins. To avoid the fin effect and increase the wetted surface area, while potentially decreasing the foot print surface temperature, researchers have investigated nucleate boiling on metal surfaces with circular micro-cavities or dimples 10's to a few 100 µm in diameter.

Wright and Gebhart (1989) investigated saturation boiling of water on surfaces with micro-dimples, 4.1 µm deep and 11.5 µm in diameter. They reported a 420% enhancement in the nucleate boiling heat transfer compared to those without dimples. Miller et al. (1990) investigated the effect of using dimpled surfaces on the temperature excursion prior to boiling incipience of dielectric liquids. They used metal surfaces with dimples, 9.4 µm in diameter and 3.3 µm deep. Results showed the magnitude of the temperature excursion to depend on the immersion time of the surface, for up to two days. Yu et al. (2006) studied saturation boiling of FC-72 on silicon surfaces with artificial micro-cavities that were 50 – 200 µm in diameter and 110 – 200 µm deep. Increasing the cavity depth decreased the nucleate boiling heat transfer coefficient due to the difficulty of replenishing the surface of the deeper cavities with liquid. However, CHF values were as much as 142% higher than on a plain Si surface.

Overall, surfaces with manufactured dimples are relatively easy to scale up for industrial applications including boilers, refrigeration and immersion cooling of electronics using dielectric liquids. However, more is needed to understand the effect of dimples on enhancing nucleate boiling and CHF. Furthermore, most of the reported work on nucleate boiling of dielectric liquids on dimpled surfaces and surface with micro-cavities has been for saturated boiling in the upward facing orientation. In practical applications, boiling could take place on heated surfaces in different orientations, including that of downward facing.

2.8.2 Modification of surface wettability

Takata et. al (2005) demonstrated a Cu surface coated thin layer Titanium Dioxide (TiO_2) surface exposed to ultra violet light made its water contact angle nearly zero. They measured nearly a 100% improvement in CHF over a non-coated surface. Wu et al. (2010) investigated the effect of a 1um thick TiO_2 surface coating in saturation pool boiling of water and FC-72 dielectric liquid. They reported an increase in CHF by 50.4%

and 38.2% respectively, over the non-coated surface. Ahn et al. (2012) investigated the boiling performance of anodized zirconium surfaces in water. The water static contact angles were reported to vary from 49.3^{o} to nearly 0^{o}, and the nanostructures that formed modified the surface roughness from 0.15 to as much as 0.32um. The CHF increased 20 – 90%, depending on the degree of surface oxidation. Kim et al. (2007) used dilute dispersions of alumina, zirconia, and silica nanoparticles in water to construct thin porous layers of nanoparticles, that ranged 20 – 100 μm thick on a wire heater. The water static contact angles were measured to be 79^{o} for the bare surface, and dropped to 8 – 36^{o}, and depended on particle composition and concentration. CHF was found to improve as much as 75%. Hsu et al. (2012a) fabricated Cu surfaces coated with silica nanoparticles, and measured static contact angles < 10^{o} for the most superhydrophilic surface. A CHF increase of over 100% was reported for the superhydrophilic surface. Chen et al. (2009) fabricated nanowire arrays of Si and Cu over a plain silicon surface and reported a water static contact angle measurement of near zero. The CHF increased nearly 100% and improved with nano-wire height.

Hendricks et al. (2011) reported the maximum increase of CHF of nanostructured aluminum and copper surfaces occurred near a water static contact angle of 20^{o}. Further decrease in contact angle resulted in a sharp decrease of CHF. Saeidi and Alemrajabi (2013) found CHF to be largely unaffected after the anodization of aluminum surfaces, even though they displayed static contact angles that were superhydrophilic. Phan et al. (2009) found heat transfer to be a minimum at about a water contact angle of 45^{o}, within a range of contact angles between 0^{o}- 90^{o}. O'Hanley et al. (2012) reported that by attempting to separate the effects of surface roughness and wettability concluded that surface wettability alone did not affect CHF in their experiments. Smooth surfaces, despite having contact angle differences of more than 100^{o} exhibited nearly the same CHFs, and therefore the surface roughness parameter was implied responsible for the increases seen in CHF.

2.9 The Effect of Surface Orientation

For the immersion cooling of microprocessors, the effect of surface orientation is of interest because the motherboard may be mounted in the horizontal or vertical directions. Several studies have investigated the effect of surface inclination on pool boiling of dielectric liquids (Mudawar, Howard, and Gersey, 1997; Chang and You, 1996; Howard and Mudawar, 1999; Rainey and You, 2001; El-Genk and Bostanci, 2003a,b; Priarone, 2005; Parker and El-Genk, 2006a,b; Parker and El-Genk, 2008; El-Genk and Ali, 2012; Ali and El-Genk, 2013).

In general, the results on effect of surface orientation have been consistent. Chang and You (1996) investigated saturation nucleate boiling of FC-72 on upward facing ($\theta = 0^o$) and vertical ($\theta = 90^o$) surfaces. They reported an increase of the boiling heat transfer coefficient low superheats and the inclination angle increased. Rainey and You (2001) reported similar results the saturation boiling of FC-72 on smooth Cu surfaces that measured 20 x 20 mm and 50 x 50 mm. The nucleate boiling heat transfer coefficient diminished for surface inclination angles exceeding 90^o. The difference in the boiling heat transfer rate diminished as the size of the boiling surface increased from 10 x 10 mm to 50 x 50 mm.

Wei and Honda (2003) reported the nucleate boiling heat transfer rate in 25 K subcooled FC-72 was higher on a vertical smooth silicon surface 10 than on the same surface in the horizontal upward facing ($\theta = 0^o$) orientation. Reed and Mudawar (1999) indicated that at low surface superheats, the nucleate boiling heat transfer improved as the surface inclination angle increased. Conversely, at high surface superheats, the nucleate boiling heat transfer coefficient decreased as the inclination angle increased.

El-Genk and Bostanci (2003a, 2003b) performed experiments of saturated and subcooled boiling of HFE-7100 on 10 x 10 mm Cu surfaces. In saturation boiling at low surface superheat, the nucleate boiling heat transfer coefficient increased as the surface inclination angle increased from upward the facing (0°) orientation, to the downward facing (180°) one. The trend was reversed at high surface superheats. For subcooled boiling, they reported that for $0^o < \theta < 90^o$, the nucleate boiling heat transfer coefficient decreased slightly with increased inclination angle, but increased as the subcooling increased. At low surface superheats, the nucleate boiling heat transfer coefficients were almost the same, or increased slightly as the inclination angle increased.

Parker and El-Genk (2005) investigated the effect of surface orientation on the nucleate boiling and CHF of FC-72 on porous graphite and smooth Cu surfaces sized 10 x 10 mm. The inclination angle of the surfaces increased from $\theta = 0^o$ (upward-facing) to 60^o, 90^o, 120^o, 150^o, and 180^o (downward facing). At low surface superheats, the nucleate boiling heat transfer coefficient, $h_{NB,}$ increased as θ increased. Conversely, h_{NB} decreased at high surface superheats as θ increased. These results, along the obtained decrease in the CHF as θ increased, were consistent with those reported earlier by other investigators for dielectric and other liquids (Beduz, Scurlock, and Sousa, 1988; El-Genk and Guo, 1993; Chang and You, 1996; Mudawar, Howard, and Gersey, 1997; Howard and Mudawar, 1999; Rainey and You, 2001; Priarone, 2005; Nishikawa et al. 1984; Vishnev et al., 1976). On smooth surfaces and micro-porous coatings, the reported fractional decreases in the CHF with increased inclination angle were almost identical, though markedly larger than those measured by (Chang and You, 1996; Howard and Mudawar, 1999; Rainey and You, 2001; El-Genk and Bostanci, 2003a,b; Priarone, 2005) for the porous graphite surface. Typically, the reported CHF in the downward-facing position ($\theta = 180^o$) has been ~10-20% of that in the upward-facing position, compared to ~53.3 % on porous graphite (Parker and El-Genk, 2005). Therefore, enhancement the porous graphite had on the CHF grew, relatively, as θ increased.

Ali and El-Genk (2013) performed pool boiling experiments that investigated the effect of inclination angle on the saturation CHF of PF-5060 dielectric liquid on seven Microporous Copper (MPC) surfaces of different thickness that ranged from 80 to 230 μm. The morphology of these surfaces, deposited using an electrochemical processes, varied with the thickness of the layer. The inclination angles investigated were 0^o, 60^o, 90^o, 120^o, 150^o, 160^o, 170^o and 180^o. The CHF decreased as the MPC surface thickness decreased, and inclination angle increased. For all MPC surfaces, the CHF values in the downward facing orientation were ~28% of those in the upward facing orientation. The developed CHF correlation that accounted for the effects of MPC thickness and inclination angle was in good agreement with the presented experimental data, to within ± 8%.

Despite the minor differences in the angular dependence of nucleate boiling heat transfer coefficient, there has been a general agreement on the effect of inclination angle on CHF. Reported results have shown CHF to decrease slowly as the surface inclination increased up to 90º degrees (vertical surface orientation), then rapidly decrease to its minimum value at the 180º inclination angle (horizontal-downward facing) (Chang and You, 1996; Reed, 1996; Howard and Mudawar, 1999; Rainey and You, 2001; El-Genk and Bostanci, 2003a; Priarone, 2005; Parker and El-Genk 2006). From these results, CHF correlations and analytical models have been developed (El-Genk and Guo, 1993; Vishnev,1976; Brusstar at al. 1997; Chang and You, 1996; El-Genk and Bostanci, 2003a; Howard and Mudawar, 1999), for dielectric and other liquids.

3. Pool Boiling Experiments

This chapter describes the pool boiling experiments carried out in this research that used PF-5060 dielectric liquid at the local pressure in Albuquerque, NM, of 0.085 MPa. The pool boiling facility, test section, and experimental preparations and procedures designed to minimize uncertainties and provide reproducible results are discussed. The facility used, and the experimental setup and the procedures are similar to those used earlier by El-Genk and Bostanci (2003a, 2003b), El-Genk and Parker (2005, 2006) and Parker (2008), and by El-Genk and Ali (2010, 2012, 2013).

3.1 Experimental Facility

A schematic of the experimental facility is shown in Figure 3.1. (El-Genk and Bostanci, 2003; El-Genk and Parker 2005, 2006, 2008; Ali and El-Genk, 2010, 2012, 2013) It consists the following components: (a) A heated water bath in an acrylic tank, (b) A polycarbonate test vessel filled with dielectric liquid, (c) The assembled test section mounted onto a manual control rotation assembly, (d) Equipment for controlling and monitoring the hot water bath temperature, the dielectric liquid pool temperature, and the temperatures of the boiling surface, (e) A computer controlled DC power supply to the heating element, and to monitor and record the voltage reduction across and the current through the element, (f) A computer controlled data acquisition unit, and (g) A water cooling loop with a reflux condenser and two submerged coils in the test vessel connected and driven by a water supply chiller with a temperature control.

The test vessel undercover cooling coil condensed the vapor generated in the experiments and helps maintain a constant ~8cm liquid height above the test section and atmospheric pressure (~0.085 MPa) within the vessel. The submerged coils maintained the liquid pool temperature at the desired targets in the saturation and subcooled experiments. Additionally, the vessel was submerged in the hot water bath that helped maintain consistent liquid pool temperature during the experiments, as well as minimize heat losses from the side of the test vessel. Figure 3.2 shows a photograph of the experimental setup used to perform the present pool boiling experiments.

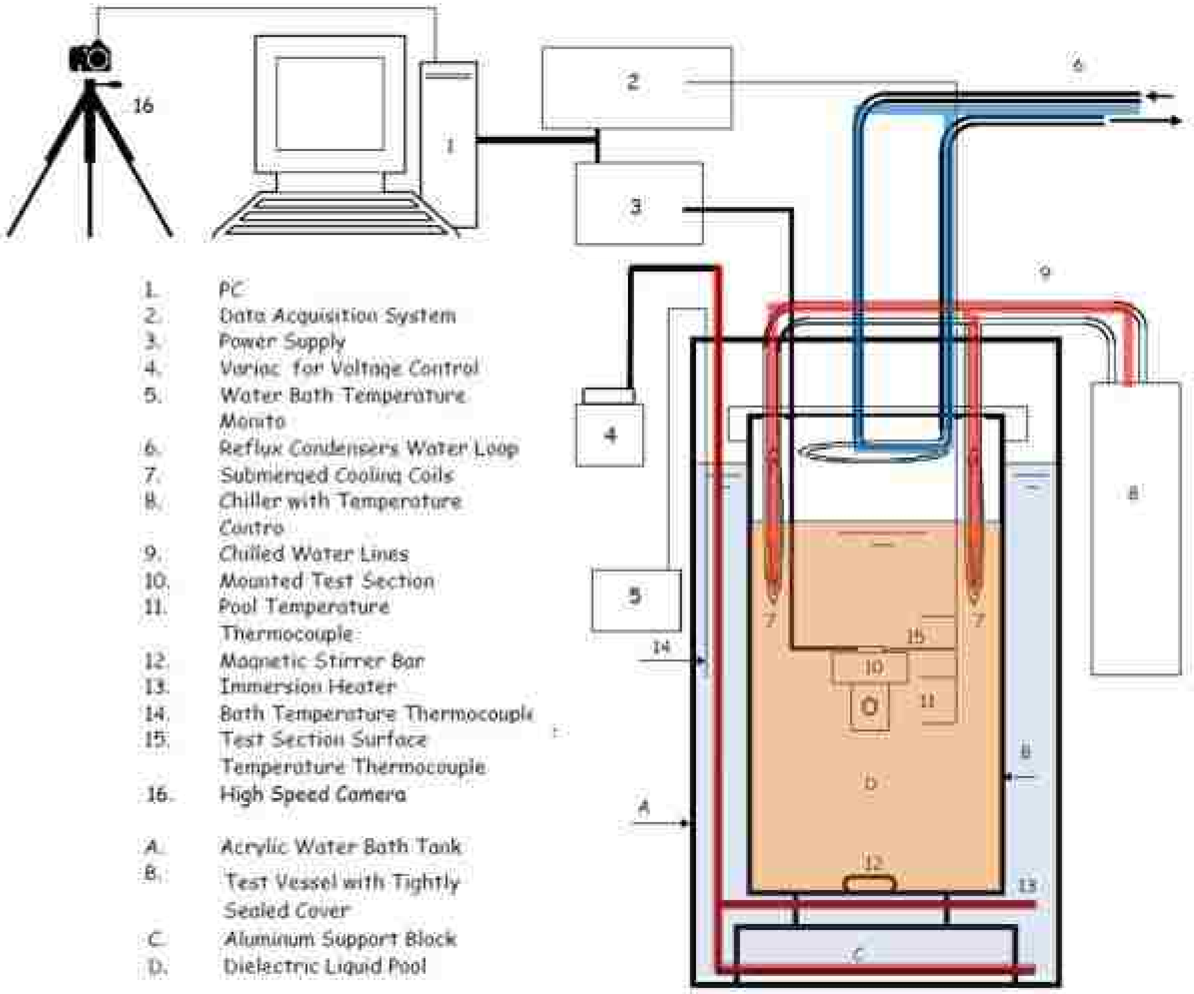

Figure 3.1. A schematic of the pool boiling test facility (El-Genk and Parker, 2005).

The test section (labeled 10 in Figure 3.1) is encased by a 40 x 40 x 20 mm acrylic block, which was attached to a rotational assembly within the test vessel (Figure 3.3) A Teflon block which holds the assembled test section was inserted into the acrylic block, and served to insulate the bottom of the test section from heat losses. Superlock fastener attached to the bottom of the acrylic block attached the test section to a rotational assembly within the test vessel (Figure 3.3). The rotational assembly was mounted in the vessel by an acrylic rod insert with two wheel bearings on each end of the rod, which sat in two wheel wells on opposite walls of the test vessel.

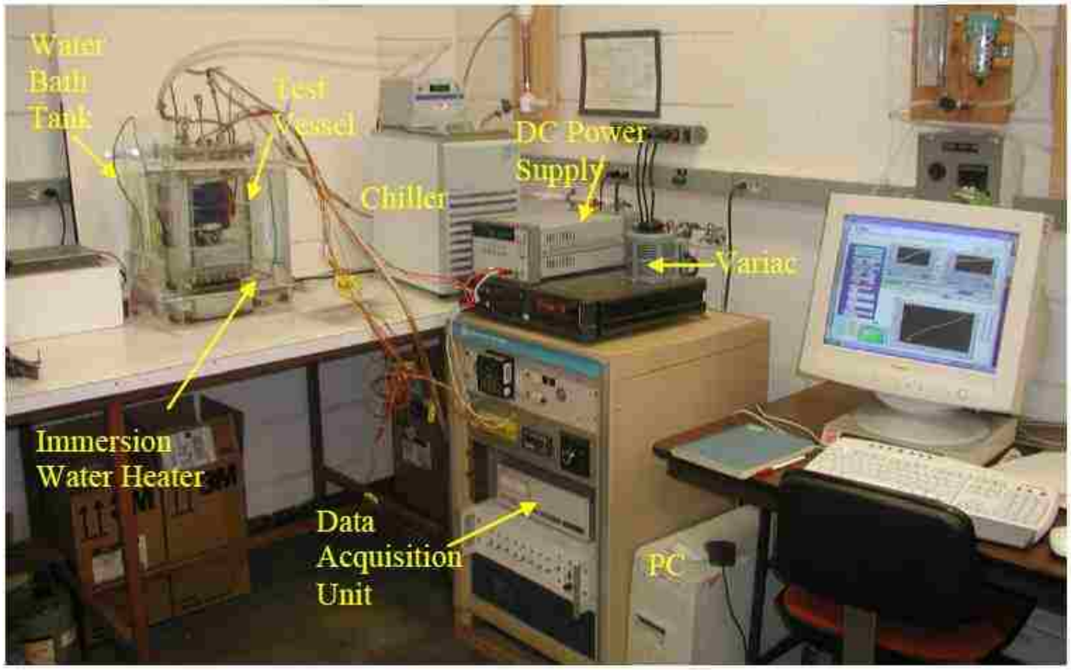

Figure 3.2. Photograph of the pool boiling facility (Parker, 2008).

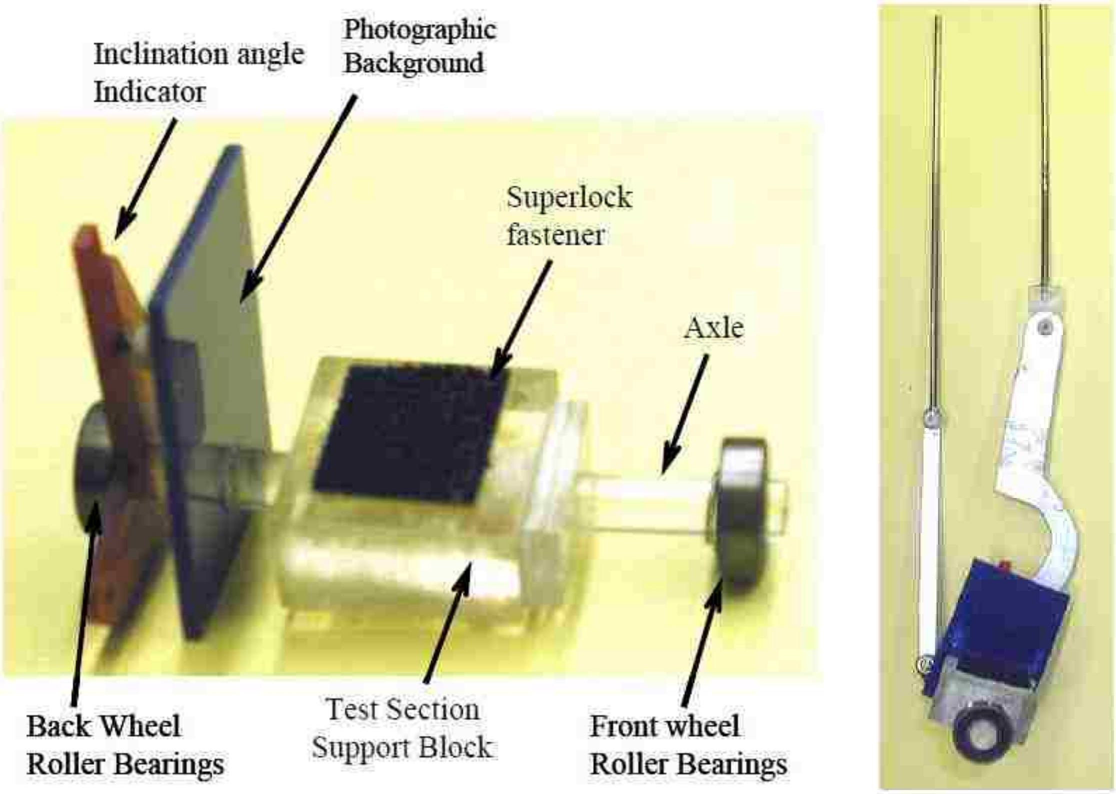

Figure 3.3. Fully assembled test section support and fully assembled rotation mechanism (Parker, 2008).

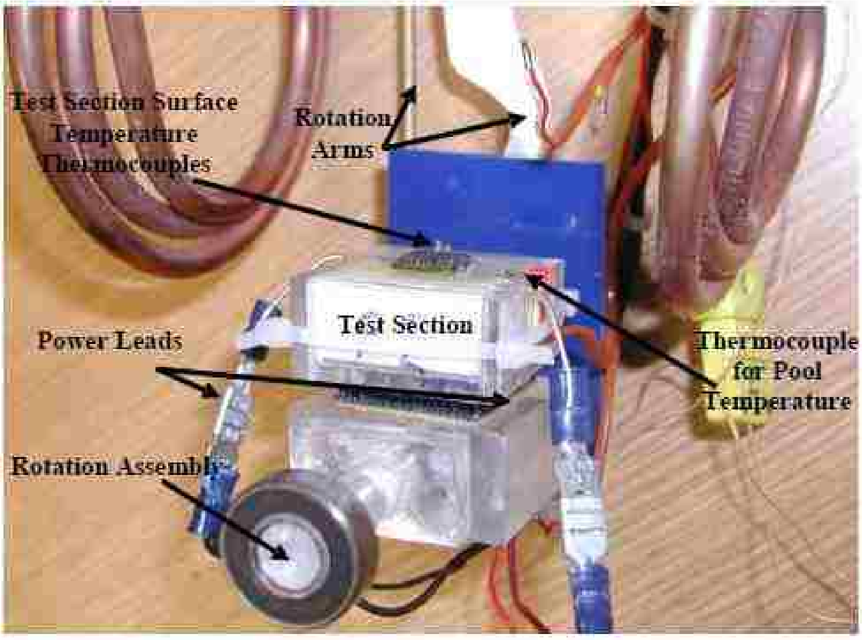

(a) Test section on rotational mechanism

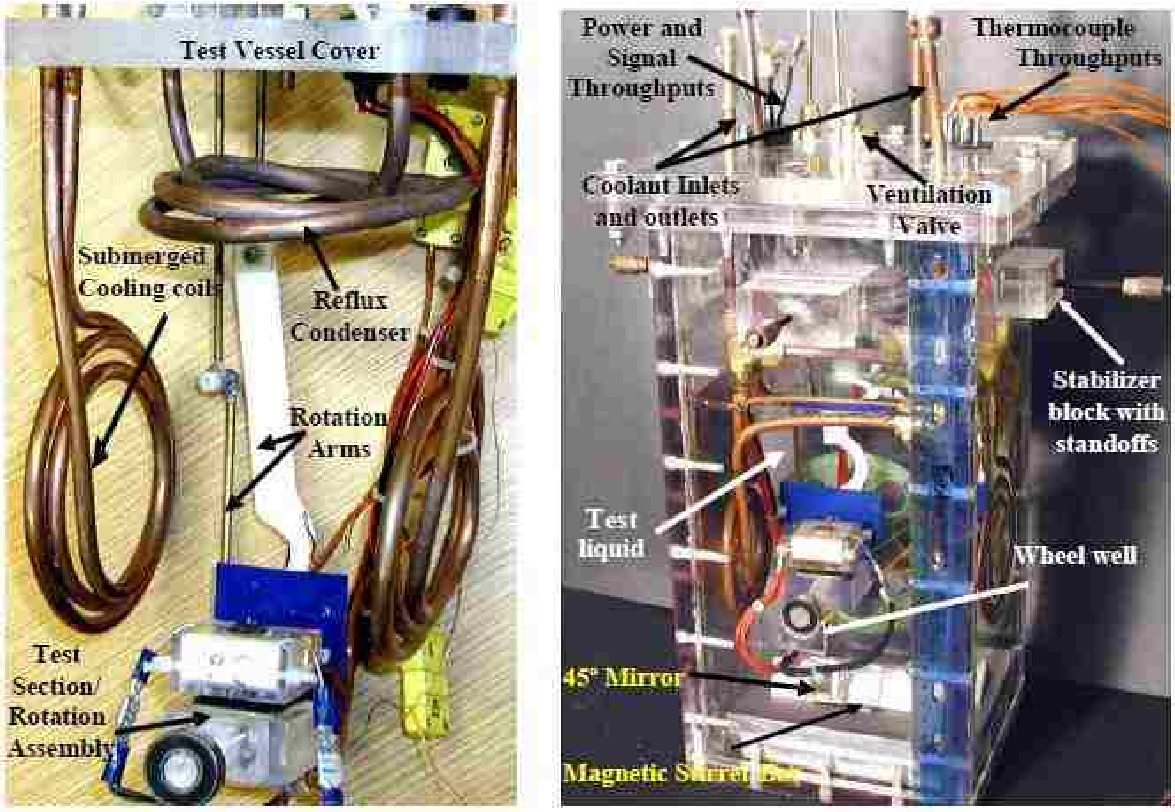

(b) Reflux condenser and submerged cooling coils

(c) Assembled test vessel

Figure 3.4. Photographs of pool boiling test vessel and assembly (Parker, 2008).

The inclination angles of the experiments were controlled using the rotational assembly (Figure 3.3). A square piece of blue acrylic was attached to the back half of the rod to provide a contrasting background for photographs and video. The two arms attached to the rotational assembly extended through the cover of the test vessel with $^1/_8$ inch diameter brass rods and allowed for manual control of the test section inclination angle in between experiments to within $\pm$ 0.5°.

The test vessel is made of ½ inch thick Lexan that is 290 x 120 x 140 mm (Figure 3.4). The container that holds the liquid pool was assembled using fast curing solvent cement, and all inside edges were perfectly sealed with epoxy. An O-ring was fit into a groove in the top cover ensured a tight seal between the cover and container. The cover of the test vessel provided throughputs for the heating element leads, thermocouples in the bulk liquid and assembled test section, the cooling coils, and the rotation mechanism (Figure 3.4). All throughputs were properly sealed both on the inside and outside. Because dielectric are highly volatile due to their low vapor pressures, and are also low surface tension and highly wetting, extra precautions were taken to ensure the test vessel was tightly sealed to prevent leakage. Prior to filling the test vessel with PF-5060 liquid, the test was tested for leaks by sealing it, pressurizing it with air, and fully submerging it in the hot water bath.

3.2 Test Section

The assembled test section for the pool boiling experiments consists of a 30 x 30 x 12.7 mm Teflon block with a 2 mm deep intrusion sized 10 x 10 mm to fit the Cu surface (Figure 3.5a), and a 40 x 40 x 20 mm acrylic block encasing. The 10 x 10 x 1.6 mm Cu surface, with two thermocouples embedded, was attached to an underlying heating element with a total resistance of ~16 Ω. The heating element is capable of proving up to 250 W of dissipated power. It, together with the Cu surface, was secured into a 10 x 10 mm intrusion of the Teflon block (Figure 3.5b). The Teflon block provided for good thermal insulation and minimized heat losses through the sides and underside of the heating element, and ensured that the heat generated by the heating element was transferred to the boiling surface.

The surface temperature used for constructing the boiling curve is the average reading of the two thermocouples in the Cu (Figure 3.5c) after correcting for the temperature drop due to heat conduction to the surface (0.1–0.5 K, depending on the input power). These thermocouples were installed in two ~0.8 mm diameter holes ~5 mm deep, located ~0.8 mm below the Cu surface. A two part rapid curing high thermal conductivity epoxy secured and ensured good contact between the thermocouples and Cu piece.

The heating element, with power leads attached and attached Cu piece with thermocouples ((Figure 3.5c), were secured into place in the Teflon block using slow cure thermal epoxy filler (Figure 3.5 Figure 3.6). The epoxy took at least ~8 hours to cure at room temperature, however, provided a perfectly smooth surface absent of any potential bubbles nucleation sites during experimentation. Additionally, it further insulated the sides of the heating element and Cu surface, as well as insulated the attached power leads that extended outward from to the heating element (Figure 3.5b-c).

The Lexan frame that enclosed the Teflon block (Figure 3.5d) was for the handling and mounting of the assembled test section inside the test vessel, as well as attaching two additional thermocouples. The two additional thermocouples attached to the outside of the acrylic block (Figure 3.5d) were used to monitor the bulk liquid temperature, in the test vessel. This temperature was taken as the average of the two thermocouple readings placed within 5-10 millimeters of the Cu surface.

Figure 3.6 shows a schematic and cross section view of the fully assembled test section. This assembled test section was used in the experiments facility (Figure 3.4). A thermal analysis was performed using ANSYS, a commercial finite element code package to estimate the heat losses from the test sections (El-Genk and Parker, 2006, 2008; Parker, 2008) during experimentation. The analysis compared the heat generation rate by the heating element to that removed by nucleate boiling and natural convection from the exposed heated surface and through the sides of the test section in the liquid. The total heat losses were estimated to be less than 3%. Thus, the power removed by nucleate boiling from the uniformly heated 10 x 10 x 1.6 mm rough Cu surfaces in the present experiments equaled that supplied to the underlying heating element by the DC power supply, after accounting for the side heat losses.

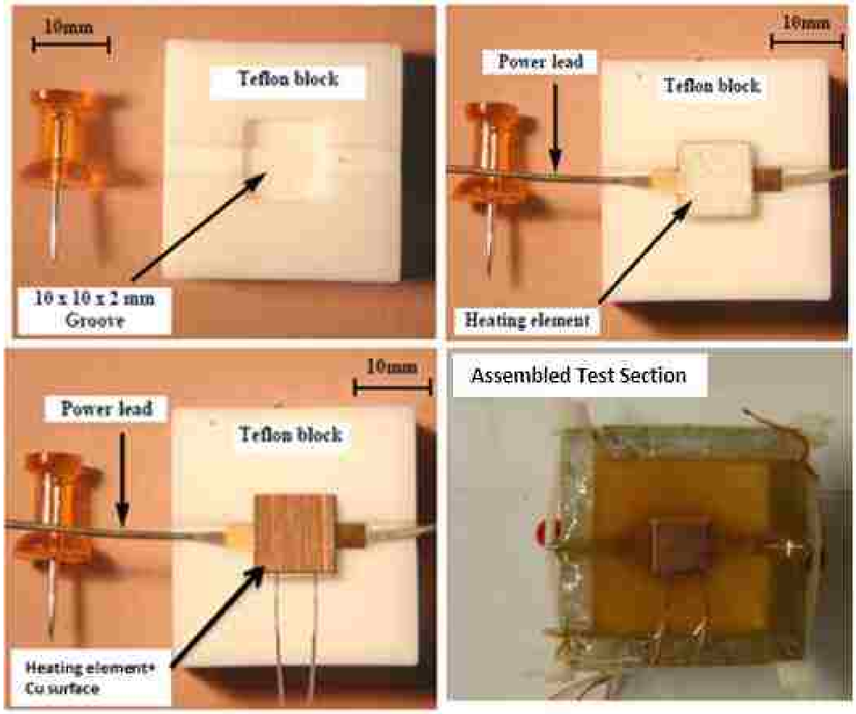

Figure 3.5. The construction of the test section assembly.

3.3 Experimental Setup and Preparations

The PF-5060 dielectric liquid used in the present experiments was regularly cleaned using a closed loop evaporation cycle to remove any contaminants that may have been present from previous experiments. This was typically done overnight as the evaporation process took ~8 hours to complete, and so fresh clean liquid was available the next morning. Thermocouples attached to the LabVIEW monitoring system were calibrated using boiling water and a mercury based thermometer temperature reading as a reference. A digital thermometer was also used to verify the temperature reading of the mercury thermometer. For all experiments in the present work, thermocouple calibrations showed the LabVIEW monitoring system to be accurate within ± 0.1 K.

After the thermocouples were calibrated, the test vessel was partially filled with the dielectric liquid such that the surface of the test section was submerged ~8 cm in the liquid pool at the upward facing surface orientation. This liquid head was kept consistent for all experiments. The test vessel was then assembled (Figure 3.4c) and placed into the

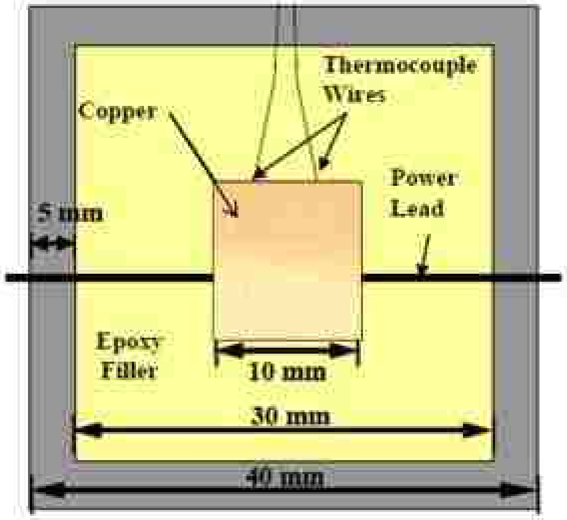

(a) Plane view (Schematic)

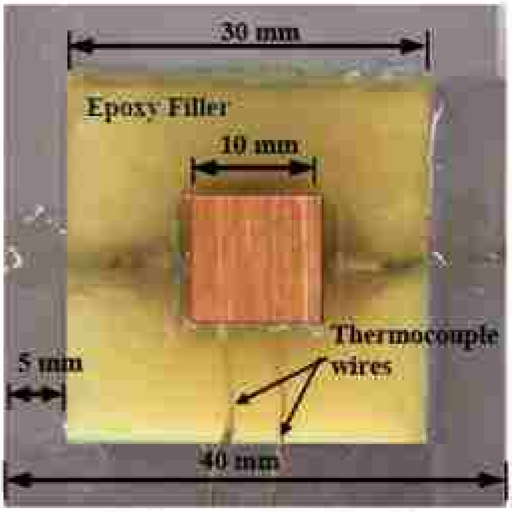

(b) Plane view (photograph)

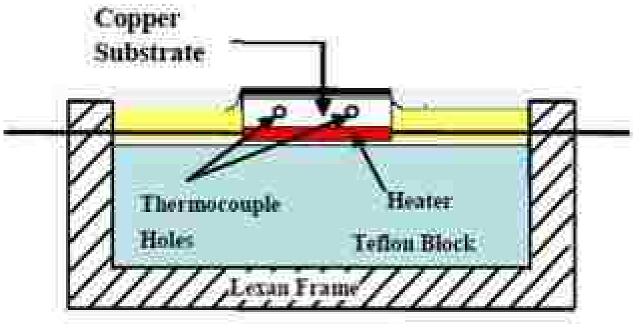

(c) Sectional view

Figure 3.6. Cross sectional views of the fully assembled test section. (El-Genk and Bostanci; 2003; El-Genk and Ali, 2012)

hot water bath, and connected to the water chiller unit and LabVIEW monitoring program (Figure 3.2).

Due to the high air solubility in dielectric liquids of 48% by volume for FC-72 (PF-5060 is nearly identical in properties (Table 2.1)) (You et al., 1995), degassing of the liquid pool in the test vessel was accomplished by heating the water bath outside of the test vessel to 5 – 10K above saturation temperature of the dielectric liquid, and it allowing it to boil for several hours. The released gas was vented from the test vessel through a needle valve in the cover (Figure 3.4c). Typically after two hours, there was no more gas venting from the test vessel, indicating the dielectric liquid was degassed.

After liquid degassing and prior to experimentation, the water chiller unit was adjusted manually until the two thermocouples measuring the pool liquid read an average temperature that matched the saturation temperature of the dielectric liquid (51.4 ^{o}C for PF-5060 in Albuquerque NM) to within ± 0.2K. Once the desired liquid pool temperature was within range, a separate program in LabVIEW, which controlled the electrical power supplied to the heating element in small increments of < 0.2V, was activated to begin the experiment.

As the supplied power to the underlying heating element increased, the voltage increment was decreased to ensure the stable construction of the boiling curve. With more vapor generated by nucleate boiling at higher powers, the condenser coils responsible for condensing the vapor back into liquid, either required more time at each increment with a constant voltage step, or a smaller voltage step at each increment, to maintain the closed test vessel at ambient pressure. The experiments conducted in the present work chose the latter option as it provided more data points. The applied voltage and the current through the heating element were measured simultaneously to determine the dissipated heat flux through the surface of the test section.

Following each voltage increment to the heating elements, steady state temperature readings of the thermocouples embedded in the test section were recorded. Each temperature reading recorded by the LabVIEW monitoring program was the average of 30 or more successive measurements by each of the two thermocouples – depending on when the boiling surface reached steady state. Steady state in the present experiments was determined when the difference between three successive surface temperature measurements were within ± 0.5 K of each other, or within the uncertainty of the thermocouples. After steady state was reached, the recorded values of the surface average temperature and power to the underlying heating element in the experiment were used to construct the pool boiling curves. When approaching CHF, the increment in power supplied to the heating element was reduced to less than 0.05 W. This was done to accurately determine the CHF value and avoid a temperature surge, which could burn the heating element.

3.4 Image Capture

Images of nucleate boiling and bubble transient growth were captured using a high speed video camera (Figure 3.7) operating at 210 frames per second (fps). The images were used for bubble visualization studies, at an applied heat flux of ~0.5W/cm^2. Images were captured after a full set of boiling experiments were completed.

Figure 3.7. The high-speed video camera used to capture images of individual bubble transient growths at 210 fps.

Post pool boiling experimentation and before any images were captured, the test vessel was allowed to cool for ~2 hours. Power was then supplied to the Cu surface to reactivate bubbles nucleation. This was conducted through two steps: first, a heat flux of ~10W/ cm^2 was applied to the heating element for about ~1 minute to activate bubble nucleation sites. This applied power is well within the fully developed region of nucleate boiling for all present experiments (Figure 2.6). The applied heat flux was then decreased to ~0.5W/cm^2 and left for at least ~2 minutes before recording images. This allowed the Cu surface sufficient time to stabilize from the sudden decrease of applied heat flux, as well as ensure that all potential bubble nucleation sites were active at the reduced power. After verifying the thermocouple temperature readings matched those recorded for the prior experimentally constructed boiling curves, the camera was focused to, and captured images of the entire boiling surface. These images were used to identify discrete bubbles, such as those circled in Figure 3.8. After a discrete bubble was identified, the camera was refocused and captured the chosen bubble for greater detail and precision, for better accuracy of determining bubble growth diameters.

Figure 3.8. An example of a single captured frame of the full boiling surface used to identify discrete bubble locations in saturated boiling of PF-5060 dielectric liquid.

Post-processing was performed on captured images to help clarify them, and included brightness and contrast adjustments, sharpening filter applications, and pixel noise reductions. From the post-processed images, the individual bubble transient growth measurements were obtained. To reduce statistical uncertainty of the measurements, multiple sets of images were captured and analyzed for each discrete bubble, and some bubbles had as many as 6 ebullition cycles captured.

3.5 Surface Preparation and Characterization

This section discusses the preparation procedures and characterization methods used for the different investigated surfaces in the present work, for pool nucleate boiling nucleate boiling experiments of PF-5060. The surfaces investigated: (a) rough Cu (b) oxidized Cu and (c) dimpled Cu, measuring 10 x 10 x 1.6 mm, are discussed in their own sub-sections next.

3.5.1 Rough Cu Surfaces

The present work investigated 13 rough Cu surfaces, with an average roughness, Ra, ranging from 0.039 (smooth polished) to 1.79 μm. These surfaces were prepared in a consistent manner to ensure reproducibility of surface characteristics and nucleate boiling experimental results.

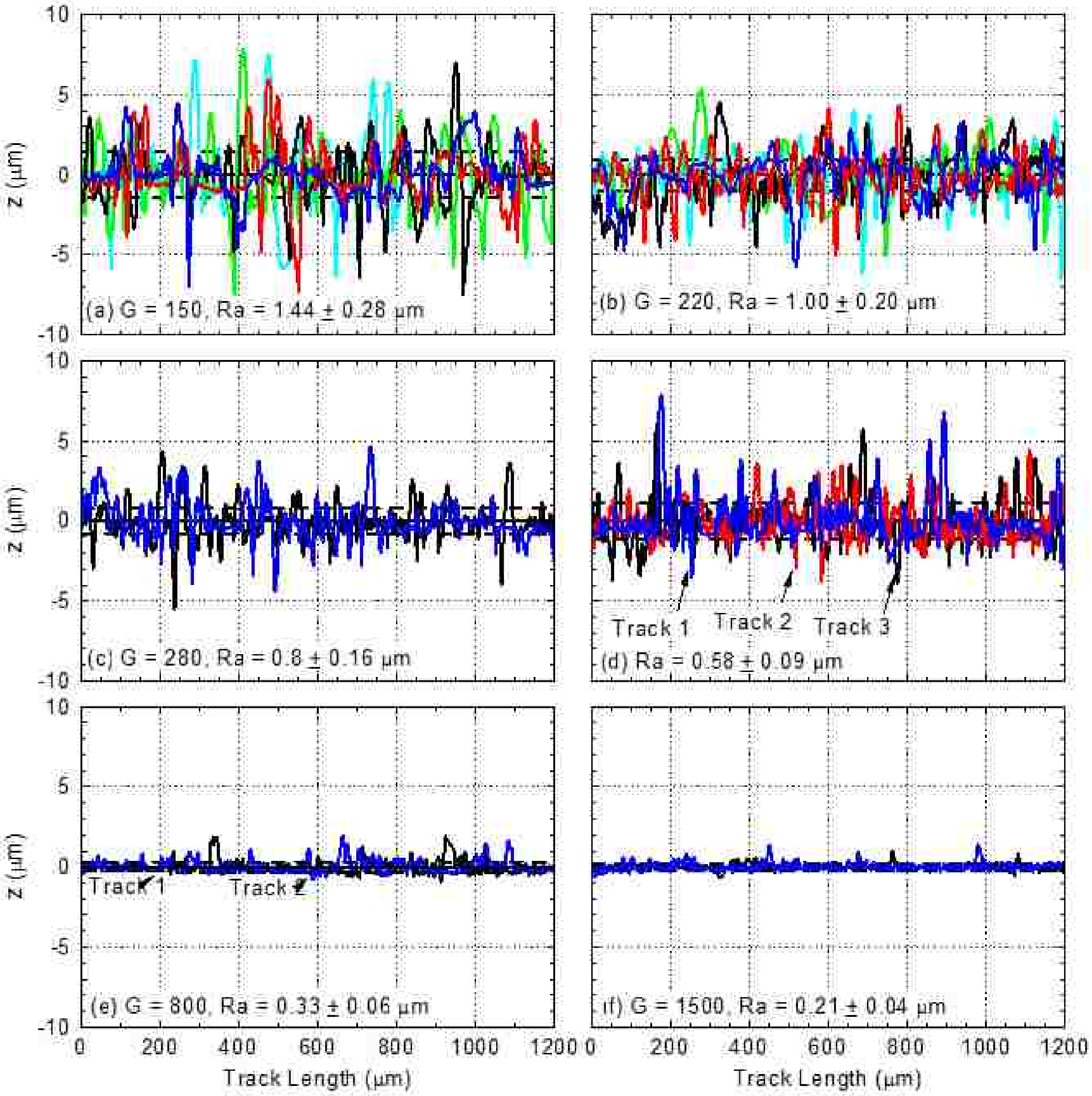

Figure 3.9. Surface topography profiles for six of the rough Cu surfaces.

First any oxidation and attached particles were removed using a 1500 grit emery paper. The surfaces were then polished to a near mirror finish using a metal polisher, and rinsed with alcohol and distilled water multiple times. Surface polishing brought each Cu surface to a near mirror finish with Ra $\leq$ 0.05 µm. Surface roughening was then carried out in one of two ways.

For a target Ra $\leq$ 0.71 µm, the cleaned, polished, and rinsed Cu surfaces were prepared with emery papers of the appropriate grit sizes by applying five strokes each in the forward and perpendicular directions then the surfaces are rinsed clean. For higher roughness, the cleaned, polished, and rinsed Cu surfaces were prepared first with 280 grit emery papers and then with the emery papers of the appropriate grit sizes using the same procedures. Figure 3.9 shows the measured profiles of six of the prepared rough Cu surfaces investigated in the present pool boiling experiments.

Surface topology measurements were taken without filtering (Figure 3.9) using a Dektak 150 contact profilometer. A 3mg measuring force and 0.04 µm resolution were used for all measurements, for consistency. The measured surface topology for each surface consisted of five 1.2 mm long equally spaced strips. The strips were spaced 1.5 – 2.0 mm apart on the surface. Each 1.2 mm long track generated 120,000 data points. Additional surface roughness measurements were taken with the Cu surface rotated 30^o, 45^o, 60^o, and vertically, and ensured there was minimal bias of roughness measurement along the stroke directions. The obtained topography measurements were used to estimate the average roughness, Ra, for each surface, as:

$$\boldsymbol{R_a} = \frac{1}{n}\sum_{i=1}^{n}|y_i| \tag{3.9}$$

Figure 3.9 shows surface roughness profiles for Cu surfaces that measured Ra = 1.44 µm, 1.00 µm, 0.80 µm, 0.58 µm, 0.33 µm and 0.21 µm. The 20% uncertainty in surface roughness measurements comes from additional sets of measurements on different Cu surfaces that were prepared in the same manner (Figure 3.10). Figure 3.10 plots the determined Ra values for 12 of the 13 Cu prepared in this work, versus the grit counts of the emery papers used in final stage of the surface preparation. The smooth-polished surface with Ra of 0.039 µm is not included in Figure 3.10, because it was prepared without emery paper.

The average surface roughness measurements were used to estimate the increase in the total wetted surface area with increased roughness (Figure 3.11). This was done by taking the total length of the scanned profiles, and dividing them by their respective scanning lengths. The results in this Figure 3.11 show the fractional increase in the wetted surface area with increased by less than 5% at the maximum Ra of 1.79 µm. While accounted for, the fractional increase in the wetted surface area is a minor factor, for the enhancement of nucleate boiling in the present experiments. Figure 3.12 shows the optical microscope images of the smooth-polished Cu and three of the rough Cu surfaces in the present work. In this figure, the length scale of the surface micro-features increases with increasing surface roughness.

Due to the very low surface tension and highly volatile nature of PF-5060, obtaining contact measurements using this dielectric liquid was not feasible. Instead, DI water static contact angle measurements were taken at room temperature are used not as a substitute, but for illustrative purposes only to show the relative changes in surface wettability with increased surface roughness. At least eight measurements were taken per surface to improve the statistical uncertainty.

Each Cu surface had a ~1 mm^3 droplet of water applied using a special syringe, and 5-10 seconds were allowed to pass before the water/Cu interface was captured using a digital camera. The static contact angle, ϕ, was measured using the captured images. Figure 3.13 displays a ~1mm^3 droplet of water on the (a) smooth polished surface (Ra = 0.039 µm) and two rough Cu surfaces of Ra = (b) 0.58 and (c) 1.79 um. In these images, the ϕ was measured to be ~77^o, ~58^o, and ~46^o, respectively. Figure 3.14 shows the effect of surface roughness on the static contact angle of water on Cu. It decreases with increasing roughness, showing the Cu surfaces followed the Wenzel (1949) model of wetting.

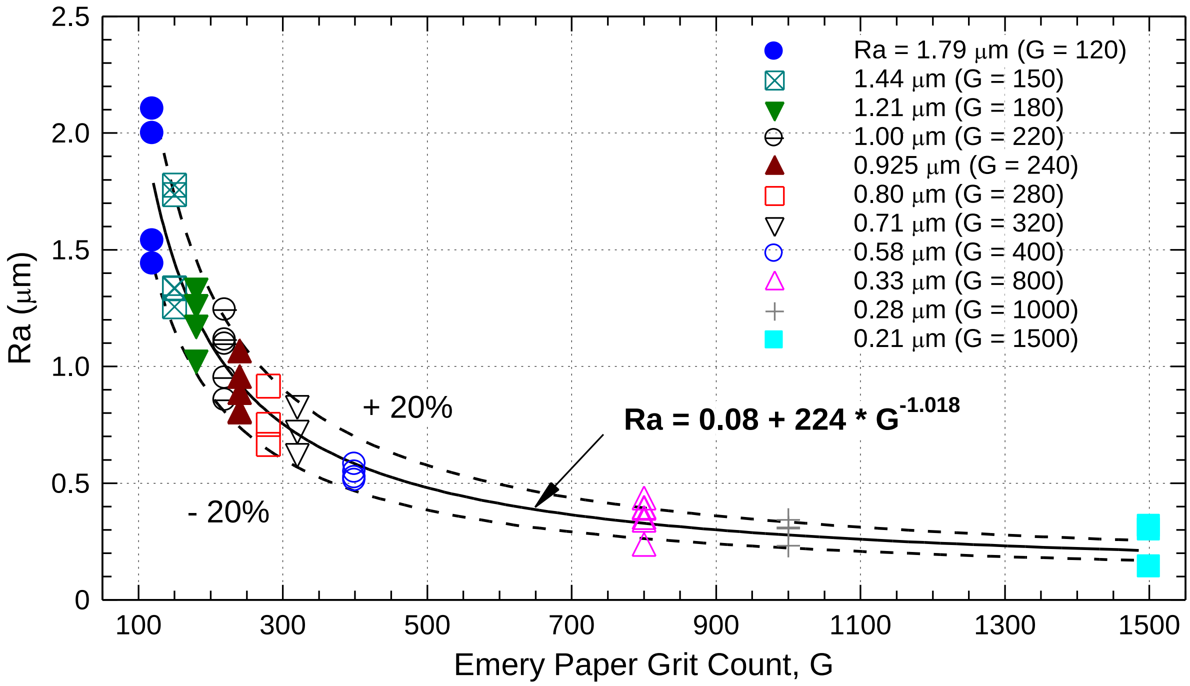

Figure 3.10. Surface roughness versus emery paper grit count.

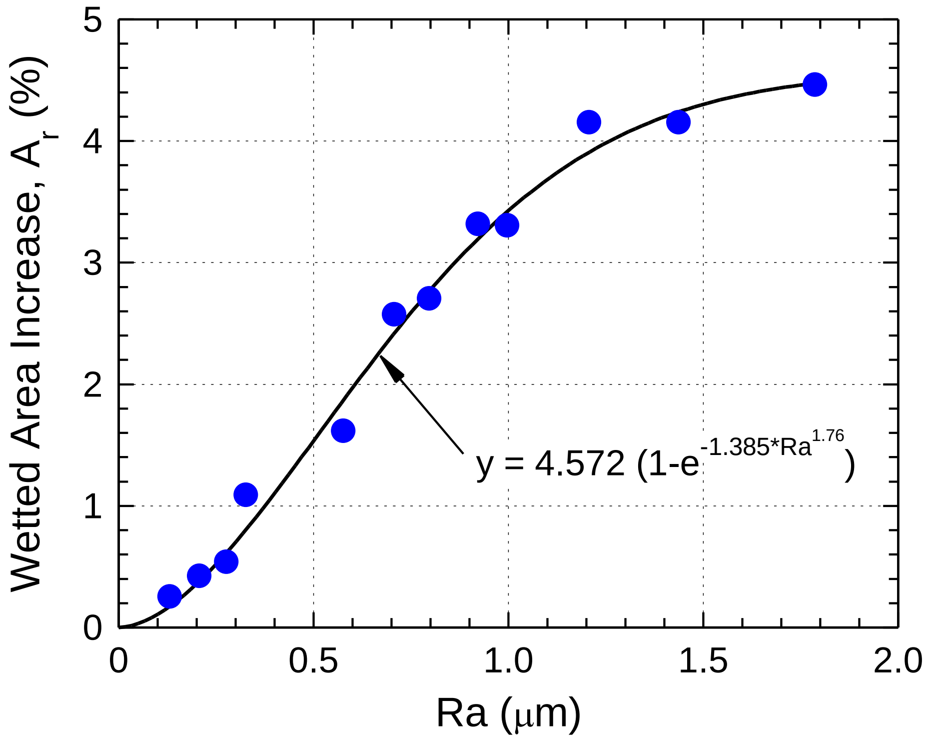

Figure 3.11. The calculated increased in the wetted surface area caused by surface roughening.

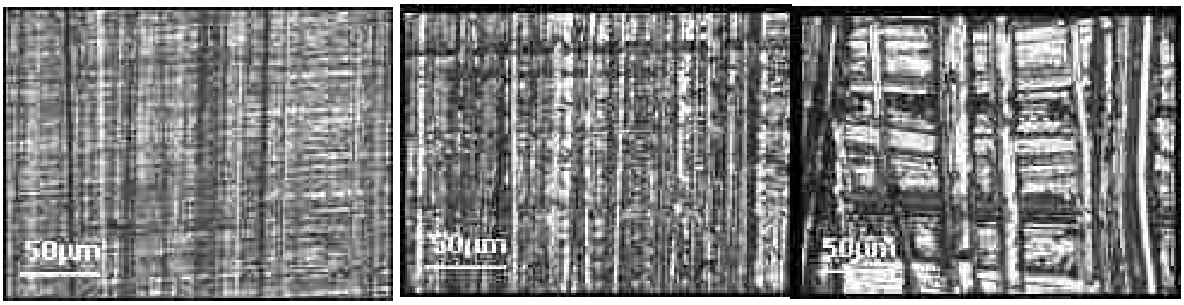

(a) Ra = 0.21 μm **(b) Ra = 0.58 μm** **(c) Ra = 1.79 μm**

Figure 3.12. Optical images of rough Cu surfaces.

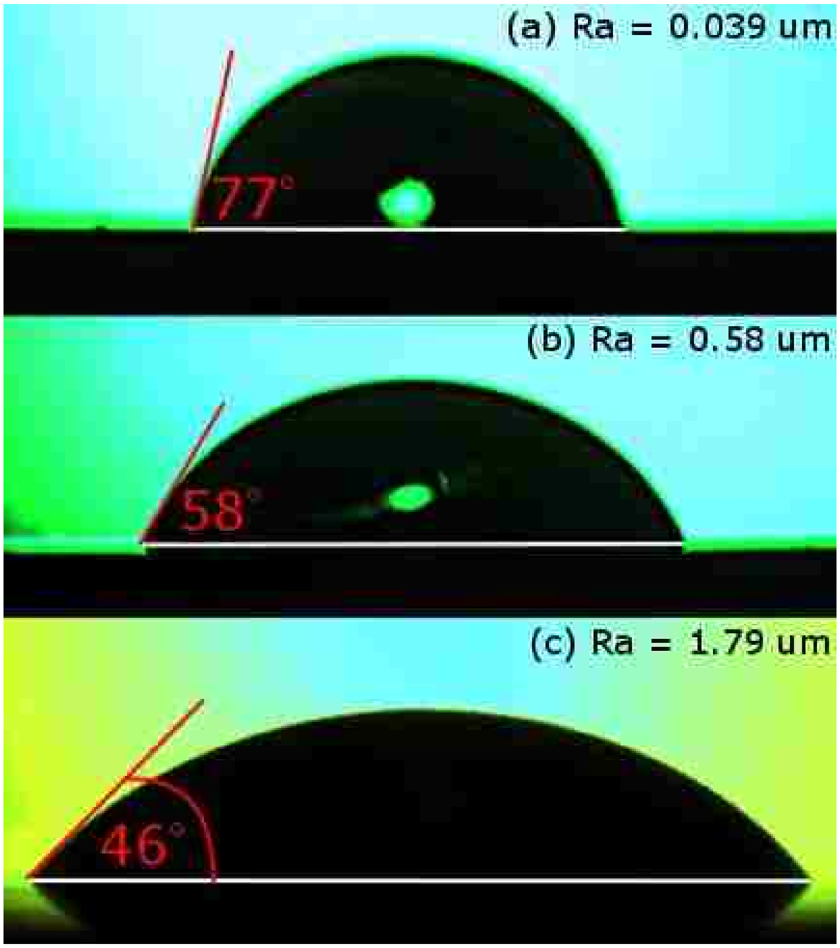

Figure 3.13. Digital images displaying the difference of contact angles of various rough Cu surfaces.

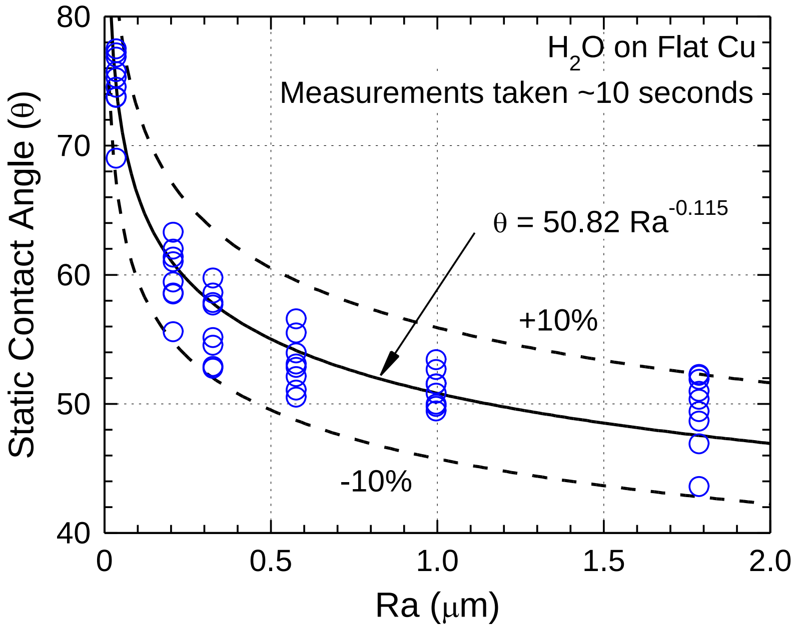

Figure 3.14. Water static contact angles of various Cu surfaces prepared for experimentation.

3.5.2 Oxidized Cu Surfaces

Oxidized Cu surfaces were prepared to study the effect of surface aging on nucleate boiling heat transfer. They were first prepared in the same manner as the rough Cu surfaces, with an additional step of leaving the prepared 10 x 10 x 1.6 mm rough Cu surface in an oven overnight at 200 ^oC (roughly ~15 hours). This amount of time allowed a dark oxide layer to form and uniformly cover the Cu surface. Before removing the oxidized Cu piece from the oven, the oven was cooled down at a slow rate back to room temperature over the course of ~1 hour. This procedure avoided thermal shocks cracking the oxide layer, allowing it to peel off the Cu substrate.

The surface oxidation was found to slightly increase the roughness ~0.1 µm for both smooth and rough Cu surfaces. Figure 3.15 shows SEM images of a before and after oxide layer formation. This figure shows how the oxide layers had a puffy texture to them for both smooth and rough Cu. Additionally, the oxide layer follows the Cu surface topography filling in grooves and crevices present.

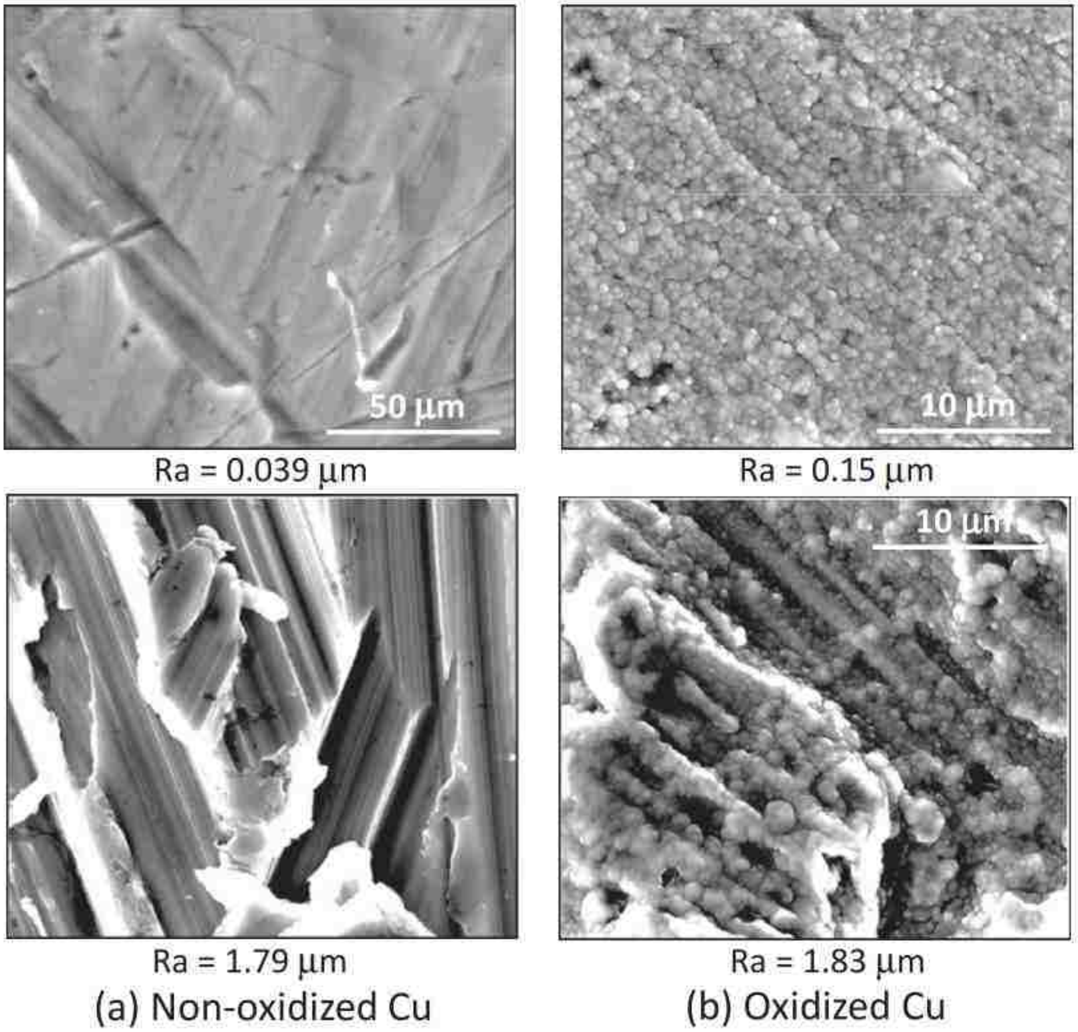

(a) Non-oxidized Cu (b) Oxidized Cu

Figure 3.15. Scanning Electron Microscope (SEM) images of some rough Cu surfaces before and after oxidation.

3.5.3 Dimpled Cu Surfaces

The text of this section was provided courtesy of Dr. Krishna (El-Genk et al. 2015) of New Mexico State University. The dimpled Cu surfaces were also provided courtesy of Stephen Wooton of New Mexico State University. An economical approach, which facilitated control over surface roughness features at microscale, was employed to the machine dimpled surfaces. CAD drawings (Figure 3.16) of 300 µm, 400 µm, and 500 µm dimples were fed to a CNC machine. Appropriate sized ball end-mills were moved in the *Z* direction to a desirable depth - equal to the height of the dimples, or 200 µm, to create the dimples with characterizeable features on plain Cu surfaces. To isolate the simultaneous effect of more than one parameter on the nucleate boiling performance, the depth and pitch-to-diameter ratio of the dimples were kept constant at 200 µm and 2.0, respectively. Only the dimple diameter was varied. The 10x10x1.6 mm Cu surfaces with 300 µm, 400 µm and 500 µm diameter dimples contained 295, 149 and 105 dimples respectively. Thus, the resulting ratio of geometrical to footprint surface area is 1.35, 1.19, and 1.13 for the 300, 400, and 500 µm dimpled surfaces, respectively.

The excess material removed/displaced during the milling of a dimple was found to form along the circumference of the dimple. In addition, copper build up on the mill bits was found to form a weld at high speeds. Therefore, a low RPM was chosen for the CNC machine (~600-1000 RPM as against >2000 RPM) and a non-sticking lubricant (mineral oil with ~10% lard oil) was used during the machining process. Cu lumps and peaks around dimples were removed using a lubricant combined with polishing using a 2000 grit sand paper. Samples were washed with distilled water to remove the copper powder settled inside dimples during polishing. A comparison of the surface before and after employing this approach is shown in Figure 3.17.

Figure 3.18 shows the finished dimpled surfaces. High resolution scanning electron microscopy (SEM) analysis along with confocal microscopy (TCS SP5 II) was used to comprehensively measure the dimensions which were found to deviate from the intended sizes by a maximum of ±11 µm. The maximum variation was found to be in the pitch between the dimples, while a minimum variation of ±5 µm was observed in the dimple depth. These deviations can be primarily attributed to the wobbling of the mill bit in the Computer Numerical Control machine. The dimpled surfaces did not have surface roughness or other features measured.

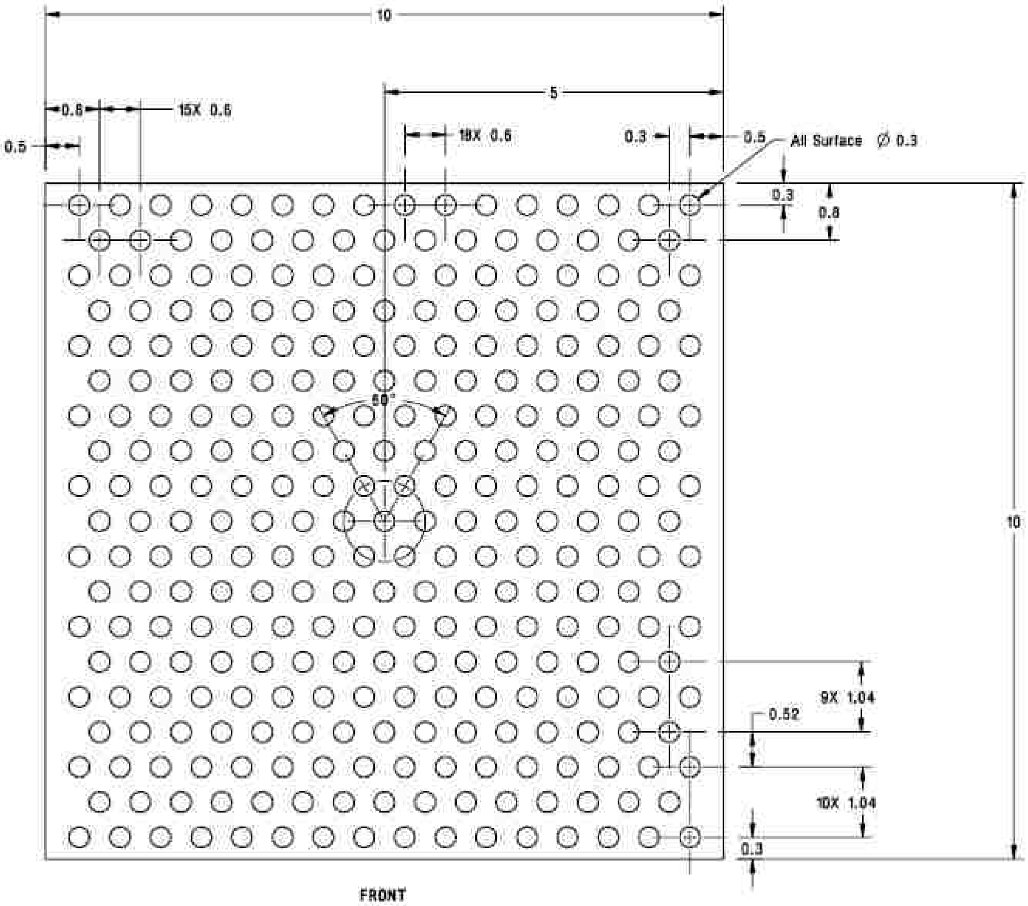

Figure 3.16. CAD drawing showing geometric features of a surface with 300 µm dimples. (El-Genk et al. 2015)

Figure 3.17. Comparison of surface finish of a dimpled surface before (left) and after (right) employing lubricating agent-assisted polishing. (El-Genk et al. 2015)

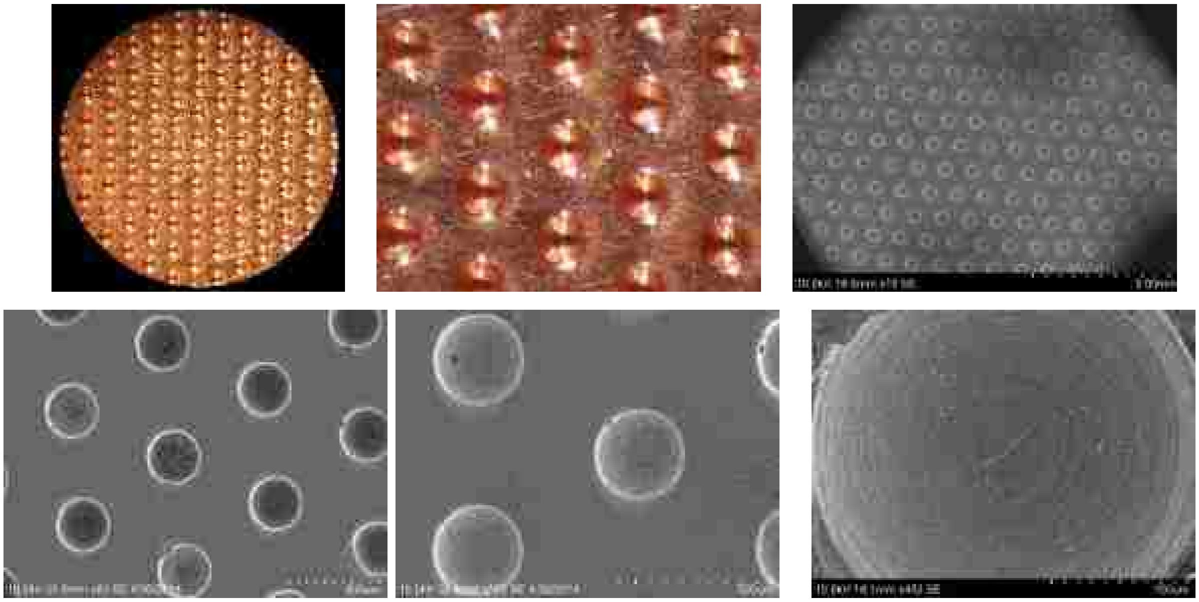

Figure 3.18. Images of a surface with dimples of 300 µm footprint diameter; nanoscale roughness generated due to machining (visible at 450x) coupled with engineered microscale roughness of the dimples generates a roughness hierarchy on the surface. (El-Genk et al. 2015)

3.6 Experiments Uncertainties

3.6.1 Uncertainty in Experimental Data

The experimental uncertainties were determined from the manufacturers' stated specifications and uncertainties associated with measuring. The total estimated uncertainties were obtained using the following method described by Kline and McClinktock (1952), using the following function:

$$W_G = \left[\sum_{i}^{n} \left(\frac{\partial G}{x_i} \Delta x_i \right)^2 \right]^{1/2} \tag{3.1}$$

where G is a variable of interest from the experiments that may be represented as:

$$G = G(x_1, x_2, \dots x_n) \tag{3.2}$$

For the variable of interest G, Δx_i is the associated uncertainty in the individual measurement or independent variable.

The overall uncertainties in the measurements were estimated by the standard deviation of the systematic and random uncertainties, ΔM, as:

$$\Delta M = (\Delta M_{sys}^2 + \Delta M_{rand}^2)^{1/2} \tag{3.3}$$

The manufacturer stated systematic and random uncertainties in the measurements for the power provided to the heating element in the test section by a direct current are 0.05% and ± 5mV for the applied voltage and 0.15% and ± 5mA for the supplied electrical current, respectively (Agilent, 2000). Thus, the calculated uncertainties in the applied voltage and current are <<1% and <1%, respectively.

The power removed from the boiling surface is the product of the applied current and voltage drop across the underlying heating element. By applying the product of voltage (V) and current (I) to Equation 3.3, this results in the uncertainty of power measurement as:

$$\frac{\Delta P}{P} = \left[\left(\frac{\Delta V}{V}\right)^2 + \left(\frac{\Delta I}{I}\right)^2\right]^{1/2} \tag{3.4}$$

The power supplied to the underlying heating element may also be written in terms of heat flux removed through the boiling surface as:

$$q = \frac{P}{A} \tag{3.5}$$

where A is the surface area of the boiling surface. Thus the uncertainty in applied heat flux was estimated using the following equation:

$$\frac{\Delta q}{q} = \left[\left(\frac{\Delta P}{P}\right)^2 + \left(\frac{\Delta A}{A}\right)^2\right]^{1/2} \tag{3.6}$$

The uncertainty in the applied heat flux is a function of the applied current and voltage drop across the underlying heating element (systematic error), and uncertainty in the measured surface area of the boiling surface (random error) (Equation 3.6). For all experiments in the present work, the uncertainty in heat flux ranges from 3.2% at low heat fluxes (~5 W/cm^2) and improves slightly to 3% at high heat fluxes (~20 W/cm^2).

The reported heat transfer coefficients, h_{NB}, were calculated from obtained experimental data as:

$$h_{NB} = \frac{q}{T_w - T_b} \tag{3.7}$$

where T_w is the temperature of the boiling surface, and T_b is the liquid pool temperature. Thus, the associated uncertainty with h_{NB} may was calculated from:

$$\frac{\Delta h_{NB}}{h_{NB}} = \left[\left(\frac{\Delta q}{q}\right)^2 + \left(\frac{\Delta(T_w - T_b)}{(T_w - T_b)}\right)^2\right]^{1/2} \tag{3.8}$$

As the uncertainty of a single thermocouple used in the experiments is $\pm$ 0.2 K, the uncertainty in the difference the obtained readings of the surface temperature and bulk liquid $\Delta(T_w - T_b)$ is $\pm$ 0.4 K. The estimated overall uncertainties of h_{NB} for the present experiments range consistently from ~5.1% at low heat fluxes (~5 W/cm^2) and improve to ~3.8% at high heat fluxes (~20 W/cm^2).

The uncertainty of the wall temperature at the CHFs reported is that of the arbitrarily chosen experimental termination condition, and is typically anywhere from 1 – 5 K depending on the size of the power increment just prior to CHF. The uncertainty of the heat flux at CHF is that of the calculated systematic uncertainty of q at high heat flux (~3%) plus the additional uncertainty in the power increment just prior to CHF. The exact CHF occurred in between the two final experimental power steps. However, the difference in these two final power steps was typically very small at <0.05W. Thus, the additional uncertainty for CHF is <0.25% for CHFs > 20 W/cm^2. Thus, there is a total maximum uncertainty of ~3.25% in the value of heat flux at CHF.

3.6.2 Uncertainty of Image Capture Measurements

The uncertainties in the present measurements of the size of the bubble on the smooth and rough Cu surfaces are $\pm$ 32 – 35 μm, and are that of the image's pixel size in relation to the known size of the Cu surface (10 mm), as well as focusing distance of the camera. The uncertainty of the measured detachment frequency is $\pm$ 0.5 frames, as the departure event itself was never captured, but known to happen within the frame between the last bubble captured in the ebullition cycle and subsequent frame. The uncertainty in the calculated detachment frequency in Hz is also that of the camera frame rate (210fps), as well as the bubble ebullition cycle length. Longer ebullition cycles contain less uncertainty, as the half frame of uncertainty in measured detachment frequency is smaller compared to the total number of frames that make up that full ebullition cycle. For the smooth and rough Cu surfaces, the uncertainty in the calculated detachment frequency was typically ± 5.9% and ± 7.7%, respectively.

Table 3.1. The uncertainties of the obtained experimental data (ΔT_{sat}, q, h_{NB}, CHF) and measured bubble transient growth (D_b , D_d , f_d).

Parameter	Uncertainty
Surface Superheat, ΔT_{sat}	± 0.4 K
Temperature, T	± 0.2 K
Surface Area, A	± $(0.02\ \text{mm})^2$
Applied Heat Flux, q	3 – 3.2 % for all q
Nucleate boiling heat transfer coefficient, h_{NB}	3.8 – 5.1 % for all h_{NB}
Critical Heat Flux, CHF	3.25 – 3.45 %
$T\ at\ CHF$	± 1 – 5 K
Bubble Diameter $D_b\ and\ D_d$	± 32 – 35 μm
Bubble detachment frequency, f_d	5.9 – 7.7 %
Dimple Bubble Diameter $D_b^* and\ D_d^*$	± 55 – 66 μm
Dimple Bubble detachment frequency, f_d^*	7.6 – 11.7 %

For the bubbles captured on the dimple Cu surfaces, the bubble grew into an ellipsoid with a maximum observed aspect ratio of 1.2 before departing. Therefore, two measurements were taken – one of the ellipsoid major axis, a, and the other of the minor axis, b. The depth of the ellipsoid, c, was assumed to be the same as the b. The departure diameter, and associated uncertainty, was obtained from the equivalent volume of a sphere as:

$$D_d^* = (8ab^2)^{1/3} \tag{3.9}$$

$$\frac{\Delta D_d^*}{D_d^*} = \left[\left(\frac{1}{3} \frac{\Delta a}{a} \right)^2 + \left(\frac{2}{3} \frac{\Delta b}{b} \right)^2 \right]^{1/2} \tag{3.10}$$

Appendix A2 provides sample calculations of the uncertainty in the measurement of the dimple bubble growth. The uncertainties in D_d^* ranged from $\pm$ 55 – 66 μm depending on the size of the dimple. Table 3.1 lists the uncertainties of the experimental and measured data of the present work. Appendix A1 provides sample calculations of the uncertainties in Table 3.1.

The next chapter presents the obtained results for the saturation and subcooled pool nucleate boiling experiments that were performed using PF-5060 dielectric liquid on rough Cu surfaces.

4. Nucleate Pool Boiling of PF-5060 on Smooth and Rough Cu Surfaces

This chapter presents the experiments that investigated the effect of surface roughness, Ra, inclination angle, θ, and liquid subcooling, ΔT_{sub}, on the nucleate pool boiling of degassed PF-5060 dielectric liquid on Cu surfaces. The 10 x 10 x 1.6 mm Cu surfaces investigated have an average roughness of 0.039 µm (smooth Cu), 0.134 µm, 0.21 µm, 0.28 µm, 0.33 µm, 0.58 µm, 0.71 µm, 0.80 µm, 0.925 µm, 1.00 µm, 1.21 µm, 1.44 µm, and 1.79 µm. Up to nine inclination angles of 0^o (upward facing), 30^o, 60^o, 90^o (vertical), 120^o, 150^o, 160^o, 170^o, 180^o (downward facing), and five liquid subcooling of 0 K (saturation), 5 K, 10 K, 20 K, and 30 K were experimented with.

Correlations for nucleate pool boiling of PF-5060 on smooth and rough Cu surfaces were developed for: (i) the fully developed nucleate boiling heat transfer coefficient, h_{NB}, in terms of surface superheat and Ra, (ii) the maximum nucleate boiling heat transfer coefficient, h_{MNB}, in terms of Ra and the surface inclination angle, θ (iii) the Critical Heat Flux (CHF) in terms of Ra, θ, and the liquid subcooling, ΔT_{sub}, and (iv) the natural convection heat transfer, q_{NC} and h_{NC}, in terms of the applied heat flux and / or surface superheat. The developed correlations were checked against the experimental data, and compared with others reported in the literature for PF-5060 or other dielectric liquids on different structured surfaces (Cooper, 1984; Gorenflo et al. 1993; Rainey and You, 2000; El-Genk and Bostanci, 2003; Jabardo and Ribatski, 2003; Wei and Honda 2003; Priarone, 2005; Parker and El-Genk, 2005, 2008; Sathymurthi et al. 2009; Ali and El-Genk 2013)

4.1 Reproducibility of Results

To ensure reproducibility of the results, separate experiments with Cu surfaces of the same average roughness were conducted multiple times each. Figure 4.1 presents the obtained saturation pool boiling curves for PF-5060 on two Cu surfaces with Ra of 0.21 and 1.44 µm, in the upward facing orientation. Each of these figures includes 3 – 4 boiling curves for separate experiments performed at least ~2 hours, and sometimes 1 – 2 days apart. The repeated experiments with the same test section, as well as with different

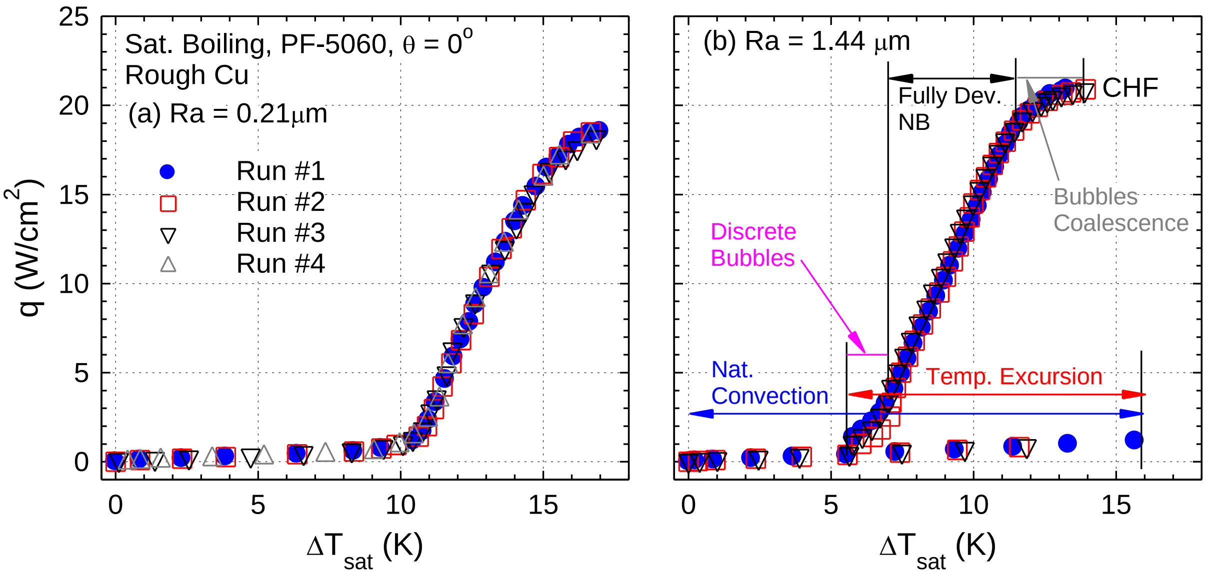

Figure 4.1. Reproducibility of the pool boiling curves of saturation nucleate boiling of PF-5060 on rough Cu show repeated runs to be consistent. Each region of the pool boiling curve is also labeled in (b).

test sections of Cu surfaces of the same average roughness, confirm the fidelity and consistency of the procedures used prepare the rough Cu surfaces and conduct the pool boiling experiments.

4.2 Nucleate Boiling Results

This section presents the results on the effect of surface roughness, Ra, inclination angle, θ, and liquid subcooling, ΔT_{sub}, on nucleate pool boiling of degassed PF-5060 dielectric liquid. As a brief introductory overview to this section, the pool boiling curves in Figure 4.2 and Figure 4.3 show how increased surface roughness enhances nucleate boiling and increased CHF (the last data points in the pool boiling curves), for all inclination angles 0^o – 180^o. A shift of the pool boiling curve to the left indicates the enhancement in the nucleate boiling heat transfer. When the boiling curve shifts to the left, for the same applied heat flux, the decrease in surface superheat, ΔT_{sat}, increases the nucleate boiling heat transfer coefficient, h_{NB}. Figure 4.2 and Figure 4.3 show this behavior for the rougher Cu surfaces. Conversely, the increase of inclination angle, θ, decreases both the maximum nucleate boiling heat transfer coefficient, h_{MNB}, and the CHF.

The obtained pool-boiling curves (Figure 4.2) with incrementally increasing the input power include temperature excursions prior to boiling incipience of ~17 K. This temperature excursion is more than 10 K smaller than has been reported (Chang and You, 1997; Rainey and You, 2001; El-Genk and Bostanci, 2003) and over 20 K smaller than measured in this work on the smooth Cu (Ra = 0.039 μm) Temperature excursions typically occurred when testing the rough Cu surfaces for the first time, or after a prolonged cool down time. Despite the relatively low saturation temperatures of the dielectric liquids, such as PF-5060, for nucleate boiling immersion cooling of high-power computer chips, an excursion in the surface temperature prior to boiling incipience is undesirable. This is because it could raise the junctions' temperatures beyond the manufacturers' recommendations. Nevertheless, surface roughening lessened the temperature excursion compared to smooth Cu. The temperature excursion prior to boiling incipience indicates the extent of the natural convection region (Suszko and El-Genk, 2014) and is a direct consequence of the high surface wetting and the very low surface tension (Table 2.1) of the PF-5060 dielectric liquid. Following temperature excursion is the incipience of boiling and the discrete bubbles region (Figure 2.6) followed by the fully developed nucleate boiling region, bubbles coalescence, and CHF (Figure 4.1).

The entirety of the investigations of the effect of Ra, θ, and ΔT_{sub} on nucleate boiling of PF-5060 on smooth and rough Cu surfaces is broken up and presented in the following sub-sections: (i) fully developed nucleate boiling heat transfer coefficient, h_{NB}, (ii) maximum nucleate boiling heat transfer coefficient, h_{MNB}, (iii) Critical Heat Flux (CHF) and (iv) natural convection heat transfer. The discrete bubbles region was also investigated, and is part of the visualization study that observed bubble growth dynamics, presented in the later sections of this chapter. The first sub-section presents the results of the fully developed nucleate boiling of PF-5060 on smooth and rough Cu surfaces.

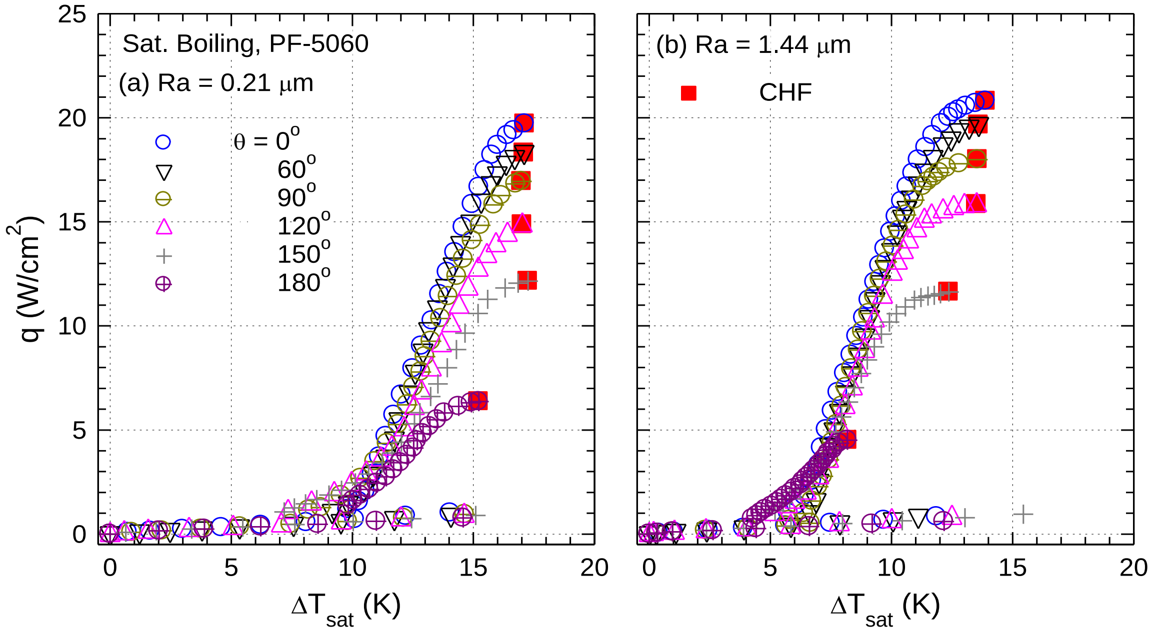

Figure 4.2. Pool boiling curves of saturation nucleate boiling of PF-5060 on rough Cu surfaces of Ra = (a) 0.21 μm and (b) 1.44 μm, at inclination angles 0° – 180°. The CHF decreases with increasing inclination angle.

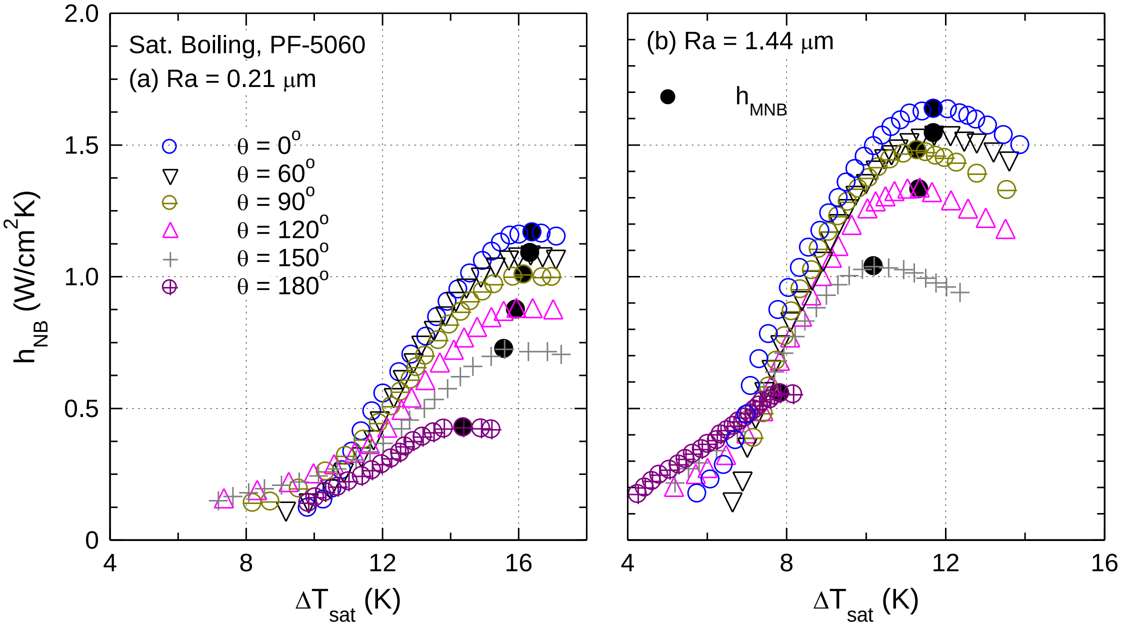

Figure 4.3. Nucleate boiling heat transfer coefficient curves of saturation nucleate boiling of PF-5060 on rough Cu surfaces of Ra = (a) 0.21 μm and (b) 1.44 μm, at inclination angles 0° – 180°. The h_{MNB} decreases with increasing inclination angle.

4.2.1 Effects of Ra on Fully Developed Nucleate Boiling

The majority of the pool boiling curve is made up of the fully developed region (Figure 2.3, Figure 4.1). In this region, all sites for potential bubbles nucleation are active, and nucleate boiling heat transfer coefficients are highest and increase with increasing heat flux, until reaching the maximum nucleate boiling heat transfer coefficient, h_{MNB}. The end of the fully developed region is marked $h_{\mathrm{MNB},}$ which is discussed in the following sub-section.

In the nucleate boiling literature, the fully developed nucleate boiling heat transfer coefficient, h_{NB}, has often been correlated in the following form: (Kozitskii, 1971; Nishikawa et al. 1982; Cooper, 1984; Gorenflo et al. 1993; Jabardo and Ribatski, 2003);

$$h_{NB} = Aq^{B} \tag{4.1}$$

where coefficients “A” and “B” are empirically determined. The form of Equation (4.1) fit the obtained experimental data well, for the upward facing inclination angle (Figure 4.4a–c). Further analysis of the pool boiling experiments results for the upward facing inclination showed the coefficients “A” and exponent “B” to both be functions of surface roughness, Ra (Figure 4.4c), as:

$$A(Ra) = 0.20\ Ra^{0.24} \tag{4.2}$$

$$B(Ra) = 0.71\ Ra^{-0.04} \tag{4.3}$$

These correlations for the coefficients “A” and “B” are within ± 8% and ± 4 % of the obtained experimental data for Ra = 0.039 – 1.79 µm (Figure 4.5). The coefficient “A” increases with Ra to nearly the 1/4th power, and conversely the exponent “B” is a weak function of Ra that decreases as Ra increases. The coefficient “A” increases from ~ 0.09 to 0.23 (Figure 4.5a) , while the exponent “B” decreases from ~0.81 to 0.69 (Figure 4.5b), as Ra increases from 0.039 – 1.79 µm. The values of the coefficient “A” are higher those reported in the literature for saturation boiling of different liquids on rough cylinders and plates (Danilova and Bel’skii, 1965; Nishikawa et al. 1982; Jones et al. 2009; Jabardo, 2010). The exponent “B” is reported by others to vary from 0.6 – 0.8 (Kozitskii, 1971; Nishikawa et al. 1982), depending on surface characteristics, which is consistent with the values obtained for smooth and rough Cu surfaces (Figure 4.5b). It is also reported to be a constant of ~ 2/3 (Cooper, 1984).

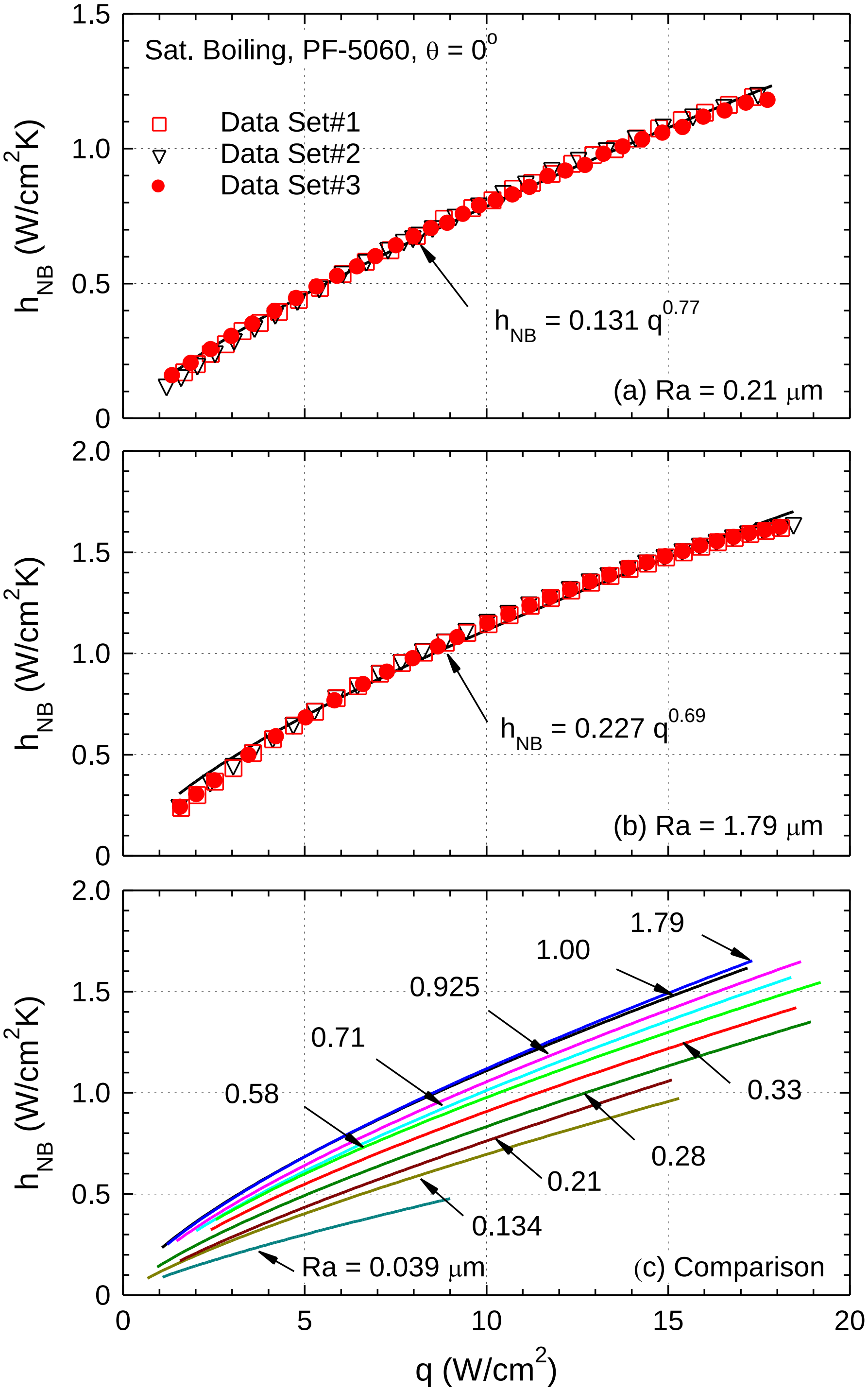

Figure 4.4. The nucleate boiling heat transfer coefficient, h_{NB}, in terms of the applied heat flux, q. The experimental data fits the proposed form of h_{NB} α Aq^B well.

The developed correlation of h_{NB} for the upward facing inclination angle in the combination of Equations (4.2) – (4.3), is given as:

$$h_{NB}(Ra, \theta = 0^o) = 0.20\, Ra^{0.24} q^{0.71\, Ra^{-0.04}} \tag{4.4}$$

Figure 4.6 plots the predictions of the h_{NB} correlation in Equation (4.4) versus the experimental data at the same surface superheats. This figure shows that for all Ra investigated in this research, Equation (4.4) agrees with the experimental data to within ± 12%. At the heat flux of q ~ 15 W/cm^2 (Figure 4.4c) h_{NB} for the surface roughness of 0.21 μm is ~ 1.1 W/cm^{2}K, and ~1.5 W/cm^{2}K on the Cu surface with the highest roughness of 1.79 μm. This represents a 36% enhancement in h_{NB}, solely due to surface roughening, at this applied power. The next sub-section presents the comparison of the predictions made by the developed h_{NB} correlation (Equation (4.4)) at the upward facing angle, against those provided by others (Gorenflo et al. 1993, Jabardo 2003, Cooper, 1984).

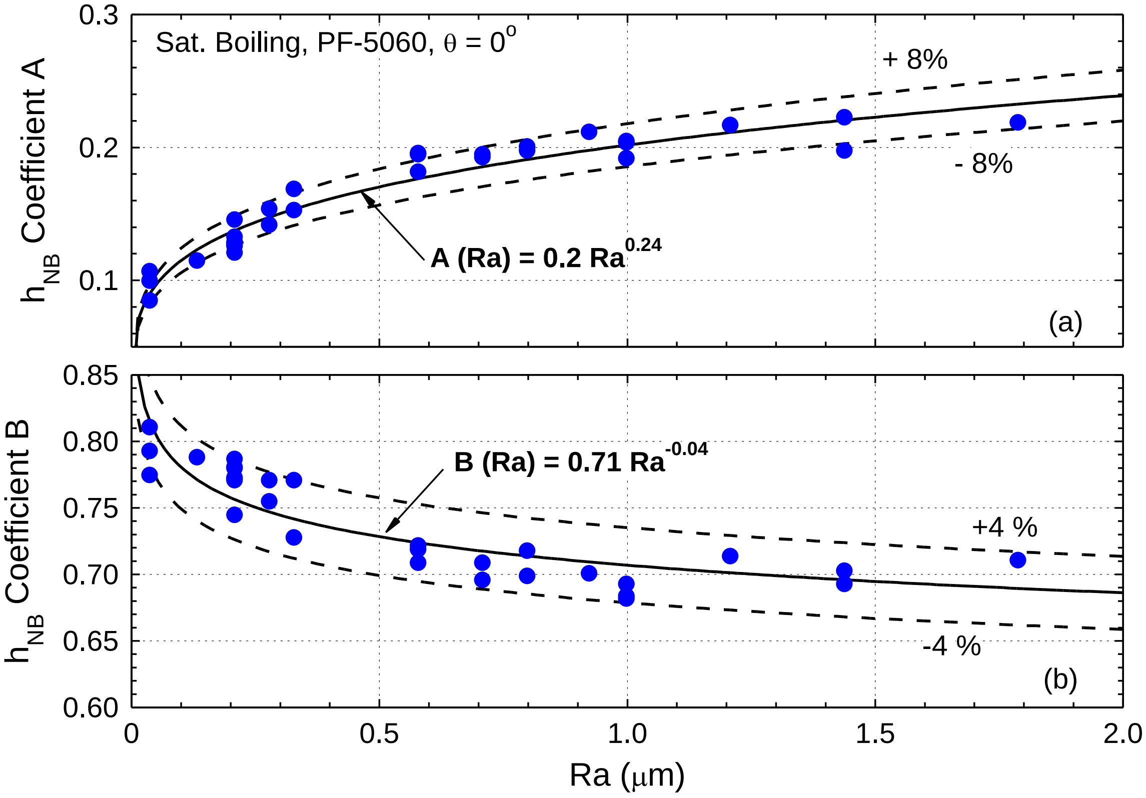

Figure 4.5. The h_{NB} coefficient "A" and exponent "B" as functions of Ra.

4.2.2 Comparison with Other Nucleate Boiling Correlations

Figure 4.7 compares the predictions of the h_{NB} correlation (Equation (4.4)) obtained for saturation nucleate boiling of PF-5060 dielectric liquid on rough Cu surfaces in the upward facing orientation, with those of Gorenflo et al. (1993), Jabardo (2003), and Cooper (1984). In this figure, each envelope is the range of h_{NB} predicted by a specific correlation for a range of heat flux, q, and surface roughness, Ra. The left and right boundaries of all envelopes were chosen to be for an applied q of ~5 W/cm^2 and ~15 W/cm^2. This range of q ensured all predictions of h_{NB} were of the fully developed nucleate boiling region. The lower and upper boundaries of each envelope are for Ra = 0.039 µm and 1.79 µm, respectively, to match the range of Ra investigated.

For nucleate boiling of saturated PF-5060 on rough Cu surfaces at the upward facing inclination angle, Cooper's correlation gives the largest spread in the values of h_{NB} (Figure 4.7) with surface roughness. The upper boundary of the h_{NB} envelope for the present correlation (Equation (4.4)) for Ra = 1.79 µm is slightly higher than of that calculated using Gorenflo et al.'s (1993) correlation, and much higher than the calculated values using Jabardo's (2003) correlation. The upper boundary of Cooper's (1984) correlation for Ra = 1.79 µm is much higher than that of the present correlation, with the difference increasing as q increases (Figure 4.7). The lower boundary of the h_{NB} envelope using the present correlation (Equation (4.4)) that corresponds to Ra = 0.039 µm is generally higher than those calculated by the other correlations. The closest is that calculated by Jabardo's (2003) correlation, followed closely by Gorenflo et al.'s (1993) correlation. Cooper's (1984) correlation predicts the lowest h_{NB} values on smooth surfaces with Ra = 0.039 µm (Figure 4.7).

As shown in Figure 4.7, the predictions of the developed h_{NB} correlation in this work (Equation (4.4)) were generally consistent with those of Gorenflo et al. (1993) for the roughest Cu surface (Ra = 1.79 µm). Cooper's (1984) correlation over predicted h_{NB} for the roughest Cu surface, and under predicted its values for the smooth Cu surface. The h_{NB} predictions using Jabardo's (2003) correlation were consistently lower than the present correlation (Equation (4.4)). However, it is worth noting that the spread in the calculated h_{NB} values in Figure 4.7 using Jabardo's (2003) correlation is similar to that for the present correlation (Equation (4.4)). Therefore, Jabardo’s (2003)

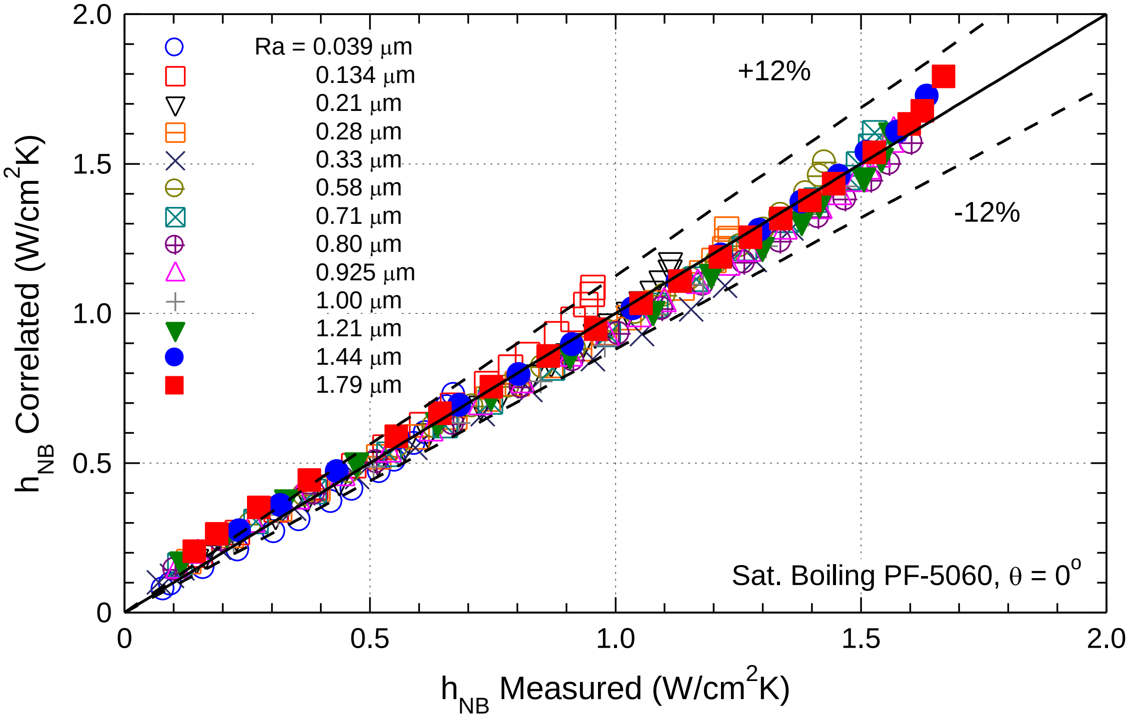

Figure 4.6. The measured vs calculated prediction of h_{NB} by the developed correlation in Equation (4.4) for saturation nucleate boiling of PF-5060 on smooth and rough Cu surfaces at the upward facing inclination.

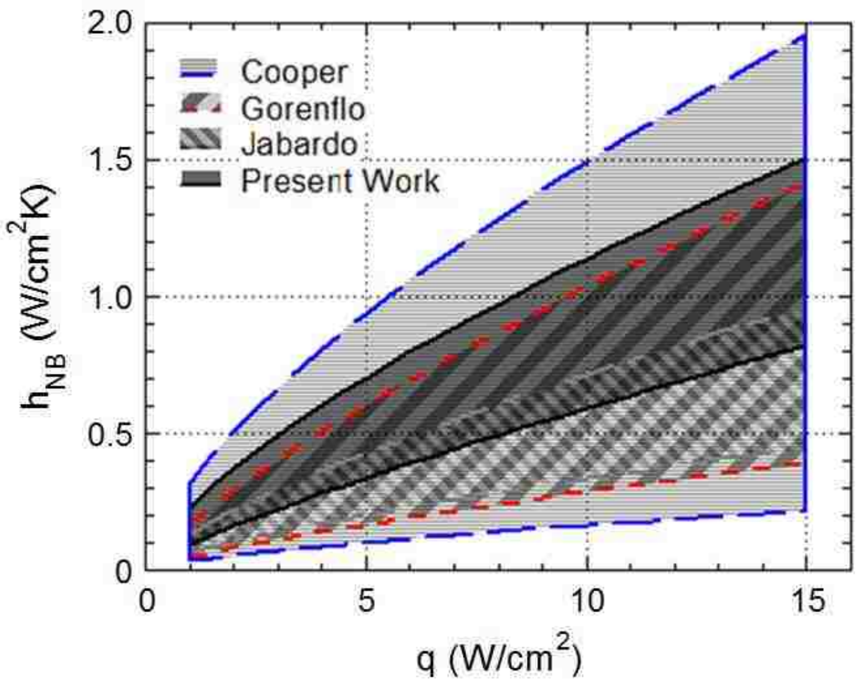

Figure 4.7. The predictions of h_{NB} from various correlations in fully developed nucleate boiling of PF-5060 on rough Cu surfaces of Ra = 0.039 - 1.79 µm. Each envelope is for a different correlation.

correlation predicts roughly the same relative impact of Ra on h_{NB}, with a different leading constant that may be depend on the thermophysical properties of the boiling liquid and / or heated surface.

The present values of h_{NB} for saturation nucleate boiling of PF-5060 on Cu surfaces are in the middle of the predicted ranges of the correlations by Cooper (1984), Gorenflo et al. (1993), and Jabardo (2003). The developed correlation (Equation (4.4)) is much simpler and the scattering of the experimental data used for developing the correlation was relatively small (Figure 4.6). However, the h_{NB} data used to develop Equation (4.4) were of only one dielectric liquid (PF-5060) on a single surface material (Cu), whilst those of Cooper (1984), Gorenflo et al. (1993), and Jobardo (2003) are based on comprehensive databases involving different liquids and surface materials, and sometimes data from different sources. Furthermore, reported surface roughness values from different sources carry measurable uncertainties due to the variances in the methods used to prepare the surfaces, and the techniques used to estimate Ra.

Very little difference was observed in the trend of h_{NB} vs q when the surface inclination angle, θ, was varied. However, the maximum nucleate boiling heat transfer coefficient, h_{MNB}, which marks the end of the fully developed nucleate boiling region, was observed to change with θ. The following sub-section presents the results that quantify the effects of the inclination angle and Ra, on h_{MNB}, for saturation nucleate boiling of PF-5060 on smooth and rough Cu surfaces.

4.2.3 Effects of Ra and Inclination Angle on h_{MNB}

Figure 4.8 presents the experimental results that show the effect of inclination angle, θ, from $0^{o} – 180^{o}$, on h_{MNB}, for saturation boiling of PF-5060 dielectric liquid on smooth and rough Cu surfaces. This figure shows that at any surface inclination, h_{MNB} increased as Ra increased. However, for any given Ra, h_{MNB} was highest for the upward facing orientation. It decreased gradually as inclination angle increased, to the lowest value in the downward facing orientation. The values of h_{MNB} in the downward facing orientation were typically ~40% of those in the upward facing orientation (Figure 4.8b)

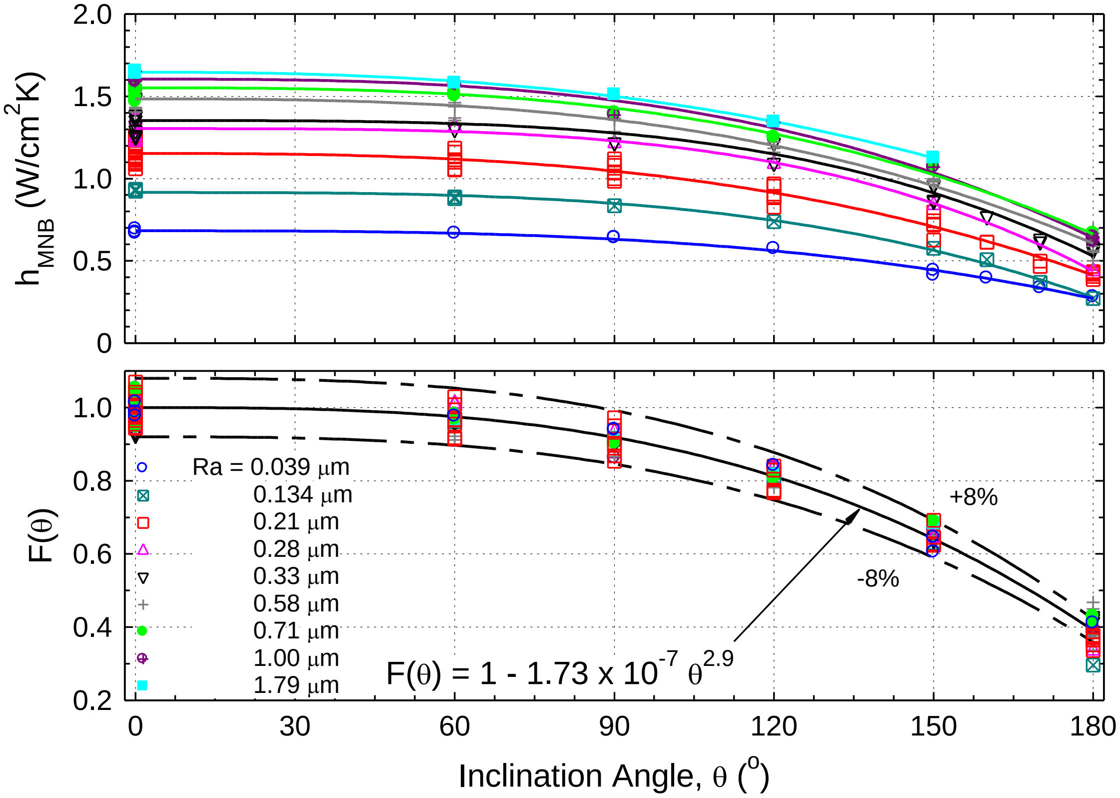

Figure 4.8. The effects of surface inclination angle and roughness on the h_{MNB}, show the h_{MNB} to be independent of Ra with increasing inclination angle.

The increase of h_{MNB} with increased Ra was highest in the upward facing orientation, and lowest in the downward facing orientation (Figure 4.8a). When θ equaled 0^o, h_{MNB} increased from ~ 0.67 to ~1.65 W/cm^2 K, as Ra increased from 0.039μm to 1.79 μm. For the same range of Ra in the downward facing orientation, h_{MNB} increased from ~ 0.27 to ~0.64 W/cm^2 K. These numbers show the relative increase of h_{MNB} is highest in the downward facing orientation.

Despite the differences in the values of h_{MNB} on the different rough Cu surfaces with increased inclination, the normalized values of h_{MNB} (for each Ra) at each inclination angle, relative to those in the upward facing orientation, collapsed onto a single curve (Figure 4.8b). This curves shows h_{MNB} to be almost independent of Ra with increasing θ. The small spread of the normalized h_{MNB} values in Figure 4.8 is comparable to the estimated experimental uncertainties. The effect of surface roughness and inclination angle on the h_{MNB} of PF-5060 on smooth and rough Cu surfaces was correlated in the following form:

$$h_{MNB}(Ra,\theta) = F(\theta)\ h_{MNB}(Ra,\theta = 0^{o}) \tag{4.5}$$

where $F(\theta)$, the normalized values of h_{MNB} with surface inclination was found to be:

$$F(\theta) = 1 - 1.73 \times 10^{-7}\ \theta^{2.9} \tag{4.6}$$

This correlation is within ± 8% of the experimental data in Figure 4.8b. The h_{MNB} for saturation boiling of PF-5060 liquid on rough Cu surfaces in the upward facing orientation was correlated (Figure 4.9) in terms of Ra, as:

$$h_{MNB}(Ra,\theta = 0^{o}) = 1.63\ Ra^{0.227} \tag{4.7}$$

This correlation agrees to the experimental data to within $\pm$ 10% (Figure 4.9). The full form of Equation (4.4), given as:

$$h_{MNB}(Ra,\theta) = (1 - 1.73 \times 10^{-7}\theta^{2.9})1.63\ Ra^{0.227} \tag{4.8}$$

This correlations agrees with the h_{MNB} values for all rough Cu surfaces investigated, of saturation nucleate boiling of PF-5060 at inclination angles 0^{o} – 180^{o} , to within $\pm$ 12% (Figure 4.10).

Figure 4.11 is a map of the obtained values of h_{MNB} for saturation boiling of PF-5060 on smooth and rough Cu surfaces, at different inclination angles. The map is a grid of intersecting curves that represent different Ra and inclination angles. It shows h_{MNB} increases when θ decreases, or Ra increases. The highest values of h_{MNB} are in the upward facing orientation. In that orientation, h_{MNB} increases from ~0.67 W/cm^{2} K on the smooth Cu surface of Ra = 0.039 μm, to ~1.72 W/cm^{2} K on the rough Cu surface of Ra = 1.44 μm. This represents more than 150% enhancement in the maximum nucleate boiling heat transfer coefficient due to surface roughening. The lowest values of h_{MNB} are in the downward facing orientation. In that orientation, h_{MNB} increases from ~0.27 W/cm^{2} K on the smooth Cu surface of Ra = 0.039 μm, to ~0.8 W/cm^{2} K on the rough Cu surface of Ra = 1.44 μm. This represents nearly 200% enhancement in the maximum nucleate boiling heat transfer coefficient due to surface roughening, for this inclination angle. For the other inclination angles of 60^{o}, 90^{o}, 120^{o}, and 150^{o}, h_{MNB}

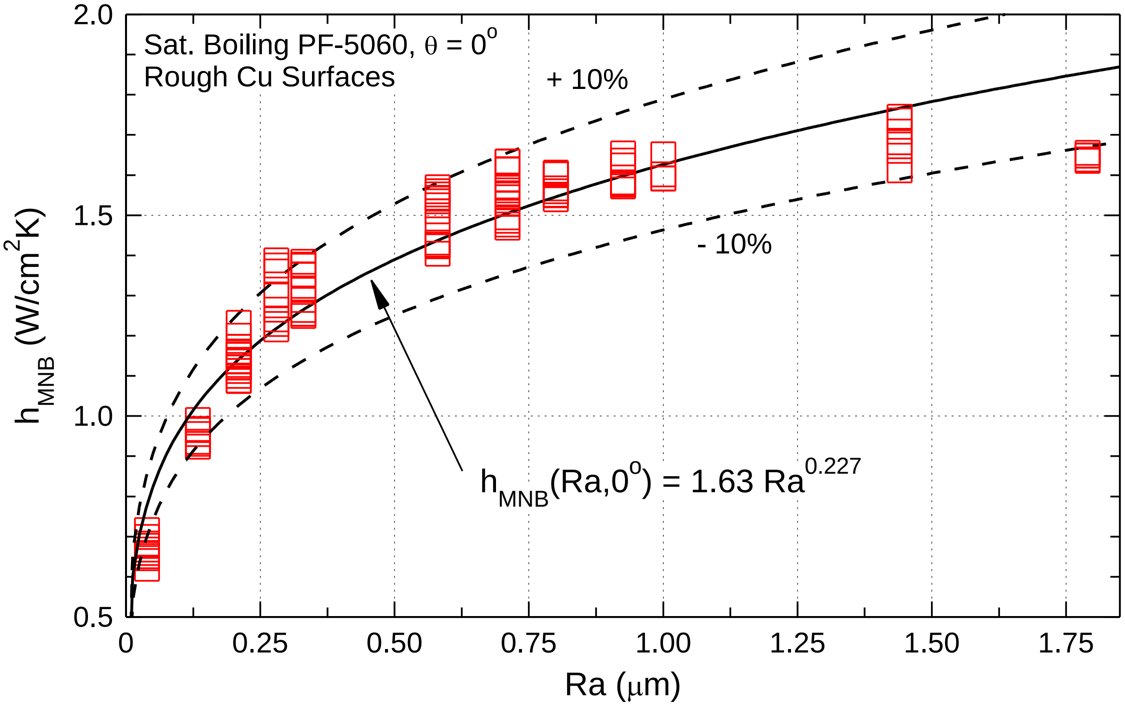

Figure 4.9. The dependence of *h*$_{MNB}$ on surface roughness in saturation nucleate boiling of PF-5060 on smooth and rough Cu surfaces at the upward facing orientation.

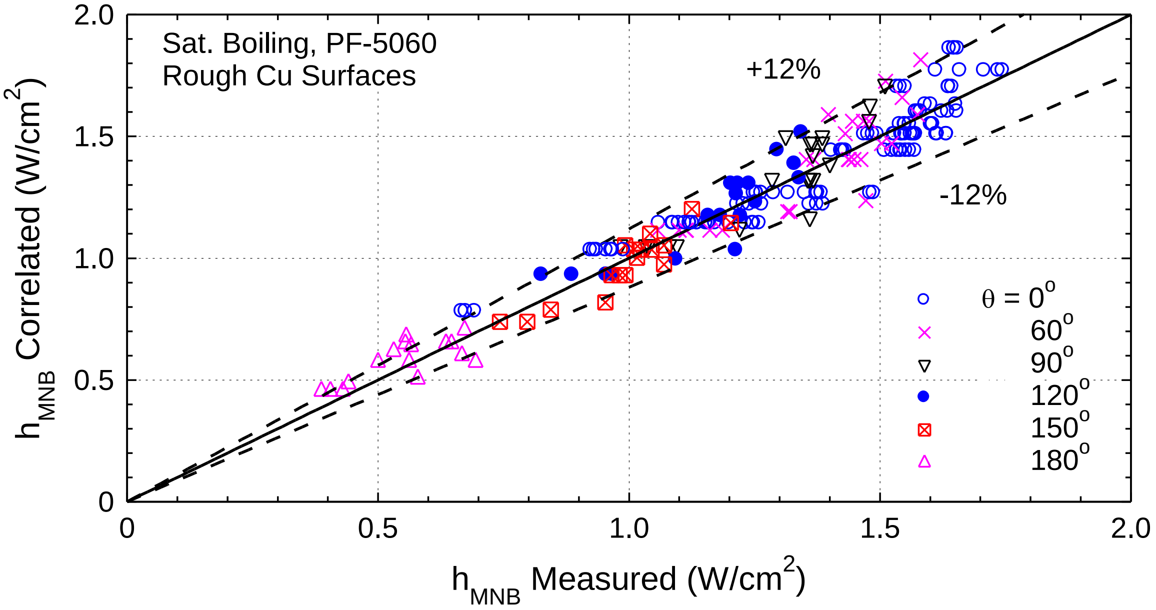

Figure 4.10. Comparison of *h*$_{MNB}$ predictions from Equation (4.8) against the experimental measurements show good agreement.

increases ~159%, ~143%, ~144%, and 155%, receptively, as Ra increases from 0.039 to 1.79 µm (Figure 4.11).

The increases of h_{NB} and of h_{MNB} are directly related to the increased active nucleate sites density for bubbles nucleation, which is discussed more in detail later this chapter. The next section presents the results of the effects of surface roughness, inclination angle, and liquid subcooling on the CHF of PF-5060 dielectric liquid on smooth and rough Cu surfaces.

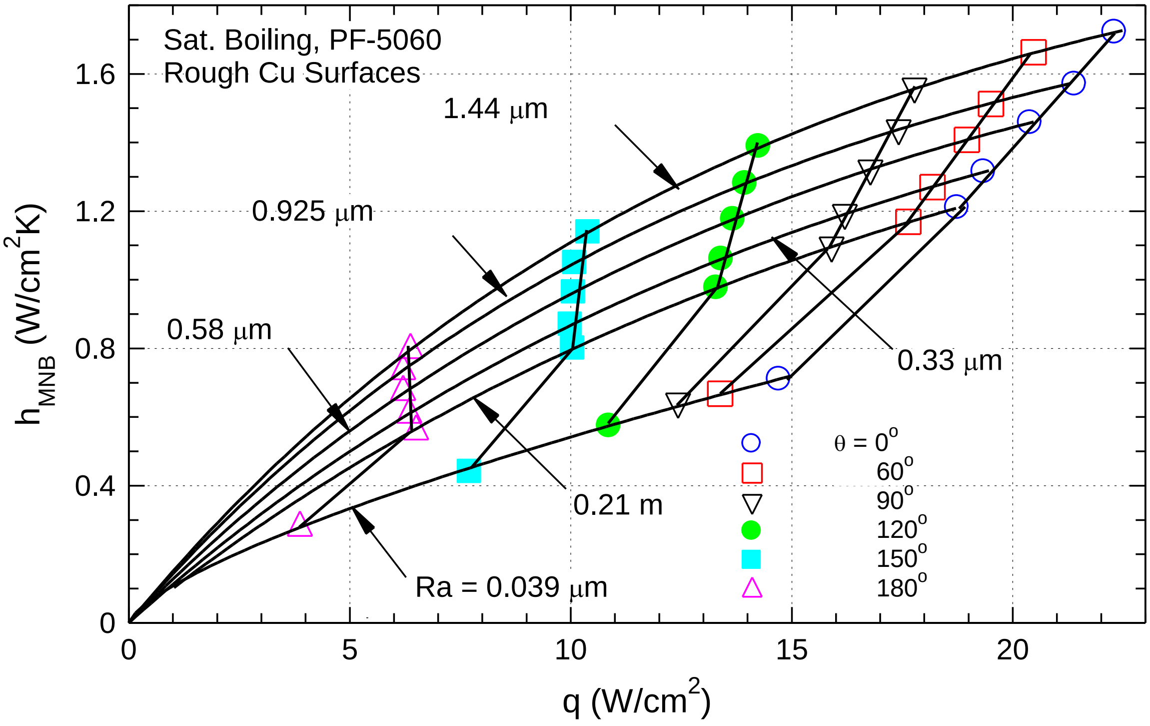

Figure 4.11. A performance map for the h_{MNB} of saturation nucleate boiling of PF-5060 on rough Cu surfaces at inclination angles 0° – 180°.

4.3 Critical Heat Flux

For applications involving nucleate boiling, it is desirable to know the location of the Critical Heat Flux. This section presents the results on the effects of surface roughness, Ra, inclination angle, θ, and liquid subcooling, ΔT_{sub}, on the critical heat flux (CHF) of degassed PF-5060 dielectric liquid, on smooth and rough Cu surfaces. The obtained and correlated results are presented in the following sub-sections: (i) effect of Ra on CHF, (ii) effect of θ on CHF, and (iii) effect of ΔT_{sub} on CHF.

As a brief introduction to this section, Figure 4.12a and Figure 4.12b show the obtained pool boiling and h_{NB} curves for saturation nucleate boiling of PF-5060 on Cu surfaces with Ra = 0.039, 0.134, 0.21, 0.28, 0.58, 0.925, and 1.79 µm, in the upward facing orientation ($\theta = 0^{o}$). These figures denote the CHF_{sat} at the end of the pool boiling curves, by the solid square symbols. These were the last experimental data points recorded by the LabVIEW program before departure from nucleate boiling occurred. For the upward facing inclination angle, the values of the CHF_{sat} increased, while the corresponding ΔT_{sat} decreased, as Ra increased (Figure 4.12a). Thus the general trend for the enhancement of CHF (as well as h_{NB}) is upward and to the left, as shown in Figure 4.12a with increased surface roughness. The effect of Ra on the CHF_{sat} is discussed more detail in the first sub-section, next.

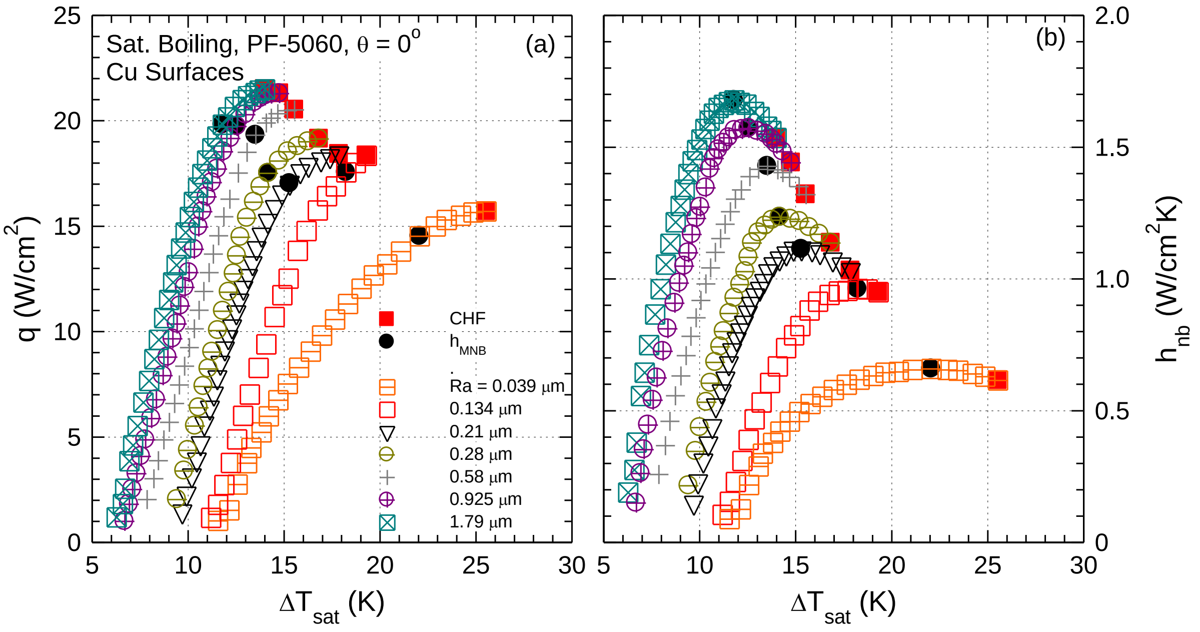

Figure 4.12. The pool boiling and h_{NB} curves for saturation nucleate boiling of PF-5060 on smooth and rough Cu sufaces at the upward facing orientation.

4.3.1 The Effect of Surface Roughness on the CHF

Figure 4.13 plots the experimentally obtained values of CHF_{sat} for PF-5060 dielectric liquid on smooth and rough Cu surfaces, in the upward facing orientation (θ =

0^o), versus Ra. The CHF_{sat} of PF-5060 increases proportionally to Ra, to the power 0.078. It is ~15.5 W/cm^2 on the smooth Cu surface (Ra = 0.039 µm) and ~21.5W/cm^2 on the Cu surface with Ra = 1.79 µm (Figure 4.13).

All experimentally obtained values of the CHF_{sat} in the upward facing orientation were correlated using the general form independently proposed by Zuber (1959) and Kutateladze (1952 and 1961), as:

$$CHF_{sat}(Ra, \theta = 0^o) = C_{CHF,sat}(Ra, \theta = 0^o)\ h_{fg}\sqrt{\rho_g}[\sigma(\rho_l - \rho_g)]^{0.25} \quad (4.9)$$

In this correlation, the liquid and vapor properties were evaluated at the saturation temperature of PF-5060 at ~0.085 MPa of the experiments (Table 2.1).

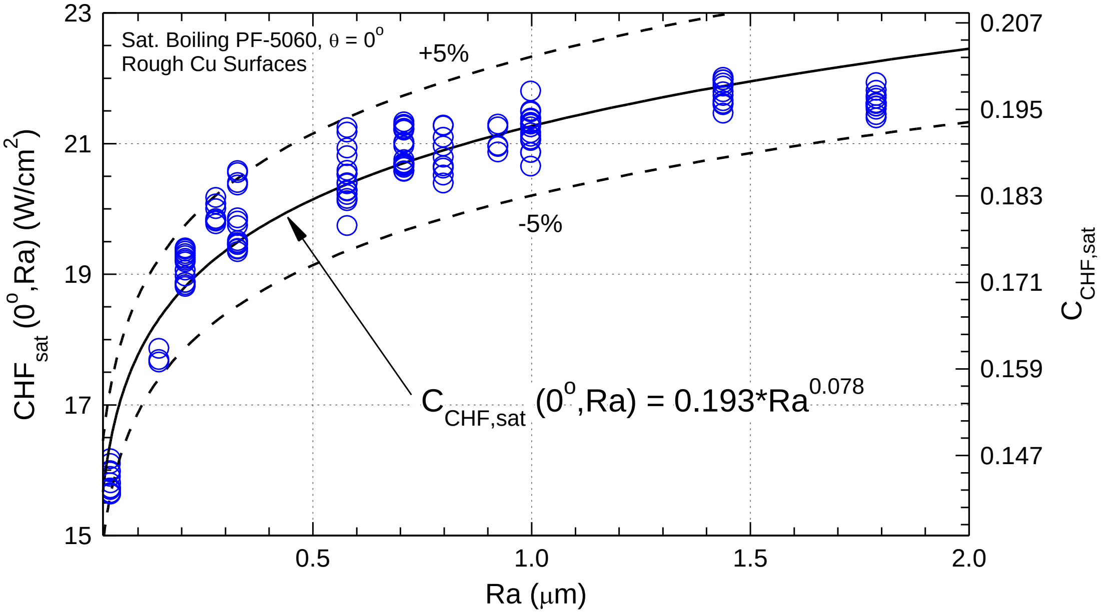

Figure 4.13 The obtained CHF values for PF-5060 on smooth an rough Cu surfaces in the upward facing orientation.

The dimensionless coefficient $CHF_{sat}(Ra, 0^o)$ in Equation (4.9) was correlated as a function of Ra (Figure 4.13), given as:

$$C_{CHF,sat}(Ra, 0^o) = 0.193\ Ra^{0.078} \quad (4.10)$$

This correlation of CHF_{sat} for saturation boiling of PF-5060 on any uniformly heated Cu surface with Ra = 0.039 – 1.79 µm, in the upward facing inclination angle, is in good agreement with the experimental data, to within ± 5%.

The CHF_{sat} increased with increased surface roughness by as much as ~39%, within the range of Ra investigated. Additionally, the increase of Ra also decreased the wall temperature at which the CHF_{sat} occurred, by as much as 12 K (Figure 4.12a–b). In pool boiling applications, the surface may be oriented in any non-upward facing direction ($\theta > 0^{\circ}$). For example, a CPU and add-in circuit boards that are oriented parallel and perpendicular to the motherboard, respectively, may be oriented 0°, 90°, or 180° depending on the orientation of the chassis that holds the motherboard. The next sub-section presents the results that quantify the effect of the surface inclination angle, θ, on the CHF_{sat}.

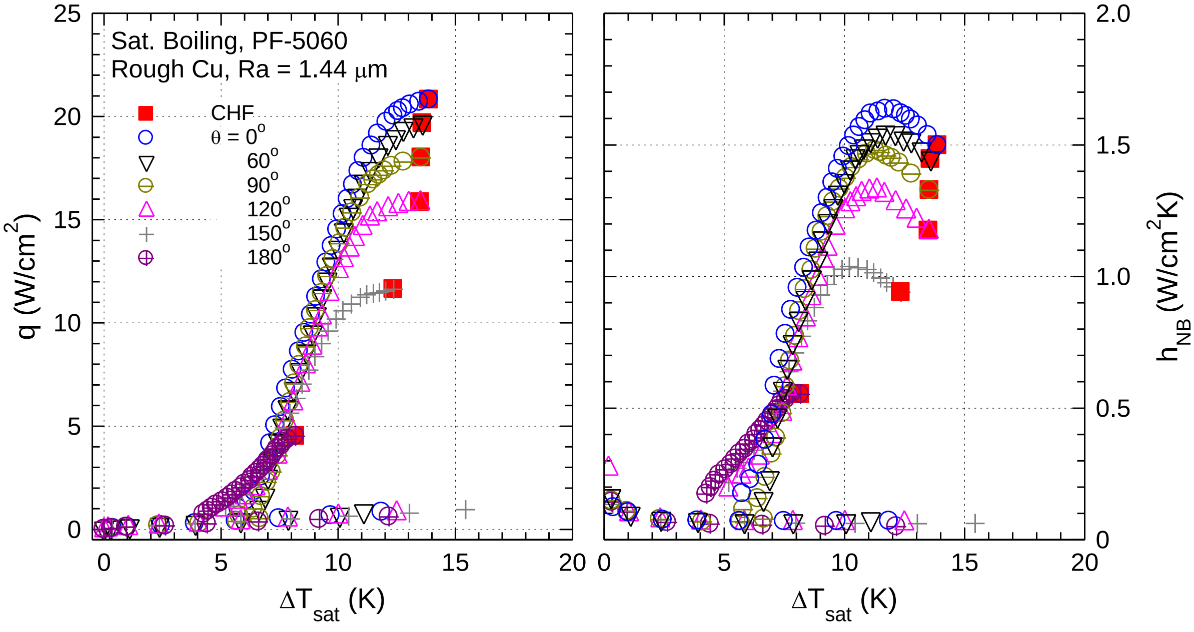

Figure 4.14. Saturation pool boiling curves of PF-5060 on a Cu surface with Ra = 1.44 um and inclination angles 0° – 180°.

4.3.2 Effect of Surface Inclination on CHF

Separate pool boiling experiments with each of the thirteen rough Cu surfaces (Figure 3.10 and Figure 3.12) were performed at the inclination angles of: $\theta = 0^{\circ}$ (upward facing), 60°, 90° (vertical), 120°, 150°, 160°, 170° and 180° (downward facing). The obtained saturation pool boiling and h_{NB} curves of PF-5060 on the Cu surfaces of Ra = 0.21 μm and 1.44 μm, at inclination angles 0° – 180°, are displayed for comparison in Figure 4.14a and Figure 4.14b. The last data points of the pool boiling curves in Figure

4.14a, marked by square solid symbols, indicate the CHF_{sat} at the respective inclination angle. In these figures, the CHF_{sat} is highest on both Cu surfaces in the upward facing orientation, and decreases with increasing inclination angle, as does the corresponding surface superheat, ΔT_{sat}.

Figure 4.15 presents the obtained values of the CHF_{sat} for PF-5060 on the Cu surfaces with Ra = 0.039, 0.21, 0.33, 0.58, 1.00 and 1.79 µm are given versus the inclination angle, θ. The CHF_{sat} decreases very little as the θ increases from the upward facing orientation ($\theta = 0^{o}$), to 60^{o}. However, the further increase of θ resulted in a progressively faster decrease of CHF_{sat}. This was due to the increased accumulation of vapor bubbles in the boundary layer along the heated inclined surfaces at higher surface superheats. These accumulated bubbles coalesced with other active bubble nucleation sites. Such accumulation was almost non-existent in the upward facing orientation, as departed bubbles moved directly away from the heated Cu surface. Conversely, accumulation was highest in the downward facing orientation ($\theta = 180^{o}$), as departed bubbles were pushed back up against the heated surface by the buoyant force that acted upon the bubbles. The CHF_{sat} values were lowest in the downward facing orientation. On the roughest surface (Ra = 1.79 µm), the CHF_{sat} of PF-5060 was between 35-52% higher than that on the smooth Cu surface (Ra = 0.039 µm), depending on the surface inclination angle.

For each Ra, the CHF_{sat} values at each inclination angle were normalized to those in the upward facing orientation. Figure 4.15b shows the CHF_{sat} values of Figure 4.15a normalized to those in the upward facing orientation. Despite the increases of CHF_{sat} at all inclinations angles as Ra increased, the normalized values to those in the upward facing orientation (R_{sat} in Figure 4.15b) are almost independent of Ra, and solely dependent on θ. The trend for the normalized CHF_{sat} vs θ of PF-5060 in Figure 4.15c is consistent with those reported previously for other dielectric liquids on plain Cu (Priarone, 2005; El-Genk and Bostanci, 2003), microporous coatings (Rainey and You, 2000), porous graphite (El-Genk and Parker, 2008) and others (Howard and Mudawar, 1999; El-Genk, 2012; Parker and El-Genk, 2009).

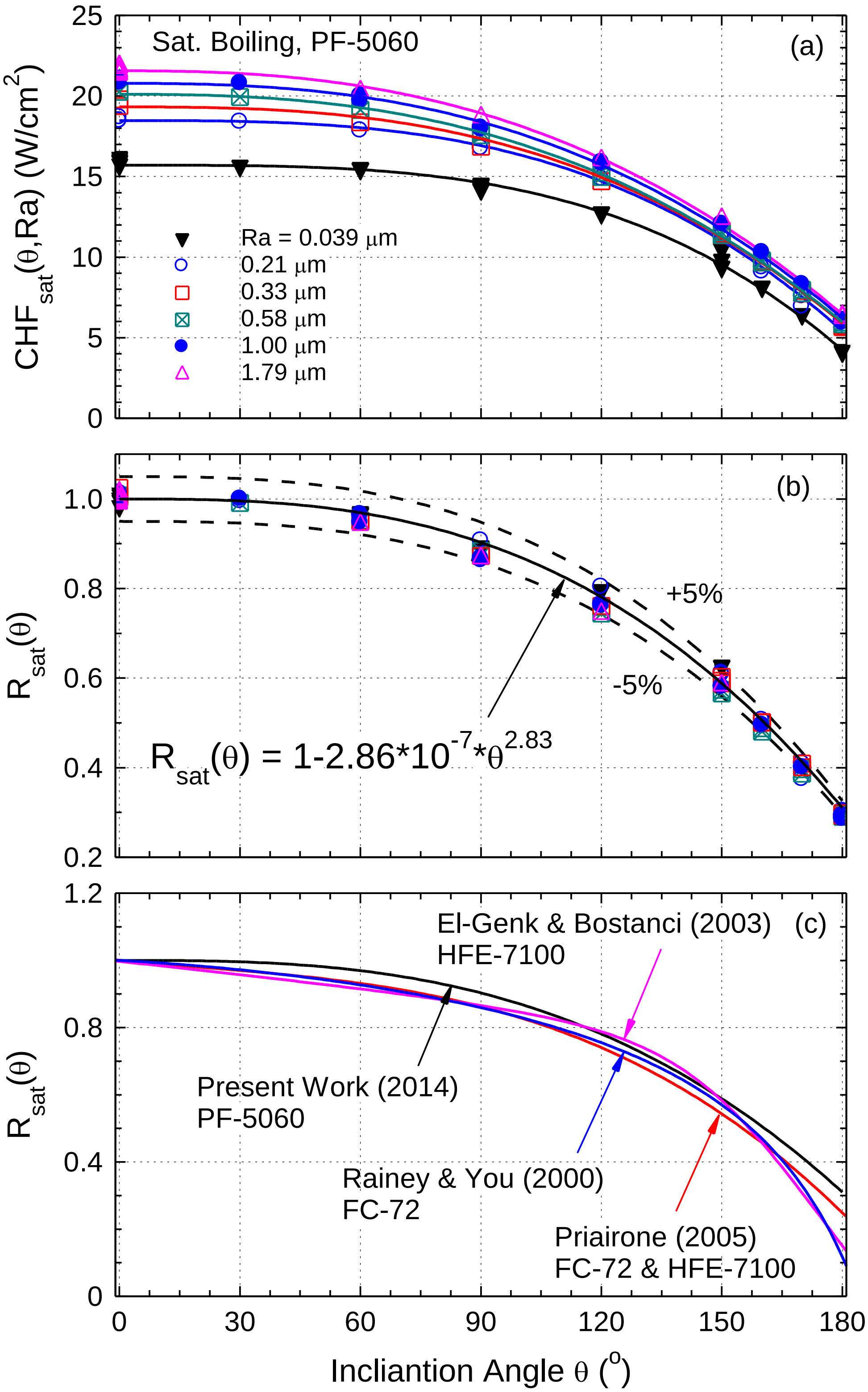

Figure 4.15. The effect of inclination angle on the *CHF*sat for PF-5060 on rough Cu surfaces and comparison to others.

The normalized CHF_{sat} in Figure 4.15b was correlated in terms of the inclination angle, θ, as:

$$R_{sat}(\theta) = \frac{C_{CHF,sat}(Ra,\theta)}{C_{CHF,sat}(Ra,0^o)} = 1 - 2.86 \times 10^{-7}\theta^{2.83} \qquad (4.11)$$

This expression, that describes the effect of the inclination angle on the CHF_{sat} of PF-5060, is in good agreement with the experimental data to within $\pm$ 5%. The CHF_{sat} values for the PF-5060 on the rough Cu surfaces at the inclination angles of 60^o, 90^o, 120^o, 150^o, and 180^o are ~ 96.8%, 90%, 63.5%, 58.5% and 31% of those in upward facing orientation, respectively (Figure 4.15a).

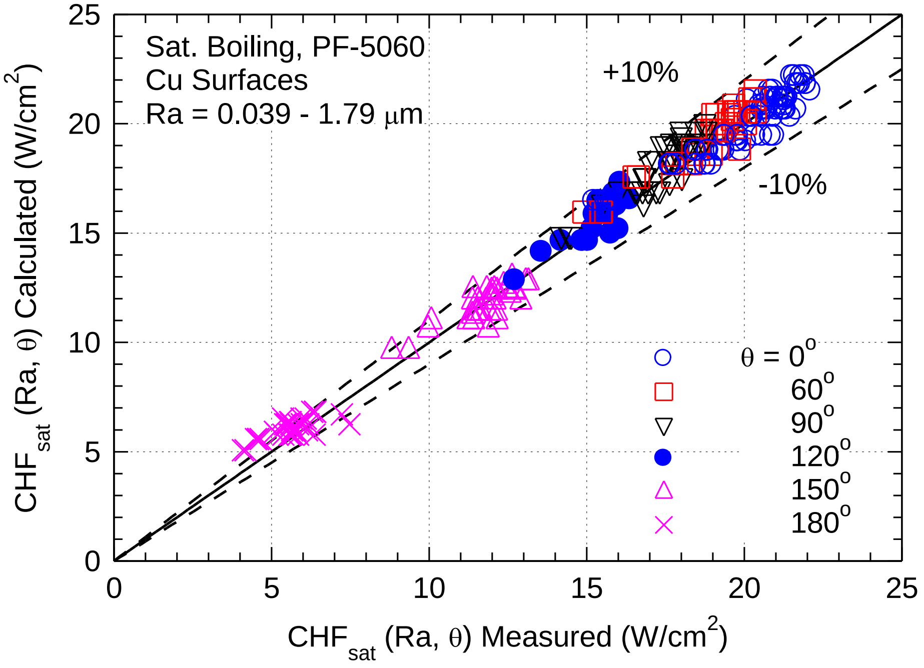

Figure 4.16. Comparison of the developed CHF_{sat} correlation (Equation (4.12)) to the present experimental data.

The CHF_{sat} correlation that incorporates both the effect of surface roughness, Ra, and inclination angle, θ, may be expressed as:

$$CHF_{sat}(Ra,\theta) = C_{CHF,sat}(Ra,0^o)\, R_{sat}(\theta)\, h_{fg}\sqrt{\rho_g}\left[\sigma\left(\rho_l - \rho_g\right)\right]^{0.25} \qquad (4.12)$$

This correlation, which accounts for both of the effects of Ra and θ, on the CHF_{sat} of PF-5060, agrees with all experimental data for smooth and rough Cu surfaces of Ra = 0.039

– 1.79μm, at inclination angles of $\theta = 0^o - 180^o$, to within $\pm$ 10% (Figure 4.16). Up until this point, all of the presented results on the CHF are for the experiments that were performed at the saturation boiling temperature of PF-5060 (Table 2.1). The next sub-section presents the effect of the liquid subcooling, ΔT_{sub}, on the CHF of PF-5060.

4.3.3 Effect of Liquid Subcooling

This subsection presents the results of the effect of liquid subcooling, ΔT_{sub}, on the nucleate boiling and CHF of PF-5060 on smooth and rough Cu surfaces, at inclination angles of $\theta = 0^o - 180^o$. Figure 4.17a – b show the pool boiling curves for subcooled nucleate boiling of PF-5060 on the smooth Cu (Ra = 0.039μm) and rough Cu of Ra = 1.79μm, in the upward facing orientation ($\theta = 0^o$). The boiling curves in Figure 4.17a-b are denoted by a different symbols, and are for a different liquid subcooling, ΔT_{sub}, of 0 K (saturation), 10 K, 20 K and 30 K. The last data points at the end of the boiling curves indicate the CHF at the respective ΔT_{sub}. The results presented in Figure 4.17a-b are for subcooled nucleate boiling in the upward facing orientation on (a) a smooth Cu surface with Ra = 0.039 μm, and (b) a rough Cu surface with Ra = 1.79 μm. These results show increased liquid subcooling up to 30 K resulted in higher nucleate boiling heat transfer at lower wall superheats, increased lengths of the fully developed region, and increased CHFs.

The CHF, as well as the corresponding ΔT_{sat}, increased as the liquid subcooling increased. The results displayed in Figure 4.18a – f demonstrate the effects of ΔT_{sub} and Ra, on the CHF for subcooled nucleate boiling of PF-5060 on three rough Cu surfaces with Ra = 0.039, 0.80 and 1.79 μm, at inclination angles $0^o - 180^o$. In the upward facing orientation (Figure 4.18a), $\theta = 0^o$, the CHF increased linearly with ΔT_{sub} at a rate of 2.2%/K. For the other inclination angles (Figure 4.18b – 4.20f) the CHF increased linearly with increased ΔT_{sub} at a rate of 2.35%/K, 2.6%/K and 4%/K at $\theta = 60^o$, 90^o, and 180^o, respectively. Thus, the rate of increase of CHF with increased ΔT_{sub} depends on the surface inclination angle. From these results, the subcooling coefficient, $C^*_{\mathrm{sub}}(\theta)$, which accounts for the dependence of the subcooled CHF on the inclination angle, was determined and is discussed next.

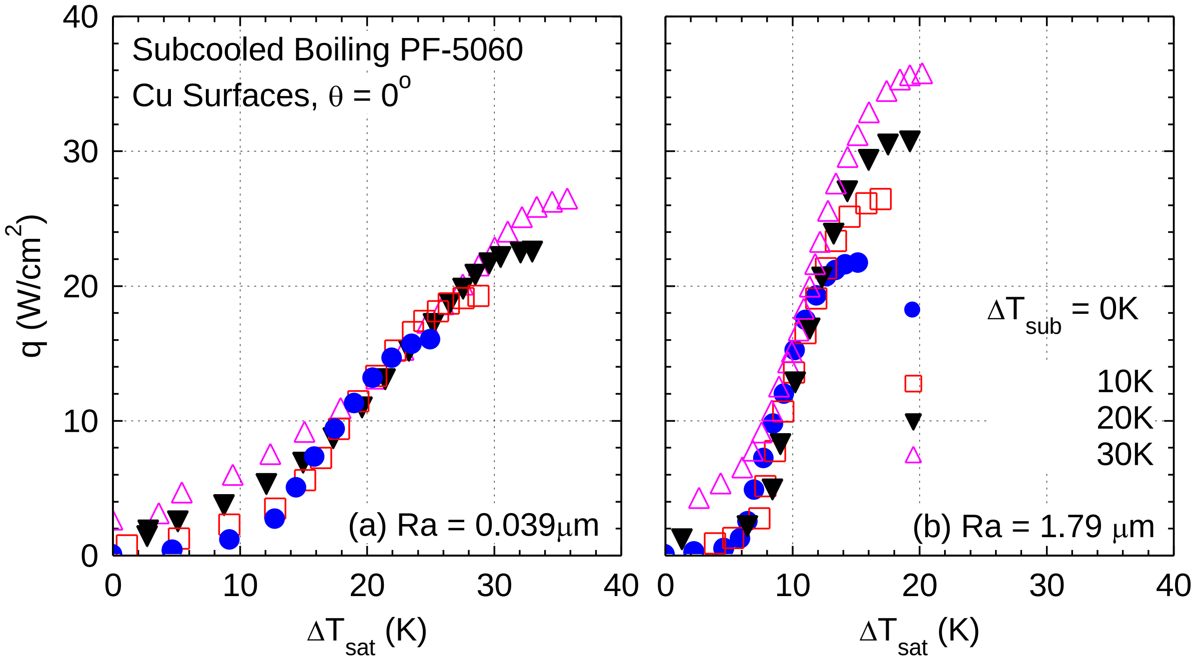

Figure 4.17. The effect of subcooling on the boiling curves for PF-5060 liquid on rough Cu surfaces with Ra = 0.39 and 1.79 µm.

The values of the dimensionless subcooling coefficient, $C^*_{\text{sub}}(\theta)$, for the three rough Cu surfaces in Figure 4.18a – 4.18f, are also plotted in Figure 4.19 against θ. Figure 4.18 and 4.19 shows the $C^*_{\text{sub}}(\theta)$ had very little dependence on Ra for each inclination angle, however was different for each θ. The dependence of the $C^*_{\text{sub}}(\theta)$ on θ is plotted in Figure 4.19. This figure shows how $C^*_{\text{sub}}(\theta)$ increases with increasing θ. From the results in Figure 4.18 and 4.19, $C^*_{\text{sub}}(\theta)$ was correlated solely in terms of the inclination angle, to within ± 6% of the experimental data, as:

$$C^*_{sub}(\theta) = 0.022 + 8.47 \times 10^{-8}\theta^{2.36} \tag{4.13}$$

Figure 4.20 compares the obtained results from the effect of liquid subcooling on the CHF for PF-5060 dielectric liquid on smooth and rough Cu surfaces, in the upward facing orientation (θ = 0°), to those reported by others (Honda et al., 2002; Wei and Honda, 2003; Sathyamurthi et al., 2009) for both PF-5060 and FC-72 dielectric liquids on silicon surfaces. These liquids have identical properties, except the surface tension of PF-5060 is only slightly higher (~3 – 5%) at the saturation temperature at 0.1 MPa (Table 2.1).

The results in Figure 4.20 show that the obtained subcooling coefficient at the upward facing angle, $C^*_{\mathrm{sub}}(0^{\mathrm{o}})$ = 2.2%/K, is consistent with the data reported by others for both PF-5060 and FC-72 on Silicon (Figure 4.20) (Honda et al., 2002; Wei and Honda, 2003; Sathyamurthi et al., 2009). Although the obtained values of the CHF_{sat} were different, the rate of increase in CHF as ΔT_{sub} increased was similar to, within $\pm$ 6%. The next section presents the developed general CHF correlation, based off of the present experimental results on the CHF of PF-5060 dielectric liquid on smooth and rough Cu surfaces, at inclination angles 0$^{\mathrm{o}}$ – 180$^{\mathrm{o}}$, and liquid cooling 0 – 30 K.

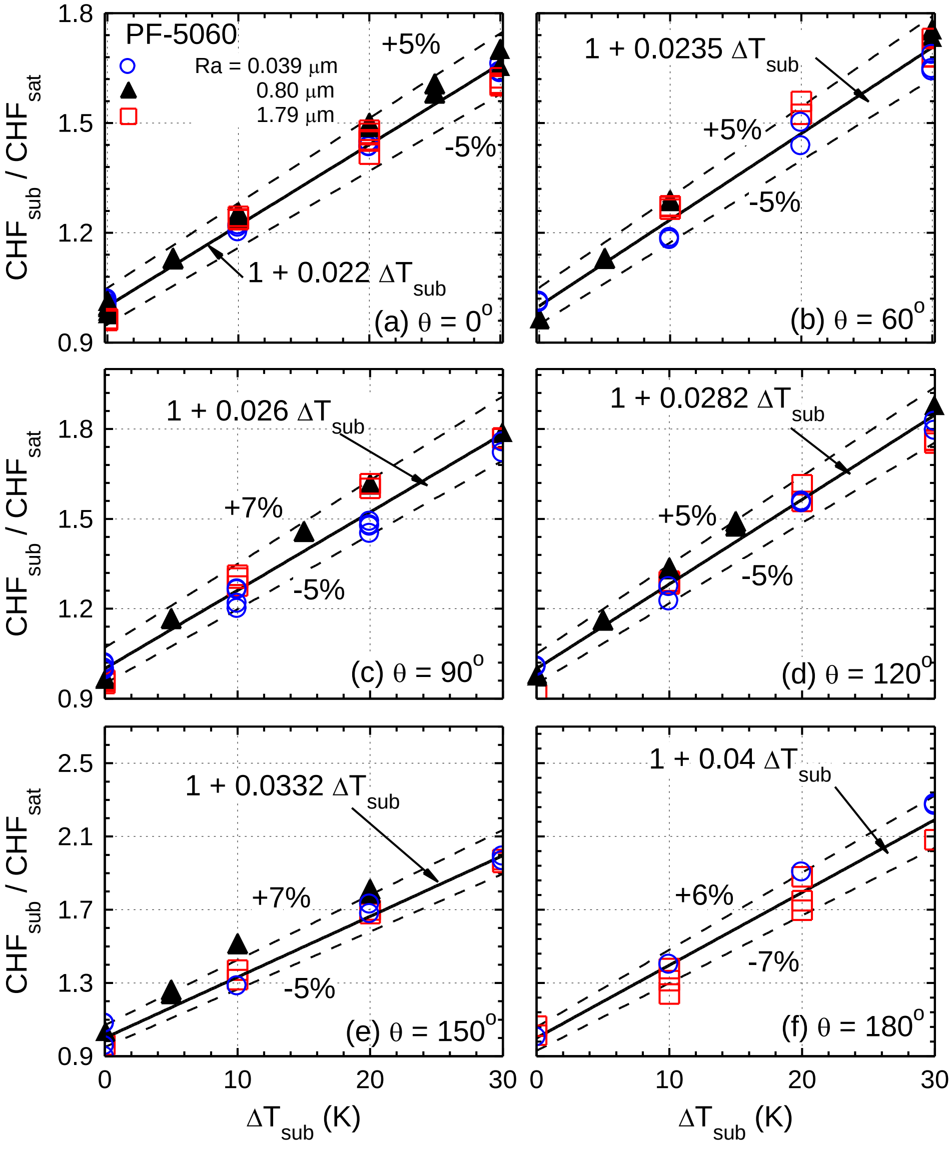

Figure 4.18. Effect of ΔT_{sub} on the CHF for PF-5060 liquid on inclined rough Cu surfaces. The rate of CHF increase with increasing ΔT_{sub} is different for each inclination angle.

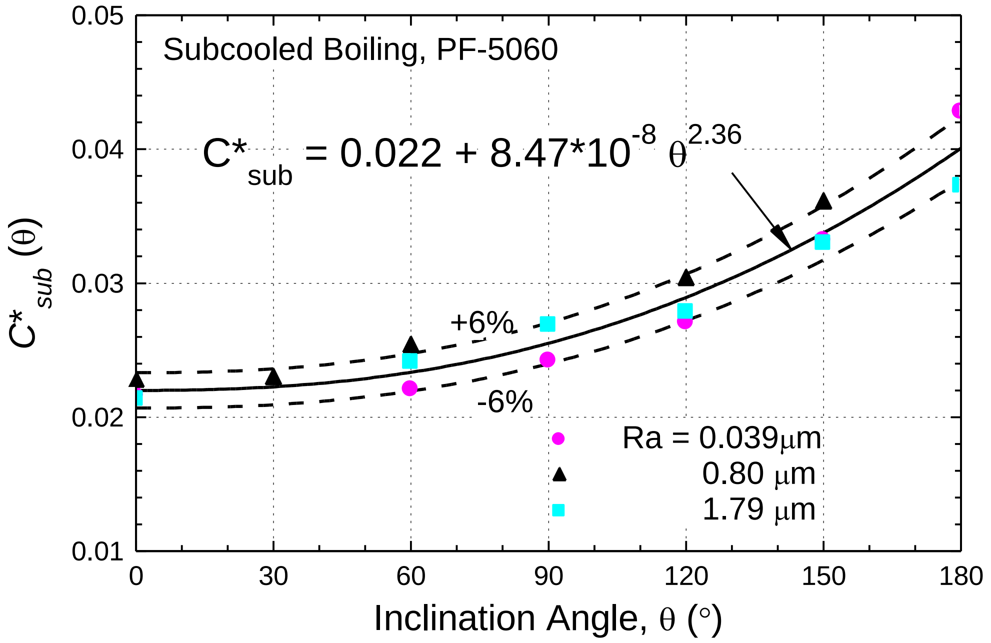

Figure 4.19. The CHF subcooling coefficient C^*_{sub} on versus the inclination angle in subcooled nucleate boiling of PF-5060 on rough Cu surfaces.

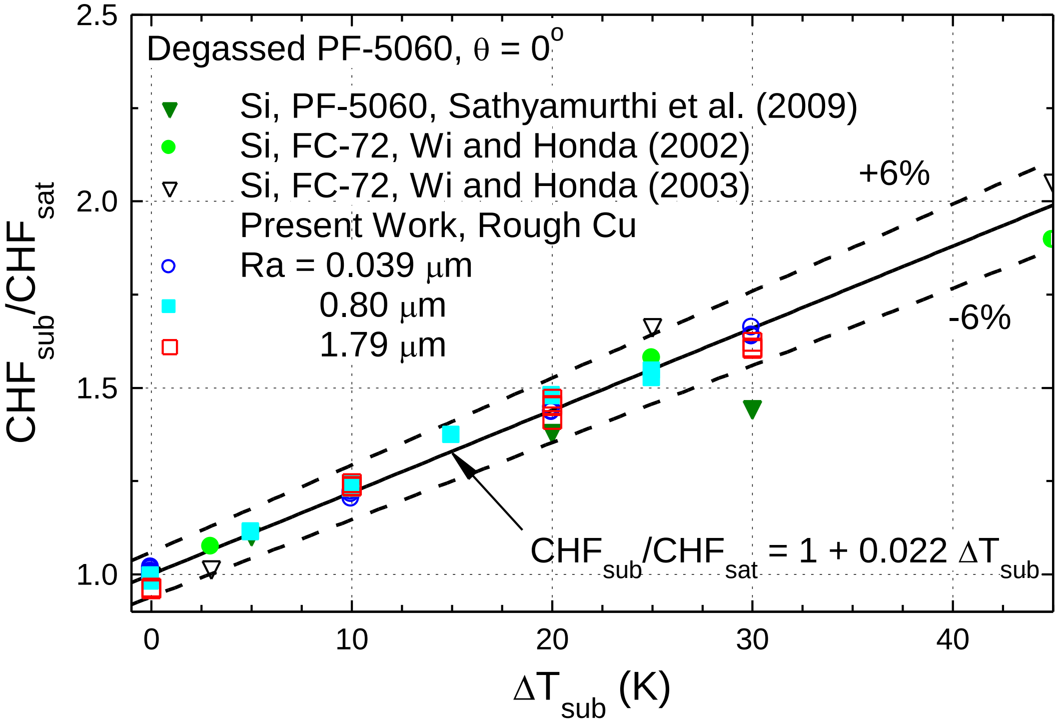

Figure 4.20. Comparison of normalized CHF for subcooled PF-5060 on rough Cu surfaces with those reported for FC-72 and PF-5060 on silicon, in the upward facing orientation.

4.3.4 General CHF Correlation

The developed general CHF correlation that accounts for the combined effects of the surface roughness, Ra, inclination angle, θ, and the liquid subcooling, ΔT_{sub}, may be expressed as:

$$CHF\ \ (Ra,\theta,\Delta T_{sub}) = C_{CHF,sat}(Ra,\theta)(1 + C^{*}_{sub}(\theta)\Delta T_{sub}) \tag{4.14}$$

The first term on the right hand side of Equation (4.14) is of the saturation boiling critical heat flux for the PF-5060 on the smooth and rough Cu surfaces at inclination angles of 0^{o} – 180^{o}; given by Equation (4.12). The second term is of the effect of the liquid subcooling on the critical heat flux of PF-5060 on the smooth and rough Cu surfaces. In this term, the subcooling coefficient, $C^{*}_{\text{sub}}(\theta)$, is only a function of the inclination angle; given by Equation (4.13). Thus, the general correlation to predict the CHF for saturation and subcooled nucleate boiling of PF-5060 on smooth and rough Cu surfaces with Ra = 0.039 – 1.79µm, $\theta = 0^{o} - 180^{o}$, and $\Delta T_{\text{sub}} = 0 - 30$ K, is given as:

$$\begin{gathered} CHF\ \ (Ra,\theta,\Delta T_{sub}) = (0.193Ra^{0.078})(1 - 2.86\ \times\ 10^{-7}\theta^{2.83}) \times \\ \{1 + (0.022 + 8.47 \times 10^{-8}\theta^{2.36})\Delta T_{sub}\}(h_{fg}\sqrt{\rho_g}[\sigma(\rho_l - \rho_g)]^{0.25}) \end{gathered} \tag{4.15}$$

Figure 4.21 plots the calculated CHF values using the correlation in Equation (4.15), against the experimentally obtained values for PF-5060 on smooth and rough Cu surfaces, within the complete range of parameters investigated. Some 300+ experimental CHF data points are included in Figure 4.21. The calculated CHF values from Equation (4.15) are in good agreement with all experimental data points to within ± 10%. With the developed general CHF correlation now presented, the next provides additional discussion on the observed dependence of the CHF on Ra, θ, and $\Delta T_{\text{sub.}}$

4.3.5 Discussion of CHF Results

The increase in the CHF with increased surface roughness can be explained by the increase of the overall wetted surface area and wettability caused by roughening.

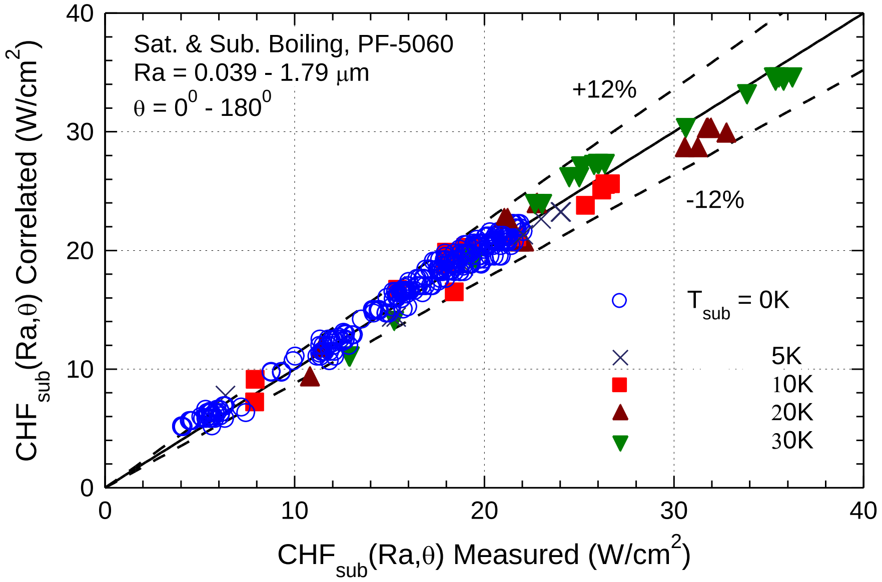

Figure 4.21. Comparison of calculated CHF values using Equation (4.15) against those measured, for subcooled boiling of PF- 5060 on rough Cu surfaces at different orientations.

However, the fractional increase of surface area with increased roughness was small, and only about ~4.5% at the highest Ra of 1.79 μm, and near zero for all Ra $\leq$ 0.33 μm (Figure 3.11). Therefore, the increase of wettability is likely the primary cause of the enhancement of CHF observed from the increase of Ra. The increases in the CHF_{sat} for the PF-5060 dielectric liquid with the increased surface hydrophilicity (or wetting) of the rough Cu surfaces is consistent with results reported by others (Son et al. 1999; Kandlikar 2001; Takata et al. 2003, 2005; Wu et al., 2010; Ahn et al., 2012; O'Hanly et al. 2003). Wu et al. (2010) reported a 38% increase in the CHF_{sat} for the FC-72 dielectric liquid on a superhydrophilic TiO surface in the upward facing orientation. Their work demonstrated that even a very highly wetting dielectric liquid exhibits increases in CHF after enhancing surface wettability. Ahn et al. (2010) compared the CHF_{sat} values for water on treated zircaoly-4 surfaces with static contact angles of < 10°, to untreated zircaloy surfaces with a static contact angles ~ 53°. They reported a large increase of the CHF_{sat} on the treated zircaloy surfaces, and that the even small changes in the surface wettability at very low static contact angles, ϕ, ($\leq$ 10°) greatly affected the CHF_{sat}. Additionally, increased surface wetting would promote capillary wicking along surface micro features, which would more readily replenish dry spots, thus increasing CHF.

The decrease of CHF (along with h_{NB}) with the increase of surface inclination angle can be explained based on the bubble residence time in the boundary layer along the heated surface after departure. This bubble residence time grew as θ increased. Figure 4.22a – 4.22f show images of saturation nucleate on a Cu surface in PF-5060 at an applied heat flux q = 5 W/cm^2. The image of the boiling surface is rotated by its respective θ in each row, to show how the increase of θ affects bubble departure and subsequent movement, relative to the heated surface. Due to buoyant forcing acting upon departed bubbles, the departed bubbles increasingly favored staying within the boundary layer along the Cu surface as θ increased. While such behavior enhances h_{NB} at lower heat fluxes (Figure 4.14) due to bubble shear of discrete bubbles, the increased accumulation of vapor near the heated Cu surfaces at higher heat fluxes lowers h_{NB}, as it leads to bubble coalescence (Figure 4.22a – 4.22f). Bubble coalescence becomes much more pronounced at higher heat fluxes, and excessive bubble coalescence is a precursor to the surface dryout that triggers CHF.

The increase of CHF with increased ΔT_{sub} for the upward facing inclination has been a well-documented (Honda et al., 2002; Wei and Honda, 2003; Parker and El-Genk, 2005; El-Genk and Parker, 2008; Sathyamurthi et al. 2009; El-Genk and Ali, 2011). However, less information has been reported of the relative increase of the CHF with ΔT_{sub} and θ (Figure 4.19). Close up images of subcooled nucleate boiling at the upward facing inclination angle suggested that additional resistance to the departing vapor bubble was present at higher values of ΔT_{sub}. In subcooled pool boiling, there is additional resistance in forming the thermal boundary layer suitable for bubble ebullition, caused by the difference between the subcooled and saturation liquid temperatures. Additionally, the subcooled bulk liquid also may promote condensation along the growing bubble vapor-liquid interface farther away from the heated surface, causing resistance to bubble growth. Growing bubbles were seen to take longer to grow, and "dance" along the heated Cu surface before departure into the bulk liquid at higher ΔT_{sub} ($\geq$ 20 K). This additional resistance to bubble departure had less impact at higher surface inclination angles, since buoyancy assisted bubble departure. At higher inclinations, the bubbles were observed to slide off of the heated surface, as opposed to reside for additional periods of time like observed for the upward facing orientation.

13a. θ = 0°, q = 5W

13b. θ = 60°, q = 5W

13c. θ = 90°, q = 5W

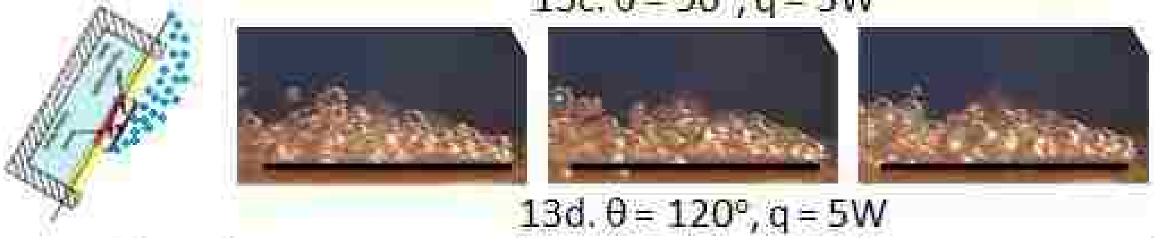

13d. θ = 120°, q = 5W

13e. θ = 150°, q = 5W

13f. θ = 180°, q = 5W

Figure 4.22. Images of saturation boiling of PF-5060 liquid of Rough Cu at different surface inclination angles show how departed bubbles increasingly hugged the heated surface with increased surface inclination.

The developed correlation in Equation (4.15) is a useful tool for the design and development of cooling applications that involve the nucleate boiling of PF-5060 dielectric liquid. The correlation should also be applicable to the FC-72 dielectric liquid, which has nearly identical thermophysical properties to PF-5060 (Table 2.1). The correlations developed in this research are for clean Cu surfaces. However, Cu oxidizes as it ages. Since microprocessors are expected to operate for years, it was desirable to examine the effects of surface aging on nucleate boiling heat transfer. The next section presents the effect of surface oxidation on the nucleate boiling of PF-5060 on the same rough Cu surfaces.

4.4 The Effect of Surface Aging

Two oxidized Cu surfaces were fabricated (Section 3.5.2) and used in pool boiling experiments to study the potential effect of surface aging on the nucleate boiling heat transfer of PF-5060. Over time, Copper oxidizes and forms a thin oxide layer that affects nucleate boiling performance. For the cooling of high performance electronics, heat sinks have a life expectancy on the order of the chip life (~10 years). Because the naturally occurring Cu oxidation process is very slow, a sped up process that involved placing the Cu surfaces in an oven at 200 ^{o}C overnight was utilized. The dark oxide layers that fully covered the surface (Figure 3.15) were found to increase the measured surface roughness, Ra, by no more than ~0.1 µm, for both Cu surfaces investigated. Two Cu surfaces that measured 0.134 µm and 1.79 µm, before oxidation, were re-measured to be 0.225 µm and 1.83 µm after oxidation, respectively. Therefore, the oxidation negligibly impacted Ra, and was thus assumed to be a non-contributing factor in the obtained nucleate boiling data. Additionally, the static contact angles of the two Cu surfaces decreased by ~10^{o} and ~3^{o}, respectively, indicating slight changes of surface wettability from oxidation.

Figure 4.23 and Figure 4.24 present the saturation nucleate boiling and heat transfer coefficient curves of PF-5060 on two Cu surfaces before and after oxidation, in the upward facing inclination angle ($\theta = 0^{o}$). In Figure 4.23 and Figure 4.24, the CHF is denoted by the solid squares, and h_{MNB} by the solid circles. The results show both Cu surfaces had a decreased maximum nucleate boiling heat transfer coefficients and CHF after oxidation. The Cu surface with Ra = 1.79 µm had h_{MNB} decrease from ~1.6 W/cm^{2}K to ~1.4 W/cm^{2}K, and CHF decrease from ~21.5 W/cm^2 to 20.3 W/cm^2, before and after surface oxidation, respectively. These values represent a decrease of 12.5% and 5.6% in the h_{MNB} and CHF, respectively. On the Cu surface of Ra = 0.134 µm (Figure 4.23 – 4.24), the h_{MNB} decreased from ~0.95 W/cm^{2}K to ~0.78 W/cm^{2}K, and CHF decreased from ~18.3 W/cm^2 to 17.4 W/cm^2, before and after oxidation, respectively. These values represent a decrease of 17.9% and 4.9% in the h_{MNB} and CHF, respectively. Conversely,

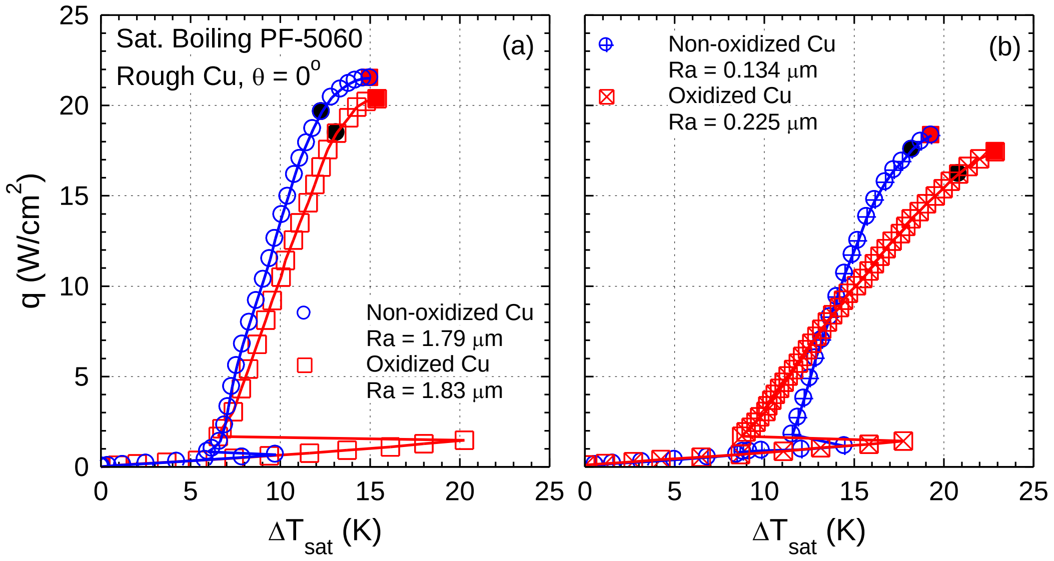

Figure 4.23. The saturation nucleate boiling curves of PF-5060 on Cu surfaces before and after oxidation), at the upward facing inclination angle.

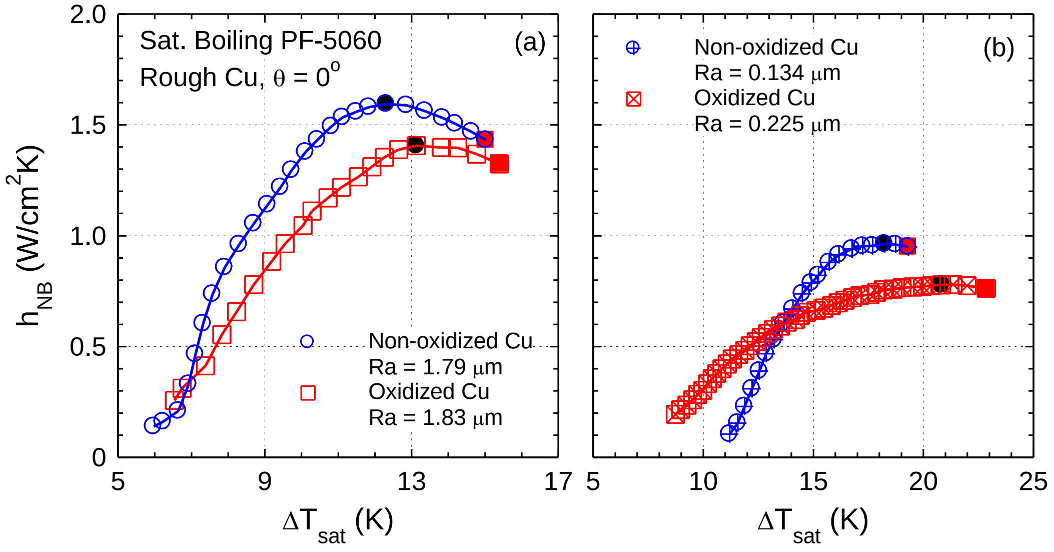

Figure 4.24. The saturation nucleate boiling heat transfer coefficient curves of PF-5060 on Cu surfaces before and after oxidation, at the upward facing inclination angle.

some enhancement in nucleate boiling was observed at lower heat fluxes, and was much more prominent for the less rough of the two Cu surfaces (Figure 4.23b and 4.24b). The temperature excursion prior to boiling incipience was also seen to increase for both Cu surfaces after oxidation (Figure 4.23a – b), though only by few degrees. The temperature excursions went away with subsequent runs, like with the non-oxidized Cu surfaces.

The decreased nucleate boiling heat transfer of the oxidized Cu surfaces may be explained by two reasons. First, the SEM images (Figure 3.15) suggest that some surface cavities for bubbles nucleation may have been filled in by the oxide layer, lessening the density of active nucleation sites. However, the increased performance at low power, for the Cu surface of Ra = 0.134 μm, indicates this was not the case, and that in fact the oxide layer created active nucleate sites. However, these sites may have favored bubbles nucleation at low heat fluxes, as opposed to high heat fluxes. The second possible reason for the diminished h_{MNB} is from the additional thermal resistance of the oxide layer. An increase of the total thermal resistance to thermal conduction increases the temperatures within the surface. More work still needs to be conducted to determine and conclude the effect of surface aging and/or oxidation on Cu surfaces. The results briefly investigated in this research suggest a worst case scenario of a ~20% decrease in the h_{MNB} and ~5% decrease in the CHF, over long term operation of Cu surfaces cooled by saturation nucleate boiling of PF-5060 dielectric liquid. These results were determined to be consistent and reliable, as repeated experiments on the same oxidized surfaces as much as ~4 weeks apart (Figure 4.25), returned almost the same nucleate boiling data.

For microprocessor cooling applications, it is important to consider the natural convection cooling that occurs prior to the onset of nucleate boiling (Figure 2.6). At low powers such as the standby mode of a computer chip, the primary mode of cooling will be that of natural convection. For heat spreaders sized 40 x 40 mm (a common size for high powered quad core chips) or greater, this mode of cooling may remove > 48 W depending on the liquid subcooling, and / or magnitude of the temperature excursion prior to boiling incipience. The next section presents the results on the effect of surface roughness, inclination angle, and liquid subcooling, on the natural convection heat transfer of PF-5060 dielectric liquid on Cu surfaces.

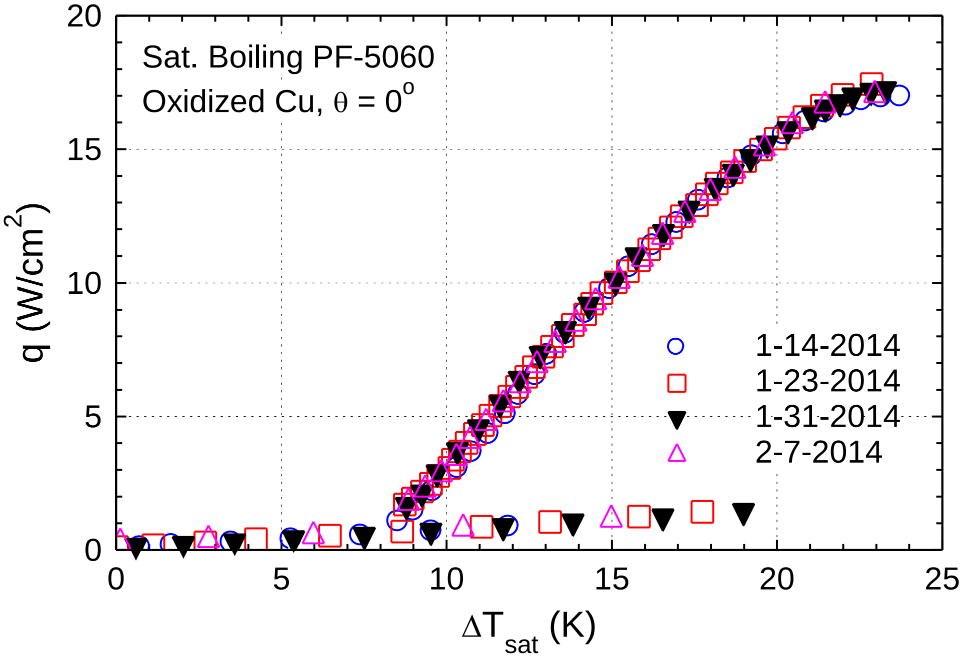

Figure 4.25. Repeated experiments for saturation boiling of PF-5060 on an oxidized Cu surface performed weeks apart, showing the long term stability of the nucleate boiling performance on aged surfaces.

4.5 Natural Convection

This section presents the experimentally obtained results on the effects of surface roughness, Ra, inclination angle, θ, and liquid subcooling, ΔT_{sub}, on the natural convection of PF-5060 on uniformly heated smooth and rough Cu surfaces. Oxidized Cu surfaces of Ra = 0.15 µm and 1.83 µm are also included in the analysis. The obtained experimental data was used to correlate the natural convection heat transfer coefficient, h_{NC}, as a function of θ. The h_{NC} was found to be independent of Ra and ΔT_{sub}. The developed natural convection correlation is compared with those reported by others for the dielectric liquids PF-5060, FC-72 and HFE-7100 on different surfaces.

4.5.1 Effect of Surface Roughness and Oxidation on Natural Convection

Figure 4.26a – c present the obtained natural convection cooling data for saturation and subcooled PF-5060 on Cu surfaces with Ra = 0.039, 0.80 and 1.79 µm, in the upward facing orientation ($\theta = 0^o$). The slopes of the natural convection surface heat

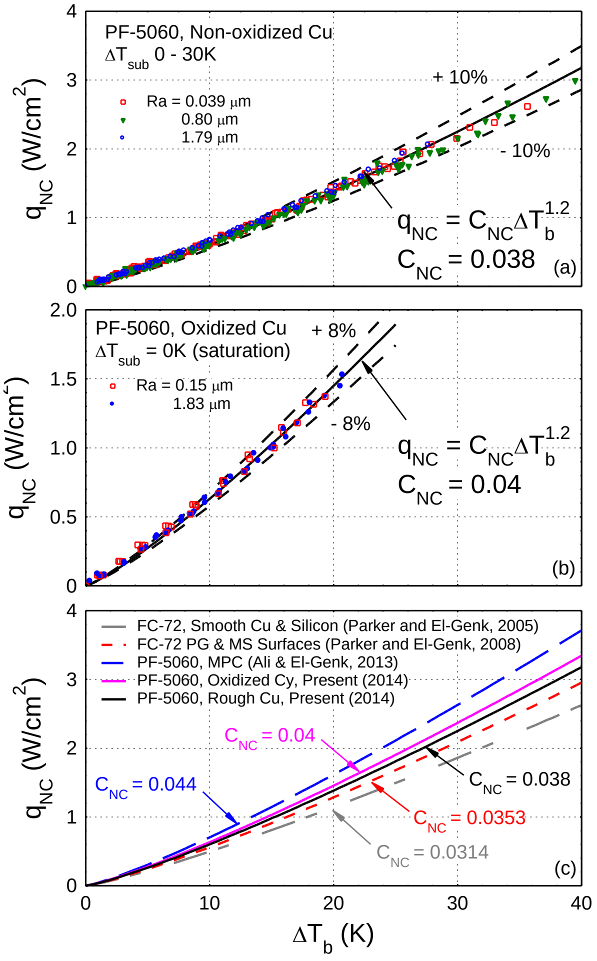

Figure 4.26. Natural convection cooling data and correlations for uniformly heated surfaces in the upward facing orientation.

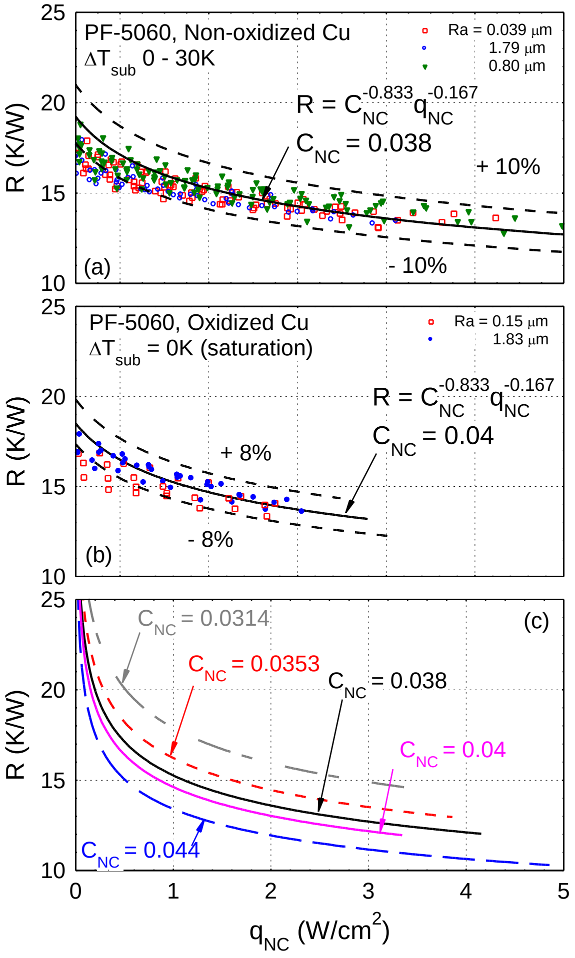

Figure 4.27. Thermal resistances for natural convection cooling with dielectric liquids on uniformly heated surfaces.

flux curves, q_{NC}, versus the bulk liquid superheat, ΔT_b, were almost identical and irrespective of the surface roughness and liquid subcooling. Increased liquid subcooling extended the range of the natural convection regime in the experiments, as the wall superheat to initiate boiling became further away as ΔT_{sub} increased. For example, for the ΔT_{sub} of 30 K, q_{NC} reached as high as 3 W/cm^2, whereas at saturation temperature (ΔT_{sub} = 0 K), q_{NC} was typically $\leq$ 0.5 W/cm^2.

For natural convection cooling of computer chips, it is preferable to express the cooling results in terms of the thermal resistance versus the total thermal power removed, q_{NC}. Figure 4.27a – c expresses the present results from Figure 4.26a – c in terms of the natural convection cooling resistance, R_{NC}. The R_{NC} decreases as the wall superheat, $\Delta T_{b,}$ increases. This is because the natural circulation of the PF-5060 was stimulated as the difference in liquid density near the heated wall and bulk liquid grew, or ΔT_b, increased. This natural convection lowered the thermal resistance. The present data of natural convection cooling resistances, R_{NC}, was correlated as:

$$R_{NC}(K/W) = C_{NC}^{-0.833}(0^o)\, q_{NC}^{-0.167} \tag{4.16}$$

This correlation agrees with the present experimental data to within ± 8 – 10% for the oxidized and non-oxidized Cu surfaces, respectively. The natural convection data in Figure 4.26 was correlated in terms of ΔT_b to the power 1.2, as:

$$q_{NC}(\theta = 0^o) = 0.038\, \Delta T_b^{1.2} \ \ , or \ \ h_{NC}(\theta = 0^o) = 0.038\, \Delta T_b^{0.2} \tag{4.17}$$

This correlation agrees to the experimental data to within ± 10%. Thus, the natural convection heat transfer, at the upward facing inclination angle, is independent of Ra and ΔT_{sub}. This finding is also applicable to the natural convection cooling heat transfer of PF-5060 on oxidized Cu surfaces. For these surfaces, the natural convection data was correlated also as:

$$h_{NC}(\theta = 0^o) = 0.04\, \Delta T_b^{0.2} \tag{4.18}$$

This correlation agrees with the present experimental data to within ± 8%. While this correlation predicts h_{NC} values that are ~5.2% higher than for non-oxidized Cu surfaces, the increase is within the experimental uncertainty of h_{NC}, as well as scattering of the data itself. Thus, neither surface roughness, nor oxidation (that provides a similar Ra within the range of non-oxidized surfaces), as well as the liquid subcooling, significantly affect the rate of heat removal by natural convection.

4.5.2 The Effect of Surface Inclination on Natural Convection

Figure 4.28a – f show the natural convection results for PF-5060 at saturation temperature, on rough Cu surfaces at different inclination angles of 0^o – 180^o. The results in Figure 4.28a – f are of multiple sets of experimental data obtained at the same conditions. For the same surface superheat, ΔT_b, the cooling rate by natural convection decreased slowly with the increase of inclination angle to 60^o (Figure 4.28a – b), and then

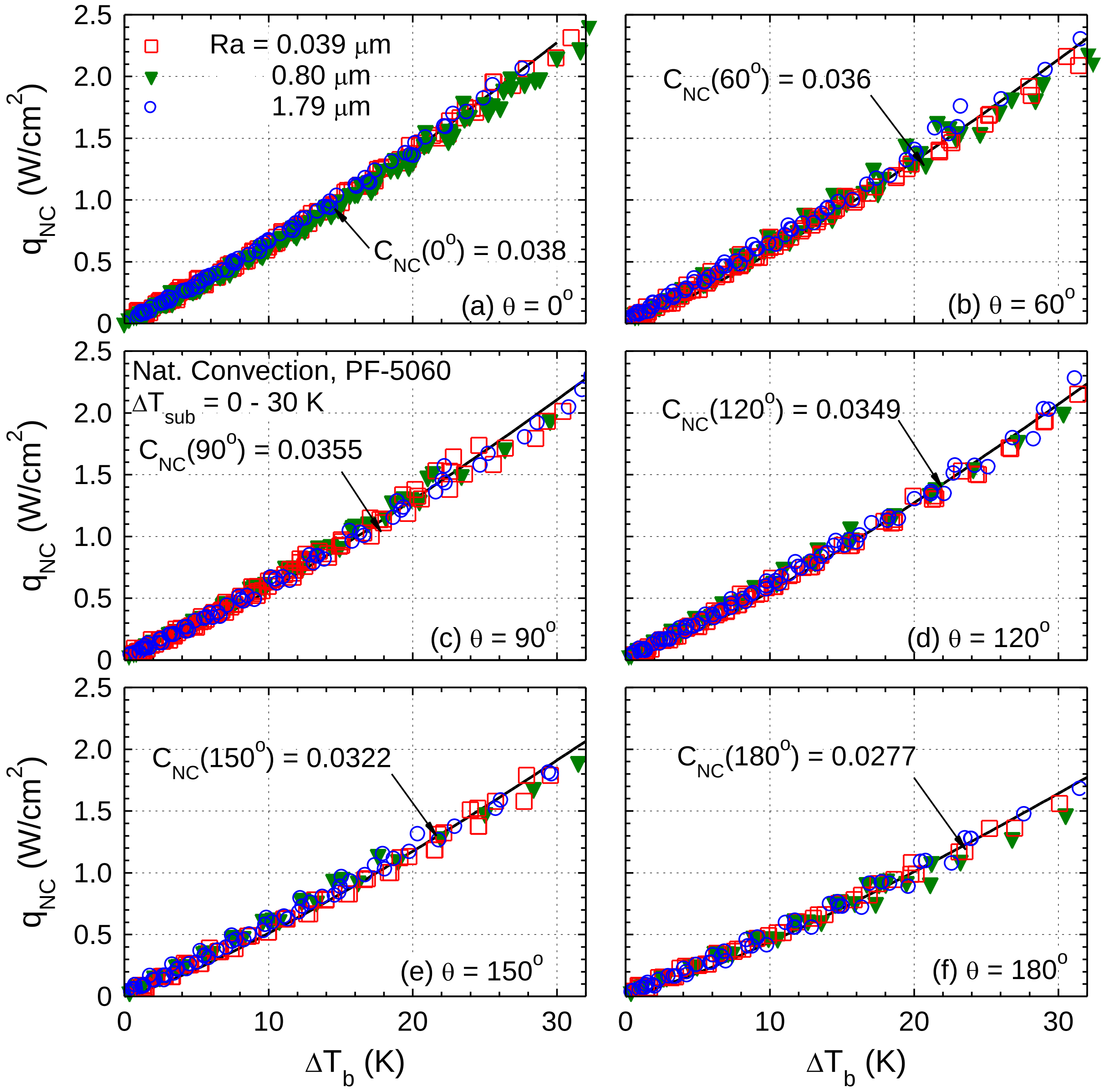

Figure 4.28. The effect of inclination angle on natural convection cooling of saturated and subcooled PF-5060 on rough and oxidized Cu surfaces.

decreased progressively faster with further increase of θ (Figure 4.28c – e). The lowest natural convection cooling rate is in the downward-facing orientation, and is 73% of that in the upward facing orientation (Figure 4.28a).

The values of the natural convection coefficient, $C_{NC}(\theta)$ in Figure 4.28a – f show the decrease in the cooling rate as the inclination was increased. This coefficient is 0.038 for the upward facing orientation (θ = 0^o), 0.0355 for the 90^o inclination and only 0.0277 for the downward facing orientation ($\theta = 180^o$). The natural convection heat transfer coefficient may be expressed as a function of surface inclination, as:

$$h_{NC}(\theta) = C_{NC}(\theta = 0^o)a(\theta)\,\Delta T_b^{0.2} \tag{4.19}$$

In this expression, the coefficient $a(\theta)$ reflects the effect of the inclination angle on the cooling rate by natural convection, relative to that in the upward facing orientation. The obtained values of this coefficient were correlated (Figure 4.29), as:

$$a(\theta) = 1 - 1.57 \times 10^{-6}\,\theta^{2.32} \tag{4.20}$$

This correlation is within ± 2% of the experimental data (Figure 4.29).

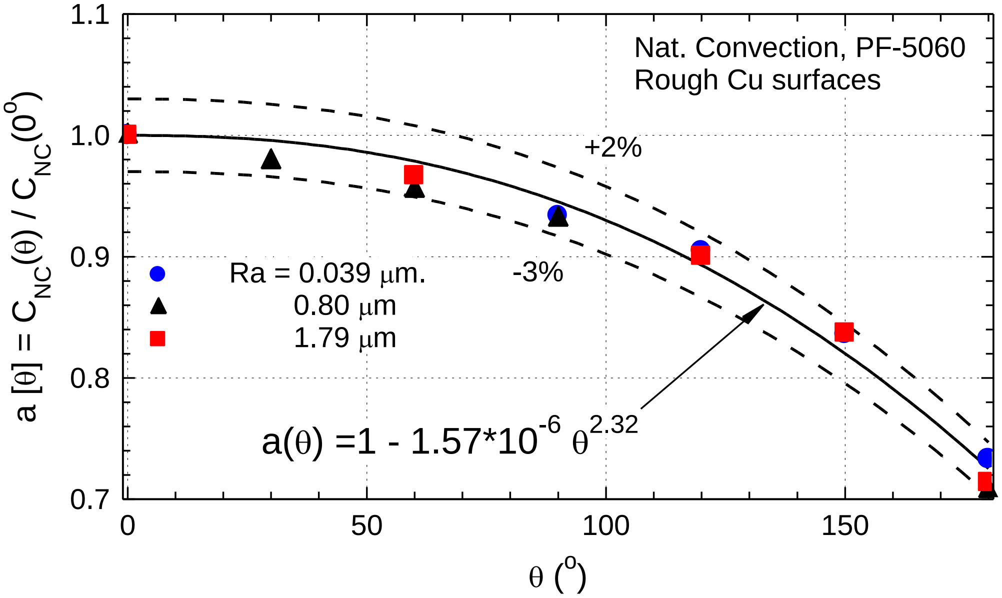

Figure 4.29. The effect of inclination angle on natural convection PF-5060 on rough and oxidized Cu surfaces, normalized to the upward facing inclination angle.

The exponent of the inclination angle in Equation (4.20) reflects the degradation in the liquid mixing along the heated surface with increased inclination angle. Such degradation is also due to the decrease in the liquid circulation rate from the bulk liquid pool along the heated surface. The liquid mixing and circulation at the heated surfaces were most effective in the upward facing orientation, and least effective in the down facing orientation. For $\theta = 0^o$, the density driven flow was free above the heated surface, whereas for $\theta = 180^o$, the flow was directly impeded by the heated surface itself.

The developed natural convection correlation, from Equations (4.17) – (4.20), is given as:

$$h_{NC}(\theta) = 0.038(1 - 1.57 \times 10^{-6}\theta^{2.32})\,\Delta T_b^{0.2} \tag{4.21}$$

This correlation for the h_{NC} of PF-5060 applies to uniformly heated smooth, rough, and oxidized Cu surfaces, for any inclination angle 0° – 180°, is in good agreement with the present experimental data of non-oxidized and oxidized Cu surface within ± 10%.

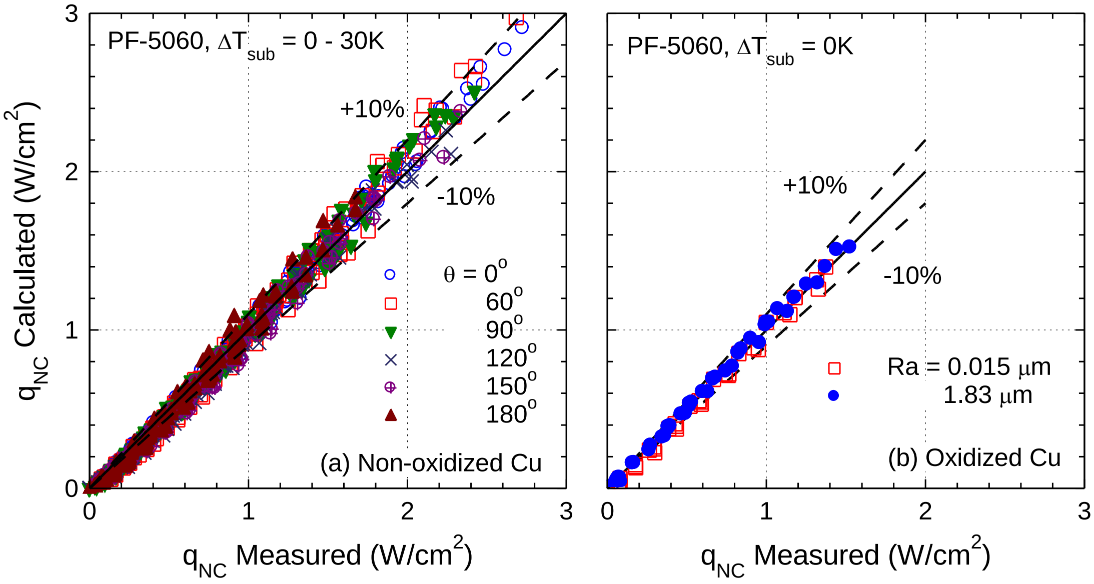

Figure 4.30. Comparison of calculated q_{NC} (Equation (4.21)) values versus measured for subcooled PF- 5060 on rough and oxidized Cu surfaces at different inclination angles.

4.5.3 Summary and Discussion

The results in Figure 4.28 and Figure 4.30 show that the cooling high power computer chips in standby mode by natural convection of PF-5060, is capable of removing as much as 3.0 W/cm^2, depending on the temperature of the surface and subcooling of the PF-5060. This translates into as much as 48 W of thermal power for heat spreaders sized 40 x 40 mm. The cooling rate by natural convection in this work is almost independent of the surface roughness and oxidation, and the liquid subcooling. It decreases with increasing inclination angle of the heated surface. In the downward facing orientation (θ = 180°), the rate of heat removal by natural convection is 73% of that in the upward facing inclination (θ = 0°). The obtained natural convection correlations are a useful design tool for thermal management of high power computer chips cooled by nucleate boiling of the PF-5060 dielectric liquid, and may be used in conjunction with the other developed correlation for h_{NB}, h_{MNB}, presented previously.

To help interpret the effect of surface roughness on nucleate boiling of PF-5060, an extensive visualization was carried out as part of this research. The next section presents the visualization study of the discrete vapor bubble on the smooth and rough Cu surfaces in saturation nucleate boiling of PF-5060 dielectric liquid.

4.6 Discrete Bubble Visualization Study

Bubble growth dynamics play an important role in determining observed nucleate boiling performance. For example, researchers were able to determine the effects of surface characteristics, applied surface heat flux and the bubble growth dynamics of various liquids (Rinni et al. 2001; Ramswamy et al. 2002; El-Genk and Bostanci 2003; Demiray and Kim 2004; Nikmar et al. 2006; McHale and Garimella 2008; McHale and Garimella 2010; Hutter et al. 2010; Hsu et al. 2012a; Hsu et al. 2012b; McHale and Garimella 2013). Surfaces that decrease the bubble departure diameter and increase the detachment frequency, enhance nucleate boiling. Additionally, surface modifications that increase the active density of bubble nucleation sites may be quantified using bubble visualization studies.

4.6.1 Visualization Study Approach

After pool boiling experiments were completed, the test vessel was allowed to cool for ~2 hours. Following, the supply of the DC power to the underlying heating element to active sites for discrete bubbles nucleation on the surface was done in two steps: first, a heat flux of ~10W/ cm^2 was supplied to the underlying heating element for about ~1 minute to activate nucleation sites on the Cu surface. The heat flux was then decreased to ~0.5W/cm^2 and left for at least ~2 minutes before recording any images of growing bubbles. This allowed the nucleate boiling sufficient time to stabilize, and the reduction of power also ensured that all potential sites for bubbles nucleation remained active at the reduced power. After the thermocouple temperature readings were verified to match those from the boiling curves of the prior experiments at the same applied heat flux, the camera was focused to, and captured the entire boiling surface. Entire surface images were used as a reference scale, as well as to identify discrete bubbles, such as those circled in Figure 4.31. The camera was then refocused to, and captured the selected discrete bubbles for greater detail and precision. Examples of discrete bubbles captured just before departure are shown in Figure 4.32. The next section presents the obtained bubble growth measurements for the smooth and rough Cu surfaces, and subsequent estimation of active nucleation sites density for these surfaces during nucleate boiling.

Figure 4.31 A single frame of the full boiling surface with Ra = 1.44 µm used to identify discrete bubble locations.

Figure 4.32 Captured images of discrete bubbles on various surfaces just before departure.

4.6.2 Transient Bubble Growth

This section presents images of the bubbles transient growth and the measured departure diameter and detachment frequency in saturation nucleate boiling of PF-5060 dielectric liquid, at an applied heat flux of 0.5 W/cm^2. These measurements were used to estimate the surface average density of active nucleation sites, N, as a function of the surface roughness and wall superheat, for the smooth and rough Cu surfaces of Ra = 0.039 – 1.79 µm.

Figure 4.33a – g display still photographs of discrete bubbles on various rough Cu surfaces. Growing bubbles at the low heat flux of 0.5 W/cm^2 were not influenced by others at neighboring sites. Figure 4.34a – d show a representative set of photographs used for measuring the transient growth of a single vapor bubble, at a selected site on Cu surfaces with an average roughness of 0.039 µm, 0.80 µm, 0.925 µm, and 1.44 µm. The last photograph, or frame, in Figure 4.34a – d, is of the growing bubble prior to departure. The bubble departure event actually occurred after the last frame, but before the additional frame that followed, or 4.76 ms. Because of the relatively modest recording speed (210fps), it was not possible to capture images of the growing bubble earlier than 4.76 ms, while in the inertia driven stage of growth. This stage typically occurs in the first few milliseconds of the ebullition cycle, when the bubble grows much faster than in the thermal controlled stage (Ivey, 1967).

The measured data of the transient growth of the vapor bubbles in saturation boiling of PF-5060 on smooth and rough Cu surfaces is displayed in Figure 4.35. Figure 4.35 plots the recorded bubble diameter, D_b, versus the square root of growth time, $t_b^{0.5}$ ($t_b = t_0+t$). The bubble growth measurements for the smooth and rough Cu were correlated to within ± 15% and ± 8%, respectively, as:

$$\mathrm{D_b(\mu m)} = 234 + 81\sqrt{\mathrm{t_b}} \text{ (on smooth Cu)} \tag{4.22a}$$

$$\mathrm{D_b(\mu m)} = 206 + 48\sqrt{\mathrm{t_b}} \text{ (on rough Cu surfaces)} \tag{4.22b}$$

There was little difference in transient growth between the rough Cu surfaces (Figure 4.35), and the scatter of the data is within the uncertainty of the measurements. The transient growth of the bubbles on the rough Cu surfaces is very similar to those reported by El-Genk and Ali (2013), of saturation nucleate boiling of PF-5060 on microporous Cu (MPC) surfaces, with varying MPC layer thickness, at an applied heat flux of ~0.5W/cm^2 (Figure 4.35c). McHale and Garimella (2010) saw some changes in bubble departure diameter and growth with surface roughness in saturation nucleate boiling of FC-72; however the change may have been due to the varying of heat flux. In another work by McHale and Garimella (2012), surface roughening had little effect on bubble departure diameter of FC-72 at low heat flux. Therefore, they concluded that the

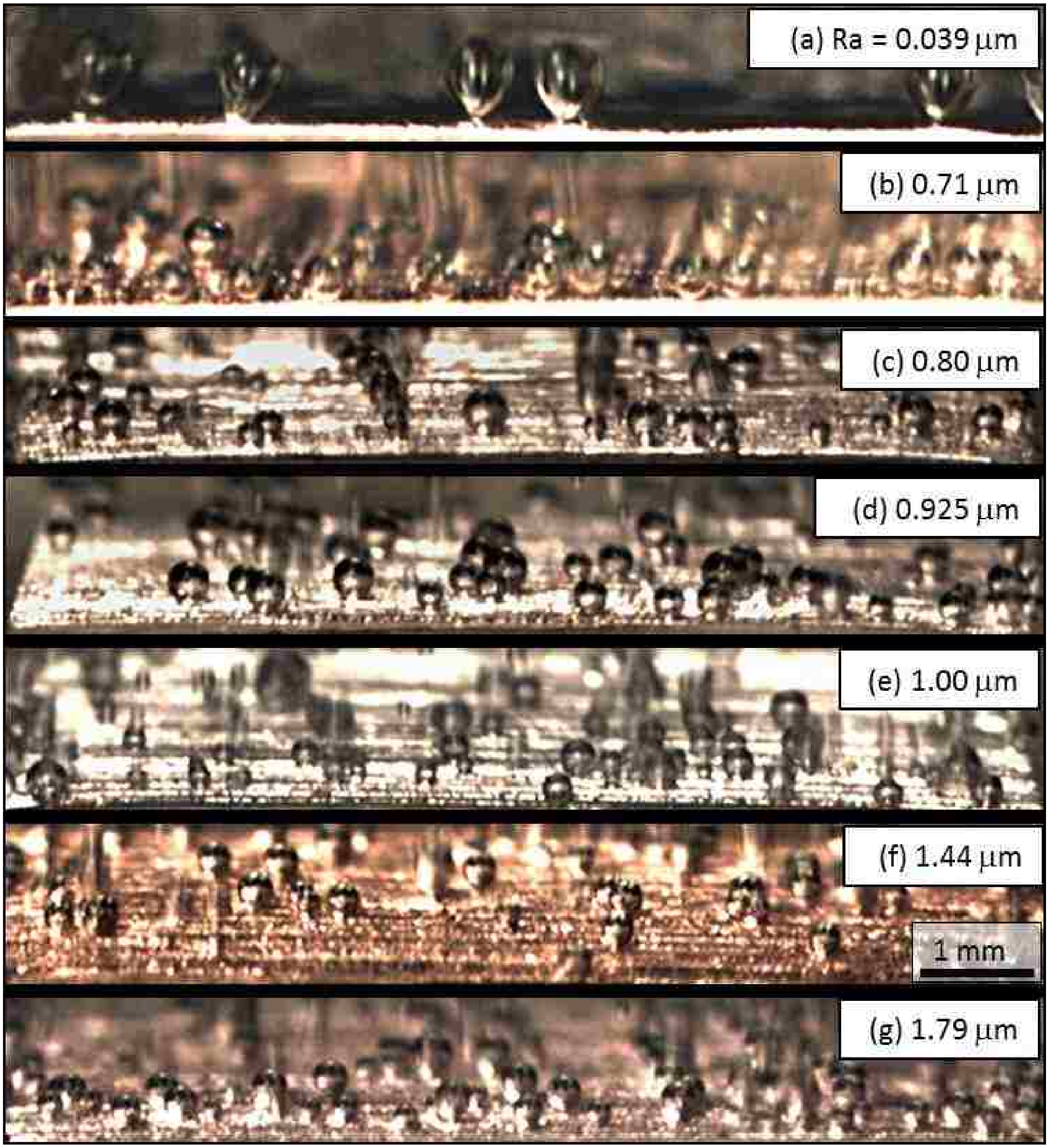

Figure 4.33 Photographs of various rough Cu surfaces recorded at an applied heat flux of ~0.5W/cm^2, with discrete bubbles. These images show discrete growing bubbles along the smooth and rough Cu surfaces.

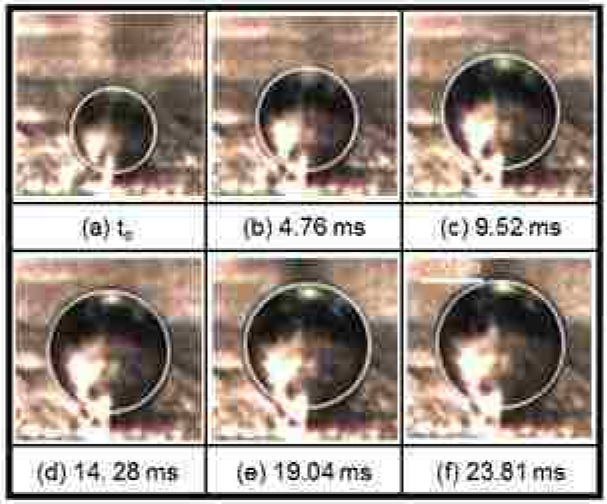

(b) Ra = 0.80 µm

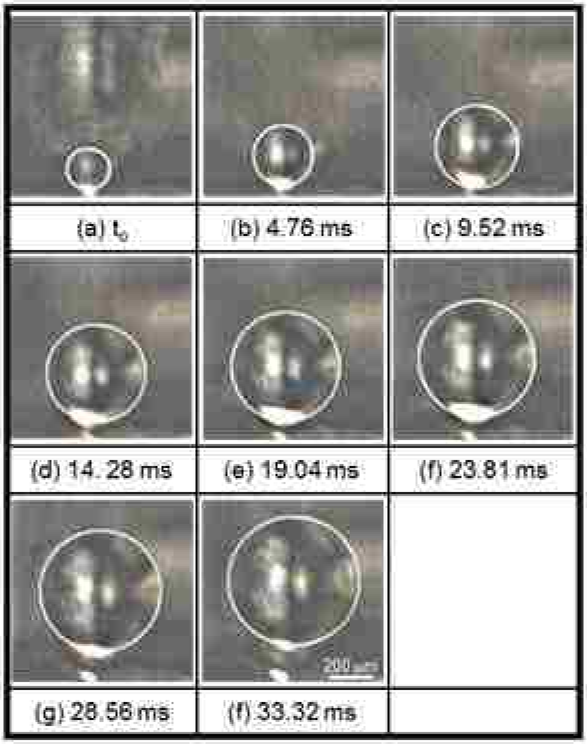

(a) Ra = 0.039 µm

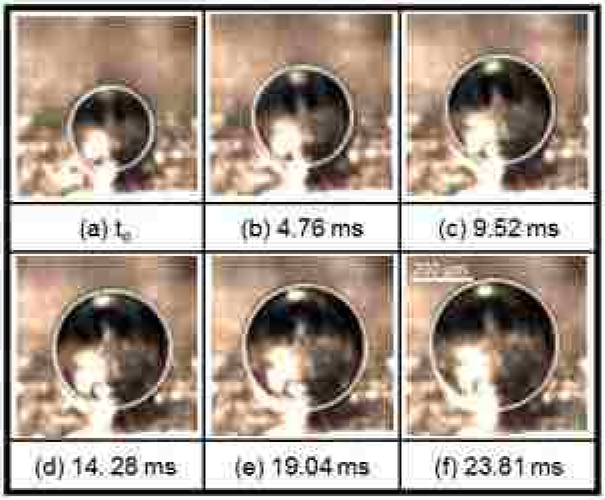

(c) Ra = 0.925 µm

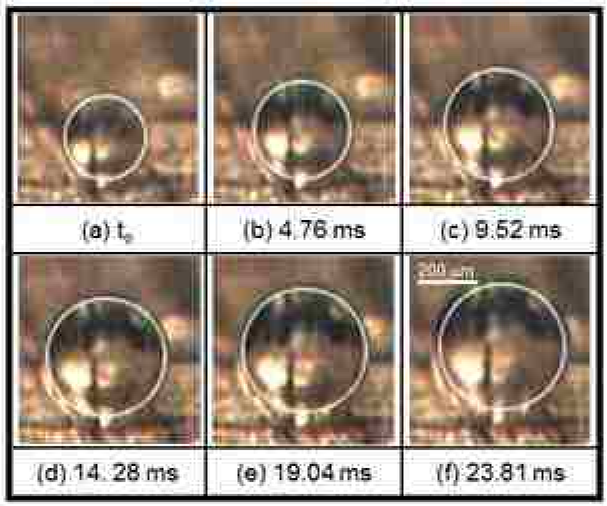

(d) Ra = 1.44 µm

Figure 4.34 Transient growth images of vapor bubbles in saturation boiling of PF-5060 on upward facing smooth and rough Cu surfaces with (a) Ra = 0.039 µm, (b) Ra = 0.80 µm, (c), Ra = 0.925 µm and (d) Ra = 1.44 µm. The last images are those of the bubbles just prior to departure.

surface roughness parameter itself or other related topology characteristics had no effect on discrete bubble growth at low applied heat fluxes.

The present set of results in (Figure 4.35a) show the measured transient growth on the smooth Cu surface was much different than on the rough and MPC surfaces (Figure 4.35b – c). The bubbles on the smooth Cu surface showed a different growth rate (Figure 4.35a), and departure diameter and detachment frequency. The bubble departure diameter and detachment frequency were 50% larger and 18.4% lower, respectively, than of those on the rough Cu surfaces. Figure 4.34 also shows the growing bubbles were noticeably larger on the smooth Cu surface (Figure 4.34a) at the same applied heat flux of 0.5 W/cm^2, than on the rough Cu surfaces (Figure 4.34b – g).

The different growth rate of the bubbles on the smooth Cu surface may have to do with distribution of the cavities present. The smooth Cu surface required the highest wall superheat before boiling incipience and was thus likely comprised of either much smaller or larger cavities for bubbles nucleation compared to the rough Cu surfaces (Hsu, 1962). This notion came from Hsu’s (1962) model which predicts a larger range of cavity size for bubbles nucleation, with increased wall superheat. The measured bubble transient growth on the smooth Cu (Figure 4.36b) suggested the physical cavity size distribution for bubbles nucleation was larger than of the rough Cu surfaces. The surface preparation procedures of the rough Cu surface created a large distribution of randomly distributed (and smaller) cavities for bubbles nucleation that were absent on the smooth Cu surface.

Larger cavities provide for a larger surface tension force along the rim of the cavity. The growing vapor bubble would require a larger buoyant force to depart, which it could only obtained through growing larger. Additionally, the smooth Cu is more hydrophobic than rough Cu (Figure 3.14). Hydrophobic surfaces retain the growing bubbles longer before departure. Measurements of static contact angle with DI water on the present smooth and rough Cu surfaces demonstrated that the contact angle, or surface hydrophobicity, increases with decreasing surface roughness. Other have shown hydrophobic surfaces to contain larger and more slowly departing bubbles than of similar hydrophilic surfaces (Hsu et al. 2012a; Hsu et al. 2012b).

Despite the differences in the bubble transient growth between the smooth and rough Cu surfaces, the bubble departure diameter always increased proportionally to the square root of the time, and is consistent with those reported for a thermally driven bubble growth (Zuber 1959; Ivey 1967; Rini, Chen and Chow, 2001; Hsu et. al 2012).

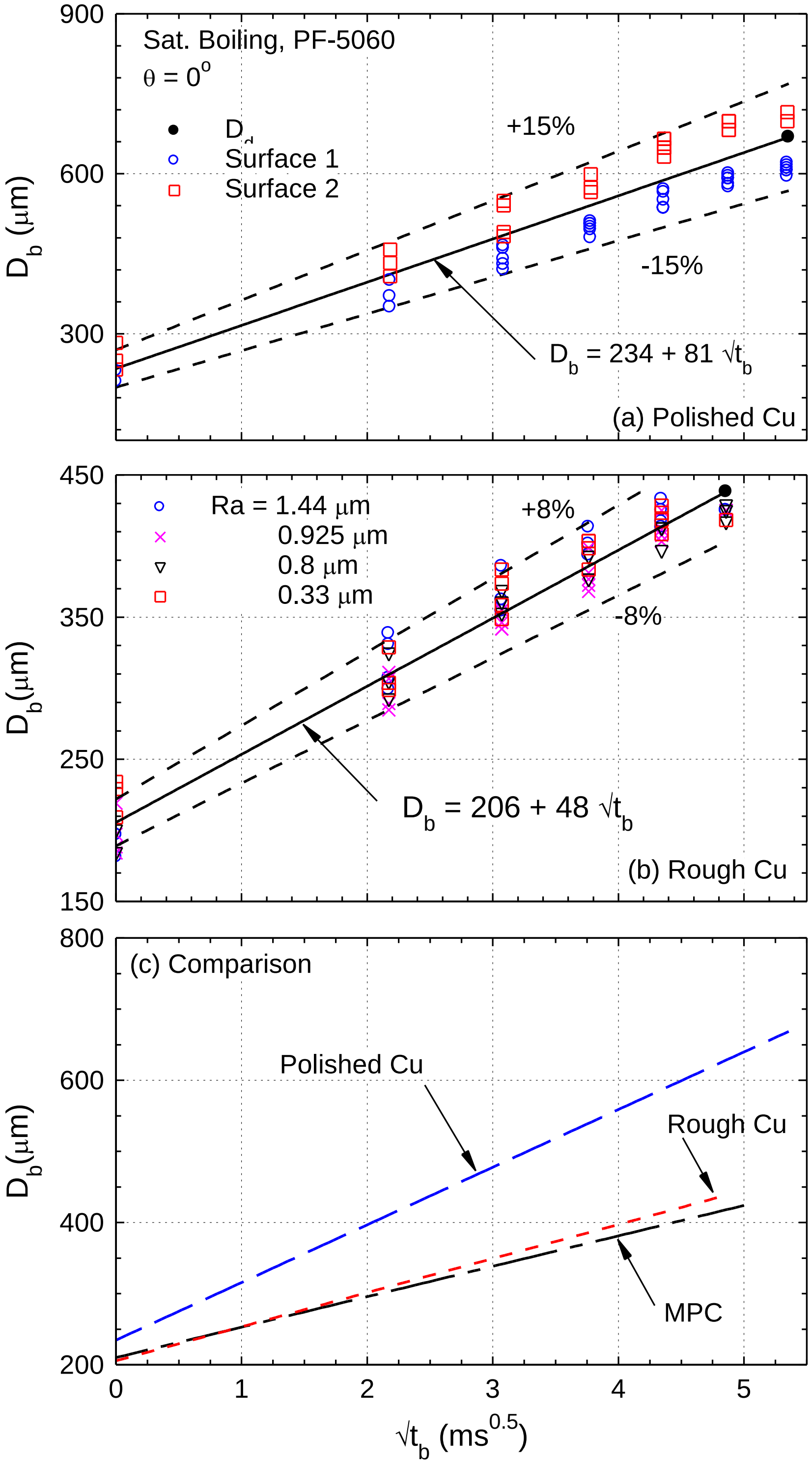

Figure 4.35 Transient Growth of Discrete Bubbles on Roughened Cu Surfaces in Saturation Boiling of PF-5060 Liquid.

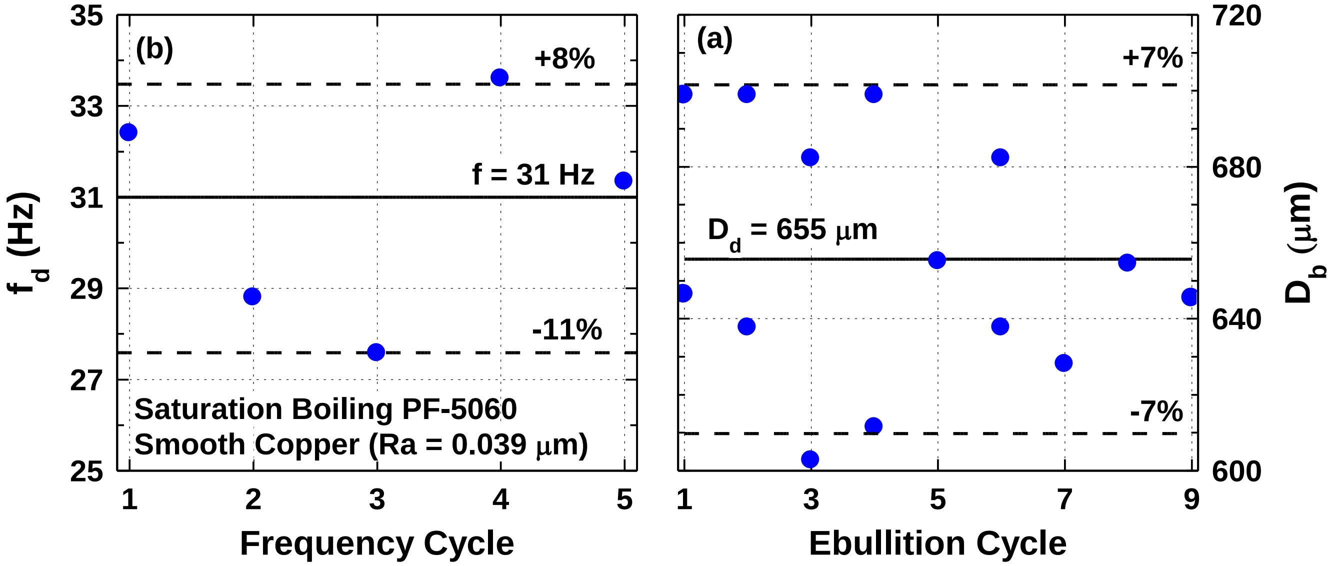

Figure 4.36 Bubble Departure Diameter and Frequency in Saturation Boiling of PF-5060 on a Smooth Polished Cu Surface.

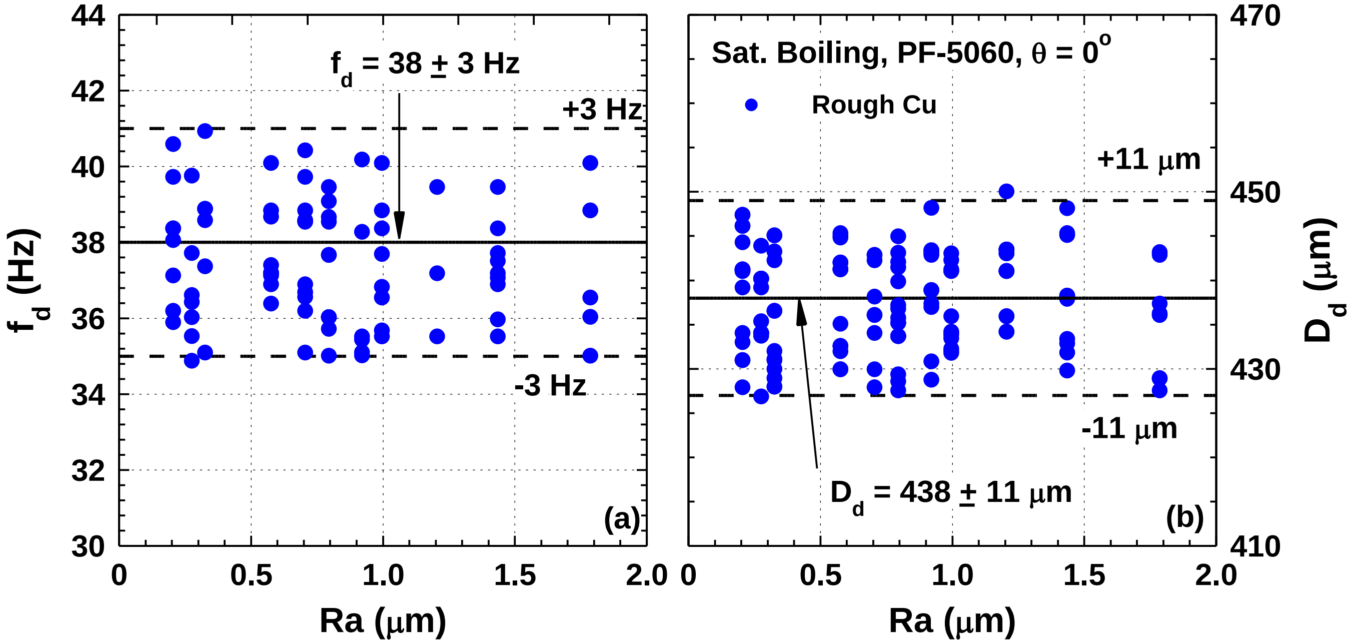

Figure 4.37 Bubble Departure Diameter and Frequency in Saturation Boiling of PF-5060 on Rough Cu Surfaces.

Table 4.1. The measured bubble departure diameter and detachment frequency in saturated boiling of PF-5060 dielectric liquid at 0.5 W/cm2 on Cu surfaces.

Present Work	Liquid	Parameter(s) Varied	D_d (µm)	f_d (Hz)
Smooth Cu	PF-5060	Heat Flux = 0.5 W/cm^2	655 µm ± 53	31 ± 4
Rough Cu	PF-5060	Heat Flux = 0.5 W/cm^2 Surface roughness	438 µm ± 36	38 ± 3

The determined mean bubble departure diameter for saturation boiling of PF-5060 dielectric liquid on the smooth and rough Cu surfaces at an applied heat flux of 0.5W/cm^2 is D_d = 655 ± 53 µm and 438 ± 36 µm (Table 4.1, Figure 4.36 and Figure 4.37), respectively. The corresponding bubble detachment frequency, $f_{d,}$ is 31 + 4Hz and 38±3 Hz, respectively (Figure 4.36 and Figure 4.37). The determined values of departure diameter for all Cu surfaces fall into the same range as those reported by others for saturated boiling of FC-72 dielectric liquid (Table 2.2) (Rinni et al. 2001; Ramswamy et al. 2002; El-Genk and Bostanci 2003; Demiray and Kim 2004; Nikmar et al. 2006; McHale and Garimella 2008; McHale and Garimella 2010; Hutter et al. 2010; Hsu et al. 2012a; Hsu et al. 2012b; McHale and Garimella 2013; El-Genk and Ali 2013). This liquid has identical thermophysical properties as PF-5060, with the exception of surface tension, which is 20% lower at room temperature, but only slightly lower at saturation temperature. Conversely, the present values of the detachment frequency were lower than most others reported in saturation boiling of FC-72 (Table 2.2). The determined values of D_d and f_d (Table 4.1) were used to estimate the average number of active nucleation sites on the smooth and rough Cu surfaces, presented next.

4.6.3 Active Nucleation Sites Density

The active nucleation sites density on the smooth and rough Cu surfaces investigated were calculated by using their respective experimental boiling curves (Figure 4.12), the determined bubble departure diameters and detachment frequencies (Table 4.1), and calculated ratio of the wetted surface to footprint area (Figure 3.11). The equation used to estimate the active nucleation sites density, N, is given as:

$$N = \frac{6\,q}{\pi\,D_b^3\,\rho_v\,h_{fg}\,f_d\,(1 + A_r)} \qquad (4.23)$$

Figure 4.38 shows the estimated active nucleation sites density versus Jacob Number (or wall superheat), for the smooth and rough Cu surfaces. The estimates are compared to those of others (Nimkar et al. 2006; McHale and Garimella 2010; El-Genk and Ali 2013). The estimates of active nucleation sites density assumed the measured discrete bubble growth parameters are also representative of those in the fully boiling developed boiling region. In reality this may not be the case, but the assumption should still provide for good estimates of N. Figure 4.38 shows the smooth Cu surface (Ra = 0.039 μm) has an active nucleation site density of 100 – 2000 sites / cm^2, depending on the Jacob number. The rough Cu surfaces have an active nucleation site density that ranges from 700 to 10000 sites / cm^2, and at lower Jacob numbers. These values of N for the smooth and rough Cu surfaces (Figure 4.38) are one order of magnitude higher than those reported by McHale and Garimella (2008) in FC-77 liquid, and are within the same range as those reported El-Genk and Ali (2013) for PF-5060 on MPC. For the same Jacob number, increasing Ra increases N. The higher population of active nucleation sites at lower Jacob numbers (or wall superheat) helps explains the increases of h_{NB} seen with increasing Ra (Figure 4.2, Figure 4.3, Figure 4.9, Equation (4.4), Equation (4.8)).

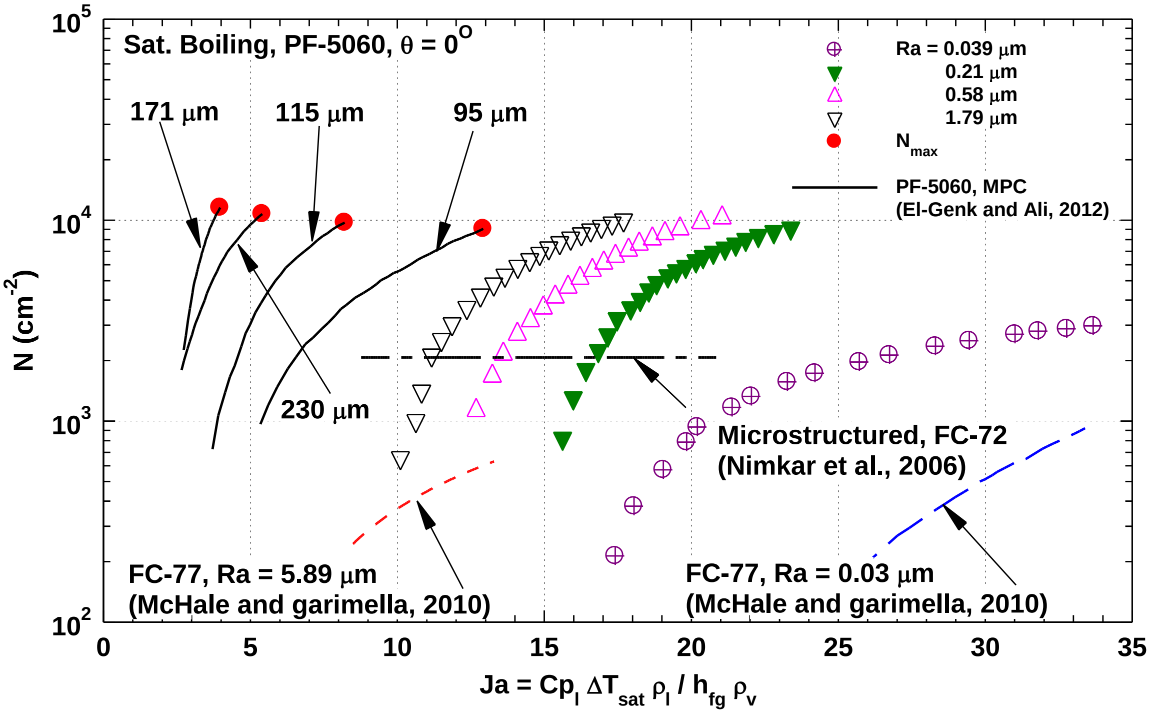

Figure 4.38 The calculated active nucleation sites density vs Jacob number for smooth and rough Cu surfaces in saturated nucleate boiling of PF-5060, and comparison with others.

4.6.4 Comparisons to Available Correlations

Reported correlations to predict the departure diameter and or detachment frequency of the discrete vapor bubble in nucleate boiling are listed in Table 2.3 (Fritz 1935, Zuber 1959, Ivey 1967, Kutateladze and Gogonin 1979, Jensen and Memmel 1986, Kim and Kim 2006; Phan et al. 2010). The importance of these correlations lies in their potential for numerical modeling of nucleate boiling, subject to rigorous experimental validation beforehand. This section compares the predictions of these correlations, of the bubble departure diameter and detachment frequency, against those determined experimentally(Table 4.1), for saturation nucleate boiling of PF-5060 on smooth and rough Cu surfaces. In the correlations that call for the static angle, the assumption is made that $\phi = 5^o$ for PF-5060. The very low surface tension and high volatility of dielectric liquids makes their static contact angles very difficult to measure.

Table 4.2. Predictions of bubble departure diameters for smooth and rough Cu surfaces in saturated boiling of PF-5060 dielectric liquid.

Author(s) (Year)	Diameter, D_d (μm)
Fritz (1935)	76
Mikic and Rosenhow (1969)	1197
Kutateladze and Gogonin (1979)*	488, 556
Jensen and Memmel (1986)*	505, 585
Kim and Kim (2006)*	283, 1134
Phan et al. (2010)	928

* If two numbers are present, the first is of rough Cu and the second of smooth Cu.

Table 4.2 lists the predictions of the bubble departure diameter in saturation nucleate boiling of PF-5060, using the correlations listed in Table 2.3. All correlations with the exception of that of Fritz (1935), predict bubble departure diameter values within the range of experimentally reported values in Table 2.2 for FC-72 dielectric liquid. FC-72 is identical in properties to PF-5060, with the exception of surface tension, which is 3% lower at saturation temperature. Table 4.2 shows that the correlation developed by Kutateladze and Gogonin (1979) predicts best the bubble departure diameter in saturation nucleate boiling of PF-5060 on rough Cu surfaces. The modified version of this correlation by Jensen and Memmel (1986) best predicts for the smooth Cu surfaces. Both of the latter correlations predict the D_d to within 11.4 – 15.2 % of the present experimental data.

While Zuber's (1959) and Ivey's (1967) correlations (Table 4.2) do not directly predict the bubble departure diameter and detachment frequency, both are consistent in relating the bubble departure diameter to the detachment frequency in saturation nucleate boiling of PF-5060 on smooth and rough Cu surfaces. From the experimentally obtained D_d and f_d values (Table 4.1), Zuber's relationship calculates the products of $f_d D_d$ from Table 4.1 to be 18.34 mm/s $\pm$ 9.2%, and Ivey's relationship calculates $f_d^{0.5} D_d$ to be 3.16 $mm/s^{1/2}$ $\pm$ 14.6%, for the smooth and rough Cu surfaces.

The next chapter presents the experiments that investigated the nucleate pool boiling of degassed PF-5060 dielectric liquid on dimpled Cu surfaces. The same experimental and visualization procedures for smooth and rough Cu surfaces were also used for the dimpled Cu surfaces. To differentiate between the smooth and rough Cu surfaces, and the dimpled Cu surfaces, the nomenclature denoted with an asterisk is for the dimpled Cu surfaces.

5. Nucleate Pool Boiling of PF-5060 on Dimpled Cu Surfaces

This chapter presents the results of the pool boiling experiments that investigated the effects of dimple diameter, Φ_d, surface inclination angle, θ, and liquid subcooling, ΔT_{sub}, on the nucleate boiling heat transfer coefficient, h_{NB}, maximum nucleate boiling heat transfer coefficient, h_{MNB}, and Critical Heat Flux (CHF) of PF-5060 dielectric liquid. The uniformly heated Copper (Cu) surfaces with machined circular dimples with diameter, Φ_d, of 300 μm, 400 μm, and 500 μm, were 200 μm deep. The dimples were spaced along the surface in triangular lattice with a pitch-to-diameter (P/D) ratio of 2.0. Each Cu surface had the same Φ_d for all machined dimples present. Six inclination angles of 0^o (upward facing), 60^o, 90^o (vertical), 120^o, 150^o, 180^o (downward facing), and three liquid subcooling of 0 K (saturation), 10 K, 20 K, and 30 K were investigated.

The results of the experiments in this chapter are broken up in three sections that focus on saturation and subcooled nucleate boiling, and natural convection. Correlations for nucleate pool boiling of PF-5060 on dimpled Cu surfaces were developed for (i) the Critical Heat Flux (CHF) in terms of θ, and the liquid subcooling, ΔT_{sub}, (ii) the h_{MNB} in terms of θ, and the liquid subcooling, ΔT_{sub} and (iii) the natural convection, h_{NC}, in terms of the applied heat flux. The results and developed correlations were compared to those for pool boiling of PF-5060 on smooth and rough Cu surfaces. Additionally, the transient growth of the vapor bubble was recorded and measured for each dimpled surface in saturation nucleate boiling of PF-5060 for the upward facing inclination angle, at an applied surface heat flux of 0.5 W/cm^2. The results from the captured images were used to quantify the nucleate boiling behavior and performance of the dimpled Cu surfaces.

5.1 Reproducibility of Results

To ensure reproducibility of the results, separate experiments with Cu surfaces of the same size were conducted multiple times each. Figure 5.1 and Figure 5.2 present the obtained saturation pool boiling and h_{NB} curves of PF-5060 on the 300 μm, 400 μm, and 500 μm dimpled surfaces for the upward facing orientation. Each of these figures includes 3 – 4 boiling curves for separate experiments performed at least ~2 hours, and sometimes 1 – 2 days apart.

The initial saturation pool boiling curves for PF-5060 liquid on the Cu surfaces with the 300 μm, 400 μm, and 500 μm diameter dimples are presented in Figure 5.1. For each surface, these figures compare results of four separate experimental runs. In the first and second runs, a temperature excursion of as much as 16 K occurred prior to boiling incipience. After 3 or 4 experimental runs, the surfaces became fully conditioned and the pool boiling results were highly reproducible (Figure 5.1). The 300 μm dimpled surface took the most runs to condition (Figure 5.1a), whereas the 400 and 500 μm dimpled surfaces were consistent after the first run. The differences in h_{NB} of the different runs (Figure 5.2) are within the uncertainties of the experiments. The repeated experiments with the same test section, as well as with different test sections of dimpled Cu surfaces of Φ_d = 400 μm and 500 μm, confirm the fidelity and consistency of the experiments and procedures. The experimental results presented and discussed in the remainder of this section are for fully conditioned dimpled Cu surfaces.

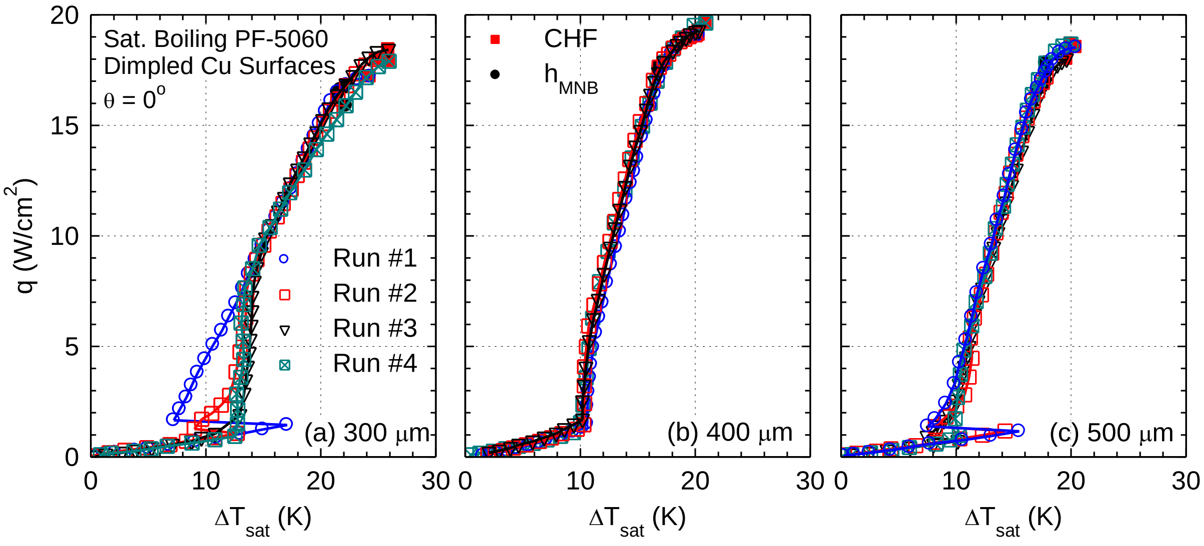

Figure 5.1 Reproducibility of the pool boiling curves of saturation nucleate boiling of PF-5060 on dimpled Cu surfaces showed good reproducibility of the dimpled surfaces of Φ_d = 400 μm and 500 μm.

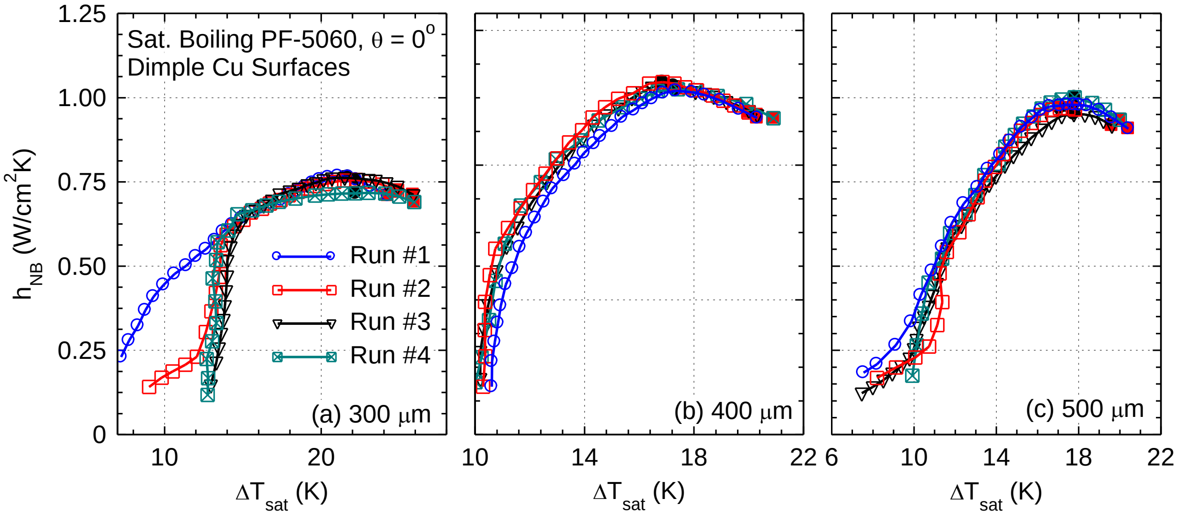

Figure 5.2. Reproducibility of the nucleate boiling heat transfer coefficient curves of saturation nucleate boiling of PF-5060 on dimpled Cu surfaces.

5.2 Saturation Nucleate Boiling on Dimpled Surfaces

5.2.1 Effect of Dimple Size on h_{NB} and CHF

Figure 5.3 presents the obtained pool boiling and heat transfer coefficient curves for the Cu dimpled surfaces investigated for saturation nucleate boiling of PF-5060, at the upward facing inclination angle ($\theta = 0^o$). The maximum nucleate boiling heat transfer coefficient, h_{MNB}, is denoted by the solid black circles and the CHF by the solid red squares. For comparison, the boiling and heat transfer coefficient curve of smooth Cu of Ra = 0.039 µm, is included in Figure 5.3.

When used for the first time, the plain and dimpled Cu surfaces experienced large excursions in surface temperature prior to boiling incipience. The excursion in temperature on the plain Cu was as much as 40 K, compared to < 17 K on the dimpled Cu surfaces. In subsequent experiments with the dimpled Cu surfaces, the temperature excursions decreased and eventually became negligible (Figure 5.3). This behavior is similar to the temperature excursions of the smooth and rough Cu surfaces with repeated use, presented in the previous chapter.

Figure 5.4 presents the conditioned pool boiling and h_{NB} curves for the saturation nucleate boiling of PF-5060, at the upward facing inclination angle. The dimpled Cu surfaces of Φ_d = 400 µm and 500 show similar results for saturation nucleate boiling of

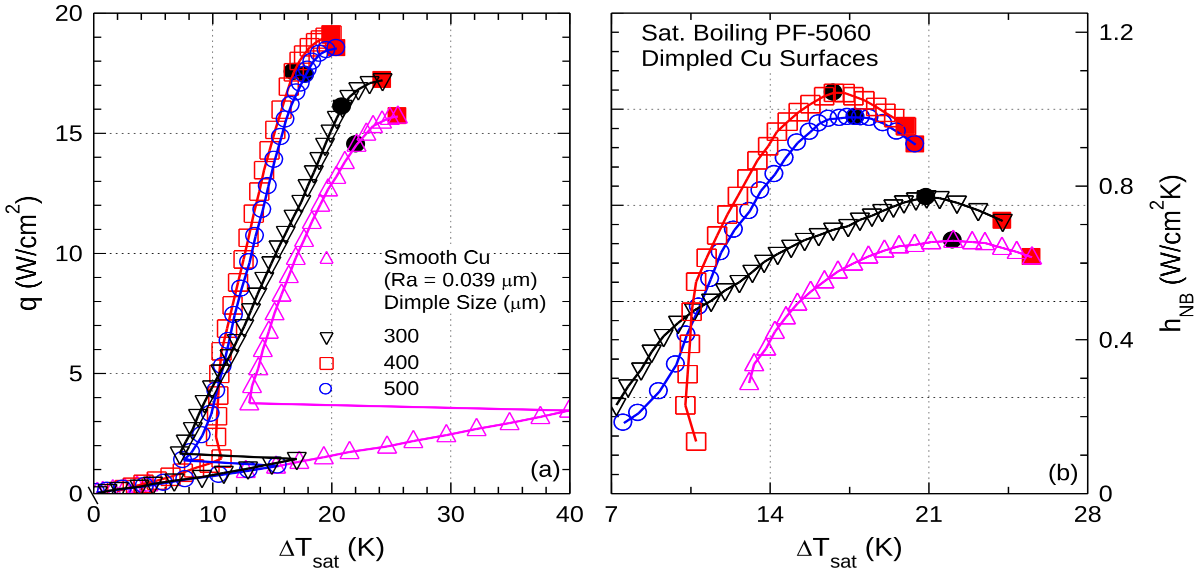

Figure 5.3. Initial runs of saturation boiling of PF-5060 on dimpled Cu surfaces; (a) pool boiling curves, and (b) h_{NB} curves.

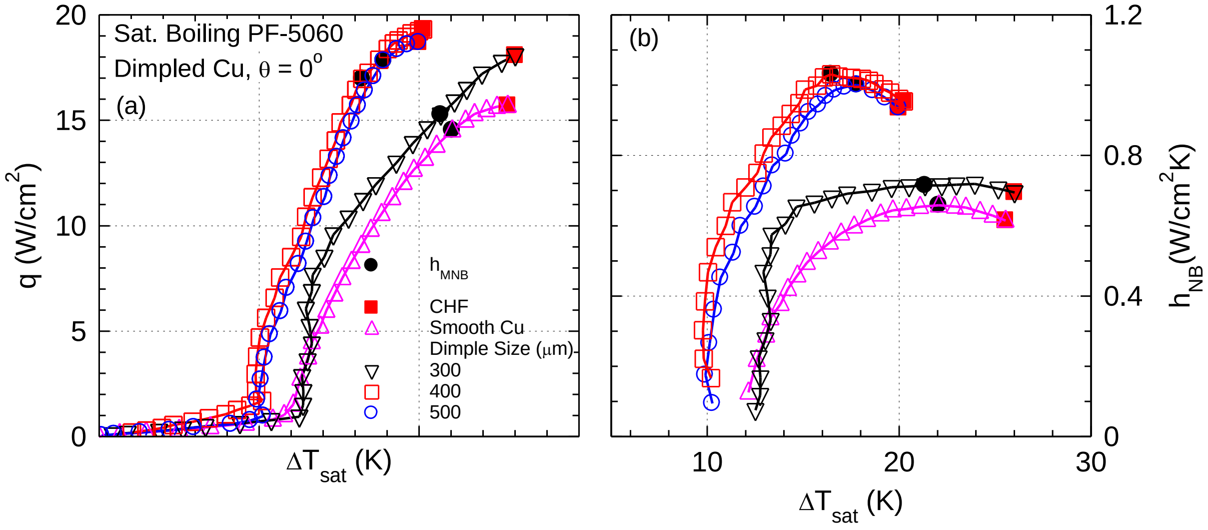

Figure 5.4. Conditioned pool boiling and h_{NB} curves of PF-5060 on plain smooth and dimpled Cu surfaces.

PF-5060 for the upward facing inclination angle. Both surfaces show good reproducibility. The dimpled surfaces of Φ_d = 300 μm were difficult to reproduce, and in some experiments, bubbles nucleation was not fully activated over the entire surface until heat fluxes of $\geq$ 8 W/cm^2. Beyond that heat flux, bubble nucleation had spread to the entire surface, resulting in a typical dependence of the surface superheat on the applied heat flux. This is evident from Figure 5.4a, which shows the 300 μm dimpled surface containing a very steep, and even negatively sloped portion of the boiling curve shortly after boiling incipience, up to heat applied fluxes of ~ 8 W/cm^2. This behavior occurred because of sudden activations of small groups of sites for bubbles nucleation, causing no change or even decreases in the wall superheat as the applied heat flux increased. This may be caused by inconsistencies in the surface roughness, as portions of the surface notably rougher than the surface average favor nucleate boiling.

Despite some difficulty in reproducing the experiments for the dimpled surfaces of Φ_d = 300 µm, these surfaces consistently showed the lowest nucleate boiling heat transfer, h_{NB}, maximum nucleate boiling heat transfer coefficient, h_{MNB}, and CHF of PF-5060, of the dimpled Cu surfaces investigated (Figure 5.4). The dimpled surfaces of Φ_d = 400 µm had the highest h_{NB}, h_{MNB}, and CHF (Figure 5.4). The values of h_{MNB} for saturation nucleate boiling of PF-5060 on the dimpled Cu surfaces of Φ_d = 300 µm, 400 µm, and 500 µm, at the upward facing inclination angle, are 0.65 – 0.72 W/cm^{2}K, 1.04 – 1.08 W/cm^{2}K, 0.98 – 1.01 W/cm^{2}K, respectively. The corresponding surface superheats are ~22.1 K, ~21.4 K, ~16.5 K and ~17.8 K, respectively. These values of saturation boiling and h_{MNB}, in the upward facing orientation, are similar to those for nucleate boiling of PF-5060 on a Cu surface of the same footprint, thickness, and average surface roughness, Ra, of 0.039 – 0.21 µm (Figure 4.4, Figure 4.9).

The CHF in saturation nucleate boiling of PF-5060 on the dimpled Cu surfaces of Φ_d = 300 µm, 400 µm, and 500 µm, for the upward facing inclination angle ($\theta = 0^o$), are ~18 W/cm^2, ~19.3W/cm^2 and ~18.3 W/cm^2, respectively. The corresponding surface superheats are ~25.5 K, ~26 K, ~20.25 K and 20 K, respectively. These values of CHF are similar to those reported for boiling on a Cu surface of the same footprint, thickness, and average surface roughness of 0.039 – 0.33 µm (Figure 4.13).

Compared to smooth Cu (Ra = 0.039 µm), the enhancement in the nucleate boiling heat transfer on the surface with the 300 µm dimples is modest and much less than on the Cu surfaces with the 400 and 500 µm diameter dimples. On the Cu surface with 400 µm diameter dimples, the values of h_{NB}, h_{MNB}, and CHF are highest, and occurred at the lowest surface superheats. Therefore much like surface roughening, the presence of the dimples enhances nucleate boiling, compared to smooth Cu surfaces.

However, the degree of enhancement was not as much as some of the rougher Cu surfaces (Ra $\geq$ 0.58 μm) investigated in the previous chapter.

5.2.2 Effect of Surface Inclination Angle on h_{MNB} and CHF

This section presents the results of the experiments that investigated the effect of the surface inclination angle on the saturation nucleate boiling of PF-5060 on dimple Cu surfaces. The pool boiling curves obtained from the surfaces with Φ_d = 400 μm and 500 μm, at inclination angles 0^o, 60^o, 90^o, 120^o, 150^o, and 180^o are given in Figure 5.5. This figure shows that relative to the upward facing inclination angle ($\theta = 0^o$), the increase of surface inclination resulted in a decrease of both h_{MNB} and CHF, as well as generally decreased the corresponding surface superheats of h_{MNB} and CHF. The h_{NB} increased at low applied heat fluxes (<5 W/cm^2) in the discrete bubbles region of the boiling curve (Figure 5.5), however decreased in the fully developed and bubbles coalescence regions, as the inclination angle increased. This behavior of increasing h_{NB} θ (at low applied heat fluxes) with increasing has been reported previously for smooth and rough Cu surfaces, and was attributed to the bubble shear of inclined surfaces enhancing nucleate boiling. The same was observed for the dimpled Cu surfaces.

In order to quantify the dependence of h_{MNB} and CHF on the surface inclination angle, the obtained values were normalized to those for the upward facing orientation ($\theta = 0^o$). Figure 5.6a and b show normalized h_{MNB} and CHF, respectively, relative to the upward facing angle. This figure reveals the effect of inclination angle on h_{MNB} and CHF, for saturation nucleate boiling of PF-5060 on dimpled Cu surfaces. The effect of the inclination angle is consistent for all three dimpled surfaces investigated (Figure 5.6a–b), and is similar to those reported in the previous chapter for smooth and rough Cu surfaces. The effect on inclination angle on h_{MNB} and CHF for the dimpled Cu surfaces is summarized, and within good agreement to the present experimental data of $\pm$ 9% and $\pm$ 5%, respectively, as:

$$F(\theta)^* = 1 - 2.505 \times 10^{-7}\theta^{2.84} \tag{5.1}$$

$$R(\theta)^* = 1 - 1.157 \times 10^{-7}\theta^{3} \tag{5.2}$$

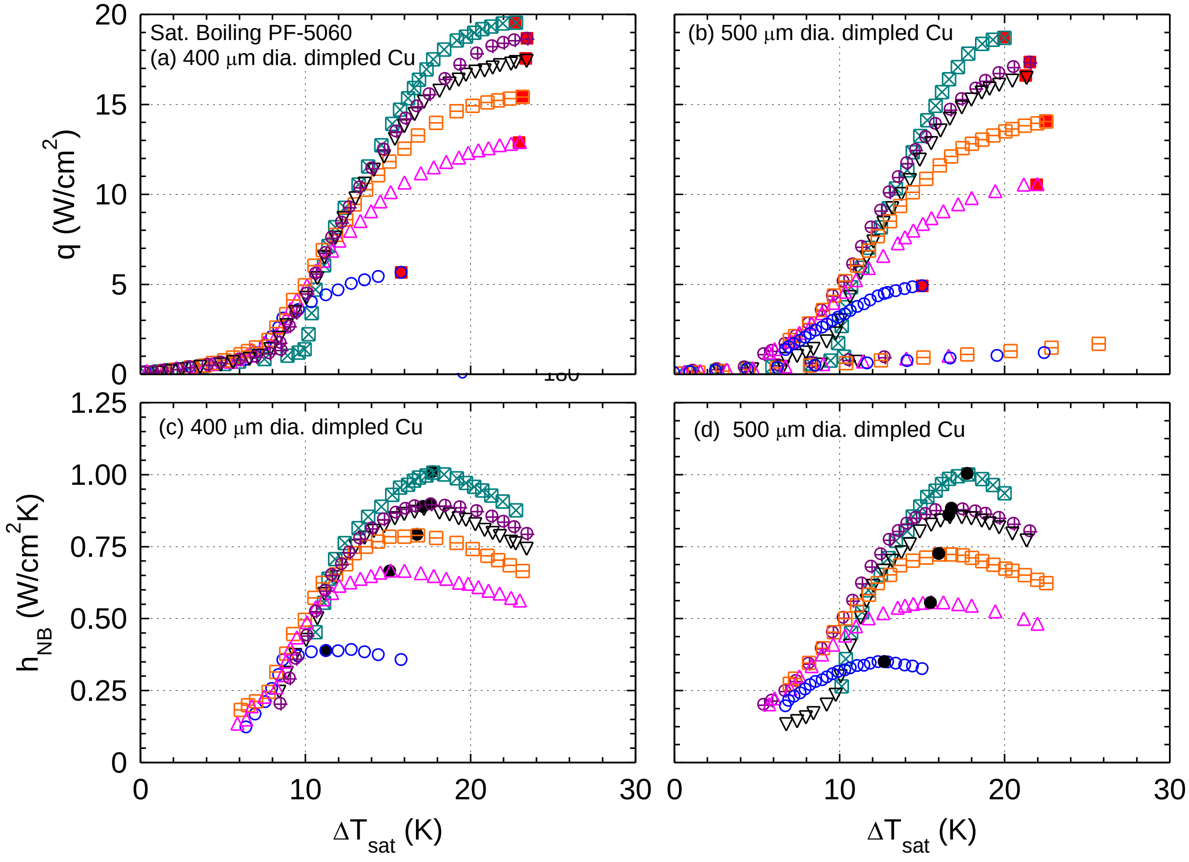

Figure 5.5. Saturation boiling curves on Cu surfaces with 400 and 500 μm-diameter dimples at inclination angles of 0°, 60°, 90°, 120°, 150°, and 180°.

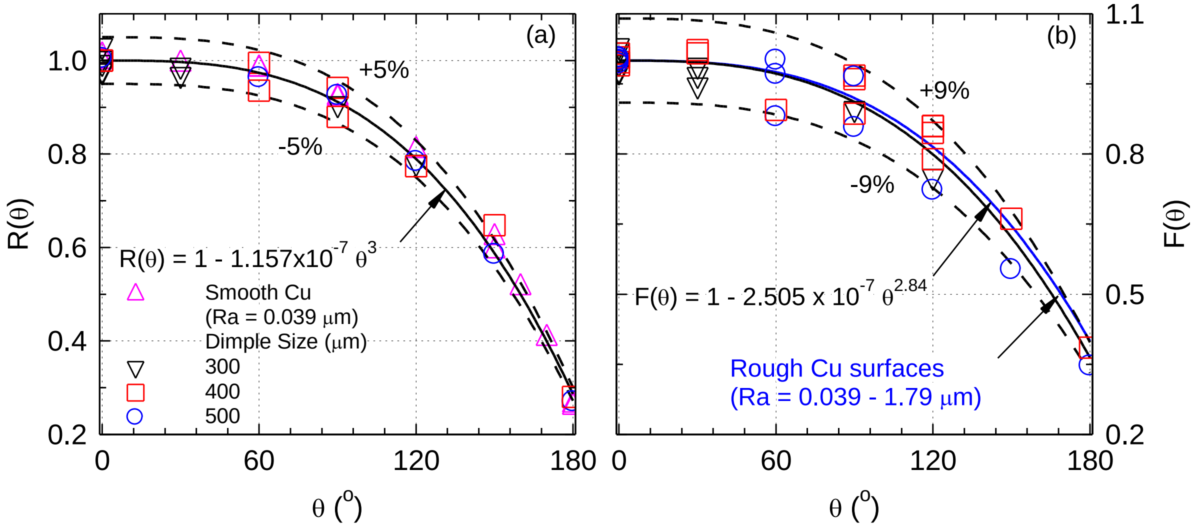

Figure 5.6. The effect of surface inclination angle on the saturation nucleate boiling of PF-5060 on dimpled Cu surfaces for (a) CHF and (b) h_{MNB}.

The $F(\theta)^*$ (Equation (5.1)) describes the effect of inclination angle on h_{MNB} relative to the upward facing inclination ($\theta = 0^{\mathrm{o}}$), and the $R(\theta)^*$ (Equation (5.2)) is the effect of inclination angle on CHF. The asterisks in both correlations are present to differentiate the dimpled Cu surfaces from the smooth and rough Cu surfaces (Equations (4.6) and (4.11)). For the three dimpled surfaces investigated, the h_{MNB} decreased to ~91%, ~80%, ~62% and 36% of its upward facing value at inclination angles 90^{o}, 120^{o}, 150^{o}, and 180^{o}, respectively. Likewise, the CHF decreased to ~92%, 80%, ~60%, and 33% of its upward facing value at inclination angles 90^{o}, 120^{o}, 150^{o}, and 180^{o}, respectively. The next section presents the effect of liquid subcooling, ΔT_{sub}, on the h_{MNB} and CHF of PF-5060 on dimpled Cu surfaces.

5.3 Subcooled Nucleate Boiling

This section presents the results for the effect of the liquid subcooling, ΔT_{sub}, on nucleate boiling and CHF of PF-5060, on the dimpled Cu surfaces for the upward facing orientation. The ΔT_{sub} of 0 K (saturation), 10 K, 20 K, and 30 K were investigated. For each subcooling, at least two sets of experimental measurements were taken to ascertain the reproducibility of the results.

Figure 5.7a–d present the obtained experimental pool boiling curves for the dimpled Cu surfaces of (a) Φ_{d} = 500 μm and (b) Φ_{d} = 400 μm, in saturation and subcooled nucleate boiling of PF-5060. These figures show the liquid subcooling minimally affects h_{NB} in the fully developed nucleate boiling region. However, increased liquid subcooling markedly increases the length of the fully developed region, and h_{NB} in the discrete bubbles region at low heat flux, and the bubbles coalescence region at high heat flux. The h_{MNB}, relative to the bulk liquid temperature, ΔT_{b}, decreases with increasing liquid subcooling (Figure 5.7c–d).

Increasing ΔT_{sub} results in large enhancements in the CHF. Results in Figure 5.7 show that the CHF values on the Cu surface with Φ_{d} = 400 μm and the corresponding surface superheats are slightly higher than on the Cu surface with Φ_{d} = 500 μm. On the latter surface, the CHF at ΔT_{sub} values of 0 K (saturation), 10 K, 20 K, and 30 K are 18.9 W/cm^2, 23.13 W/cm^2, 26.33 W/cm^2, and 29.3 W/cm^2, respectively. The corresponding surface superheats, ΔT_{b}, are 20.4 K, 31.3 K and 42.8 K, and 53.27 K, respectively. For the former surface, the CHFs are 19.95 W/cm^2, 24.15 W/cm^2, 27.72 W/cm^2, and 30.56 W/cm^2, with corresponding ΔT_b of 22.1 K, 33.73 K and 44.5 K, and 55.4 K, respectively.

Figure 5.8 is a plot of the ratios of the CHF for subcooled boiling on the dimpled Cu surfaces, to that for saturation boiling, versus liquid subcooling, ΔT_{sub}. The delineated experimental data in this figure was correlated to within $\pm$3% as:

$$\left(\frac{CHF_{sat}}{CHF_{sub}}\right) = 1 + 0.0183\,\Delta T_{sub} \qquad (5.3)$$

This expression shows that for the dimpled Cu surfaces, the CHF of the PF-5060 dielectric liquid increases linearly to ΔT_{sub} at a rate of ~1.83 %/K for the upward facing orientation (Equation (5.3) and Figure 5.8). This rate is ~20% lower than of that reported for the same dielectric liquid on rough Cu surfaces (~2.2%/K, Figure 4.20, Equation (4.13)).

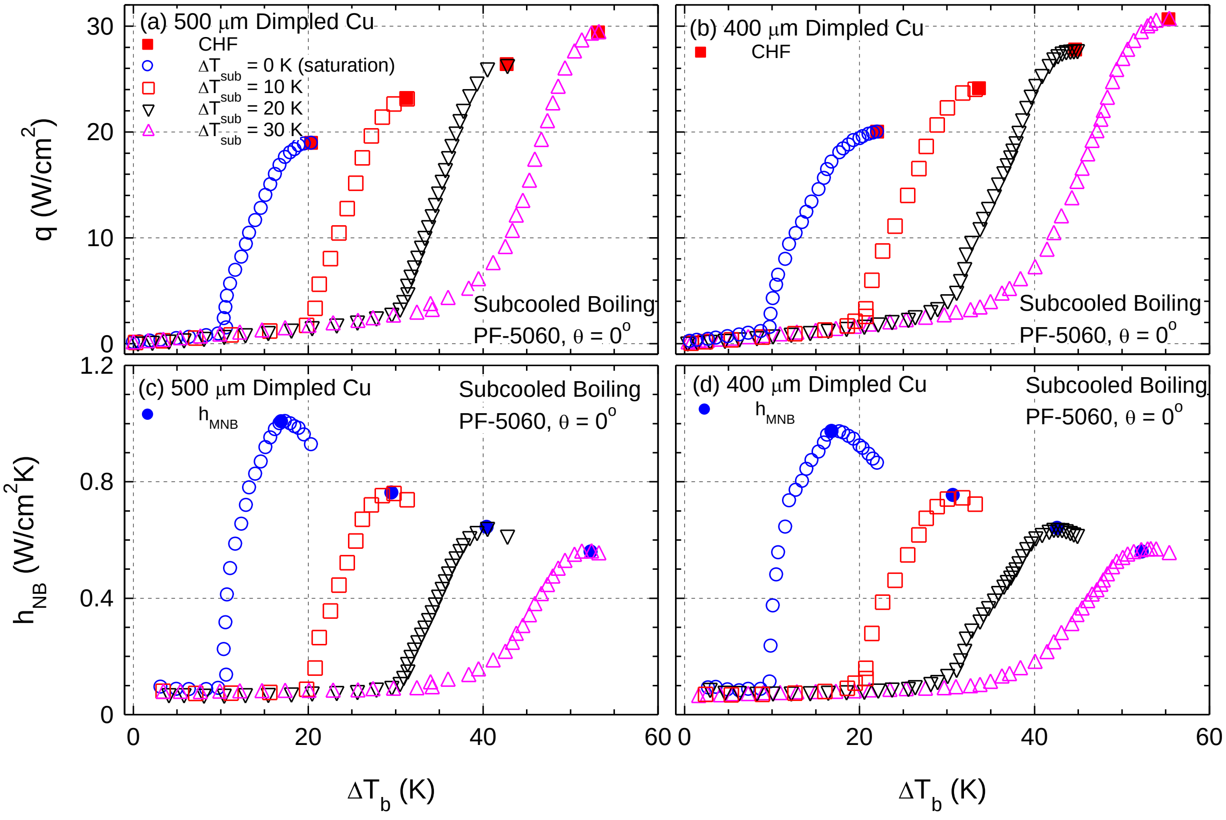

Figure 5.7. The effect of liquid subcooling on nucleate boiling of PF-5060 on Cu surfaces with (a) 500 μm-diameter dimples, and (b) 400 μm-diameter dimples.

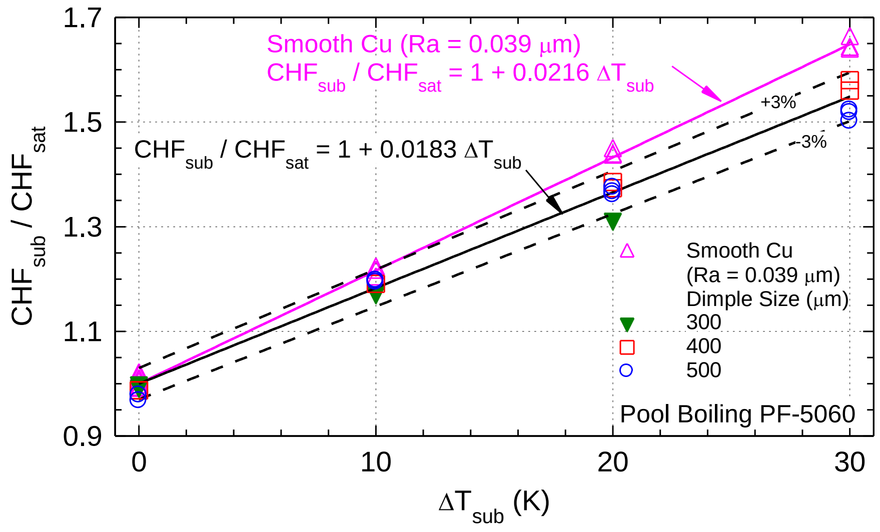

Figure 5.8. Comparison of the effect of liquid subcooling on CHF for PF-5060 dielectric liquid on dimpled and smooth Cu surfaces

Figure 5.9 plots of the ratios of the h_{MNB} for subcooled boiling on the dimpled Cu surfaces, to that for saturation boiling, versus liquid subcooling, ΔT_{sub}. The results in this figure show the $h_{MNB,sub}$ on both smooth and dimpled Cu surfaces decreases almost linearly with $\Delta T_{sub} > 10$ K. Although the value for saturation boiling, $h_{MNB,sat}$, on smooth Cu was lower than on the dimples surfaces (Figure 5.4), the ratio of ($h_{MNB,sub}$ / $h_{MNB,sat}$) was higher. Additionally, the ($h_{MNB,sub}$ / $h_{MNB,sat}$) is independent of dimple size. For liquid subcooling < 10 K, the results show a rapid decrease in ($h_{MNB,sub}$ / $h_{MNB,sat}$) with increased ΔT_{sub} on both the smooth and dimpled Cu surfaces. The experimental data (Figure 15) on dimpled and smooth Cu surfaces was correlated, as:

$$\left(\frac{h_{MNB,sat}}{h_{MNB,sub}}\right) = 1 - 0.078\ \Delta T_{sub}^{0.52}, \text{ on dimpled Cu surfaces} \tag{5.4}$$

$$\left(\frac{h_{MNB,sat}}{h_{MNB,sub}}\right) = 1 - 0.078\ \Delta T_{sub}^{0.48}, \text{ on smooth Cu surfaces} \tag{5.5}$$

These correlations show the slightly stronger dependence of the h_{MNB} for PF-5060 on dimpled Cu surfaces, on the liquid subcooling (Equation (5.4)), compared to smooth Cu surfaces (Equation (5.5)).

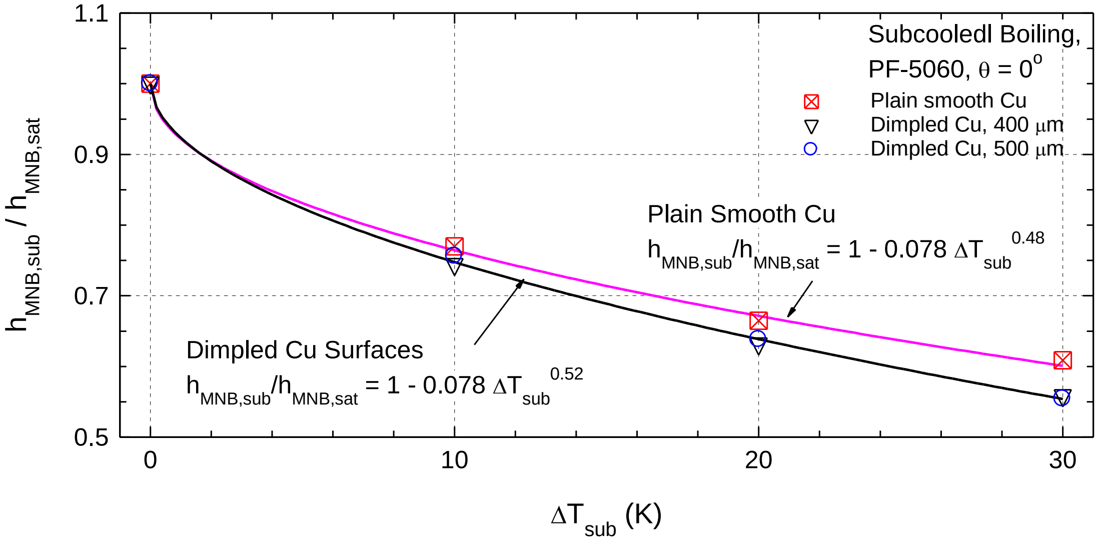

Figure 5.9. Effect of liquid subcooling on h_{MNB} for PF-5060 liquid on dimpled and plain smooth Cu surfaces.

For immersion cooling of high power chips or CPUs, it is desirable to estimate the cooling rate in the standby mode when the chip dissipation heat flux no more than a few W/cm^2. In this mode, the chip cooling is by natural convection of the dielectric liquid. The next section presents the results from the analysis of the natural convection cooling performance of saturated and subcooled PF-5060 on dimpled Cu surfaces.

5.4 Natural Convection

This section presents the experimentally obtained results on the effects of the dimple size, Φ_d, inclination angle, θ, and liquid subcooling, ΔT_{sub}, on the natural convection cooling of PF-5060 on uniformly heated dimpled Cu surfaces. The obtained experimental data was used to correlate the natural convection heat transfer coefficient, h_{NC}, as a function of θ. The Φ_d and ΔT_{sub} were found to be independent of h_{NC}. The developed correlation was compared with that obtained for smooth and rough Cu surfaces (Equation (4.17)).

Figure 5.10 presents the obtained natural convection results for saturated and subcooled PF-5060 dielectric liquid on the dimpled Cu surfaces. This figure is a plot of the applied heated flux, q, versus, $\Delta T_b = (T_w - T_b)$, which is the same as the surface superheat, ΔT_{sat} for saturated liquid.

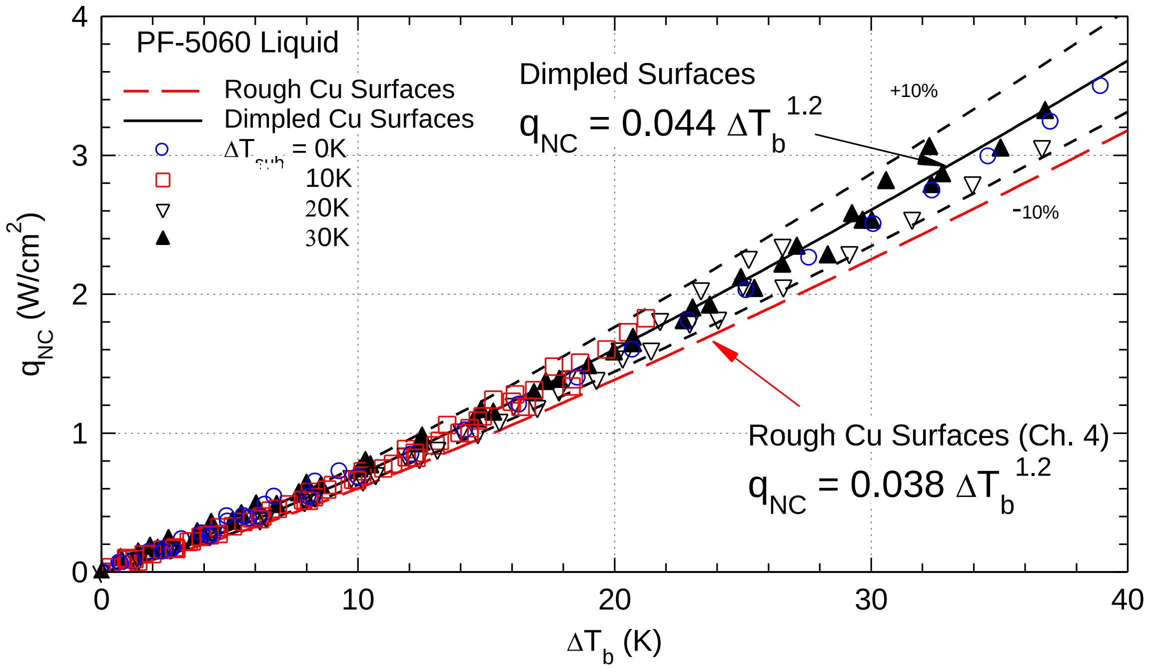

Figure 5.10 Comparison of natural convection data and correlations for PF-5060 dielectric liquid on dimpled and rough Cu surfaces.

The present data for the dimpled Cu surfaces was correlated and compared in Figure 5.10 with those reported for in the previous chapter smooth and rough Cu surfaces (Equations (4.17) – (4.18)). The heat flux for natural convection on the dimpled Cu surfaces, when based on the foot print area of 10x10 mm, is ~ 18% higher than for the same dielectric liquid on rough Cu surfaces (Equations (4.17) – (4.18)). When based on the actual wetted surface area, the natural convection cooling of the dimpled Cu surfaces is consistent with the correlation for the rough Cu surfaces. The results in Figure 5.10 also show that natural convection heat transfer is nearly independent of the size of the dimples, similar to that of the rough Cu surfaces.

To help interpret the effect of dimple size on nucleate boiling of PF-5060, an extensive visualization was carried out as part of this research. The next section presents the visualization study of the growing bubble on the dimpled Cu surfaces in saturation nucleate boiling of PF-5060 dielectric liquid for the upward facing orientation.

5.5 Dimpled Cu Surface Bubble Visualization

This sub-section presents the bubble departure diameter, D_d^*, and detachment frequency, f_d^*, of the vapor bubble in saturation nucleate boiling of PF-5060 dielectric liquid on dimpled Cu surfaces. The dimpled Cu surfaces had a much different bubble growth than of the smooth and rough Cu surfaces. On the dimpled surfaces, discrete bubbles that emanated from small surface cavities within the dimple coalesced to form one large bubble at the site of the dimple. The coalesced bubble, termed “dimple bubble” (and denoted by the asterisk for relevant nomenclature), dominated the nucleate boiling on the dimple Cu surfaces. Figure 5.11a – g shows images of saturation nucleate boiling of PF-5060 on the dimpled Cu surfaces, at low applied heat fluxes of 0.5 – 1 W/cm^2. These figures show how the majority of the nucleate boiling present coincided with the locations of the machined dimples.

From the full surface images such as those shown in Figure 5.11a – g, individual dimple locations that provided clear images of the full ebullition cycle free of disturbance from neighboring active dimples, were chosen to obtain the dimple bubble transient growth measurements. As with the smooth and rough Cu surfaces, the actual departure event itself was never captured, but known to happen within the following frame, or ~4.76 ms. The analyses of sequential images of the growing bubbles were used estimate the bubble departure diameter, D_d^*, and detachment frequency, f_d^*, in saturation nucleate boiling of PF-5060 dielectric liquid on dimpled Cu surfaces.

The following sub-sections present the investigation of the effect of the dimple size on the transient growth, departure diameter, D_d^*, and detachment frequency, f_d^*, of the dimple bubbles in saturation nucleate boiling of PF-5060 dielectric liquid at an applied heat flux of ~0.5 W/cm^2. At this low heat flux, the bubbles are discrete, and their growth is not influenced by neighboring growing bubbles on the surface. The results are compared to those obtained for saturation nucleate boiling of PF-5060 on smooth and rough Cu surfaces with the same applied heat flux. Additionally, the results are used to help explain the observed behaviors and performances of the dimpled Cu surfaces in saturation nucleate boiling of PF-5060.

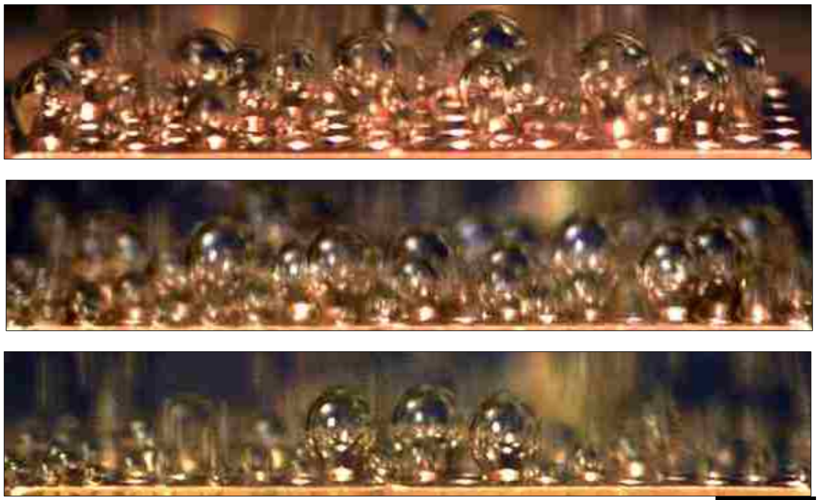

(a) 500 μm dimpled Cu [redacted]

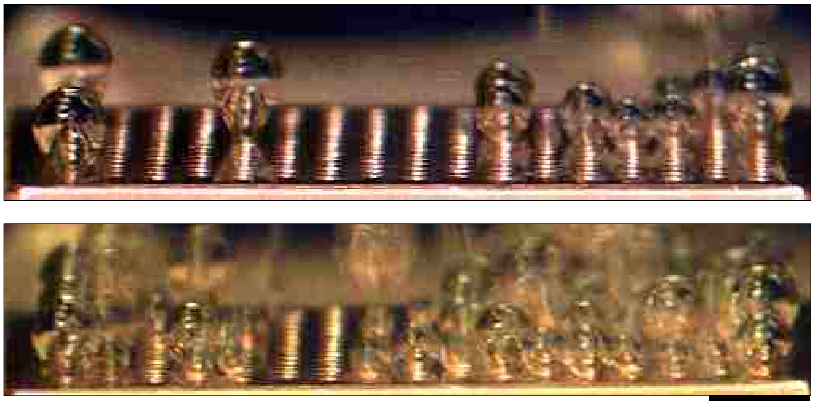

(b) 400 μm dimpled Cu [redacted]

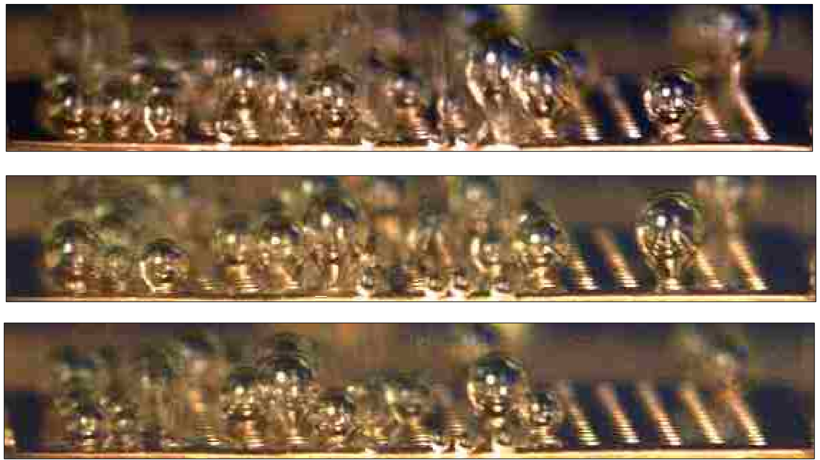

(c) 300 μm dimpled Cu [redacted]

Figure 5.11 Recorded photographs of growing bubbles on uniformly heated dimpled Cu surfaces in saturation nucleate boiling experiments with PF-5060 dielectric liquid at an applied heat flux of 0.5-1.0 W/cm2. Growing bubbles are associated with dimples; only a few nucleate on the plain flat portion of the surface between dimples.

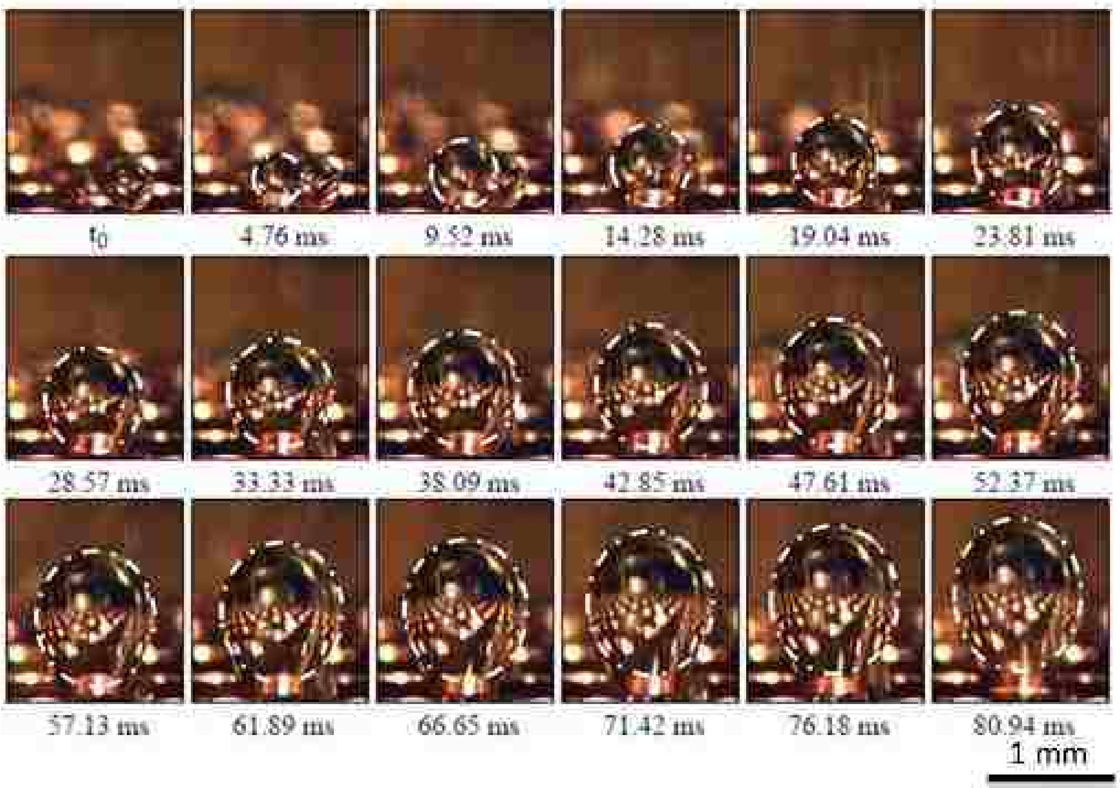

Figure 5.12. A Captured sequence of transient growth of single vapor bubble on the Cu surface with 500 μm dimples.

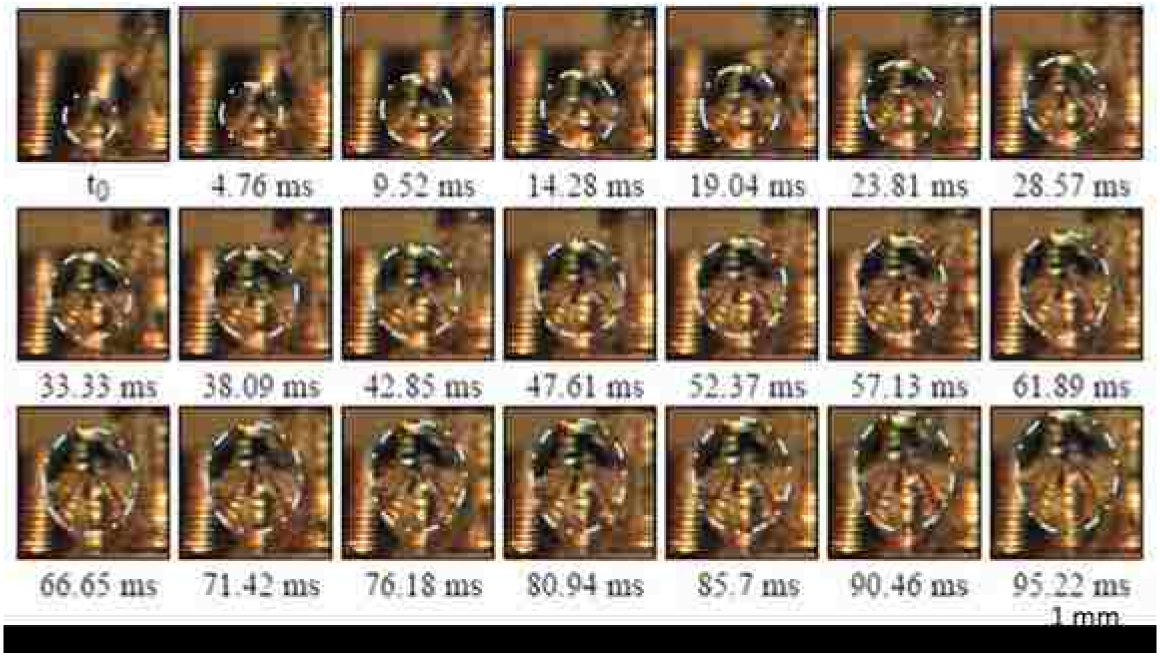

Figure 5.13. A sequence of images of transient growth of single vapor bubble on the Cu surface with 400 μm dimples.

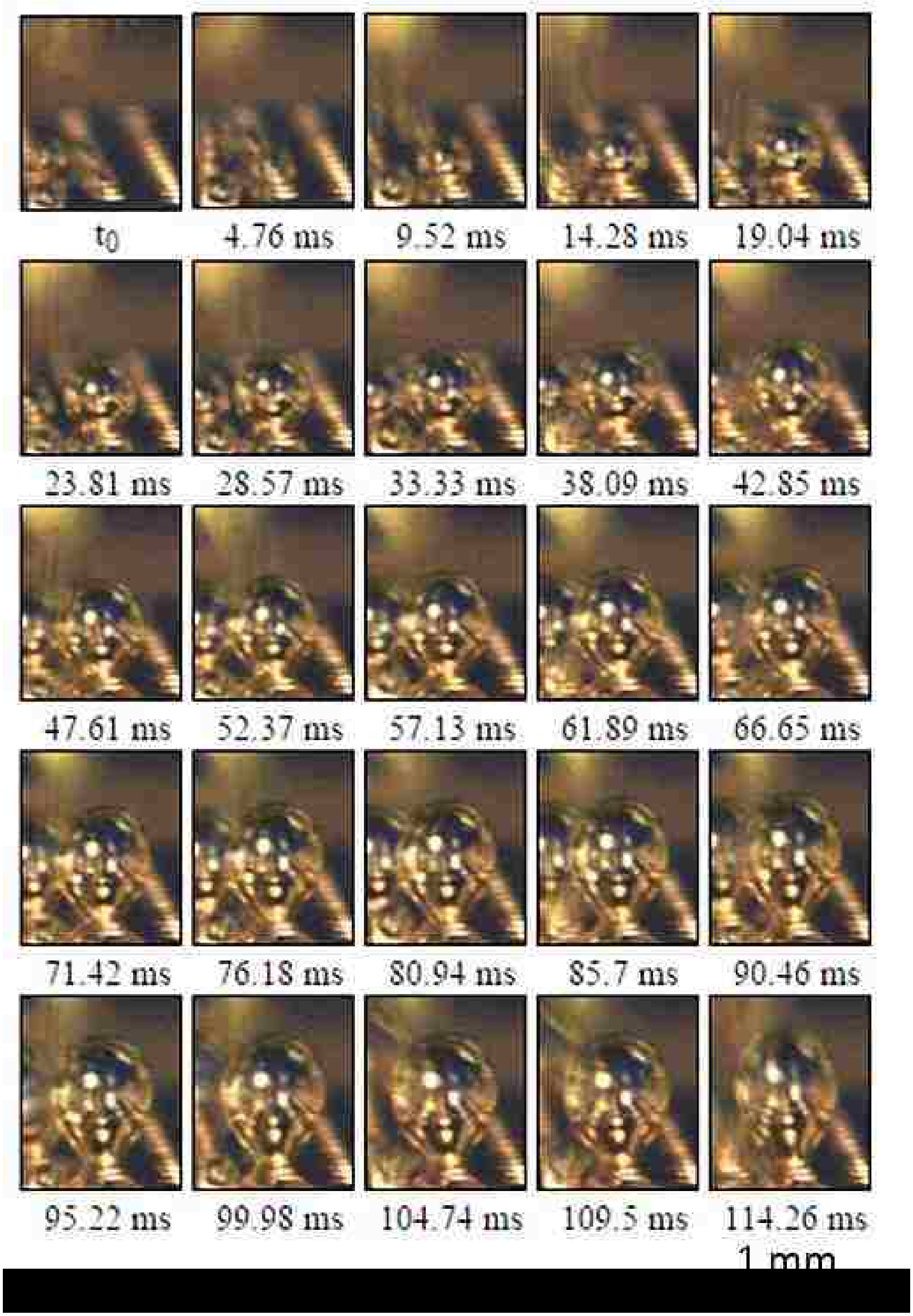

Figure 5.14. A Sequence of images of the transient growth of a single vapor bubble on the Cu surface with 300 μm dimples.

5.5.1 Bubble Growth Measurements

In nucleate boiling on smooth and rough Cu surfaces (McHale and Garimella, 2012; Suszko and El-Genk; 2015), discrete embryos or bubbles nucleate at randomly distributed active sites or crevices, and grow continuously until departure, and typically with almost the same diameter, D_d, and detachment frequency, f_d (Suszko and El-Genk; 2015). On surfaces with artificial cavities, bubbles emanate from the cavities and grow continuously until departure (Hutter el al. 2010), but with different diameters based off the cavity size. On the dimpled Cu surfaces, the growing vapor embryos at active sites along the walls of the dimples coalesce into larger bubbles that grow and depart. Theses coalesced bubbles, termed "dimple bubbles" (and denoted by the asterisk in the nomenclature list), emerge from the dimples, and continue to grow slowly while remaining attached to the surface along the perimeter of the dimples (Figure 5.11– 5.14). They eventually depart with much larger diameters and lower detachment frequencies that those reported for smooth and rough Cu surfaces, or other surface microstructures. (El-Genk and Ali, 2013; Suszko and El-Genk; 2015)(Table 2.2).

Figure 5.11a–g display still photographs of saturation nucleate boiling at PF-5060 at ~0.5 – 1.0 W/cm^2 on the dimpled Cu surfaces. In this figure, the majority of the vapor bubbles that were present on the dimpled surfaces coincide with the location of the individual dimples. These figures show very few small bubbles that infrequently nucleate on the flat portion of the Cu surface between dimples. This is because of the effective heat removal rate by nucleating and growing vapor embryos within the dimples. The flat portions of the Cu surface likely do not attain surface superheats that are high enough to initiate bubble nucleation, while the efficient vaporization process is taking place within the dimples. Therefore, the following sets of measurements presented are of a variety and between 5 – 8 different dimple sites, for each dimpled surface, at an applied heat flux of 0.5 W/cm^2.

The bubble transient volume and diameter were determined from the recorded images. Figure 5.12– 5.14 show a representative set of photographs that were used to measure the transient growth of a single dimple bubble, at a selected site on the (a) 500 μm (b) 400 μm dimpled and (c) 300 μm dimpled surfaces. Figure 5.12– 5.14 and other similar sets of captured photographs on the same surfaces were used to measure the increase of the bubble volume in sequential frames separated by a period of 4.76 ms. In these figures, the arbitrary time, t_0, is that of the first recorded image of the growing bubble as it emerges from the dimple. As shown in Figure 5.12– 5.14, during the early stage of growth ($t_b \leq t_0 + 38.09$ ms), the growing bubbles were spherical, while in the later stage of growth ($t_b > t_0 + 38.09$ ms), the bubbles acquired a pear or an ellipsoid shape. In this stage, the equivalent bubble diameters, D_b^*, are those of spheres of the same volume as those calculated for the symmetrical bubble ellipsoids.

The measured aspect ratio of the ellipsoidal shaped bubbles increased with growth time and peaked at under 1.2, just before bubble departure. This is at $t_b \sim (t_0 + 80.94\text{ms})$ and $\sim (t_0 + 90.22$ ms) in Figures 2 and 3, respectively. On the Cu surface with 300 μm dimples, the growth rate of the bubbles (Figure 5.14) is smaller and the growth time is longer ($t_b > (t_0 + 116.38$ ms)) than on the other dimpled surfaces (Figure 5.12 and 5.13). Owing to the slow growth of bubbles on the dimpled surfaces (Figure 5.12– 5.14), the systematic uncertainty in determining the departure diameter of the bubble, with a conservative assumed aspect ratio of 1.2, is ± 48, ± 57, and ± 51μm for the 300, 400, and 500 μm dimpled surfaces, receptively. These uncertainties depended on the focusing distance of the camera, as well as the image pixel resolution. To improve the statistics of the measured values and reduce their random uncertainty, the bubble growth rate, departure diameter and detachment frequency estimates are obtained from five sets of sequential images of different growing bubbles on the dimpled surfaces.

5.5.2 Bubble Volume Growth

Figure 5.15a–c present the measured bubble volumes, V_b^*, in mm^3, of growing bubbles in saturation boiling of PF-5060 dielectric liquid on dimpled Cu surfaces, versus the transient growth time, t_b in milliseconds (ms), at an applied heat flux of 0.5 W/cm^2. The results presented in these figures are for different bubbles at five different dimples on each surface. The zero time ($t_b = 0$) or t_0, is when the emerging vapor bubble from the dimple was first seen and recorded by the high-speed camera. The sequence of images that followed did not capture the actual bubble departure, but rather those of the growing bubble before. However, the bubble departure is known to occur within a single frame, or

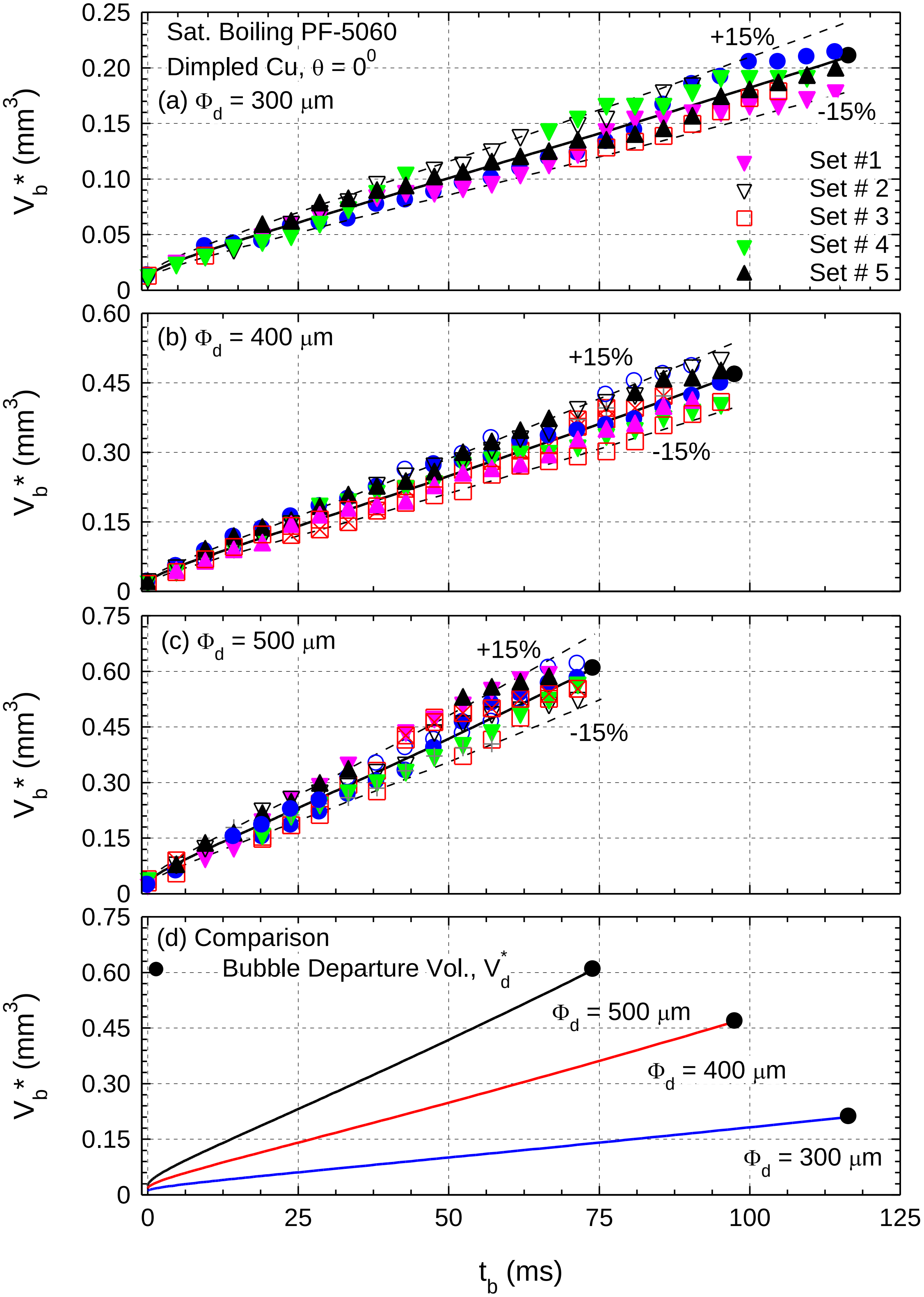

Figure 5.15. Estimates of the transient volumes of the growing bubble in saturation nucleate boiling of PF-5060 on dimpled Cu surfaces at an applied heat flux of 0.5 W/cm^2.

an additional ~4.76 ms, of the last captured image in the full sequence of bubble growth.

The volume of the departing bubble was determined from the measured bubble transient growth rates (Figure 5.15a–c), and was assumed to occur at a time that is ~2.38 ms (or half a frame) beyond that of the last recorded images of the discrete bubbles on the different dimpled Cu surfaces. The estimates of the bubble departure volume, V_d^*, are indicated by the solid black circle symbols in Figure 5.15a–d. These figures show that the bubble growth rate, but also the departure volume, increases with increasing the dimple diameter. The volumetric growth rate of the bubbles on the Cu surfaces with the 300 μm diameter dimples is the slowest, and the bubble volume is the smallest at departure (Figure 5.15c and d), compared to the 400 and 500 μm dimpled surfaces. In addition, the total growth time is much longer than on the other dimpled surfaces (Figure 5.15a,c and d). Conversely, the growth rate and residence time of the bubbles on the Cu surface with 500 μm diameter dimples are the highest and shortest, respectively.

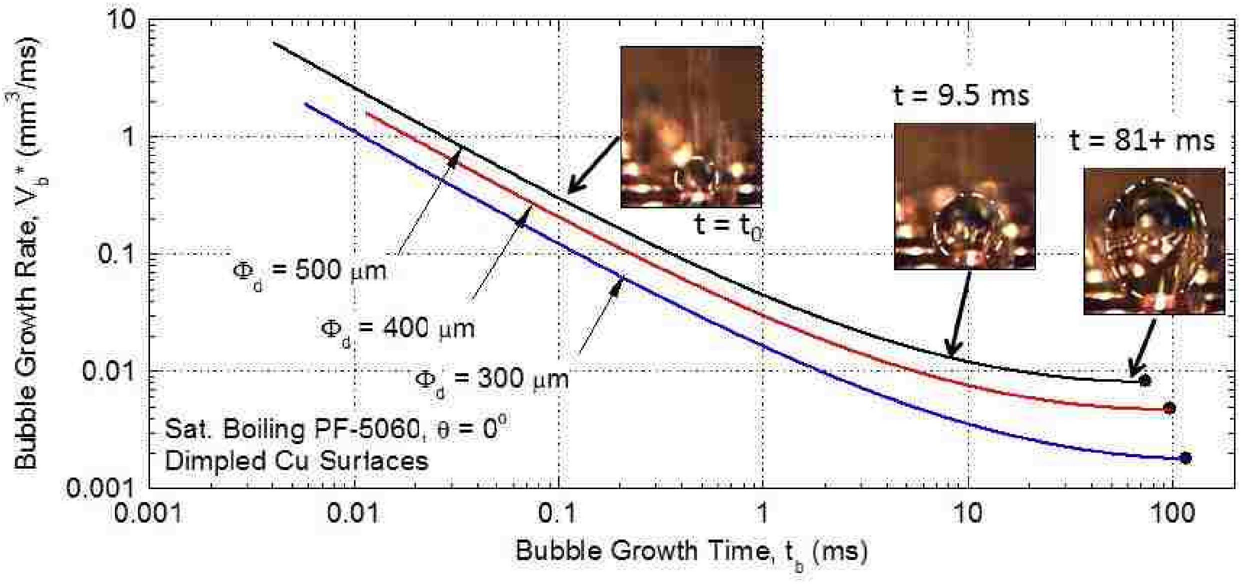

Figure 5.16. Comparison of the volumetric growth rates of vapor bubbles in saturation boiling of PF-5060 dielectric liquid on dimpled Cu surfaces.

Figure 5.16 compares the volumetric growth rates of the bubbles on the different dimpled surfaces. When the bubbles were first seen emerging from the dimple, the growth rate was relatively high and in excess of 1.0 mm^3/ms (or cm^3/s). It quickly dropped within one single frame (or 4.76 ms), to < 0.02 mm^3/ms. Growth rates of the bubbles on the dimpled Cu surfaces continued to decrease, but more slowly as the bubbles approached their departure volumes. The results in Figure 5.16, like Figure 5.15a–d show that the growth rate increases, and the time until bubble departure decreases, with increasing dimple diameter.

5.5.3 Bubble Departure Diameter and Detachment Frequency

The data presented in Figure 5.15a–c were used to calculate the corresponding average spherical bubble diameter of the same total volume. The departure diameter and the detachment frequency of the vapor bubbles on the dimpled surfaces were calculated from the determined growth rates (Figure 5.16), and are of those assumed to occur a time that equals that of the last captured image of the growth cycle, plus half the time between sequential frames (or 4.76/2 = 2.38 ms). Owing to the slight inconsistency in the determined sizes of the bubbles when first emerging from the dimples, there are some variances in the measured growth rates at the different dimples on the same heated Cu surface. This explains the small spread of data in bubble diameter, D_b^*, and detachment frequency, f_d^*, on the same dimpled surfaces (Figure 5.17a–c).

Figure 5.17a–c present the obtained data for growing bubbles from five sequential sets of recorded images of saturation nucleate boiling of PF-5060, on the three dimpled Cu surfaces at an applied heat flux ~ 0.5 W/cm^2. In these figures, the solid black circle symbols indicate the estimated bubble departure diameter and detachment time. Based on the data in Figure 5.17a–c of the transient growth of the vapor bubbles on the Cu surfaces with 300 μm, 400 μm, and 500 μm diameter dimples, the bubble transient diameter, D_b^*, was correlated in terms of the square root of growth time, $t_b^{0.5}$, as:

$$D_b^*(\mu m) = 273 + 43\sqrt{t_b}\ (\Phi_d = 300\ \mu m) \tag{5.6}$$

$$D_b^*(\mu m) = 322 + 64\sqrt{t_b}\ (\Phi_d = 400\ \mu m) \tag{5.7}$$

$$D_b^*(\mu m) = 361 + 80\sqrt{t_b}\ (\Phi_d = 500\ \mu m) \tag{5.8}$$

These correlations, as a function of the growth time, t_b, in milliseconds (ms), are in good agreement with the present data for the 300 μm, 400 μm, and 500 μm dimpled

Cu surfaces, to within ± 5% (Figure 5.17a–c). These figures and Equations (5.6) – (5.8) confirm that the bubble growth rate, departure diameter and detachment frequency on the 500 μm dimpled surface are the highest, followed by those on the surface with 400 μm dimples, and are the lowest on the surface with 300 μm dimples.

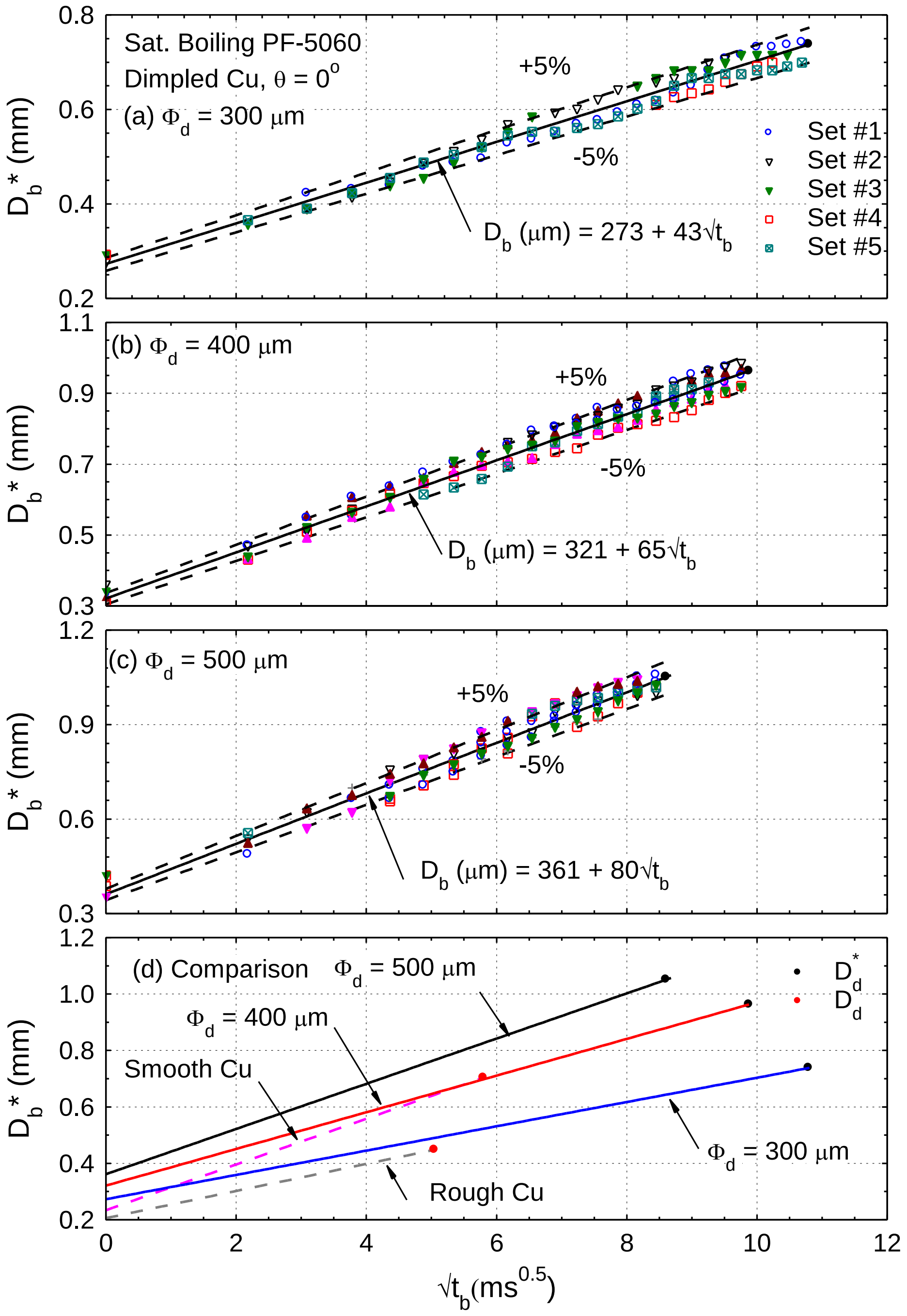

Figure 5.17. Transient growth of vapor bubbles in saturation boiling of PF-5060 liquid on dimpled Cu surfaces.

The first term in Equations (5.6) – (5.8) indicates the approximate size of the vapor bubble when first recorded by the high-speed camera operating at 210 fps. This term is smaller for the smooth and rough Cu surfaces (Equations (4.22a) – (4.22b)), than for the dimpled Cu surfaces. This is because the first recorded images of the growing bubble on the dimpled surfaces are of those that had already emerged from the dimples that are 200 μm deep. It was not possible to capture bubbles the same diameter as the dimple depth. The coefficients in the second term of Equations (5.6) – (5.8) reflect the transient growth rate of the bubbles. A higher coefficient indicates a higher growth rate and vice versa. The coefficient for the bubble growth rate on Cu surface with 500 μm diameter dimples is close to that on the plain smooth Cu (Equation (4.22a)). The bubble transient growth rate on the surface with 300 μm diameter dimples (Equation (5.6)) is only slightly smaller than on the rough Cu surfaces (Equation (4.22a)), but much smaller than those on the other two dimpled surfaces (Equations (5.7) – (5.8)).

Figure 5.17d compares the transient bubble diameters on the different dimpled Cu surfaces with those obtained for saturation boiling on PF-5060 dielectric liquid on smooth and rough Cu surfaces. Unlike the dimpled surfaces, the bubble nucleations on the smooth and rough surfaces occurred at randomly distributed individual sites, and the bubble growth rate, departure diameter and detachment frequency were consistent and highly reproducible. The growth rates of the bubbles on the dimpled Cu surfaces in this work are close, but are not as highly reproducible (Figure 5.15 and Figure 5.17).

Table 5.1. The measured bubble departure diameter and detachment frequency in saturated boiling of PF-5060 dielectric liquid on dimpled Cu surfaces.

Φ_d, N_d, and P/D	γ_d	V_d^* (mm^3)	$\dot{V}_d^*$ (mm^3/s)	Q_d^* (mW)	$\dot{m}_{g,d}$ (μg/s)	$q_{s,d}$ (W/cm^2)	D_d^* (μm)	f_d^* (Hz)
300 μm, 295, 2.0	0.85	0.21	1.81	1.99	21	1.01	738 ± 61	8.6 ± 0.7
400 μm, 149, 2.0	0.64	0.47	4.75	5.24	54	2.08	963 ± 75	10.2 ± 1.0
500 μm, 105, 2.0	0.53	0.61	8.2	9.02	94	2.8	1051 ± 73	13.5 ± 1.8

On the dimpled surfaces, the departure diameter, D_d^*, and detachment frequency, f_d^*, (Figure 5.17d and Table 5.1) are much larger than those (D_d and f_d) on smooth and rough Cu surfaces (Table 4.1) at the same applied heat flux. The determined values of D_d^* and f_d^* for saturation boiling of PF-5060 dielectric liquid on the Cu surface with 300 μm diameter dimples are 738 $\pm$ 61 μm and 8.6 $\pm$ 0.7 Hz, respectively. These are smaller than the determined 963 μm $\pm$ 75 μm and 10.2 $\pm$ 1.0 Hz on the Cu surface with the 400 μm diameter dimples, and 1051 $\pm$ 73 μm and 13.5 $\pm$ 1.8 Hz, on the surface with the 500 μm diameter dimples (Table 5.1). These detachment frequencies are much smaller than those reported on smooth (~31 Hz) and on rough Cu (~38 Hz) surfaces (Table 4.1), for the same dielectric liquid and applied heat flux.

5.5.4 Number of Active Dimples

Based on the experimental observations and detailed examination of the recorded images of nucleate boiling on the dimpled Cu surfaces, only a fraction, γ_d, of the total dimples, N_d, contributed to bubble generation and growth at the applied heat flux of 0.5 W/cm^2. This fraction depends on the diameter of the dimples, whose total number decreases with increasing the dimple diameter (Table 5.1). The determined fraction of active dimples from the present experimental results can be expressed as:

$$\gamma_d = \left(\frac{qA}{q_d^* N_d}\right) \tag{5.9}$$

In this equation, q is the applied heat flux (0.5 W/cm^2), A is the footprint area of the heated surface (1.0 cm^2), and the amount of thermal power removed from the surface by a single departing bubble from an active dimple is given as:

$$q_d^* = V_d^* f_d^* \rho_g h_{fg} \tag{5.10}$$

The fraction of the active dimples on the surface with the 300 μm diameter dimples of ~0.85 is highest, and decreases to ~0.64 and ~0.53 for the Cu surfaces with 400 and 500 μm diameter dimples, respectively (Table 5.1). These fractions are supported by images such at the one shown in Figure 5.18, that show the 300 μm dimpled surface to have far more bubble activity than the 500 μm dimpled surface, at the applied heat flux of 0.5 W/cm^2. Conversely, the amount of thermal power removed (~0.9 mW) by a single bubble from a 500 μm-diameter dimple is ~72% higher than of that removed from a 400 μm-diameter dimple, and as much as 4.5 times that removed from a 300 μm-diameter

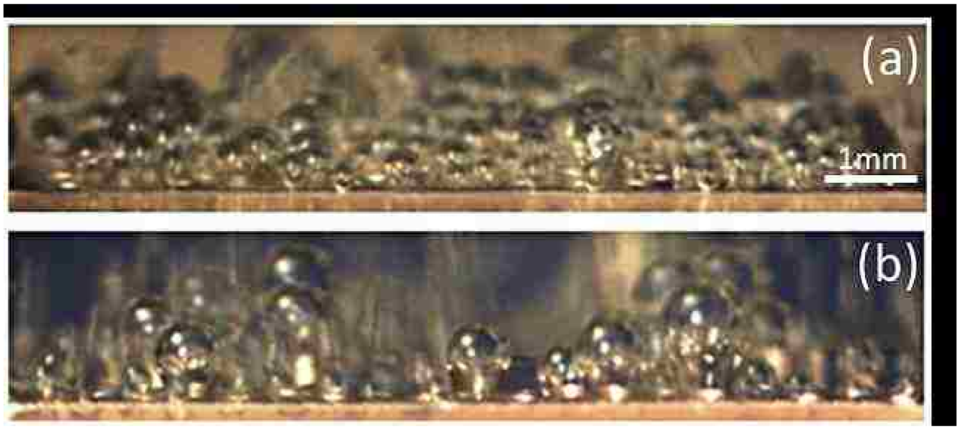

Figure 5.18. Images of growing vapor bubbles at dimple cavities in saturation nucleate boiling of PF-5060 on uniformly heated Cu surfaces with (a) 300 μm and (b) 500 μm diameter dimples, at 0.5 W/cm^2.

dimple. These numbers explain why the volume of the departing bubbles, V_d^*, on the 500 μm dimpled Cu surface, are much larger than on both the 400 and 300 μm dimpled surfaces (Figure 5.12– 5.14and Table 5.1). In addition, the growth rate of the bubbles, V_b^*, on the 500 μm dimpled surface is also much higher than on the 300 and 400 μm dimpled surfaces (Figure 5.16 and Table 5.1).

Figure 5.16 compares the transient volume growth of the bubbles on the different dimpled Cu surfaces. Beyond the first 4 frames recorded (>19 ms), and for the majority of the growth cycle, the transient bubble volumetric growth rate decreased very little. Thus, the growth rate of the bubble volume may be assumed constant and equal to that at bubble departure, as:

$$\dot{V_b}^* \approx \dot{V_d}^* = \frac{\dot{m}_g}{\rho_g} \tag{5.11}$$

The rate of vapor generation in this equation that supports the growth of the dimple bubble is given as:

$$\dot{m}_g = \frac{\pi}{6}(D_d^*)^3 f_d^* \rho_g \tag{5.12}$$

` The average heat flux at the inside surface of an active dimple cavity is given as:

$$q_{s,d} = \left(\frac{\dot{m}_g h_{fg}}{A_d^*}\right) = \frac{\pi}{6}(D_d^*)^3 \frac{f_d^* \rho_g h_{fg}}{A_{s,d}} \tag{5.13}$$

The results listed in Table 5.1 show that the volumetric bubble growth and vapor generation rate for a single dimple bubble are the highest for the Cu surface with 500 µm diameter dimples, and decrease with decreasing the dimple diameter. Conversely, the average heat flux on the inside surface of the dimple, $q_{s,d}$, decreases from ~2.8 W/cm^2 for the 500 µm-diameter dimple, to ~2.08 and ~1.01 W/cm^2 for the 400 µm and 300 µm-diameter dimples, respectively (Table 5.1).

5.5.5 Discussion

The visualization and analysis of saturation nucleate boiling of PF-5060 dielectric liquid on dimpled Cu surfaces at applied heat flux of 0.5 W/cm^2, confirm that the majority of the growing bubbles are associated with dimple cavities (Figure 5.8 and Figure 5.18), but their growth rate, departure diameter and detachment frequency, strongly depends on the diameter of the dimple. Very few bubble nucleations ensued on the flat potions of the heated Cu surfaces between dimples, since it was difficult for these portions to reach a high enough surface superheat to initiate bubble nucleations, with evaporation occurring at the dimples. The insides of the manufactured dimples were closer to the underlying heating element, and thus reached higher wall temperatures to initiate bubbles nucleation.

Thus, the nucleation of vapor embryos occurs on the inside surface of the dimples (Figure 5.19a). Once initiated, the flow of heat with in the surface diverts away from the flat portions of the heated Cu surface, to the dimples with active evaporation (Figure 5.20). Close examination of the captured images of the dimple bubbles at 210 fps (Figure 5.12 - Figure 5.14), show that following the bubble departure, the bulk liquid from the pool rushed to flood the dimple. Following a short waiting period to develop the thermal boundary layer, bubble nucleation ensued on the inside surfaces of the dimple cavities (Figure 5.19h).

The bubbles emerging from the dimple cavities grow due to the evaporation at the vapor-liquid interface, and most importantly at the solid-vapor-liquid triple interface along the perimeter of the dimples that marks the extension of the liquid microlayer (Figure 5.20). Another possible important contributor to the growth of the dimple bubbles

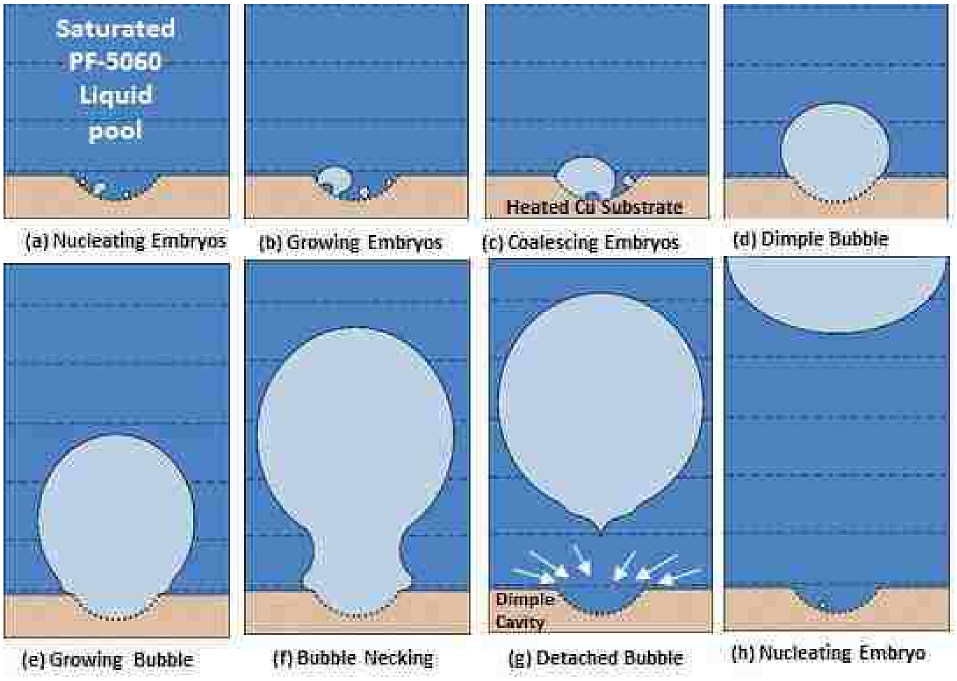

Figure 5.19. Illustrations of sequential frames depicting nucleation and growth of vapor embryos inside a dimple, coalescence into a dimple bubble, and bubble growth and eventual detachment.

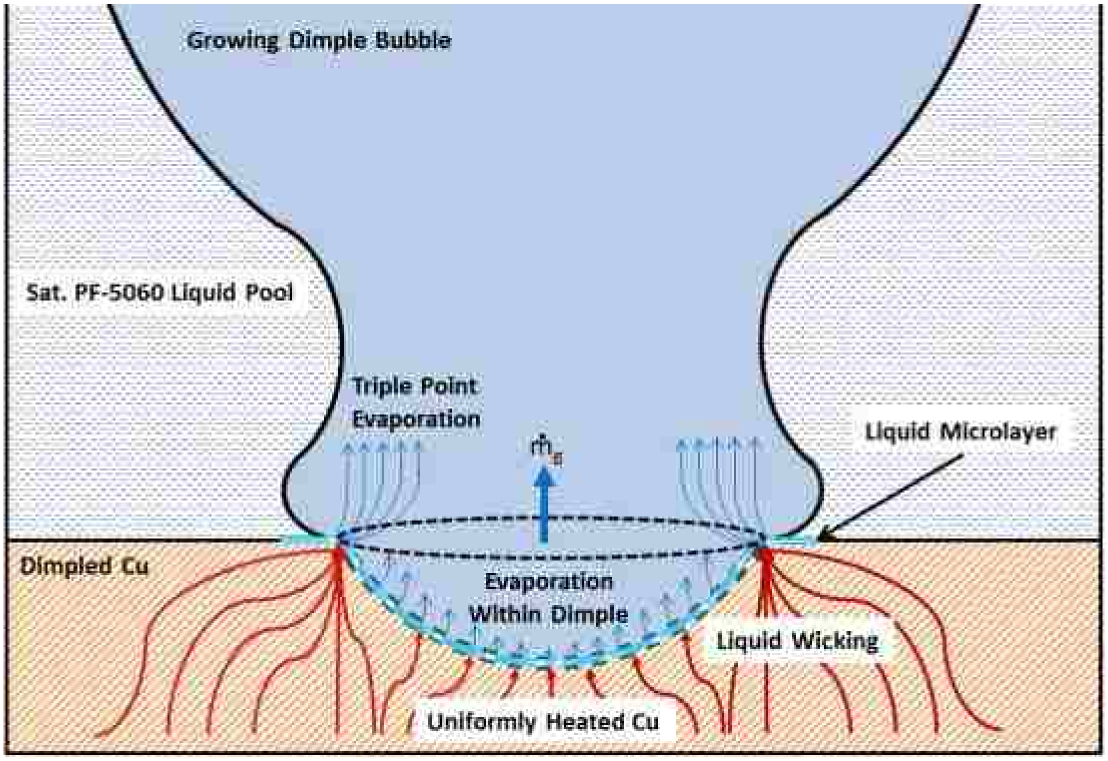

Figure 5.20. An Illustration of the growing bubble from a circular dimple. The total vapor generation depends on liquid evaporating at the triple interface along the perimeter of the dimple, as well as within the dimple from liquid wicking.

is the evaporation of thin liquid film on the inside surface of the dimple cavities. The liquid drawn into the cavities from the pool, by the wicking action of the rough inside surface of the dimples, replenishes this thin liquid film (Figure 5.20).

All fabricated dimples in this work are of the same depth, 200 μm, but have diameters of 300, 400, and 500 μm. The growth rate, departure diameter and detachment frequency of the dimple bubbles are different and depend on the dimple diameter (Table 5.1). In addition, the CHF and the surface average nucleate boiling heat transfer coefficient, h_{NB}, are different. Figure 5.4 shows that CHF and h_{NB} for the Cu surfaces with 400 μm and 500 μm dimples are close, but much higher than on the surface with the 300 μm diameter dimples.

The CHF may occur when the thickness of the liquid film on the inside of the active dimples decreases and stops replenishing the dimple surface with liquid from the surrounding liquid pool (Figure 5.20), causing a dryout. Since the rate for liquid replenishment depends on the depth and the perimeter, or the diameter of the dimple, the CHF is the lowest for the Cu surface with the smallest (300 μm) diameter dimples that have the lowest diameter-to-depth ratio of 1.5. This ratio is 2.0 and 2.5 for the dimples with diameters of 400 μm and 500 μm, for which the CHF values are the highest (Figure 5.4), but very close, suggesting that liquid replenishment of PF-5060 or other similar dielectric liquids may be at its maximum for any dimple or cavity diameter-to-depth ratios of ≥ 2.0.

In addition, the rate of vapor generation at the triple interface along the perimeter, and inside of the active dimples (Figure 5.20 and Table 5.1) increases proportional to the diameter of the dimple. The experimental data depicted in Figure 5.15 and Figure 5.17 confirm this dependency. The dimple bubble volumetric growth rate relates directly to the total rate of vapor generation, which accumulates inside the growing dimple bubble (Figure 5.20). The results (Table 5.1) show that the total vapor generation rate and the volumetric growth rate of the dimple bubbles, increases with increasing the dimple diameter. They are the highest at ~94 μg/s and ~8.2 mm^3/s, respectively, for the 500 μm-diameter dimples, and the lowest at ~21 μg/s and ~1.81 mm^3/s, respectively, for the 300 μm diameter dimples. These results suggest that the major contributors to the growth of the dimple bubbles are likely the evaporation at the triple interface, along the perimeter of the dimples, and of the thin liquid film on the inside the surface of the dimples (Figure 5.20). The average heat-flux on the inside of the large 500 μm diameter active dimple is the highest at ~2.8 W/cm^2, and the triple interface along its perimeter is the longest, and the combination of the two provide the highest vapor generation rate.

The inertia force exerted on the top portion of the surface of a growing dimple bubble directly relates to the rate of evaporation, which is highest from the large diameter dimples (Table 5.1), causing the bubbles to grow faster to larger sizes in the short time before departure. This explains the results presented in Figure 5.15 and Figure 5.17, and listed in Table 5.1. The figures show the departure diameter and detachment frequency of the dimple bubble, as well as the growth rate and time to departure, increase with increasing the diameter of the dimples. In addition, the amount of heat removed from the heated Cu surface by a departing dimple bubble, increases with increasing the dimple diameter (Equation (5.13)), and are ~1.99, ~5.24 and ~9.02 for the 300, 400, and 500 μm-diameter dimples, respectively.

The departure diameter of the dimple bubble is largely dependent on the surface tension force that holds the bubble down along the triple point rim of the dimple (Figure 5.20). A force balance of the surface tension (Table 2.1) force holding the bubble down and buoyant force pushing the bubble upward, is at equilibrium for bubble diameters of 984 μm, 1084 μm, and 1167 μm for the 300 μm, 400 μm, and 500 μm dimples, respectively, in saturation nucleate boiling of PF-5060 dielectric liquid. These numbers are not far off from the measured departure diameters of ~738 μm, ~962 μm, and ~1052 μm for the 300 μm, 400 μm, and 500 μm dimples, respectively. The force balance over predicts the departure diameter because it does not include the additional drag and viscous terms that were present in the experiments, but unable to be measured, as well as well as circulation from natural convection. Nevertheless, the force balance involving only the surface tension and buoyant forces still provides for a good ball park estimate, for the departure diameter of the dimple bubble in saturation nucleate boiling of PF-5060. The detachment frequency was a subsequence of the physics that governed the departure diameter, as well as bubble growth rate, discussed previously.

5.5.6 Summary

The transient growth of the dimple bubbles in saturation nucleate boiling of PF-5060 on surfaces with 300 μm, 400 μm, and 500 μm dimples were measured at an applied heat flux of ~0.5W/cm^2, using a high speed video camera that operated at ~210fps. The dimple bubbles were observed to have a much different growth rate, larger departure diameter, and slower departure frequency than of the smooth and rough Cu surfaces. The determined values of D_d^* on the dimpled Cu surfaces are ~738 μm, ~962 μm, and ~1051 μm for the 300 μm, 400 μm, and 500 μm dimpled surfaces, The corresponding values of f_d^* are ~8.6 Hz, ~10.1 Hz, and ~13.5 Hz, respectively.

The transient growth rate of the dimple bubbles is dictated by the dimple spacing along the Cu surface, which determined how many dimples were present on the surface, and subsequently how much heat each dimple received from the underlying heating element. Each individual dimple site on the 500 μm surface received the most heat (compared to the 300 and 400 μm surfaces), and as a result had the fastest bubble growth rate. Conversely, the 300 μm surface had the smallest dimple spacing, and slowest bubble growth rate. Thus, it is concluded that the local heat flux has a direct relationship on the growth rate of the vapor bubble.

The dimple bubble departure diameter is largely based off the force balance between surface tension force holding the bubble down along the rim of the dimple, and buoyant force pushing the bubble up. The detachment frequency is a subsequence of the transient growth rate and bubble departure diameter.

The departure diameter and detachment frequency measurement were used to estimate the number of active dimple sites along the surface. The estimations of partial boiling activity of ~85%, ~64%, ~53% of the 300 μm, 400 μm, and 500 μm dimpled surfaces, respectively, were supported by the high speed captured images. In the next chapter, experimental results are utilized in a computational analysis of advanced composite heat spreaders, aimed at enhancing the total power removed by a spreader in immersion cooling by saturation nucleate boiling of PF-5060 for the upward facing orientation.

6. Thermally Anisotropic Composite Heat Spreaders for Immersion Cooling of High Powered Microprocessors

This chapter presents the investigation of the performance of thermally anisotropic composite heat spreaders, for enhanced thermal management of high performance microprocessors. The composite spreaders are comprised of 0.5 mm-thick Copper (Cu) laments separated by a thin (δ = 0.25 – 1.0 mm) layer of thermally anisotropic material, such as graphite or highly oriented pyrolytic graphite (HOPG). The exposed rough Cu surface (Ra = 1.79μm) of the top Cu lament is cooled by saturation nucleate boiling of PF-5060 dielectric liquid, and subject to a maximum allowed local heat flux of 90% CHF, and minimum surface temperature of $\geq$ 1^{o}C boiling incipience, of that obtained in the experiments. The 20 x 20 mm underlying chip generates uniform power, or has a number of hot spots with local heat flux ratios up to 10. The analyses quantified the effect of the Figure-of-Merit (*FOM*) of the composite spreader, on the total thermal power removed by nucleate boiling, the spreader's thermal resistance, and the maximum temperature of the underlying 20 x 20 mm chip.

The composite spreaders remove 6 – 400% more power than an all Cu spreader, depending on the *FOM*. The total thermal resistances, defined as the summation of the individual resistances from the thermal interface material, heat conduction through the composite spreader, and of nucleate boiling at the spreader surface, range from 0.16 – 0.4 ^{o}C/W, depending on the thickness and properties of the thermally anisotropic layer, as well as the spreader size. The presence of the thermally anisotropic layer was found to minimally impact the effects of central and multiple chip hot spots with heat flux ratios as high as 10, on the maximum chip temperature. Additionally, oxidized or aged Cu surfaces showed little degradation for consideration of long term cooling performance.

6.1 Background

Microprocessors have substantially increased transistors density and total power dissipation and the over the past two decades, owing to the growth in complexity, performance, and parallelization of computational systems. Currently, the thermal design power (TDP) requirements are upwards of 150 W for central processing units (CPUs)

(AMD, 2015; Intel, 2015) and 250 W for graphics processing units (GPUs) (AMD, 2015; Nvidia, 2015). These power dissipation levels, representing over two orders of magnitude increase in the TDP of CPUs over the past two decades, and 500% increase for GPUs over the past decade, are expected to continue rising. Power densities for these chips are approaching on the order of ~100 W/cm^2, with surface hot spots of local heat fluxes that may reach 3 – 8 times higher than of the chip surface average (Wei, 2008). The high local temperatures at the hot spots and the induced temperature differentials cause thermal stresses that could reduce the serviceable life of the chip (Wu et al. 2002; Semenov et al. 2006).

The rapid increase in the total power dissipation and density of microprocessors has stimulated an evolution of cooling methods that are capable of removing the larger amounts of dissipated thermal power, while keeping the maximum junction temperature below $T_{j,max}$, typically 85 – 115^{o}C, depending on the application (ITRS, 2013). As the total power dissipation and density of microprocessors continues to increase, more advanced methods of cooling such as immersion pool and flow nucleate boiling, jet impingement, and spray cooling, are increasingly being considered. Among these methods, immersion pool nucleate boiling offers many advantages for the cooling of high power microprocessors. These include uniform surface temperatures, large scale cooling capability, effective mitigation of chip hot spots (El-Genk and Ali, 2013) and low thermal resistance (El-Genk and Saber, 2008; El-Genk and Ali, 2013). Additionally, using low saturation temperature dielectric liquids, such as the Fluorinert FC-72 (T_{sat} = 56^{o}C at ~ 0.1 MPa), the performance Fluid PF-5060 (T_{sat} = 56^{o}C at ~0.1 MPa), or the Novec HFE-7000 (T_{sat} = 34 ^{o}C at 0.1 MPa), (3M, 2015) help keep $T_{j,max}$ below recommend values by the manufacturers (El-Genk and Saber, 2008; El-Genk and Ali, 2013; ITRS, 2013). Other studies have reported that two-phase cooling has the potential to reduce the energy consumption for large datacenters as much as ~50% (Olivier et al. 2010; Marcinichen et al. 2012), and save floor space (Tuma, 2010) compared to using refrigerated air.

In immersion nucleate boiling cooling, the processor package that includes a heat spreader and the underlying chip is submerged in a pool of dielectric liquid. The dissipated heat by the underlying chip is removed from the exposed surfaces of the spreader by nucleate boiling. However, the maximum heat flux at the exposed surface needs to be at a sufficient margin below the critical heat flux (CHF). CHF depends on the thermophysical properties of the dielectric liquid, and the material properties and surface characteristics of the heat spreader. The CHF, indicative of the departure from nucleate boiling, is associated with a large surge in temperature that will damage the microprocessor. Thus, it is a design constraint for immersion nucleate boiling cooling of high powered chips, and could limit the heat a chip may safely dissipate.

Increasing the amount of heat removed by nucleate boiling requires enhancing the heat transfer coefficient and CHF, and / or increasing the wetted surface area. Experimental results for pool boiling of dielectric liquids have shown that microstructured, micro- and macro-finned, rough, microporous surfaces and surfaces with microporous coatings (Rainey and You, 2000; Yu et al. 2006; Arik and Bar-Cohen, 2007; El-Genk 2003, 2012; El-Genk and Parker, 2008; El-Genk and Suszko, 2014) enhance both nucleate boiling and CHF. Despite the increases in the nucleate boiling heat transfer coefficients on these surfaces, in immersion nucleate boiling cooling of high power microprocessors, the total power dissipated by the underlying chip and removed from the exposed surfaces of the spreader also largely depend on the conductance for lateral heat spreading.

A numerical investigation of immersion cooling of computer chips by nucleate boiling of PF-5060 dielectric liquid, using 1.6 – 3.2 mm thick Copper (Cu) spreaders with 85 – 230 μm thick surface layers of microporous Cu (MPC) was recently reported by El-Genk and Ali (2013). The MPC surface layer, deposited using conventional electrochemical processes at room temperature, enhances both nucleate boiling and CHF. In this work, the MPC coated spreaders were capable of removing > 85 W of dissipated thermal power by an underlying 10 x 10 mm chip, while keeping its maximum chip temperature well below 100°C. However, the removed powers by the spreaders in this study were not limited by $T_{j,max}$, but by the limited heat spreading of the underlying Cu substrate and maximum allowed surface heat flux of 90% CHF.

In a study by Campbell and Tuma (2012), the results showed that immersion cooling of bare chips (no heat spreading) by pool nucleate boiling of FC-72 liquid could only remove up to 4 W of dissipated power and operated near CHF, and thus determined the mode of cooling to be too limiting for future generations of higher power chips.

Olivier et al. (2011) mentioned CHF to be a design constraint for a two-phase thermosyphon cooling high powered chips, and noted a minimum pumping requirement to avoid it. Revellin et al. (2008) experimentally showed that surface underlying hot spots, with local heat fluxes $\geq$ 200 W/cm^2, significantly decreased the surface mean heat flux before CHF was triggered.

El-Genk and Saber (2008) investigated the cooling performance of composite heat spreaders for underlying 10 x 10 mm computer chips with uniform and non-uniform power dissipation. These spreaders were comprised of a Cu substrate with varying thickness, and a thin surface layer of porous graphite, cooled by saturation or subcooled nucleate boiling of FC-72 dielectric liquid. The results showed that, even though porous graphite enhances nucleate boiling and CHF (El-Genk and Parker, 2008) , the isotropic thermal conductivity of the Cu substrate limited lateral heat spreading, which limited the surface area cooled by nucleate boiling, and hence the total removed. The composite spreader with a surface area of 4.9 cm^2 removed a maximum of ~72 W thermal power dissipated by the underlying chip. Additionally, the poor heat spreading of porous graphite only spreaders further limited the total power removed to < 51 W. (El-Genk and Saber, 2008).

Lateral spreading of the heat dissipated by the underlying high power chips is important because the chip dissipation heat flux (~50 W/cm^2) (Intel, AMD, Nvidia, 2015), is much higher than that for nucleate boiling of dielectric liquid on the exposed surfaces of the spreaders (15 – 30 W/cm^2) Rainey and You, 2000; Yu et al. 2006; Arik and Bar-Cohen, 2007; El-Genk, 2003, 2012; El-Genk and Parker, 2008; El-Genk and Suszko, 2014) (Chapters 4 and 5). The problem with the traditional Cu based heat spreader for immersion nucleate boiling cooling, is that local surface heat fluxes approach that of the (experimental) CHF (and typically at the center) long before the majority of the spreader may become efficient in removing power through boiling. Because nucleate boiling heat transfer coefficients are very temperature sensitive, heat spreaders suffer a problem analogous to corner pinned surfaces and the “fin effect” (Rainey and You, 2000, El-Genk and Parker, 2008, Figure 6.1a). Boiling efficiency decreases moving laterally away from the heat source, along the surface of a heat spreader (Figure 6.1b), much like it does moving along the extension of a pin (Figure

6.1a). Thus, in immersion nucleate boiling cooling of microprocessors, with power dissipations that may reach or exceed 150W (Intel, AMD, Nvidia, 2015), enhancing lateral spreading of the dissipated thermal power is necessary. Hence, there is a need to investigate heat spreaders with not only exposed surfaces for enhancing nucleate boiling, but also materials for enhancing lateral heat spreading.

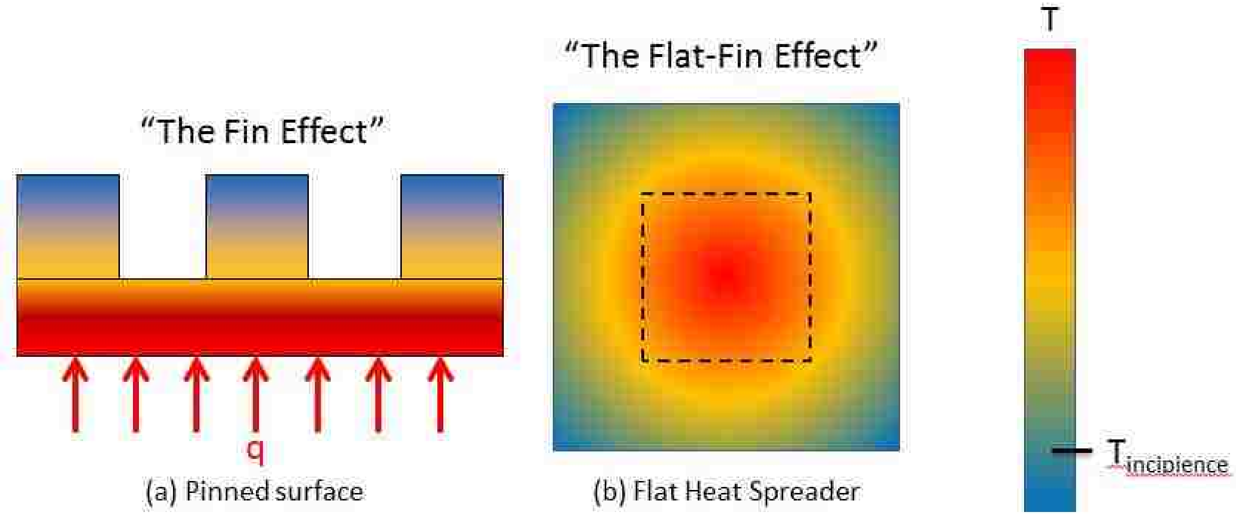

Figure 6.1. The rapid decrease of surface temperature moving away from the center of a flat heat spreader causes a loss in boiling efficiency analogous to the fin-effect for corner pinned surfaces subjected to a uniform heat flux.

In order to effectively dissipate more power through immersion cooling by nucleate boiling, thermally anisotropic materials may be used within the spreaders themselves. Surveys on materials for cooling of high power electronics, conducted by Zweben (2006) and Coppola et al. (2007), list highly ordered pyrolytic graphite (HOPG) as a "third generation" heat sink material. HOPG is very highly anisotropic in its thermal conductivity. The very high in-plane (k_x) thermal conductivity and low through-plane (k_z) conductivity, along with commercial availability makes HOPG the prime candidate for enhancing the heat spreading of a heat spreader. Encapsulated HOPG is already being used in ground-based radars and aerospace printed circuit board heat sinks (Zweben, 2005). A brief background on how HOPG is produced is discussed next.

Pyrolytic graphite (PG) is produced by heating a hydrocarbon over a graphite substrate to its decomposition temperature - generally above 2000^{o}C. This results in the

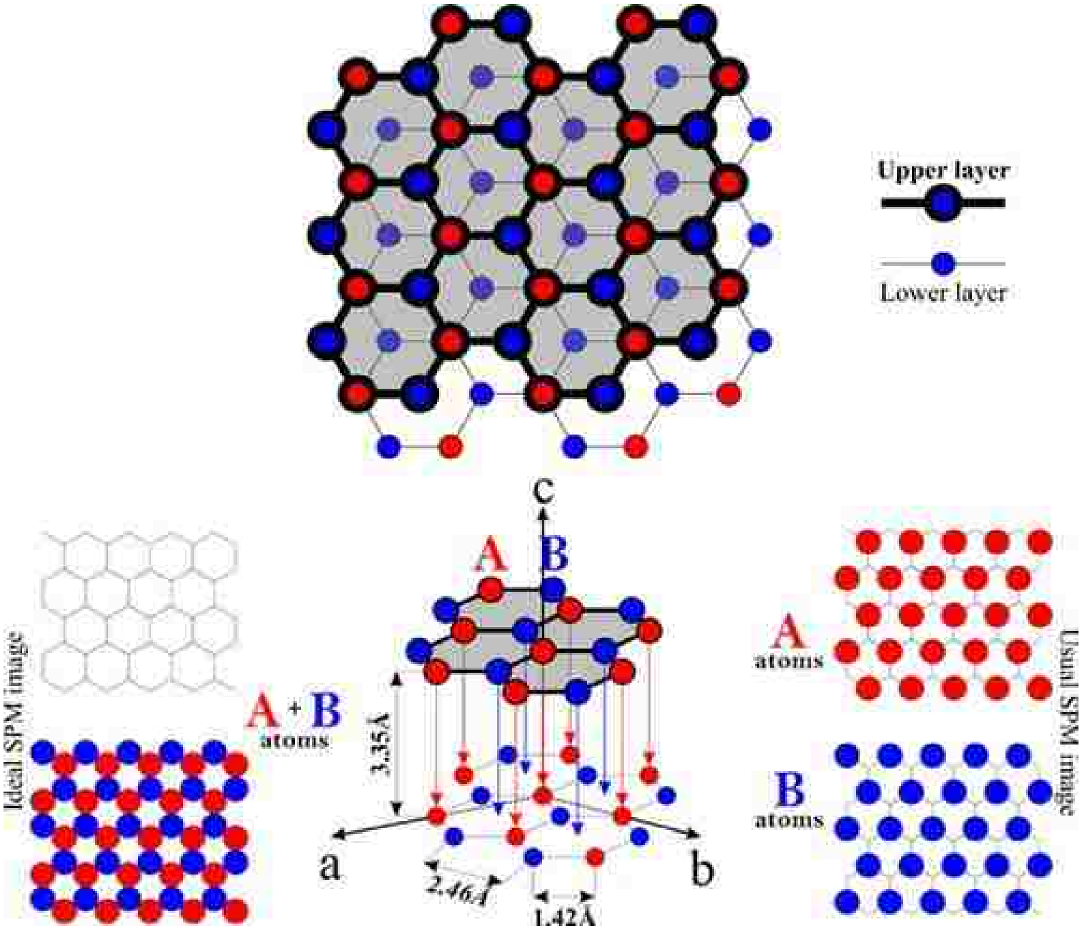

Figure 6.2. A schematic of the bulk hexagonal graphite crystal (http://nanoprobes.aist-nt.com/apps/HOPG%20info.htm)

graphite crystallites orienting their c-axes normal to the bulk substrate. To better the alignment of crystallites, PG is hot worked under a compressive stress of 300 – 500 kg/cm^2 at 3000^{o}C. Subsequent annealing at 3500^{o}C produces HOPG (Chung, 2002). HOPG contains a high degree of preferred crystallographic orientation perpendicular to its A-B plane (Figure 6.2), and as a result is extremely anisotropic. Along the c-axis (Figure 6.2), HOPG acts as an insulator with a low thermal conductivity, k_z, that ranges from 5 – 20 W/mK. In the A-B plane, HOPG acts a super conductor, with a thermal conductivity, k_x, that ranges from 1000 – 2000 W/mK (Slack 1962, Klein 1964, Taylor 1965, Tong 2011) Additionally, by reducing the number of layers of HOPG, researchers have produced multi-layer graphene as well as single layer graphene, and have reported basal plane thermal conductivities as high as ~5500 W/mK (Ghosh et al. 2009, Balandin et al. 2008).

Because HOPG is expensive and has a high cost to performance ratio (Droefnik and Kolar, 2006), a cheaper alternative, such as graphite, may also be considered. Like HOPG, graphite is thermally anisotropic. Graphite has been investigated for the cooling of electronics devices ranging from microprocessors, to small hand held devices, hard drives, and even large devices such as plasma screen televisions (Smalc et al. 2005, Shooshtari et al. 2006, Xiong et al. 2008).The anisotropic thermal conductivity of the graphite has been shown to mitigate the magnitude of hot spots, as well as increase cooling performance for some devices. Smalc et al. (2005) showed graphite to mitigate the temperature gradient of a hard drive from 11.1 to 2.9^{o}C. Xiong et al. (2008) showed a high grade graphite to reduce the hot spot temperature of a hand held device by over 20^{o}C. In a numerical investigation by Gao et al. (2013), a graphene based heat spreader was found to reduce the hot spot temperature by 13^{o}C for a microprocessor.

The objective of the present work in this chapter is to conduct 3-D numerical analyses to investigate the performance of thermally anisotropic composite spreaders with a rough Cu surface, cooled by saturation nucleate boiling of PF-5060 dielectric liquid, for enhanced thermal management of a 20x20 mm high performance microprocessor chip. The composite spreaders are comprised of two 0.5 mm-thick Cu laments separated by a thin layer ($\leq$ 1.0 mm) of thermally anisotropic material, such as graphite or HOPG. The analyses quantify the effects of the thickness and thermal conductivities (k_x = 325 – 2000 W/mK, and k_z = 5 – 20 W/mK) of the anisotropic layer on the total thermal power removed by nucleate boiling from the exposed rough Cu surface, the total thermal resistance, and the maximum temperature of underlying chip.

The exposed rough Cu surface of the spreader is assumed to have a Ra = 1.79 µm. As shown in Chapters 2 and 4, rough surfaces enhance nucleate boiling and CHF of dielectric liquids, and are scalable for manufacturing. The analyses limit the maximum heat flux and the minimum surface temperature of the spreader, to 90% of CHF and $\geq$ 1^{o}C higher than that at boiling incipience, respectively. The performed numerical analyses varied the thickness of the thermally anisotropic layer from 0.25 to 1.0 mm, and investigated underlying chips with uniform heat dissipation, and with a 0.5x0.5 mm and 1.0 x 1.0 mm central and multiple hot spots. The local heat fluxes at the hot spots are 5.0 and 10 times that of the chip average (HFR = 5, 10), respectively.

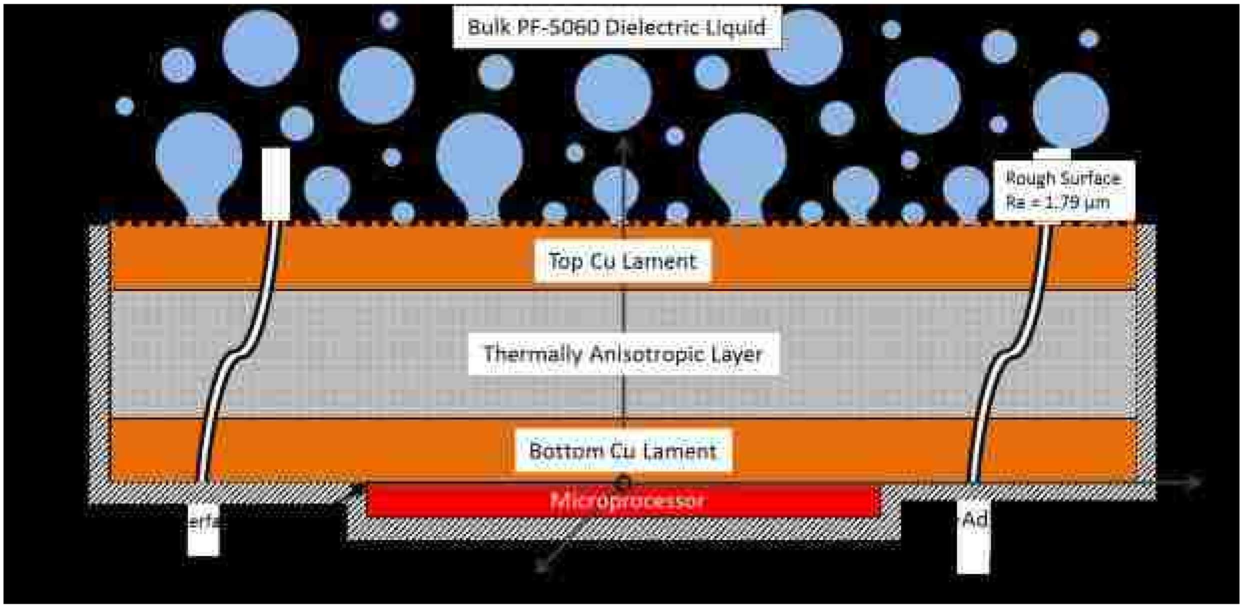

Figure 6.3 A schematic of the HOPG embedded Cu heat spreader cooled by saturated nucleate boiling of PF-5060 with relevant boundary conditions listed.

6.2 Problem Statement

Figure 6.3 is a schematic of the composite heat spreader, comprised of a thermally anisotropic layer that represents materials like graphite or HOPG. This layer varies from 0.25 to 1.0 mm thick, and is between two Cu laments with fixed thickness (0.5 mm), that provide the layer with protection from handling, packaging, and use. The exposed surface of the top Cu lament has an average roughness of 1.79 µm, and is cooled by saturation nucleate boiling of PF-5060 dielectric liquid. The thermal interface material (TIM) between the bottom Cu lament and the underlying chip (Figure 6.3) is a 0.5 mm thick low melting point solder alloy (Koide et al. 2006) with an assumed thermal conductivity of 40 W/mK, which provides a low thermal resistance of ~0.03 K/W.

The thermally anisotropic layer is used to enhance the lateral spreading of the heat dissipated by the underlying chip, thus increasing the spreader surface area as well as the total thermal power removed. An increase in the thermal power dissipated increases the chip surface temperature, which investigated in this work. The thermal conductivities of the anisotropic layer in the lateral direction, k_x, is varied from 325 to 2000 W/mK, while that in the axial direction, k_z, is much smaller, varying from 5 – 20 W/mK. In addition to the higher thermal conductivity in the lateral direction, increasing the thickness of the thermally anisotropic layer, δ, would enhance heat spreading. To account for the different variables in the analyses, a Figure-of-Merit (*FOM*) is defined as:

$$FOM = \frac{k_x}{k_z}\delta^2 \tag{6.1}$$

The *FOM* is proportional to the square of the thickness of the thermal anisotropic layer and has units of area. It is the ratio of the axial through-plane thermal resistance, R_z, to the lateral in-plane thermal resistance, R_x, of the thermally anisotropic layer (Figure 6.3), multiplied by the exposed surface area cooled by nucleate boiling, w^2, as:

$$FOM = \left(\frac{R_z}{R_x}\right) w^2 \tag{6.2}$$

where
$$R_x = \frac{w}{k_x w \delta} \; and \; R_z = \delta / k_z w^2 \tag{6.3}$$

Thus, the *FOM* increases as the thermal conductivity ratio (k_x/k_z) and/or the thickness of the thermal anisotropic layer, δ, increases. However, increasing *w* does not increase the *FOM*, as increasing *w* decreases the ratio of (R_z / R_x) by the same amount (Equation (6.2)). For the investigated values of k_x, k_x, and δ in present analyses, the *FOM* of the composite spreaders varies up to 400 mm^2. A *FOM* of zero indicates all Cu spreader with a total thickness, t_{sp}, of 1.0 mm, whereas as 400 mm^2 is for a highly anisotropic spreader.

The present analyses assume that all but the exposed surface of the top Cu lament of the spreader are adiabatic (Figure 6.3). Based on this assumption, the performance results obtained in this chapter are conservative. In reality, nucleate boiling would also cool the sides of the spreader. In addition, thermal conduction through the junctions would provide additional cooling paths, decreasing the temperature of the underlying chip.

The analyses are performed with the following conditions for the underlying chip: (a) with uniform heat dissipation, (b) with a 0.1 x 0.1, 0.5 x 0.5, and 1.0 x 1.0 mm central hot spot, and (c) with multiple 1.0 x 1.0 mm hot spots. The ratio of the local heat flux at the hot spots to that of the chip surface average, or HFR, varied from 5 to 10.

6.3 Meshing and Methodology

The solved general transient heat conduction equation in the Cu filaments and the thermally anisotropic layer of the composite spreader is given as:

$$\rho c_p \left(\frac{\partial T}{\partial t}\right) = \iint k_x \left(\frac{\partial T}{\partial x}\right) dydz + \iint k_y \left(\frac{\partial T}{\partial y}\right) dxdz \iint k_z \left(\frac{\partial T}{\partial z}\right) dxdy \qquad (6.4)$$

This equation is solved subject to adiabatic surfaces everywhere, except at the exposed surface of the spreader, where the local surface heat flux equals that removed by nucleate boiling, expressed as:

$$\left(k_z \frac{\partial T}{\partial z}\right)_{z=t_{sp}} = h_{NB}(T_s)[T_s(y,z) - T_{sat}] \qquad (6.5)$$

In this equation, the nucleate boiling heat transfer coefficient, h_{NB}, is a function of the surface temperature, T_{s}, which varies along the spreader surface, or at z = t_{SP} (Figure 6.3). At this surface, the local nucleate boiling heat flux, q, and h_{NB} are interpolated and obtained from the experimental pool boiling curves presented in Figure 6.4a and b, respectively. To avoid CHF, the performed analyses limit the surface heat flux to $\leq$ 90% CHF, marked by the red square in Figure 6.4a and b. In addition, to ensure that the entire surface of the spreader is cooled by saturation nucleate boiling of PF-5060 dielectric liquid, the lowest surface temperatures, $T_{\mathrm{s,min}}$, at the corners of square spreader, are at least 1.0 $^{\mathrm{o}}$C above that for incipient nucleate boiling, and is marked by the black squares Figure 6.4a and b.

The performed numerical analyses used a developed CUDA C++ finite volume code alongside the COMSOL Multiphysics 4.0a finite element code package (COMSOL, 2015). The CUDA++ code was verified against simple cases with known analytical solution. For the composite spreader results, the results from the CUDA C++ code are compared to those obtained using the COMSOL package. The convergence of the results using both codes is subject to a tolerance in the overall energy balance of less than 0.1%. The two codes solved Equations (6.4) and (6.5) for a Cartesian cell centered finite volume (CUDA C++), and finite element (COMSOL) mesh in the different regions of the composite spreader and the underlying chip. The generated mesh was biased towards the interfaces between the Cu filaments and thermally anisotropic layer, as well as the top and bottom surfaces of the spreader (Figure 6.3, Figure 6.5). For the cases involving an underlying chip with hot spots, additional biasing of the mesh was implemented at the locations of the hot spots (Figure 6.5b).

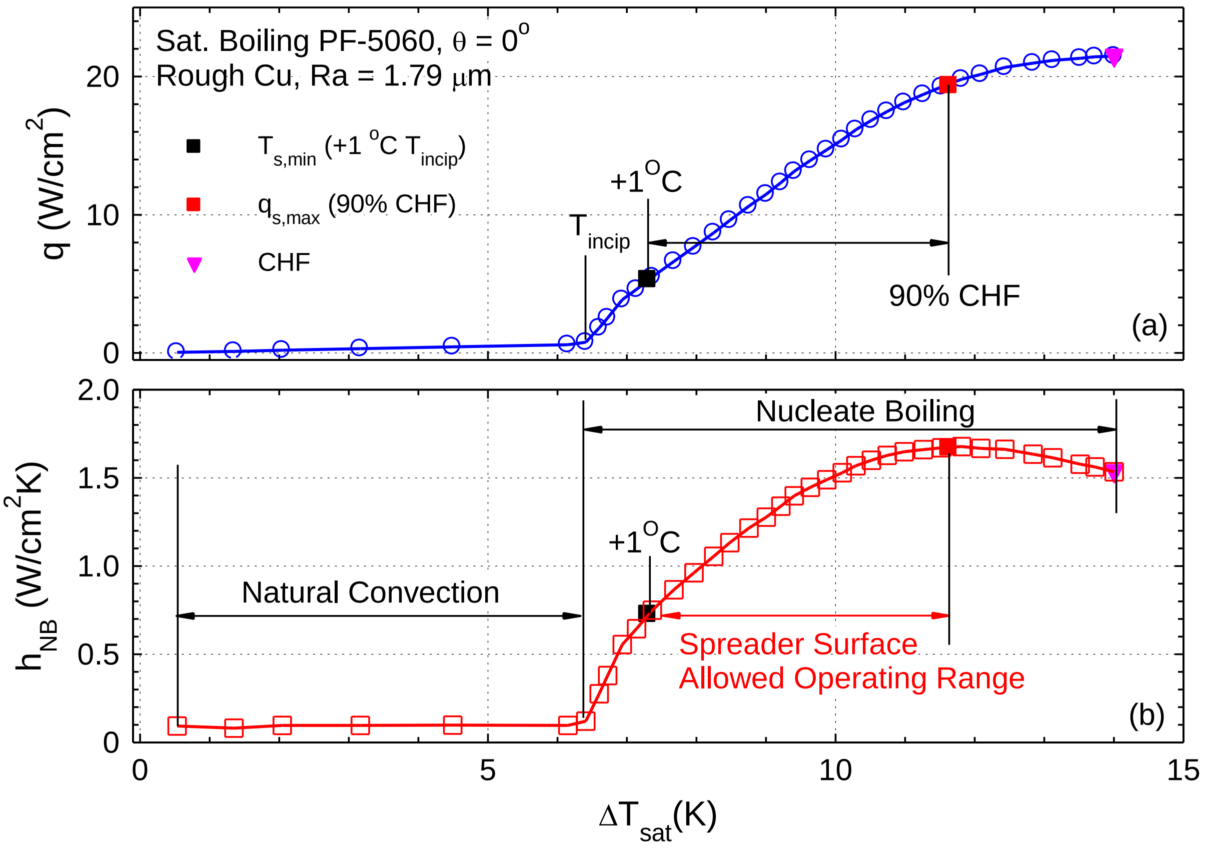

Figure 6.4. Experimental pool boiling and heat transfer coefficients curves implemented at the spreader surface cooled by saturation nucleate boiling of PF-5060 dielectric liquid.

The total number of finite volumes (CUDA C++) and finite elements (COMSOL) employed in the present analyses varies from ~50,000 to ~1,000,000, depending on the surface area, w^2, (Figure 6.5a) and thickness, t_{sp}, (Figure 6.3) of the spreader. The material properties and dimensions, assigned to the numerical elements in the computational domains of the spreader and underlying chip, are listed in Table 6.1. The spreader and underlying chip numerical domains were connected by a thin thermally resistive layer of thermal interface material (Figure 6.3). Varying the initial temperatures in the numerical domains slightly affected the computational time, but not the steady state performance results presented in this chapter.

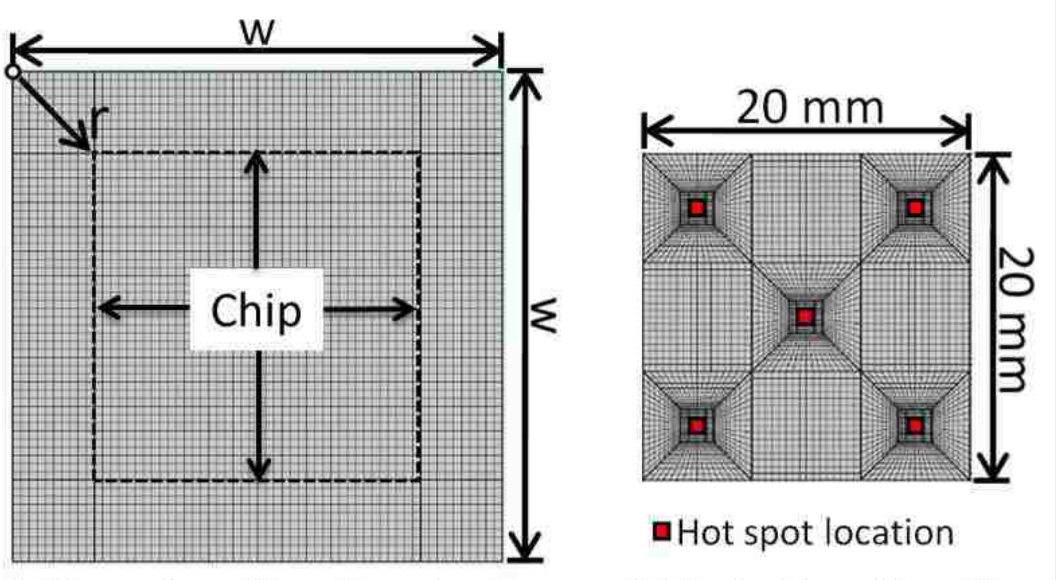

Figure 6.5. The numerical meshes used in the present numerical analyses of composite spreaders.

Table 6.1. Range of Material properties and dimensions for the analyses of composite spreaders.

Parameter	Values	References
k_{Cu} (W/m K)	400	(8)
k_x (W/m K)	325, 500, 1000, 2000, (1800)	(1 – 7)
k_z (W/m K)	5, 10, 20, (8)	(1 – 7)
k_{Chip} , k_{TIM} (W/m K)	125, 40	(8)
TIM thickness (mm)	0.5	(9)
Chip Dimensions (mm)	20 x 20 x 0.25	
thermally anisotropic layer, δ (mm)	0.25, 0.5, 0.75, 1.00	
Hotspots (mm x mm, HFR)	0.1x0.1,7.5; 0.5x0.5, 5; 1.0x1.0,10	

(1)(Zweben, 2006), (2)(Zweben, 2005), (3)(Slack, 1962), (4)(Klemens, 2000), (5)(Baladin, 2011), (6)(Chung, 2002), (7)(Tong, 2011), (8)(Lide, 2004), (9)(Koide et al. 2006)

After mesh generation, appropriate material properties are assigned to the numerical domains. For the thermally anisotropic layer in the composite spreaders, the values of the in-plane lateral thermal conductivity, k_x, and the thermal conductivity through-plane, k_z, are listed in Figure 6.1. The k_x = 325 W/m K represents a high quality graphite, as a low cost alternative to the higher performing HOPG. A k_x of 500 W/m K represents pyrolytic graphite, and 1000 W/m K represents a low-grade HOPG annealed at a lower temperature with lower oriental order, such as ZYH-grade HOPG. A k_x of 2000 W/m K represents a higher quality HOPG, such as ZYA-grade HOPG. The values of k_x = 325, 500, 1000, and 2000 W/m K, and kz = 5, 10, and 20 W/m K, cover a wide range of possible material choices for the thermally anisotropy layer in the composite spreaders (Zweben, 2005, 2006; Slack, 1962, Klemens, 2000, Baladin, 2011, Chung, 2002, Lide, 2004; Tong, 2011). One additional case analyzed, with k_x = 1800 W/mK and k_z = 8 W/m K, represents another high quality HOPG. Thus, numerical results discussed in this paper are for 13 different combinations of the thermal conductivities, and 4 different thickness, $\delta = 0.25$, 0.5, 0.75, and 1 mm, of the thermally anisotropic layer in the composite spreaders.

The developed CUDA C++ code solves the Laplace 3D Heat Equation (Equation 6.4) explicitly using a finite volume scheme for the steady state temperatures in different regions of the composite spreader as well as in the underlying chip. Steady state convergence is reached when the computed mean temperatures changed by $\leq 10^{-7}$ K, and the overall energy balance between the heat flux generated by the chip and heat removed at the spreader surface is < 0.1%. The COMSOL academic software package code (COMSOL, 2015) is used for the thermal analyses of the composite spreader for an underlying chip with central and multiple hot spots. The biased numerical mesh towards the hotspots was implemented using COMSOL's graphical user interface (Figure 6.5). The Generalized Minimal Residual Method Solver is used to compute the steady state temperatures to a more relaxed tolerance of 10^{-4}, as the implicit solver showed no further improvements with more strict tolerances, and same overall energy balance of < 0.1% as the CUDA ++ explicit solver.

6.4 Validation of Codes

For validation of the numerical analyses, the computed results for an all Cu heat spreader ($k_x = k_z = 400$ W/mK) and a composite spreader with a 1.0 mm thick HOPG thermally anisotropic layer (k_x = 1800 W/mK and k_z = 8 W/mK), returned from the developed CUDA C++ code and COMSOL Multiphysics 4.0a code package are compared in Figure 6.6. For these two analyses, the 20 x 20 x 0.25 mm underlying chips uniformly dissipate 100 W of thermal power, and the dimensions of the spreader are 40 x

40 x 2 mm. Figure 6.6a-d compare the computed axial and lateral temperature profiles in the spreaders , where *r* is the line profile along the spreader surface (Figure 3a and c), and *Z* is the direction of the axial temperature profile through the centers of both the chip and the spreader (Figure 6.6a and c). These figures show identical results for the all Cu spreader and nearly identical results for the composite spreader. The largest temperature difference of ~0.07°C at the edges of the spreader may be due to the differences in how the two codes handle the interface between the Cu filaments and HOPG layer, as well as in the solvers themselves. In COMSOL, there is a physical mating boundary between the Cu filaments and HOPG layer, whereas the developed code uses a single domain for the entire spreader. Nevertheless, the overall difference in the computed temperature fields is very small, ~0.07% – 0.12%. These results did not change with refined numerical meshes.

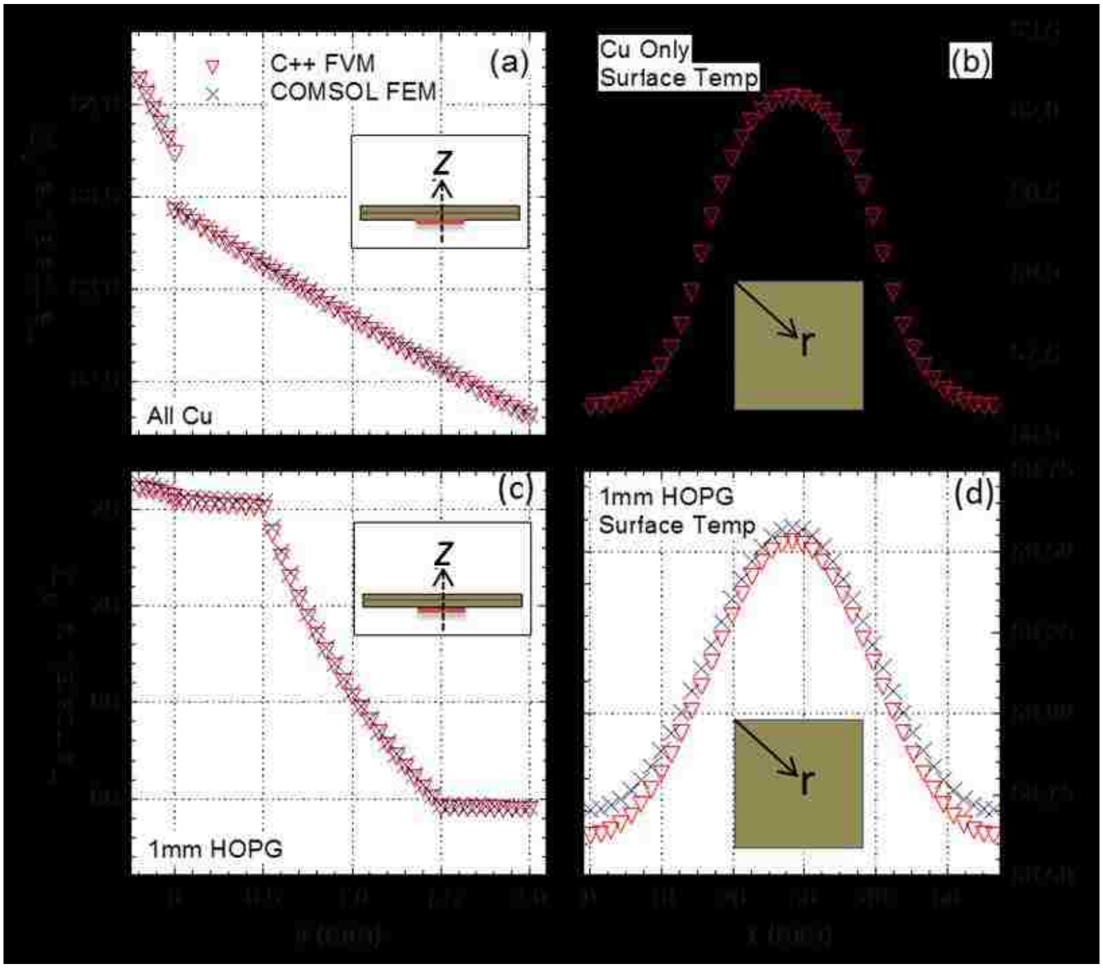

Figure 6.6. Validation of numerical results between the CUDA C++ and COMSOL codes for a Cu and a composite spreader of the same thickness.

The experimental boiling curves (Figure 6.4) computationally reconstructed using both codes are compared to the experimental data in Figure 6.7. The excellent agreements confirm the soundness of the numerical approach and analyses. The results in Figure 6.6 and Figure 6.7, which did not change with further refinement of the numerical meshes, clearly confirm the consistency of the numerical results using both the developed CUDA C++ code and the COMSOL Multiphysics 4.0a code package. As codes provided solutions with energy balance accuracy within 0.1%, the uncertainties in the computational results presented are those of the experimental data implemented into the codes (Chapter 3.6 and Appendix A).

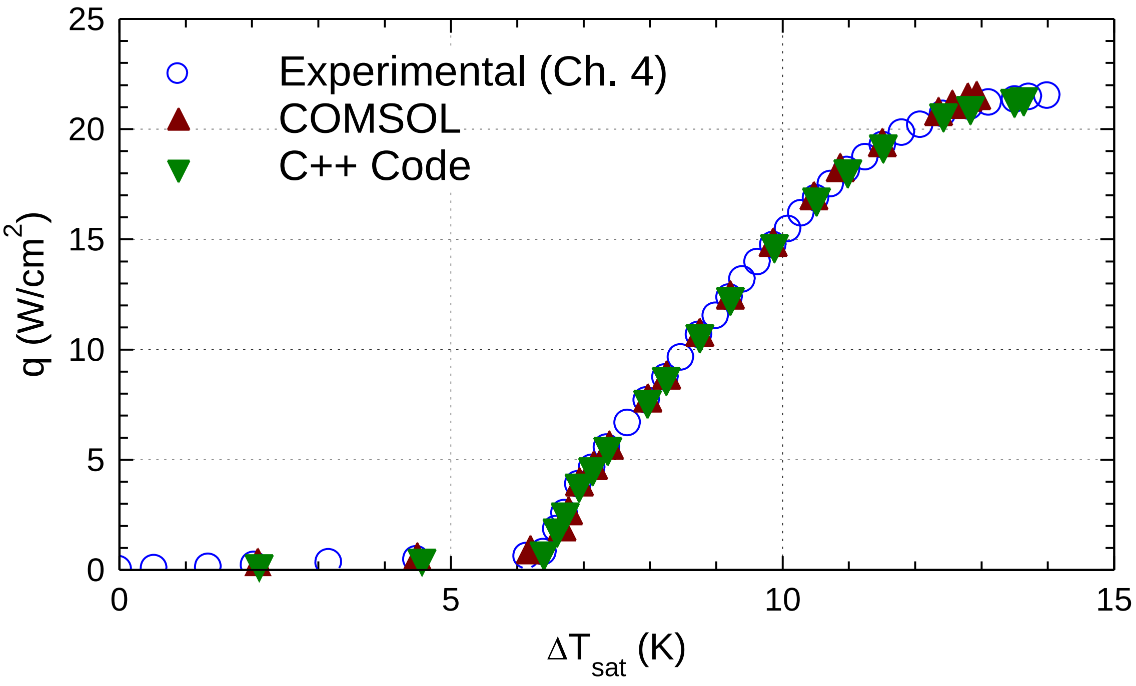

Figure 6.7. Numerical results for reconstructing the experimental pool boiling curve.

6.5 Results and Discussion

This section presents the analyzed results from all 13 cases in Table 6.1. The computations provided a large data base used to correlate the effects of the anisotropic layer thickness, δ, and thermal conductivities k_x (325 – 2000 W/mK) and k_z (5 – 20 W/mK), on the following performance parameters of the composite spreader: the total power removed, the maximum chip temperature, and total thermal resistance. The effect the thermally anisotropic layer on hot spots in the underlying is also presented, as is the effect of aging the exposed rough Cu surface of the spreaders, for consideration of long term immersion cooling performance.

6.5.1 Effect of the Thermally Anisotropic Layer

The obtained values of the total thermal power removed by three spreaders, sized 20 x 20 mm to 70 x 70 mm, and with $\delta = 0$ (all Cu), 0.25 mm , 0.5 mm , 0.75 mm, and 1.0 mm are compared in Figure 6.8. The results for the composite spreaders in Figure 6.8a and Figure 6.8d, are for the same anisotropic layer thermal conductivities ($k_x = 325$ W/mK, $k_z = 5$ W/mK). Those in Figure 6.8b and Figure 6.8e represent those with a low grade HOPG layer ($k_x = 1000$ W/mK, $k_z = 10$ W/mK) and those in Figure 6.8c and Figure 6.8f represent higher grade HOPG thermally anisotropic layer ($k_x = 1800$ W/mK, $k_z = 8$ W/mK) (Slack, 1962; Klemens 2000; Chung 2003; Zweben, 2005, 2006; Balandin 2011; Tong 2011). The black solid squares in Figure 6.8a-f indicate the highest values of the total thermal power removed and the width the spreaders, w^*, whose exposed surfaces are cooled entirely by saturation nucleate boiling of PF-5060 dielectric liquid. These are when the maximum heat flux at the surface of the spreader is limited to is 90% CHF (Figure 6.4a), and the minimum surface temperature at the corner of the spreaders is equal to 1.0^{o}C higher than at incipient boiling in the experiments (Figure 6.4a). The points to the left of the black squares, or for $w < w^*$, in Figure 6.8a-c or below the in Figure 6.8d-f are for the same maximum flux of 90% CHF, but higher minimum surface temperatures.

Increasing the thickness of the thermally anisotropic layer of the composite spreaders increases the total thermal power removed by saturation nucleate boiling of PF-5060. In addition, for the same layer thickness, increasing k_x spreads heat more effectively, and enables the composite spreader to remove more power. The composite spreaders with a thermally anisotropic material that represents graphite (Figure 6.8a) and $\delta = 0.25$ mm, 0.5 mm, 0.75 mm, and 1.0 mm are capable of removing 93 W, 101 W, 109 W, and 119 W, respectively. The composite spreaders with a thermally anisotropic material that represents higher-grade HOPG (Figure 6.8c), and the same values of δ, are capable of removing much more power; 120 W, 170 W, 238 W, and 318 W, respectively. These powers are 6% – 260% more than that removed by a ~1 mm thick Cu spreader, subject to the same cooling conditions at the exposed top surface. In comparison, increasing the thickness of the Cu only spreader from 1 to 2 mm increases its width, *w*, from ~25.4 mm to ~28.5 mm, and the total power removed by 13% to ~101 W.

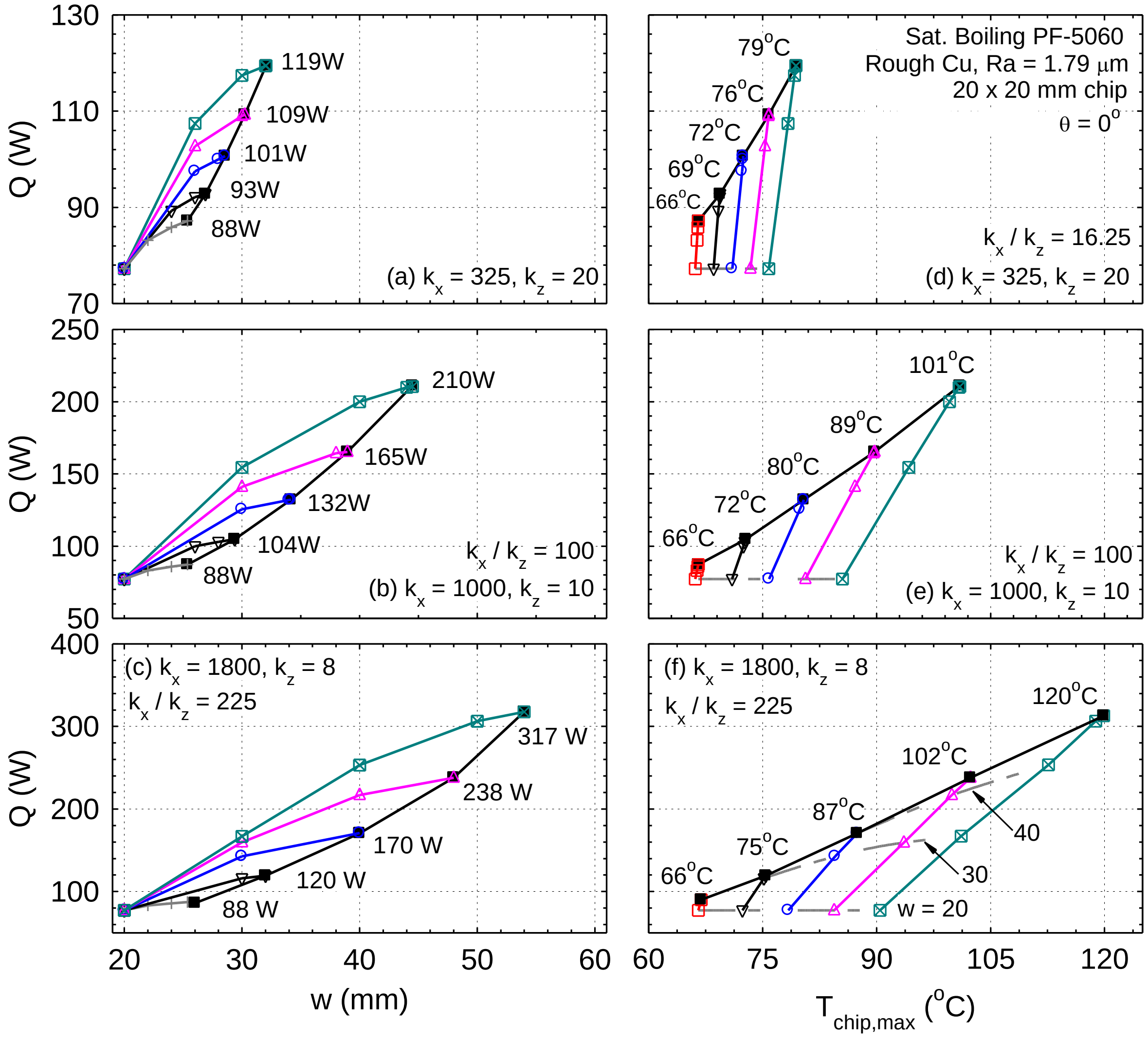

Figure 6.8. Effects of thickness and thermal conductivities of the thermally anisotropic layer on the performance and widths of composite spreaders as well as the chip surface temperature.

The composite spreader in Figure 6.8c, and Figure 6.8f (k_x = 1800 W/mK and k_z = 8 W/mK) is capable of removing up to 160 W at chip surface temperature of ~ 85°C, 228 W at a chip temperature of ~ 100°C, and 292 W at a chip surface temperature of ~ 115°C (Figure 6.8f). These performance results satisfy today's cooling requirements of high performance CPUs pushing upwards of 150 W dissipated thermal power (AMD, 2015;

Intel, 2015). For the same thermal power dissipation, increasing the thickness of the thermally anisotropic layer increases the chip maximum temperature (Figure 6.8d-f). This is because the anisotropic layer arranged by Figure 6.3 adds thermal resistance, since any path of heat flow from the chip to the spreader surface must pass through-plane of the thermally anisotropic layer, where the thermal conductivity is very low (Table 6.1).

Figure 6.9 compares the computed temperature fields in a Cu only spreader and a composite spreader of the same the same total thickness of 2 mm and the total dissipated thermal power of 80 W. The thermally anisotropic layer of the composite spreader, δ, is 1.0 mm thick and has thermal conductivities, k_x = 1800 W/mK, and k_z = 8 W/mK. Note that while the surface of the composite spreader is cooler than that of the all-Cu spreader, the maximum chip temperature is higher. However, at the 80 W dissipated thermal power, the maximum surface heat flux for the all Cu spreader is close to ~90% of CHF, while that for the composite spreader is ~45% of CHF, indicating plenty of room to dissipate more power, albeit with increased chip temperatures.

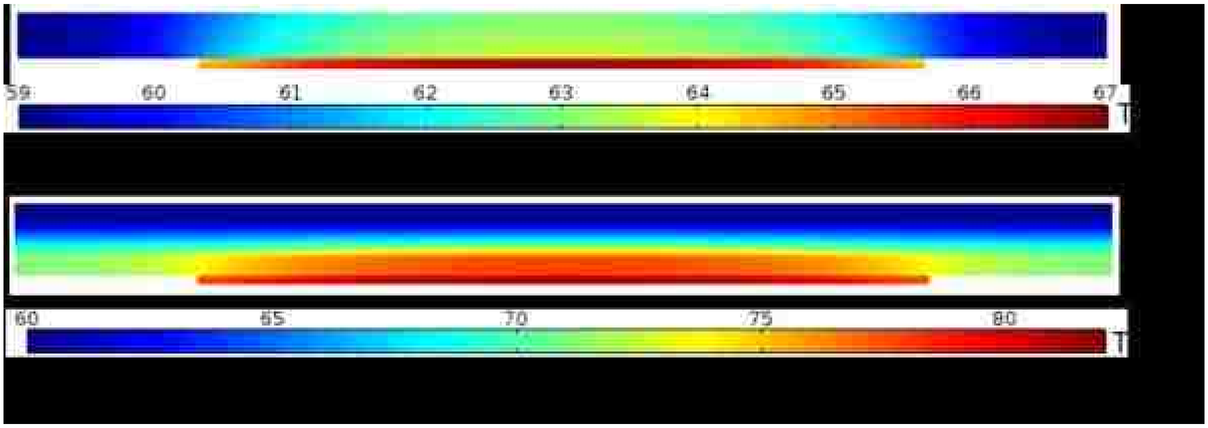

Figure 6.9. Calculated temperature fields at a total power dissipation of 80 W from 30 x 30 mm spreaders : (a) all Cu, and (b) composite with 1.0 mm-thick HOPG layer (k_x = 1800 W/mK and k_z = 8 W/mK).

6.5.2 Maximum Power Removed

The thermal power dissipated by the underlying 20 x 20 mm chip and removed from the exposed surface of the composite spreaders, *Q*, by saturation nucleate boiling of PF-5060, increases with increasing spreader width, depending on the value of spreader's

FOM. The maximum power removed, Q^*, and the corresponding spreader with, w^*, are indicated by the solid square symbols in Figure 6.10. These are for a spreader maximum surface heat flux ~ 0.9 CHF and lowest surface temperature minimum, $T_{s,min}$, that is 1^{o}C higher than that for boiling incipience in the experiments (Figure 6.4). In Figure 6.10, the lowest curve for *FOM* = 0, is that for the all-Cu spreader and t_{sp} = 1mm. The maximum thermal power removed by this spreader (~88 W) is donated as Q_o*.

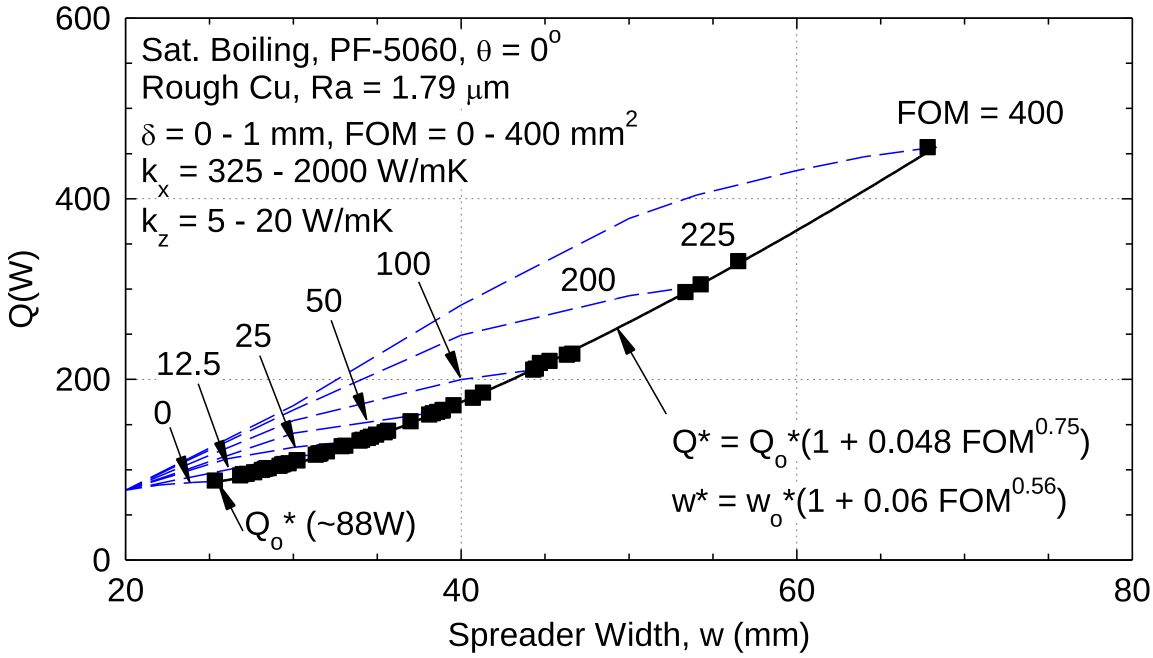

Figure 6.10. The maximum power removed and corresponding spreader a 20 x 20 mm microprocessor

The obtained values of the maximum power removed, Q^*, by the composite spreaders expressed in terms of that for the all-Cu spreader and the *FOM*, is given as:

$$\frac{Q^*}{Q_0^*} = 1 + 0.048\ FOM^{0.75} \tag{6.6}$$

Similarly, the corresponding values of the width of the composite spreader width at Q^*, w^*, are expressed in terms of that for the all-Cu spreader, w_o^*, and the *FOM* as:

$$\frac{w^*}{w_0^*} = 1 + 0.06\ FOM^{0.56} \tag{6.7}$$

In these expressions, *FOM* is in mm^2, Q_o* is ~88 W, and w_o* is 25.4 mm. The second term on the right hand side of Equation (6.6) reflects the increase in the total thermal power removed by the composite spreaders as a function of the spreader's *FOM* raised to 0.75. Similarly, the second term on the right hand side of Equation (6.7) indicates the increase in the width of the composite spreader with increasing the *FOM*. Thus, for *FOM*s of 50, 100 and 200 mm^2, the composite spreaders remove ~ 167.4 W, 221.6 W, and 466 W, respectively, which are 90%, 252% and 429% higher than that possible with an all-Cu spreader. The corresponding widths of the composite spreaders of ~39 mm, 45.5 mm, and 69 mm, respectively, represent an increase of ~ 53.6%, 79% and 172%, compared to the width of the all-Cu spreader.

The developed empirical correlations in Equations (6.6) and (6.7) are in good agreement with the computational database generated in this work, to within ± 5 and +3%, respectively (Figure 6.11a and Figure 6.11b).

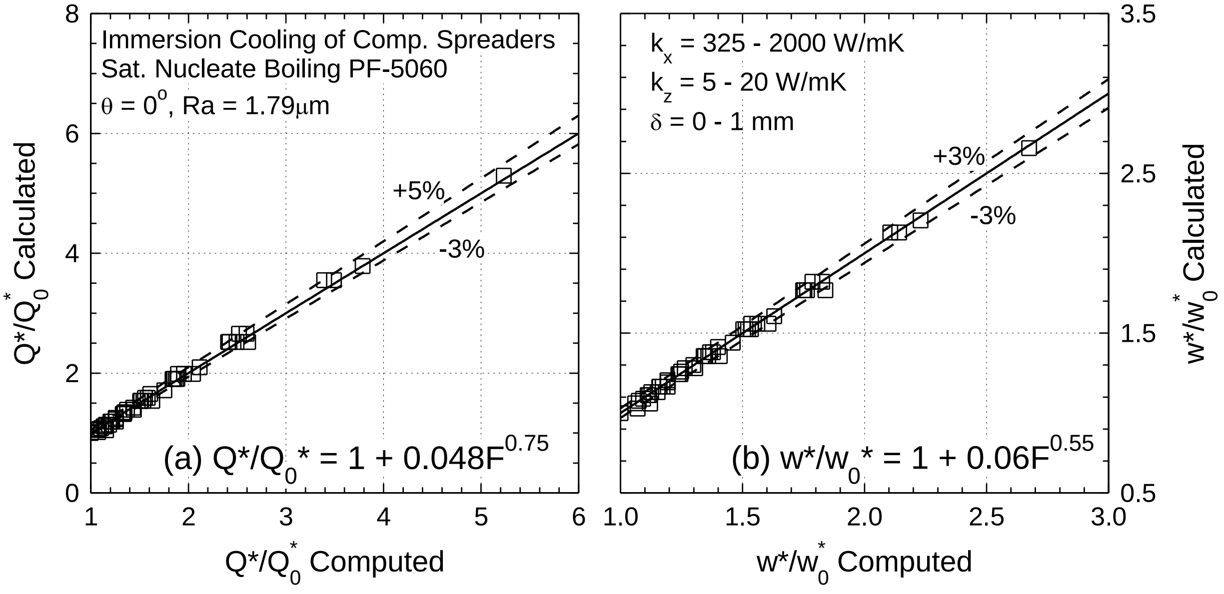

Figure 6.11. Calculated versus computed values of the maximum thermal power removed and width of the composite spreaders cooled by saturation nucleate boiling of PF-5060 dielectric liquid.

6.5.3 Effect of the Spreader Width

The results presented and discussed in the previous subsection focused on determining the highest power removed, Q^*, and width, w^*, of the composite spreaders, subject to limiting the highest nucleate boiling surface heat flux to 90% CHF, and lowest surface temperature to 1.0 ^{o}C higher than that for incipient boiling in the experiments (Figure 6.4a). However, for some applications, the thermal power dissipation by the underlying chip may be lower than Q^{*}, for which the spreader width would be less than w^{*}, or the spreader width may simply be design constrained to a value to less than w^{*}. For a composite spreader with $w < w^{*}$, the thermal power removed, Q, will be less than Q^{*}. The obtained performance curves for composite spreaders with $w < w*$, for different *FOM*s up to 200 mm^2, are presented in Figure 6.12. The curves of the same *FOM* are for different combinations of k_x, k_z, and δ (Table 6.1).

Figure 6.8a-c, Figure 6.10, and Figure 6.12 show how decreasing the spreader size from $w*$, (marked by the black squares), results in a decrease of power removed by the spreader. Because the surface average nucleate boiling heat transfer coefficient increases as the spreader size decreased, the decrease of power removed is not directly proportional to the reduced surface area. Figure 6.12 shows how sets of data with different values of k_x, k_z, and δ, but the same *FOM*, showed nearly the same increases in power removed as spreader size increased. A simple relationship defined by $Q = A(w - w_0)^{0.5}$ was found to fit each set of data with like *FOM*. Thus, the empirically developed correlation to predict the power removed by a composite spreader with $w \leq w*$, for any $\delta = 0 - 1.0$ mm, $k_x = 325 - 2000$ W/mK, $k_z = 5 - 20$ W/mK, in immersion cooling by saturation nucleate boiling of PF-5060 on a Cu surface of Ra = 1.79 µm, is given as:

$$\frac{Q}{Q_0} = 1 + 0.054\, FOM^{0.42}(w - w_0)^{0.5} \qquad (6.8)$$

In this correlation, w_o is the reference spreader width of 20 mm, which is the same as that of the underlying chip. The corresponding thermal power removed by this reference spreader, Q_o, is ~77.2 W. To better illustrate the enhancement of heat spreading, Equation (6.8) is rewritten in terms of the axial and lateral thermal resistances (Equation (6.3)), and the width of the composite spreaders, as:

$$Q = Q_o\left\{1 + 0.054\left(\frac{R_z}{R_x}\right)^{0.42} w^{0.84}\sqrt{w - w_o}\right\} \qquad (6.9)$$

Equations (6.3) and (6.9) show that for the same w, increasing the ratio of the axial to lateral thermal resistances (R_z/R_x) increases the *FOM*, thus enhancing heat spreading and

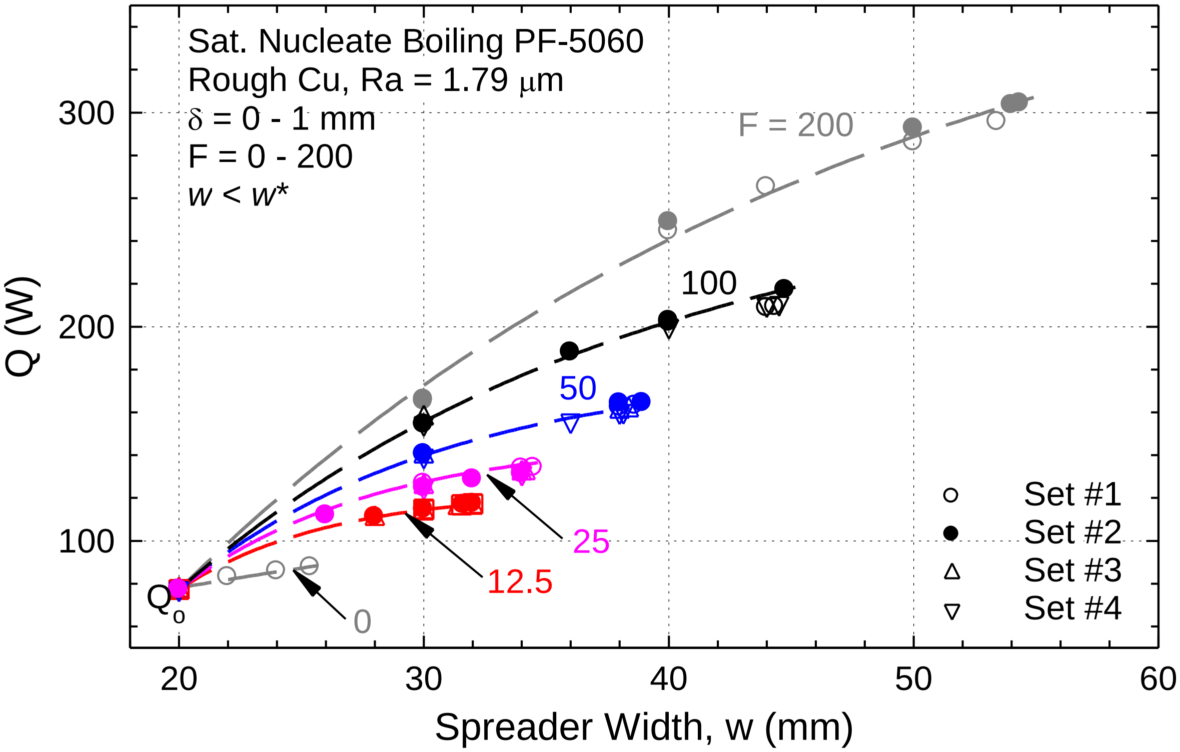

Figure 6.12. Like sets of *F* that resulted in the nearly the same enhancement of total removed by the composite spreader at different spreader widths.

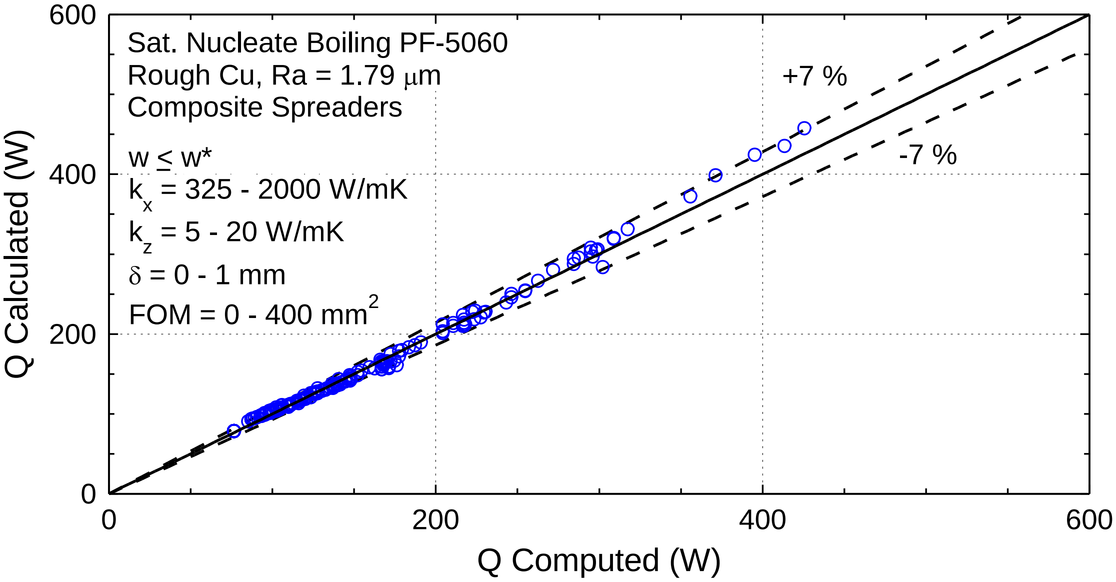

Figure 6.13. Calculated (Equation (6.8 or 6.9)) versus computed thermal power removed for the composite spreaders.

increasing both the total thermal power removed and corresponding width of the composite spreader. Figure 6.13 compares the calculated values of the thermal power removed by the composite spreaders using Equation (6.8), to those computed numerically in the present analyses, for the same spreader width and *FOM*. This figure shows that the calculated and computed values of the thermal power removed by nucleate boiling from the composite spreader's surface, are in good agreement, to within ±7%. This error may be reduced by using exponential fits to construct Equations (6.8) and (6.9), however at the cost of the simplicity the current forms provide.

6.5.4 Thermal Resistances and Maximum Chip Temperature

The total thermal resistance, R_{TOT}, is the sum of those for: (a) saturation boiling, R_{boil}, at the spreader surface and (b) heat conduction through the composite spreader, R_{sp} and (c) TIM R_{TIM} (Figure 6.14). The resistance of a thermal interface material is constant and does not change with power dissipation, but the thermal conductance of TIM varies widely depending on type of material, application thickness, and applied interfacial pressure. For the TIM used in the present computations, the calculated thermal resistance is ~0.03 ^{o}C/W. For a different TIM, the maximum chip temperature may be adjusted later on, after knowing R_{TOT}, by adding the difference of resistances between the TIM used in the present computations and the new TIM, to R_{TOT}, and then calculating the new $T_{\text{chip,max}}$.

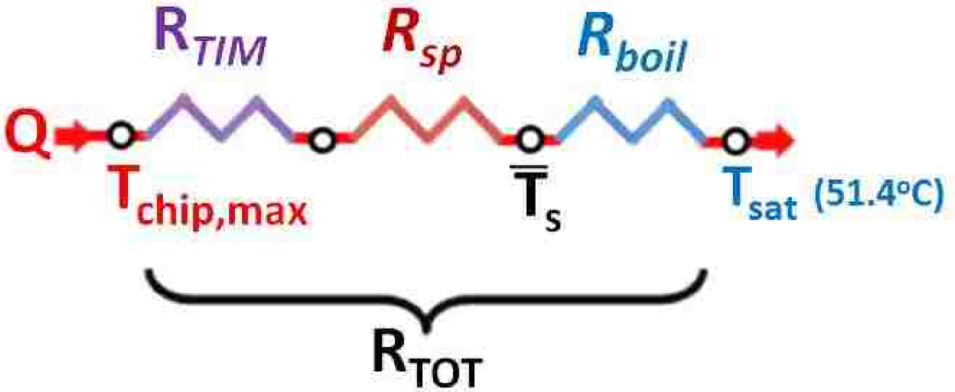

Figure 6.14. The Thermal resistance diagram of the various resistances to heat dissipation from the underlying chip.

The R_{TOT}, R_{boil} and R_{sp} for the investigated spreaders were calculated using the following expressions:

$$R_{sp} = (T_{chip,max} - \overline{T_s})/Q \tag{6.10}$$

$$R_{boil} = (\overline{T_s} - T_{sat})/Q \tag{6.11}$$

$$R_{TOT} = (T_{chip,max} - T_{sat})/Q = R_{sp} + R_{boil} + R_{TIM} \tag{6.12}$$

In these expressions, $T_{\text{chip,max}}$ is the maximum chip surface temperature, $\overline{T_s}$ is the mean surface temperature of the spreader, T_{sat} is the saturation temperature of PF-5060 dielectric liquid (51.4°C at 0.085 MPa in Albuquerque NM, where the pool boiling experiments were conducted, Figure 6.4a and b), and Q is the total power dissipated by underlying chip and removed from spreader surface by nucleate boiling.

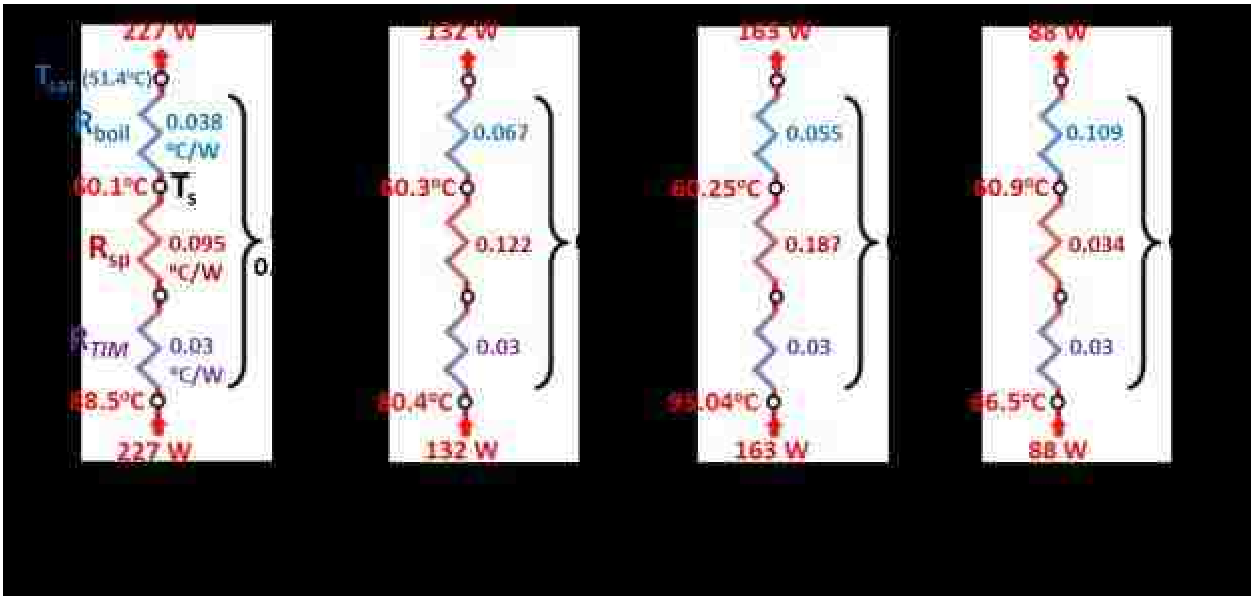

Figure 6.15. Thermal resistance diagrams for composite spreaders and all Cu spreader.

The results in Figure 6.15a-d show the thermal resistances for the various composite spreaders and an all Cu spreader (Figure 6.15d). For the composite spreaders, largest contributor to total resistance is that by conduction through the heat spreader, R_{sp}. For these spreaders, R_{sp} varies from 0.095 °C/W to 0.187°C/W, compared to 0.034 °C/W for the Cu only spreader. The R_{TOT}, varies from 0.163 °C/W to 0.27 °C/W, and $T_{\text{chip,max}}$,

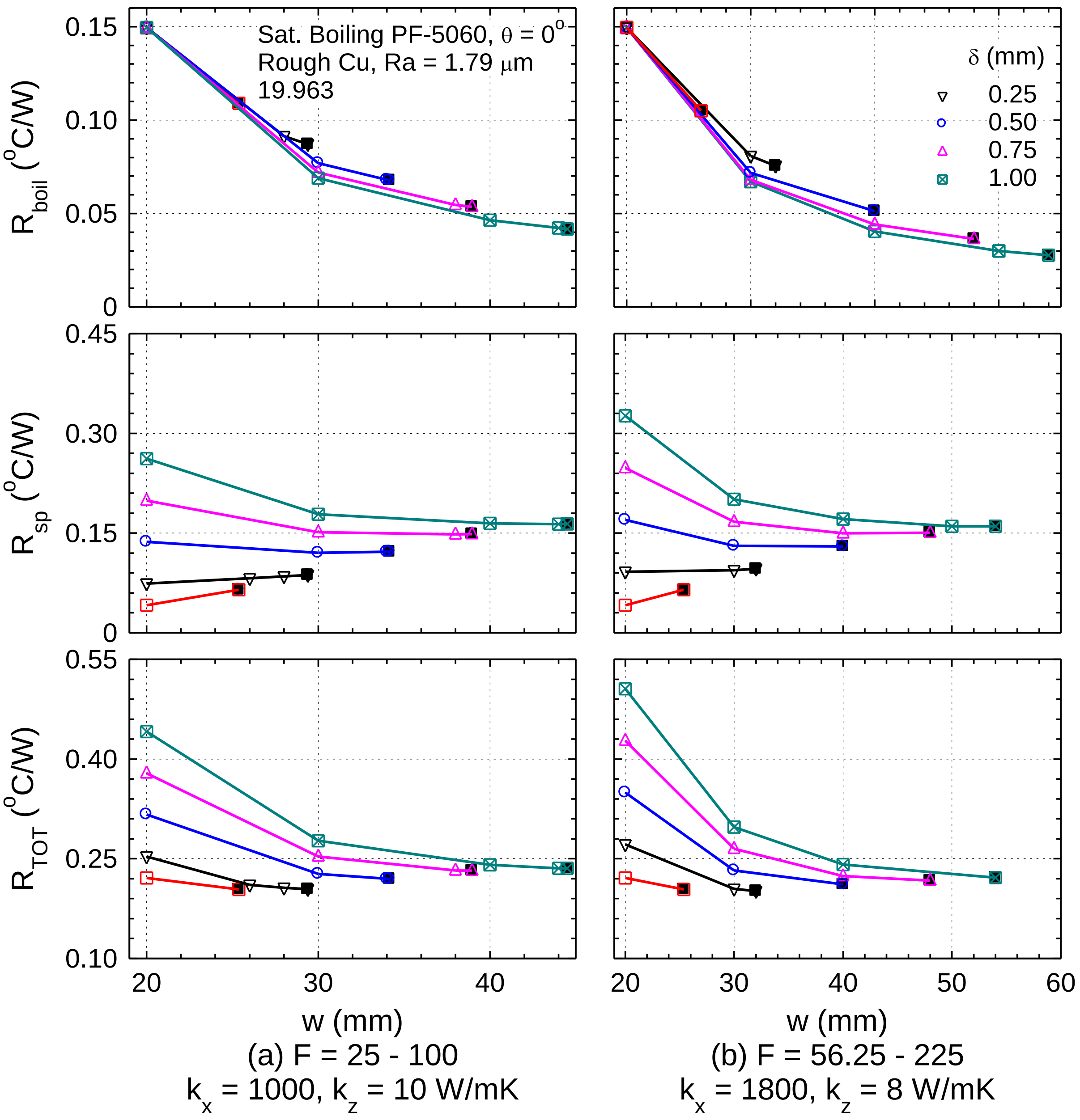

(a) F = 25 - 100

k_x = 1000, k_z = 10 W/mK

(b) F = 56.25 - 225

k_x = 1800, k_z = 8 W/mK

Figure 6.16. Effects of thickness and thermal conductivities of the thermally anisotropic layer on thermal resistances and width for the composite spreaders.

from 88.5 °C to 95.04 °C. The total thermal resistances of the composite spreaders in Figure 6.15a-c are comparable to the all Cu spreader (Figure 6.15d), and capable of removing much more power, albeit at higher chip temperature.

Figure 6.16a-f present the results showing the effect of the δ of the thermally anisotropic layer on the R_{boil}, R_{sp} and R_{TOT} for the composite spreaders with (a) k_x = 1000 and k_z = 10 W/mK and (b) k_x = 1800 and k_z = 8 W/mK. For both cases, increasing the spreader size decreases R_{boil}, which also further decreases with increasing δ. This is because the thermally anisotropic layer (Figure 6.3) stimulates boiling farther away from the center of the spreader, and to a lesser extent at the spreader center. The regions of the spreader surface far away from the center are much cooler and experience lower h_{NB} than at the center. Enhanced heat spreading increases the wall superheat and thus h_{NB} (Figure 6.4b) in these regions. This increases the surface mean h_{NB}, which increases the total power removed faster than the average surface temperature of the spreader increases, lowering R_{boil} (Figure 6.16a and 6.12d).

Figure 6.16b and 6.12e show R_{sp} increases with increasing δ. This is due to the low through-plane thermal conductivity of the anisotropic material layer (Figure 6.3, Table 6.1). This is most evident for the heat spreaders sized 20 x 20 mm, where there is no heat spreading because the underlying chip is of the same size. Thus, adding a graphite or HOPG layer makes the spreader more insulating, as the only direction for heat conduction to the exposed rough Cu surface is directly perpendicular through the layer where thermal conductivity is very low. However, as the spreader size, *w*, increases, heat spreading improves. As the high in-plane thermal conductivity is taken advantage of, R_{sp} decreases. Conversely, the spreading resistance of the all Cu spreaders increases with increasing spreader size (Figure 6.16b and 6.12e). This is because adding more thermally isotropic material results in more conductive resistance regardless of the path of heat flow. Figure 6.16b and 6.12e also show that R_{sp} decreases with increasing the composite spreader size, reaching lower asymptotic values, depending on the k_x, k_z, and δ. These values are indicated by the solid black symbols in Figure 6.16a – f.

The total thermal resistance, R_{TOT}, increases with either increasing the δ and / or decreasing the spreader size, *w* (Figure 6.16c and f). This is because with increasing δ, R_{sp} increases faster than R_{boil} decreases, leading to a net increase of R_{TOT}. However, R_{TOT} is small for spreaders $\geq$ 40 x 40 mm ($\leq$ 0.25 $^{\mathrm{o}}$C/W). High end multicore computer chips are often encased with heat spreaders sized greater than 38 x 38 mm and as high as 52.5 x 45 mm (Intel, 2015). Additionally, the benefit of dissipating far more power safely may outweigh the small increases of the total thermal resistance and higher maximum chip temperature.

The obtained values of R_{TOT} for the composite spreaders cooled by immersion cooling nucleate boiling of PF-5060 dielectric liquid (Figure 6.16c) are comparable to those of microchannel liquid cooled heat sinks, and without any pumping requirement. Schmidt (2004) reported a microchannel heat sink for the cooling of 158 W microprocessor to have a thermal resistance that varied from 0.08 – 0.55 ^{o}C/W, depending on the flow rate. Kou et al. (2008) also demonstrated that the thermal resistance of microchannel heat sinks varied from 0.06 – 0.37 ^{o}C/W, depending on flow rate. Therefore, the performance of the composite spreaders investigated this section are capable of removing large amounts of dissipated power, and without pumping, by the underlying chips with modest, but acceptable, increases in the maximum surface temperature of the chips.

The maximum chip temperature, $T_{\text{chip,max}}$ is of interest for the immersion cooling of microprocessors. The dependence of $T_{\text{chip,max}}$ on the thermally anisotropic layer parameters (Table 6.1) was empirically determined to be a function of the δ and k_z. Data of the same through-plane thermal conductance, $C_z = k_z / \delta$, of the thermally anisotropic layer, collapsed onto a single trend that is a function of the $T_{\text{chip,max}}$ and total power dissipated by the chip, Q (Figure 6.17), given as:

$$T_{chip,max} = 65 + 10.83\,(C_z)^{-1.33} + 0.117\,Q\,(C_z)^{-0.42} \tag{6.13}$$

This correlation agrees with the computed data to within $\pm$ 1% (Figure 6.18a). Combining Equation (6.13) with Equation (6.8), and rearranging the results, provides a correlation for the total thermal resistance, as:

$$\begin{aligned} R_{TOT} &= (65 - T_{sat})/Q + \frac{[10.83\,C_z^{-1.33} + 0.117 Q C_z^{-0.42}]}{Q} \\ &= [R_{boil} + R_{TIM}] + R_{sp} \end{aligned} \tag{6.14}$$

This expression agrees with all computed data within $\pm$ 4% (Figure 6.18b). The values of the computed total thermal resistances vary from ~0.16 – 0.7 ^{o}C/W, however, those > 0.4 ^{o}C/W are for the few cases where w closely matches that of the underlying chip ($w = w_0$), thus with very limited or no lateral heat spreading. For spreaders with w > 30, the total thermal resistances vary from ~0.16 – 0.4 ^{o}C/W.

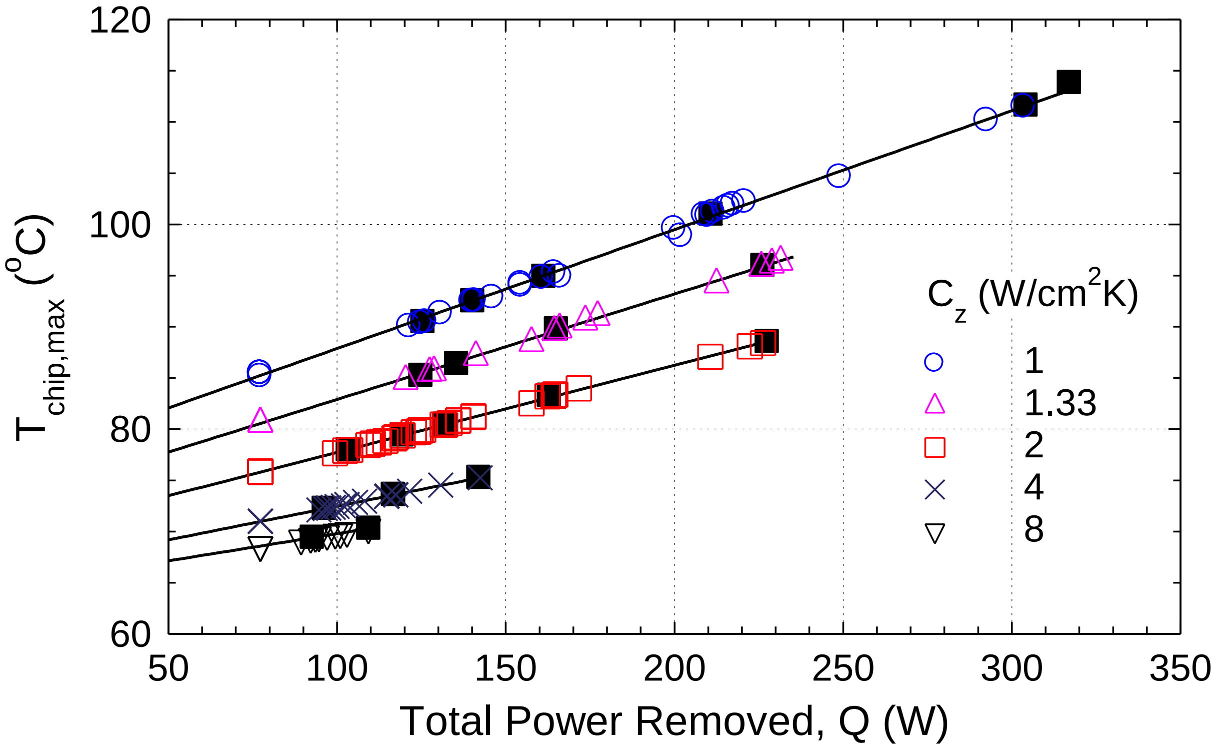

Figure 6.17. Dependence of *$T_{chip,max}$* on the total thermal power removed and thermal conductance, *C_z*, of the composite spreader.

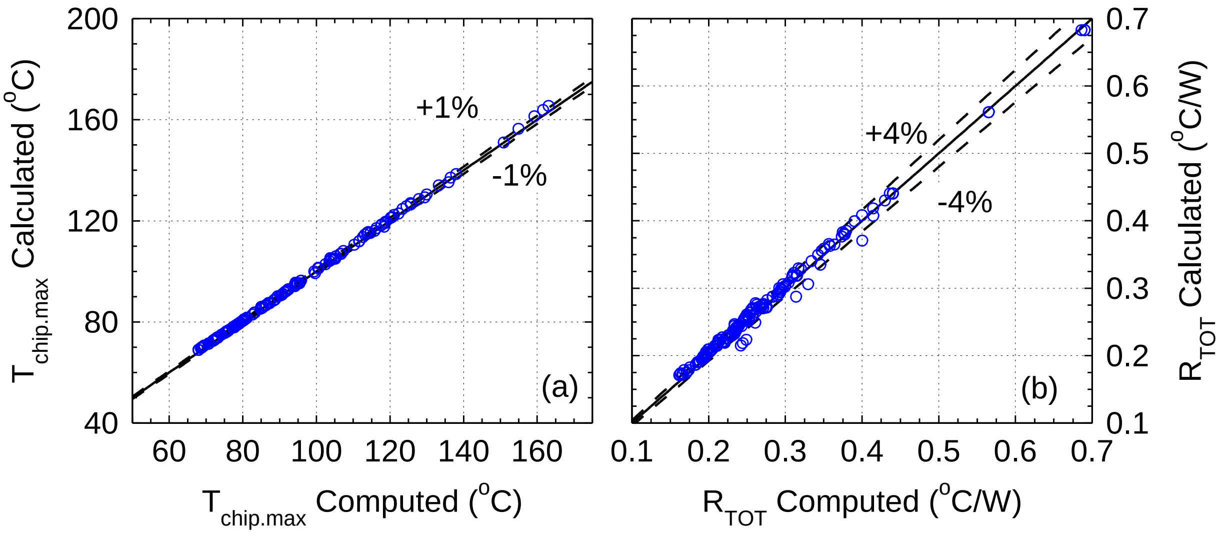

Figure 6.18. The calculated versus computed maximum chip temperatures for composite spreaders cooled by saturation nucleate boiling of PF-5060 for a 20 x 20 mm microprocessor with uniform power dissipation.

Additionally, the first two terms approximate the thermal resistances contributed by the thermal interface material and composite spreader, and the final term approximates the thermal resistance contributed by saturation nucleate boiling of PF-5060. Thus, Equation (6.14) provides accurate estimates of the total thermal resistance, R_{TOT}, and of the individual resistances that make up R_{TOT}.

The set of correlations provided by Equations (6.8) – (6.14) provide complete usefulness for the application involving the immersion cooling of microprocessors by saturation nucleate boiling of PF-5060, or similar dielectric liquids (such as FC-72) on a rough Cu surface of Ra = 1.79 µm. Additionally, they may extend to other similar arrangements (Figure 6.3) of composite heat spreaders with vapor chambers, heat pipes, or other thermally anisotropic materials, if the R_x, R_z, and C_z terms are known and within the same range investigated (Table 6.1). The next section presents the results on the investigation of the presence of a HOPG layer on the mitigation of chip hot spots.

6.5.5 Effect of Chip Hot Spots

The results presented so far have been for a 20 x 20 underlying chip with uniform heat dissipation. However, microprocessors typically dissipate heat non-uniformly, owing to the high transistors densities in some spots, referred to as hot spots. Mitigating hot spots has been a subject of extensive investigations (Hamann et al. 2006; El-Genk and Ali, 2012; Bar-Cohen and Wang, 2012), because the high local temperatures and induced thermal stresses shorten the serviceable lives of microprocessors life (Wu et al. 2002; Semenov et al. 2006). Additionally, the propagation of heat fluxes generated at hot spots to the exposed surface of the spreader cooled by nucleate boiling could cause a dryout (Revellin et al. 2008), damaging the chip. Thus, along with the effect of the hot spots on the maximum chip temperature, the present analyses also investigated the propagation of hot spots to the exposed rough Cu surface of the composite spreaders.

The first portion of this investigation involved a single chip central hot spot (CHS). A uniform heat flux of was applied to the chip, with a small area representing the hotspot (Figure 6.5a) at the center of the chip. Three CHSs were simulated: (i) 0.5 x 0.5 mm with HFR 5, (ii) 1.0 x 1.0 mm with HFR 10 and (iii) 0.1 x 0.1 mm with HFR 7.5. For all three cases, δ was varied from 0 – 1 mm. The temperature profile at the hot spot was obtained from the numerical solution, and ΔT_{hs}, the resulting rise in the maximum chip temperature due to the hot spot was determined. ΔT_{hs} is the difference in maximum chip temperature with and without the hot spot. In the second portion of this section, all five hot spots were activated (Figure 6.5b), sized 1.0 x 1.0mm with HFR 10. Both investigations determined the reduction of power removed at 90% CHF, due to the presence of the hot spots.

Figure 6.19 show the CHS size and HFR strongly affects ΔT_{hs}. For the chip with 0.5 x 0.5mm CHS and HFR = 5, ΔT_{hs} is only 2.52^{o}C, but increases to ~11 ^{o}C for the same chip, but with a larger 1.0 x 1.0 mm CHS and higher HFR=10. The thermally anisotropic spreaders, although significantly enhance the total thermal power dissipated by the underlying chip and removed by nucleate boiling from the spreaders surface, do little to mitigate the effect of hot spots on the maximum chip temperature. These results are consistent with those of Bar-Cohen and Wang (2012), indicating that only the material properties at the hot spot, affect ΔT_{hs}. Therefore, the HOPG in the composite heat spreader has neither a positive nor negative impact on thermal hot spots.

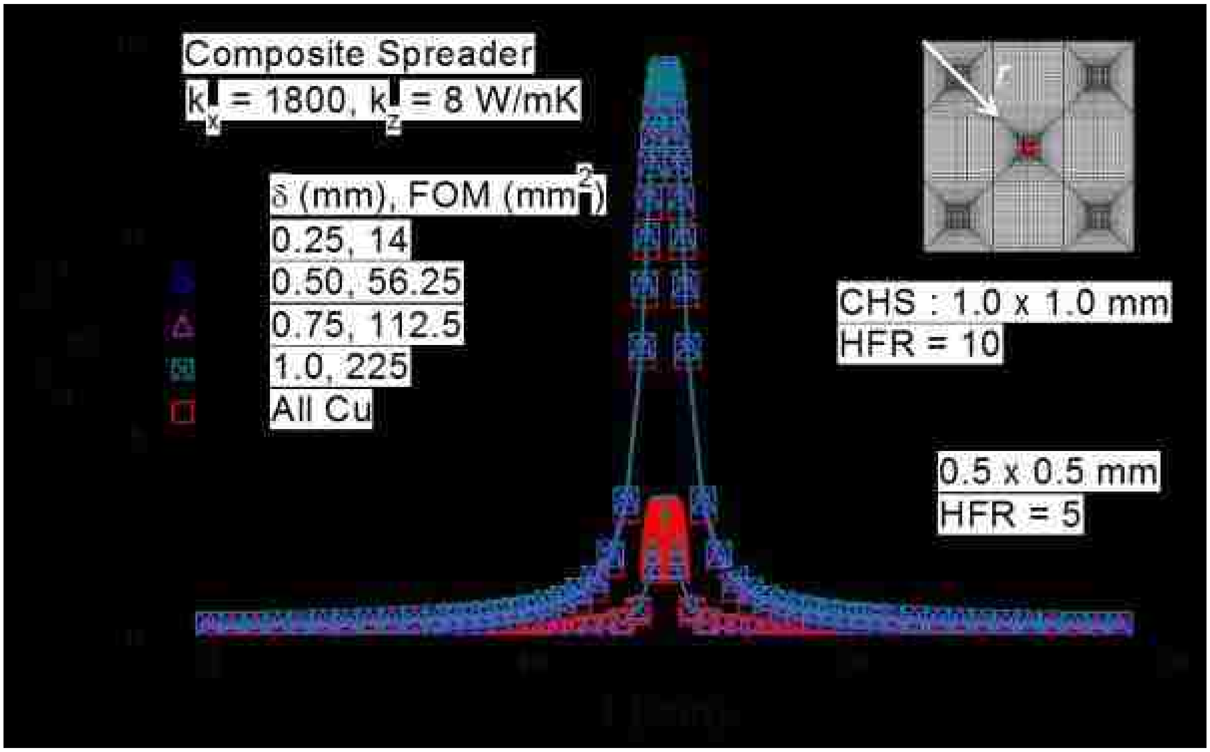

Figure 6.19. The temperature profile at the center of the chip with a central hot spot.

The main benefit of the thermally anisotropic HOPG layer is in its ability to prevent the heat flux generated at chip hot spots from propagating to the boiling surface, potentially causing early dryout at the surface analogous to those shown by Revellin et al. (2008). The performed analyses for the 20 x 20 mm underlying chip having five 1.0 x 1.0 mm hot spots with HFR= 10, show that the all Cu spreader removes ~88 W, which is ~7% lower than without the hot spots. On the other hand, the reduction in the total power removed by the composite spreaders with $\delta = 0.25$ mm and 0.5 mm is negligible, ~0.2% and ~0.1%, respectively. Increasing the thermally anisotropic layer thickness or increasing the *FOM* effectively suppresses the propagation of the hot spots to the exposed surface of the composite spreaders. With the composite spreaders, the total thermal powers removed with and without multiple hotspots are nearly the same.

Figure 6.20 presents 2-D images for comparing the local nucleate boiling heat fluxes, q_{nb}, on the exposed surfaces of an all Cu, and four 30 x 30 mm composite spreaders for a 20 x 20 mm underlying chip with five 1.0 x 1.0 mm hot spots (Figure 6.5b). The heat flux contours show that increasing the thickness, or *FOM* of the composite spreader, improves the uniformity of the local heat flux at the exposed surface of the spreader. The second row in Figure 6.20 shows the normalized (by ^{o}C) surface temperature distributions, to that of $T_{s,min}$, along the diagonal of the composite spreader surfaces, cooled by saturation nucleate boiling of PF-5060 dielectric liquid. The all Cu spreader propagates the local heat fluxes at the hot spots to the spreader surface, as indicated by the steep increases in normalized surface temperature (Figure 6.20a). Conversely, for the composite spreaders, despite the higher thermal power removed, exhibit relatively uniform distributions of surface temperature (Figure 6.20b-e). The uniformity of the surface temperature, indicating suppression of hot spots, increases noticeably with increasing δ or *FOM* of the composite spreaders.

When all five hot spots were activated, the all Cu spreader sized 30 x 30 x 1.25mm removed ~88W before 90% CHF, which is ~7% lower than that without any hot spots. The slight increase in power removed compared to the case of the CHS is due the further proximity of the additional hot spots from the center of the spreader, where CHF is typically first reached. Likewise, the reduction in total power removed for the composite spreaders with the five hot spots present is 0.2% for $\delta = 0.25$ mm and 0.1% for δ = 0.5 mm, which are also less than for the cases of the CHS. Thus, the HOPG layers are effective at preventing heat fluxes generated by chip hot spots from propagating to the surface of the spreader. These results are summarized in Table 6.2.

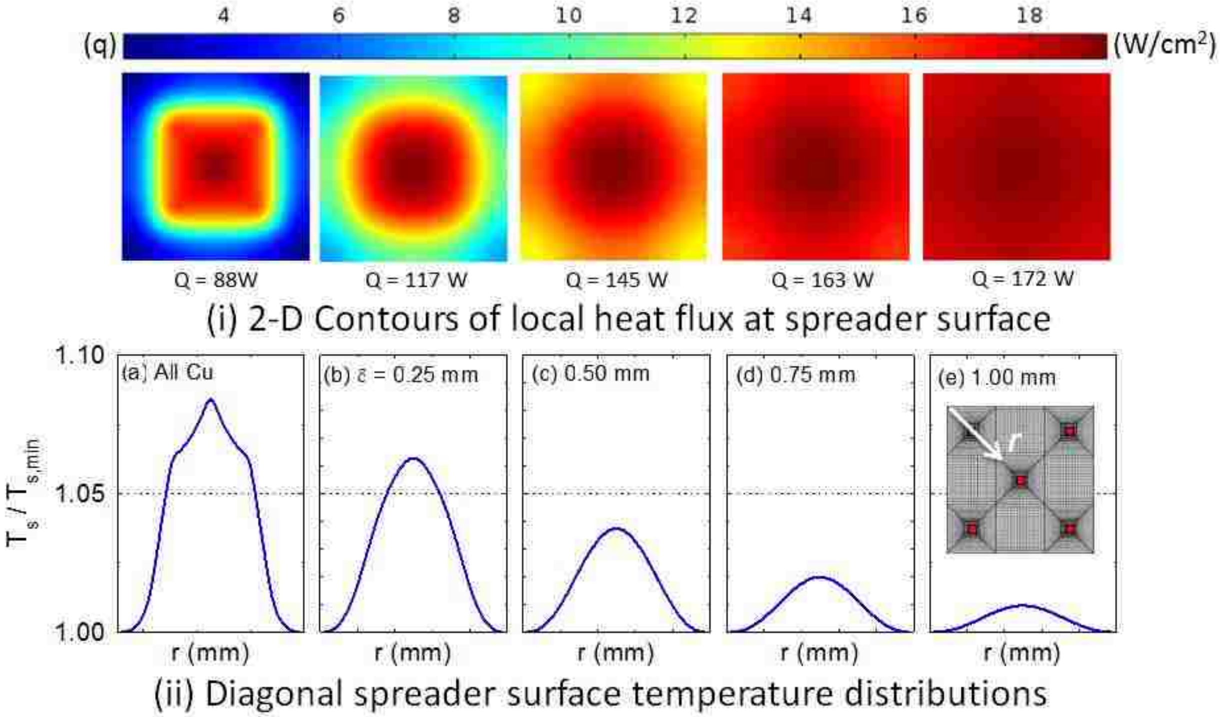

Figure 6.20. Surface power removed (row 1) and normalized temperature (row 2) of 30 x 30 mm spreaders with 5x hot spots for δ = (a) 0.0 mm, (b) 0.25 mm, (c) 0.50 mm, (d) 0.75 mm, and (e) 1.00 mm.

Table 6.2. Percentage of reduction of power removed with for a chip with hot spots present.

Chip Analyzed	All Cu	δ = 0.25 mm	δ = 0.50 mm
1x hs, 1.0x1.0 mm, HFR=10	11	2.8	1.1
5x hs, 1.0x1.0 mm, HFR=10	6.9	0.2	0.1

6.5.6 Effect of Spreader Surface Aging

Surface aging could influence immersion nucleate boiling cooling performance of high powered microprocessors, which could be expected to operate uninterrupted for years. Thus, quantifying the effect of surface aging on the total thermal power removed and the maximum temperature of the underlying chip is critical for ensuring long-term and reliable operation. This issue is investigated in this section, for all-Cu, and thermally anisotropic composite spreaders, for cooling an underlying 20 x 20 mm chip with uniform heat dissipation. Chapter 4.4 presented the effect of surface oxidation on the saturation nucleate boiling heat of PF-5060. Surface oxidation, or aging, increased the average roughness, Ra, from 1.79 to = 1.83 μm. For practical consideration, the exposed rough Cu surface of the composite spreaders investigated in this work gradually age.

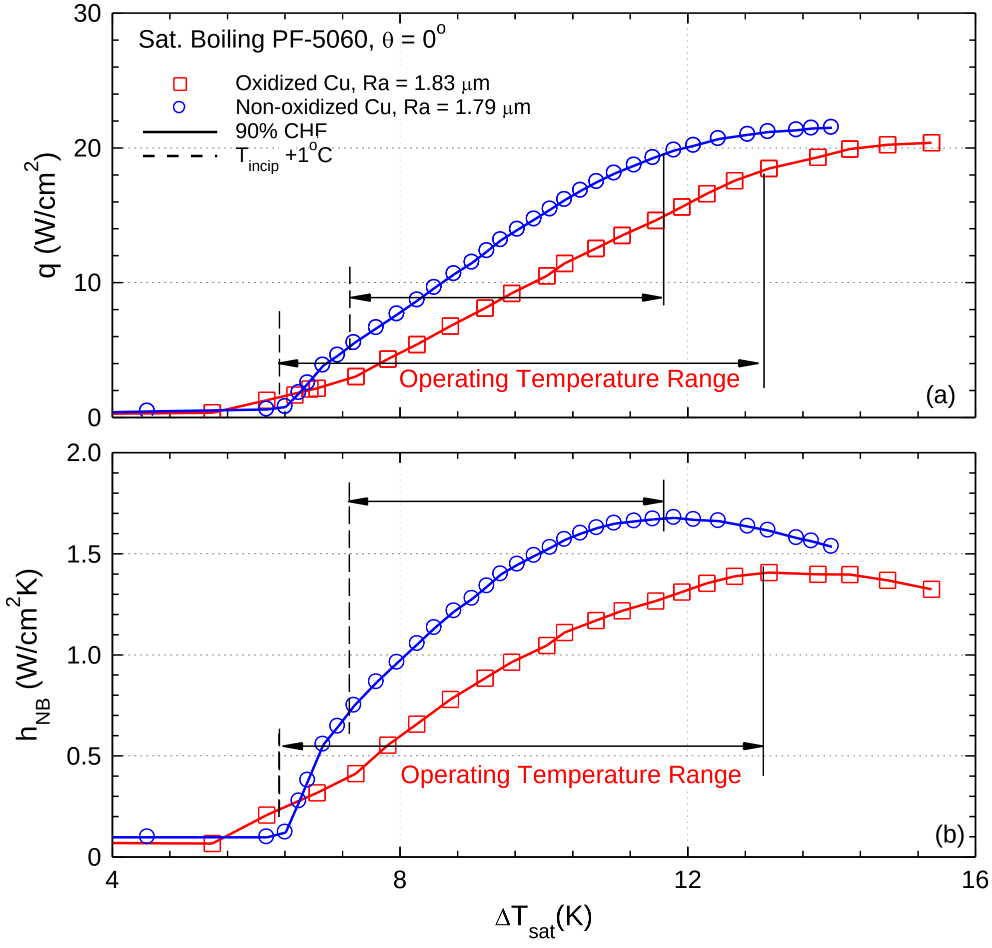

Figure 6.21 Comparisons of the experimental boiling curve of saturation nucleate boiling of PF-5060 dielectric liquid on oxidized and non-oxidized rough Cu

Despite the ~18% and ~5% decreases in h_{NB} and CHF, respectively, on the aged Cu surface (Figure 6.21), the wider range of the surface temperature for that surface (Figure 6.21) slightly enhances the maximum power, *Q**, removed by the composite spreaders. The range extending from that at 90% CHF, to 1.0 °C higher surface temperature than at incipient boiling in the experiments, is wider for the aged Cu surface than of the non-aged Cu surface. The wider temperature range increases the width of the composite spreaders, w^*, and subsequently the total thermal power removed, Q^* (Figure 6.22a and b). For a composite spreader with an aged Cu surface and *FOM* = 225, the maximum thermal power removed, Q^* ~333 W, and the corresponding spreader width, w^* of ~67 mm, are ~ 5 % higher and 24% larger than for the same spreader, but with a non-aged Cu surface.

On the other hand, the composite spreaders with an aged Cu surface remove ~5% less power than the spreaders with non-aged Cu surfaces, but of the same width, *w*. As shown in Figure 6.21, the CHF in the experiments with the aged Cu surface was ~5% lower than on the non-aged surface, which corresponds closely to the reduction of power for the same *w*, in Figure 6.22a. Additionally, for the same total power removed *Q*, the results in Figure 6.22b show that lower surface average h_{NB} on the aged Cu only slightly increases $T_{chip,max}$ of the underlying chip. These results suggest that aging of the exposed Cu surface of the composite spreaders, would minimally impact their long term performance.

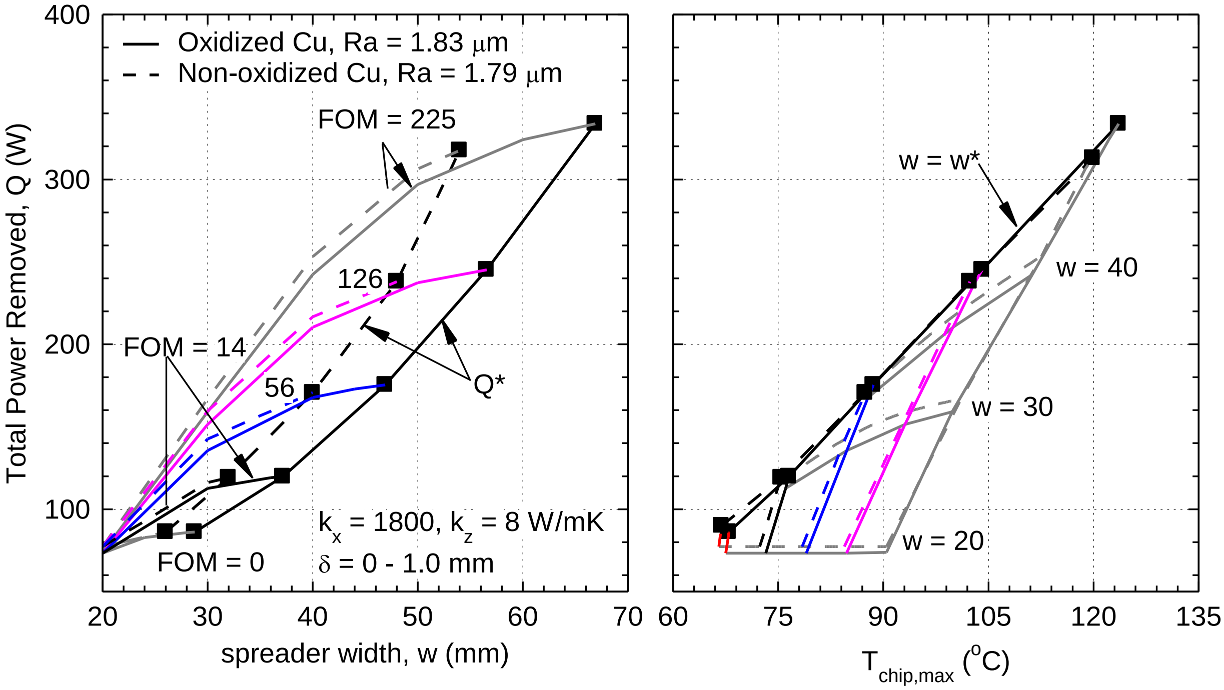

Figure 6.22. Effect of surface oxidation (or aging) on the total power removed by composite spreader and the maximum surface temperatures of the underlying 20 x 20 mm chip, with uniform heat dissipation.

6.6 Manufacturing Challenges

The present analyses of the thermally anisotropic heat spreaders with rough Cu surfaces demonstrated large increases in the total power dissipated by the 20 x 20 underlying chip and removed by the spreaders, with moderate, but acceptable increases in the chip maximum surface temperatures. These temperatures remain within the range recommended by the chip manufacturers (~85 – 125 ^{o}C) (ITRS, 2013). However, the manufacturability and the materials compatibility for the composite spreaders are important issues, which are discussed briefly herein.

The thermal expansion coefficient of the top and bottom Cu laments of the composite spreaders (~16.5 x10^{-6} K^{-1}) (Lide, 2004) is isotropic and much higher than for pure graphite (~ 2.7x10^{-6} K^{-1} and 2.9x10^{-6} K^{-1} in the parallel (or lateral) and perpendicular directions, respectively) (Tsang et al. 2005). Conversely, the thermal expansion coefficient of Cu is ~ 20% lower than of HOPG (16.6-20 x10^{-6} K^{-1}) in the perpendicular direction. In the lateral direction, the thermal expansion coefficient of HOPG is near zero and may even be slightly negative. These differences in the thermal expansion coefficients, may affect the long-term integrity of the thermally anisotropic layers of the composite spreaders, in different ways, depending on the material of these layers.

The differential thermal expansion between the Cu laments and a thermally anisotropic graphite layer, will subject the latter to tensile stress (tension) in the lateral direction, and compression in the perpendicular direction. Similarly, for the composite spreaders with the more expensive HOPG thermally anisotropic layer the slightly negative lateral thermal expansion of the HOPG, compared to that of Cu, would be under tension. In the perpendicular direction, the slightly higher thermal expansion coefficient of HOPG than that of Cu will help maintain good thermal contact with the HOPG layer. While the thermals stresses will be orders of magnitudes lower than the ultimate tensile or the compressive stresses of either materials, the common interfaces between need to be able to handle small cyclic loads (~0.01 Pa) over very long periods of time (~years). Therefore, a future investigation of the induced thermal stresses and the effect on the structural integrity of the thermally anisotropic spreaders would be useful. Nonetheless, the effect is expected to be small, owing to the low saturation boiling temperature of the PF-5060 dielectric liquid and narrow operating temperature range (Figure 6.4a).

As of the thermal resistance at the interfaces between the Cu filaments and the thermally anisotropic layer of the composite spreaders, new techniques could actually grow graphite and HOPG on Cu surfaces seeded with precursors (Li et al. 2009). Investigating the fabrication cost and the cost-added value of the composite spreaders, including comparing the results to those of the alternatives for immersion nucleate boiling cooling of high powered microprocessors, is a worthy investigation.

7. Summary and Conclusions

This research experimentally investigated the enhancement of pool nucleate boiling of PF-5060 dielectric liquid on uniformly heated, 10 x 10 x 1.6 mm rough and dimpled Cu surfaces. Fabricating these surfaces is cost effective and scalable, making them suitable for immersion nucleate boiling cooling of high powered microprocessors requiring heat spreaders of different sizes. The PF-5060 has a saturation temperature of 51.4^{o}C at ~0.085MPa – the local pressure in Albuquerque NM, where the experiments were carried out. Because various circuit board orientations and the perpendicular mounting of add-in cards, such as graphics processing units, results in chip orientations that vary from 0^{o} – 180^{o} with respect to gravity, the effects of these surface inclinations on nucleate boiling of saturated and subcooled PF-5060, are thoroughly investigated on both the rough and dimpled Cu surfaces. In the experiments, liquid subcooling varied up to 30 K.

Results on the effect of the average surface roughness, (Ra = 0.039 – 1.79µm), inclination angle ($\theta = 0^{o} - 180^{o}$), and liquid subcooling (ΔT_{sub} = 0 – 30 K) on the enhancement of nucleate boiling and Critical Heat Flux (CHF), on rough and dimpled Cu surfaces were presented and discussed throughout the dissertation. Developed correlations for h_{NB} and CHF, which agree well with the experimental results, are compared with others. Experimental nucleate boiling heat transfer coefficient curves for the rough Cu surface with Ra = 1.79 µm, were used to computationally investigate the performance of thermally anisotropic composite heat spreaders. These spreaders, cooled by saturation nucleate boiling of PF-5060 dielectric liquid, are capable of removing larger amounts of thermal power dissipated by a 20 x 20 mm microprocessor with and without hot spots, than of an all Cu spreader.

Results of systematic investigation of the natural convection, fully developed nucleate boiling region, maximum nucleate boiling heat transfer coefficient, h_{MNB}, and CHF was presented. The pool boiling facility, test section, and experimental preparations and procedures designed to minimize uncertainties and provide reproducible results were discussed. To ensure the consistency of the results, all pool boiling experiments reported in this dissertation are for degassed PF-5060 liquid and uniformly heated 10 x 10 x 1.6

mm Cu surfaces. Multiple experiments performed for the same conditions, separated by at least 2 hours, and sometimes a few days, verified the reproducibility of the results. The absence of boiling hysteresis confirmed no influence of the thermal inertia of the heated Cu surface on the nucleate boiling, but rather the thermophysical properties of the PF-5060 dielectric liquid and surface characteristics solely influenced the nucleate boiling results.

High speed visualization of nucleate boiling on the rough and dimpled Cu surfaces was conducted to determine the effects of the surface roughness or the dimple size on the dynamic growth of discrete bubbles, at an applied heat flux of ~0.5W/cm^2. The bubble departure diameter and detachment frequency were obtained, and used in conjunction with the experimental pool boiling curves to estimate the number of active nucleation sites density on the Cu surfaces of different roughness, and compared with the estimates for others on microstructured and porous surfaces in dielectric liquids.

In the upward facing surface inclination ($\theta = 0^o$), increasing surface roughness, Ra, from 0.039 to 1.79 µm, increased the maximum nucleate boiling heat transfer coefficient, h_{MNB}, by as much as ~150%, and CHF by ~39%. The h_{MNB}, increased proportional to Ra to the power ~0.23, which is slightly higher than reported in the literature for other liquids and surfaces (Danilova and Bel'skii, 1965; Nishikawa et al. 1982; Jones et al. 2009; Jabardo, 2010). The h_{MNB} increased from ~0.67 W/cm^{2}K for Ra = 0.039 µm, to ~1.65 W/cm^{2}K for Ra = 1.79 µm. The corresponding values of CHF increased proportionally to Ra to the power ~0.08, from ~15.5 W/cm^2 to ~21.5 W/cm^2, respectively. The data of the nucleate boiling heat transfer coefficient, h_{NB}, was correlated as: $h_{NB} = Aq^B$. The coefficients "A" and exponent "B" are both functions of Ra. As Ra increases from 0.039 to 1.79 µm, the coefficient "A" increases from 0.09 – 0.23, while the exponent "B" decreases from 0.81 – 0.69, which is consistent with the results reported by others (Kozitskii, 1971; Nishikawa et al. 1982; Cooper, 1984).

The effect of the inclination angle on the nucleate boiling of PF-5060 on rough Cu surfaces is independent of surface roughness. For all rough Cu surfaces investigated, h_{MNB} values in the downward facing orientation are ~40% of their values in the upward facing orientation. Similarly, the CHF decreased monotonically with increased inclination angle to the lowest values in the downward facing orientation, which are

~31% of the values in the upward facing orientation. These results are consistent with those reported by others for dielectric liquids on plain Cu (Priarone, 2005; El-Genk and Bostanci, 2003), microporous coatings (Rainey and You, 2000), porous graphite (El-Genk and Parker, 2008) and others on rough surfaces (Howard and Mudawar, 1999; El-Genk, 2012, Parker and El-Genk, 2009).

In the upward facing orientation ($\theta = 0^o$), the CHF increased with increased liquid subcooling, ΔT_{sub} at a rate of 2.2%/K. This rate is similar to those reported by others for other surfaces in FC-72 and PF-5060 dielectric liquid (Honda et al., 2002; Wei and Honda, 2003; Sathyamurthi et al., 2009). This rate of increase is independent of the Ra, but increases with increasing inclination angle, to a maximum rate of 4.0%/K in the downward facing orientation ($\theta = 180^o$).

The developed correlations for h_{NB}, h_{MNB}, and CHF, as functions of Ra, θ, and ΔT_{sub}, are in good agreement with the experimental data to within ± 8%, ± 8%, and + 12%, respectively. The developed h_{NB} correlation falls within the middle of the range of other established correlations (Cooper, 1984; Gorenflo 1993; Jabardo, 2003). However, the range of applicability by the present correlation is much narrower than those of others (Cooper, 1984; Gorenflo 1993; Jabardo, 2003).

The transient growth of the discrete bubbles in saturation nucleate boiling of PF-5060 on smooth (Ra = 0.039 µm) and rough Cu surfaces (Ra = 0.33 µm, 0.80 µm, 0.925 µm, and 1.44 µm) at an applied heat flux of ~$0.5 W/cm^2$, were recorded at ~210 fps using a high speed camera. To improve the statistics, the transient bubble growth at a number of selected discrete sites on each surface was captured for as many as six sequential ebullition cycles. The results showed that regardless of Ra, the bubble diameter increased proportional to the square root of time. The same trend was measured for smooth Cu, except the rate of bubble growth and the bubble departure diameter, D_d, and detachment frequency, f_d, are higher than those measured on the rough Cu surfaces. The measured values of D_d on the smooth and on the rough Cu surfaces are 655 ± 53 and 438 ± 36 µm, respectively, with corresponding f_d values of 31 ± 4 and 38 ± 3Hz, respectively. On the rough Cu surfaces (Ra ≥ 0.21 µm), the measured values of the D_d and f_d are 438 ± 36 µm and 38 ± 3 Hz, respectively, and independent of surface roughness. The present values of the D_d are within a the range of values reported by others for FC-72 dielectric liquid on various surfaces; however, the values of the f_d are generally much lower (Rinni et al. 2001; Ramswamy et al. 2002; Demiray and Kim 2004; Nikmar et al. 2006; Hutter et al. 2010; McHale and Garimella 2008, 2013);

The determined D_d and f_d were used in conjunction with the experimental nucleate boiling curves, along with the estimated total wetted surface areas of the rough Cu surfaces, to estimate the surface average density of active nucleation sites, N, based on the footprint area, as a function of the surface superheat. Results showed the value of N increases with increasing Jakob number, Ja, or the applied heat flux. For smooth Cu (Ra = 0.039 µm), the values of N increase from 100 cm^{-2} at boiling incipience, to 2,000 cm^{-2} at the maximum nucleate boiling heat transfer coefficient, h_{MNB}. Those for the rough Cu surfaces increase from 700 cm^{-2} to as much as 10,000 cm^{-2}. Therefore, rough surfaces enhance nucleate boiling by increasing of density of active sites for bubbles nucleation.

The performed pool boiling experiments also investigated nucleate boiling of PF-5060 on uniformly heated 10 x 10 x 1.6 mm dimpled Cu surfaces. The dimples, with diameters Φ_d = 300, 400, and 500 µm, are arranged in a triangular lattice with a fixed pitch-to-diameter ratio of 2.0. Thus, the total number of the dimples on the 10 x10 Cu surfaces decreased from 295 to 105, with decreasing the dimple diameter from 300 to 500 µm. However, the wetted geometrical surface area with the 300, 400, and 500 µm dimples, compared to that of the footprint (10x10 mm), increased by 35%, 19% and 13%, respectively.

The rate of heat removal by natural convection on the dimpled surfaces is ~16% higher than on measured on the rough Cu surfaces in this work, and independent of the diameter of the manufactured dimples. The enhancements in h_{NB} and CHF are similar to those reported for rough Cu surfaces of Ra = 0.039 – 0.33 µm. For saturation boiling in the upward facing inclination, the values of h_{MNB} and CHF, on the surface with the 400 µm diameter dimples, of ~1.06 W/cm^2 K and ~19.3 W/cm^2, respectively, are the highest. The values on the Cu surface with the 500 µm diameter dimples are ~1.0 W/cm^2 K and ~18.3 W/m^2, respectively. The surface with 300 µm diameter dimples consistently gave the lowest h_{MNB} and CHF values, ~0.7 W/cm^2 K and ~18 W/cm^2, respectively.

The effect of inclination angle on saturation boiling of PF-5060 on the dimpled Cu surfaces is similar to that reported on smooth and rough Cu surfaces. The relative changes in h_{MNB} and CHF for saturation boiling of PF-5060 on the dimpled Cu surfaces, at different inclinations (0^o – 180^o) were correlated to within $\underline{+}9\%$ and $\underline{+}5\%$ of the experimental data, respectively. In the upward facing orientation, CHF values on the dimpled Cu surfaces, increases linearly with increasing liquid subcooling at a rate of 1.83%/K. This rate is 20% lower than those obtained on smooth and rough Cu surfaces. Increasing the liquid subcooling not only extends the fully developed nucleate boiling region and increases CHF, but also increases the corresponding surface superheats at both h_{MNB} and CHF.

At an applied heat flux of ~0.5 W/cm^2, sequential images of growing bubbles on the dimpled Cu surfaces were captured using a 210 fps high speed video camera. The images showed that the growing bubbles are associated with dimple cavities, and their departure diameter and detachment frequency increase with increasing the dimple diameter. Bubble nucleation on the flat potion of the heated Cu surfaces between dimple cavities was rare, due to insufficient surface superheat. The temperature on the inside of the manufactured dimples, closer to the underlying heating element, is higher, promoting nucleation of vapor embryos. The growing embryo coalesces into a larger bubble, before emerging from the dimple, and continuing to grow. The recorded sequential images of the bubbles spanned the period from when the bubble was first seen emerging from the dimples, until the last frame before departure.

The bubble growth rate, departure diameter, and detachment frequency increase, but the growth time decreases with increasing the dimple diameter. The volumetric growth rate of the bubbles at departure, on the surfaces with the 300, 400, and 500 µm diameter dimples, is ~1.81,~ 4.75 and ~8.2 mm^3/s, respectively. The corresponding vapor generation rate of the bubbles is ~21, ~54, and ~94 µg/s, respectively. The major contributions of bubble growth are from the evaporation at the triple interface along the perimeter of the dimples, and the thin liquid film evaporation on the inside surface of the dimples. This film is replenished with liquid from the surrounding pool by the wicking action due to the roughness of the inside surface of the dimples. Increasing the dimple diameter also increases both the departure diameter and detachment frequency of the dimple bubbles. The determined departure bubble diameter on the surfaces with 300 µm, 400 µm, and 500 µm diameter dimples is ~738 $\underline{+}$ 61 µm, ~963 $\underline{+}$ 75 µm, and ~1051 $\underline{+}$ 73 μm, and the corresponding detachment frequency is ~ 8.6 ± 0.7 Hz, ~10.2 ± 1.0 Hz and ~13.5 ± 1.8 Hz, respectively. These values of are much larger and lower than on the same sized rough Cu surfaces at the same applied heat flux.

At the applied heat flux of ~ 0.5 W/cm^2, the fraction of the active dimples for bubble growth decreases, but the volume of the dimple bubbles at departure increases with increasing the dimple diameter. The estimated fractions of active dimples is ~0.85, ~0.64, and ~0.53 for the 300 μm, 400 μm, and 500 μm diameter dimpled surfaces, respectively. The corresponding dimple bubble volume at departure is ~ 0.21 mm^3, ~ 0.47 mm^3 and ~ 0.61 mm^3, and the amount of thermal energy removed by a single departing bubble is ~1.99 mW, ~5.24 mW, and ~ 9.02 mW, respectively.

The local dryout that triggers CHF occurs when the thickness of the thin liquid film on the inside of the active dimples decreases and no longer replenishes the surface with liquid from the surrounding pool, causing a dryout. Since the rate for liquid replenishment depends on the depth and the perimeter, or the diameter, of the dimples, the CHF is the lowest for the Cu surface with the smallest diameter (300 μm) dimples that have diameter-to-depth ratios of 1.5. This ratio is larger at 2.0 and 2.5 for the 400 μm and 500 μm dimpled surfaces, for which CHF values are the highest, but very close.

Overall, the results demonstrate that dimples significantly affect the bubble growth rate, departure diameter and detachment frequency, and the enhancement in nucleate boiling performance. The large number, and hence the smaller spacing of the 300 μm diameter dimples on the 10x10 mm Cu surface may have slowed the growth and increased the growth time of the dimple bubbles, as close adjacent dimples may have resided within a sphere of influence by the growing dimple bubble. This could explain the lowest h_{NB} on the surface with 300 μm diameter dimples. Future work may consider investigating the effect of the dimples' lattice (square versus triangle) and pitch on nucleate boiling enhancement and the transient growth of dimple bubbles.

The performed 3-D numerical thermal analyses of thermally anisotropic heat spreaders for 20 x 20 mm underlying high power chip with uniform heat dissipation, 0.5 x 0.5 and 1.0 x 1.0 mm central hot spots, and five 1.0 x 1.0 mm hotspots, with local heat flux ratios up to 10 times that of the chip average (HFR = 10), demonstrated superior power removal capability of these spreaders. The spreaders are comprised of two 0.5

mm-thick Copper (Cu) laments separated by a thin thermally anisotropic layer ($\leq$ 1.0 mm), representing graphite or highly oriented pyrolytic graphite (HOPG). The exposed Cu surface of the spreaders, with an average roughness, Ra = 1.79 µm, is cooled by saturation nucleate boiling of PF-5060 dielectric liquid. The analyses investigated the effects of the thickness and thermal conductivities (k_x = 325 – 2000 W/mK, and k_z = 5 – 20 W/mK) of the anisotropic layer on the total thermal power removed by nucleate boiling from the spreader surface, the total thermal resistance of the spreader, and the maximum temperature of the underlying chip. The range of the spreader surface temperature extends from that corresponding to 90% of CHF to 1.0 ^{o}C above that for incipient boiling in the performed experiments. The analyses also investigated the effect of oxidation (or aging) of the exposed Cu surface, on the spreaders performance and the maximum surface temperature of the underlying chip.

The composite spreaders are capable of removing in excess of 227 W at a chip maximum temperature of ~ 88 ^{o}C. The total thermal power removed is as much as 4 times that removed by an all Cu spreader with thickness of 1 – 2 mm. The total thermal resistances of the composite spreaders range from 0.16 – 0.4 ^{o}C/W, depending on the material properties and thickness of the thermally anisotropic layer, as well as the spreader size. These thermal resistances are comparable to those of high performance microchannels spreaders cooled by forced convection of liquid.

The developed empirical correlations for the composite spreaders calculate the total thermal power removed and the width of the square spreaders as functions of the Figure-of-Merit (*FOM*) of the anisotropic layer. The empirical correlation that predicts the thermal power removed agrees to the computed data to within $\pm$ 7%. Increasing the *FOM* from 0 (all Cu) to 400 (highly anisotropic) increases the total thermal power removed from ~88 to ~450 W, and corresponding width of the spreader from ~25 to ~69 mm. Additionally, the thermally anisotropic layer successfully prevents the propagation of hot spots in the underlying chip, to the exposed surface of the composite spreaders. The computed results of the chip maximum temperature, $T_{\mathrm{chip,max}}$, are correlated in terms of axial conductance of the thermally anisotropic layer, C_z, and the total thermal power removed, Q. This developed correlation agrees to the computed results to within $\pm$ 1%.

Aging the Cu surface of the spreaders decreases h_{NB} and CHF, but increases the operating temperature range for nucleate boiling at the exposed surface of the spreader. This increases the maximum total power removed, as well as the maximum width of the spreader, but at the expense of increasing $T_{\mathrm{chip,max}}$. For a composite spreader with an aged Cu surface and FOM = 225, the maximum thermal power removed, Q^* of ~333 W, and corresponding spreader width, w^* of ~67 mm, are 5% higher and 24% larger than of the same spreader, but with a non-aged surface, and smaller corresponding w^*. However, for the same FOM and same spreader size, w, the total powered removed decreases ~5%, which corresponds closely to the decrease in CHF seen in the experiments with the aged Cu surfaces. Additionally, for the same power removed Q, the lower surface average h_{NB} on the aged Cu surface only slightly increases $T_{\mathrm{chip,max}}$ of the underlying chip. These results suggest that aging of exposed Cu surface minimally impacts long term nucleate boiling cooling performance.

For electronics cooling applications, thermally anisotropic spreaders are highly promising for high power microprocessors with total thermal power dissipations in excess of 150 W. The developed empirical correlations in this work are useful design and performance assessment tools, subject to the same composite spreader material properties, dielectric liquid PF-5060 or similar (such as FC-72), and the size of the chip investigated in this work.

In conclusion, thermally anisotropic spreaders with scalable surfaces that enhance nucleate boiling, such as rough or machined circular dimples, are highly recommended for immersion nucleate boiling cooling of PF-5060 for high power computer chips with total thermal power dissipations in excess of 150 W. For microprocessors concerned with maximum operating temperatures, higher through-plane thermal conductivities and thinner thermally anisotropic layers are desirable, however at the reduction of the power removal capability of the spreader. Additionally, the $T_{\mathrm{chip,max}}$ may be reduced by increasing the operation margin of maximum nucleate boiling heat flux at the spreader to > 20% from CHF.

Recommendations for Future Work

Based on the current review of the literature and the results obtained in this research, future research may consider:

(1) *Investigating surfaces of modified hydrophobicity in highly wetting dielectric liquids*. In an attempt to separate the effect of the surface roughness parameter from that of the surface wetting, researchers have recently begun to investigate the pool boiling of water on surfaces of varying hydrophobicity. The research conducted in this dissertation investigated nucleate boiling of highly wetting PF-5060 dielectric liquid on rough Cu surfaces. A good follow up research may investigate highly wetting PF-5060 dielectric liquid on surfaces of nearly fixed roughness, but modified hydrophobicity or surface wettability. Techniques to accurately measure the near zero contact angle of PF-5060 would need to be developed and verified.

(2) *Performing experimental investigation of nucleate boiling on dimpled surfaces*. Working with dimples surfaces to examine nucleate boiling at the locations of the dimples, these surfaces may provide much needed insight of the nucleation of vapor embryos. More parameters to be investigated for the nucleate boiling on dimpled surfaces include a wider range of dimple diameter, varying dimple depths, and pitch-to-diameter ratios of triangular and square lattices. In addition, investigating the effect of roughness on the inside surface of the dimples on nucleate boiling enhancement, along with the transient growth, departure diameter and detachment frequency of the dimple bubbles would be a worthy contribution.

(3) Experimentally validate the obtained numerical results on the performance of thermally anisotropic heat spreaders for immersion cooling of high powered microprocessors. A low cost option that utilizes a thin graphite layer was presented, and may serve as a low cost experimental validation.

8. References

3M, Technical Data Sheets, (2015), www.3M.com

Advanced Micro Devices Corporation, (2015), www.amd.com

Allied Control Corporation, (2015), www.allied-control.com/immersion-cooling

Abbasi, Bahman, and Jungho Kim. "Prediction of PF-5060 spray cooling heat transfer and critical heat flux." Journal of Heat Transfer 133.10 (2011): 101504.

Ahmad, S. W., Karayiannis, T. G., Kenning, D. B. R., & Luke, A. (2011). Compound effect of EHD and surface roughness in pool boiling and CHF with R-123. Applied Thermal Engineering, 31(11), 1994-2003.

Ahn, H. S., Kim, J., & Kim, M. H. (2012). Investigation of pool boiling critical heat flux enhancement on a modified surface through the dynamic wetting of water droplets. Journal of Heat Transfer, 134(7), 071504.

Anandan, S. S., & Ramalingam, V. (2008). Thermal management of electronics: A review of literature. Thermal science, 12(2), 5-26.

Anderson, T. M., & Mudawar, I. (1989). Microelectronic cooling by enhanced pool boiling of a dielectric fluorocarbon liquid. Journal of Heat Transfer, 111(3), 752-759.

Arik, M., Bar-Cohen, A., & You, S. M. (2007). Enhancement of pool boiling critical heat flux in dielectric liquids by microporous coatings. International journal of heat and mass transfer, 50(5), 997-1009.

Bahadur, R., & Bar-Cohen, A. (2005). Thermal design and optimization of natural convection polymer pin fin heat sinks. Components and Packaging Technologies, IEEE Transactions on, 28(2), 238-246.

Balandin, A. A., Ghosh, S., Bao, W., Calizo, I., Teweldebrhan, D., Miao, F., & Lau, C. N. (2008). Superior thermal conductivity of single-layer graphene. Nano letters, 8(3), 902-907.

Bar-Cohen, A., & Wang, P. (2012). Thermal management of on-chip hot spot. Journal of Heat Transfer, 134(5), 051017.

Beduz, C., Scurlock, R. G., & Sousa, A. J. (1988). Angular dependence of boiling heat transfer mechanisms in liquid nitrogen. In Advances in cryogenic engineering (363-370). Springer US.

Benjamin, R. J., & Balakrishnan, A. R. (1996). Nucleate pool boiling heat transfer of pure liquids at low to moderate heat fluxes. International Journal of Heat and Mass Transfer, 39(12), 2495-2504.

Berenson, P. J. (1962). Experiments on pool-boiling heat transfer. International Journal of Heat and Mass Transfer, 5(10), 985-999.

Bico, J., Thiele, U., & Quéré, D. (2002). Wetting of textured surfaces. Colloids and Surfaces A: Physicochemical and Engineering Aspects, 206(1), 41-46.

Bon, B., & Klausner, J. (2011, January). Pool boiling heat transfer of highly wetting fluids on smooth metallic surfaces. In *ASME/JSME 2011 8th Thermal Engineering Joint Conference*, American Society of Mechanical Engineers, T10182-T10182.

Brusstar M. J., Merte H., Keller R. B., and Kirby B. J., (1997), "Effects of heater surface orientation on the critical heat flux: I. An experimental evaluation of models for subcooled pool boiling," Int. J. Heat Mass Transfer, 40, 4007-4019.

Campbell, L., & Tuma, P. (2012, March). Numerical prediction of the junction-to-fluid thermal resistance of a 2-phase immersion-cooled IBM dual core POWER6 processor. In Semiconductor Thermal Measurement and Management Symposium (SEMI-THERM), 2012 28th Annual IEEE, 36-44.

Cengel, A. Y., (2002), Heat Transfer: A Practical Approach, McGraw-Hill, 2nd edition., New York, USA.

Chang, J. Y., & You, S. M. (1996). Heater orientation effects on pool boiling of micro-porous-enhanced surfaces in saturated FC-72. Journal of Heat Transfer, 118(4), 937-943.

Chowdhury, S. R., & Winterton, R. H. S. (1985). Surface effects in pool boiling. International Journal of Heat and Mass Transfer, 28(10), 1881-1889.

Chung, D. D. L. (2002). Review graphite. Journal of materials science, 37(8), 1475-1489.

Chung, D. D. L., & Takizawa, Y. (2012). Performance of isotropic and anisotropic heat spreaders. Journal of electronic materials, 41(9), 2580-2587.

Clark, H. B., Strenge, P. S., & Westwater, J. W. (1959). Active sites for nucleate boiling. Chem. Eng. Progr., 55.

Cooper, M. G. (1984, July). Saturation nucleate pool boiling—a simple correlation. In Inst. Chem. Eng. Symp. Ser (Vol. 86, No. 2, 785-793).

Coppola, L., Huff, D., Wang, F., Burgos, R., & Boroyevich, D. (2007, June). Survey on high-temperature packaging materials for SiC-based power electronics modules. In Power Electronics Specialists Conference, 2007. PESC 2007. IEEE (2234-2240). IEEE.

Corty, C., & Foust, A. S. (1953). Surface variables in nucleate boiling.

Danilova, G. N., and Bel'skii, V. K., (1965), "Study of Heat Transfer on Boiling of Freon 113 and Freon 12 on Pipes of Differing Roughness," Kholod. Tekh., 4, 24–28.

Demiray, F., & Kim, J. (2004). Microscale heat transfer measurements during pool boiling of FC-72: effect of subcooling. International Journal of Heat and Mass Transfer, 47(14), 3257-3268.

Drofenik, U., & Kolar, J. W. (2006, June). Analyzing the theoretical limits of forced air-cooling by employing advanced composite materials with thermal conductivities> 400W/mK. In Integrated Power Systems (CIPS), 2006 4th International Conference on VDE, 1-6.

El-Genk, M. S., & Guo, Z. (1993). Transient boiling from inclined and downward-facing surfaces in a saturated pool. International journal of refrigeration, 16(6), 414-422.

El-Genk, M. (2003). Combined effects of subcooling and surface orientation on pool boiling of HFE-7100 from a simulated electronic chip. Experimental heat transfer, 16(4), 281-301.

El-Genk, M. S., and Bostanci, H., (2003a), "Saturation Boiling of HFE-7100 from a Copper Surface, Simulating a Microelectronic Chip," Inter. J. Heat & Mass Transfer, 46, 1841-1854.

El-Genk, M. S., and Bostanci, H., (2003b), "Combined Effects of Subcooling and Surface Orientation on Pool Boiling of HFE-7100 from a Simulated Electronic Chip," Experimental Heat Transfer, 16, 281-301.

El-Genk, M. S., & Ali, A. F. (2010). Enhanced nucleate boiling on copper micro-porous surfaces. International Journal of Multiphase Flow, 36(10), 780-792.

El-Genk, M. S., & Ali, A. F. (2009, January). Saturation Boiling of PF-5060 Dielectric Liquids on Micro-Porous Copper Dendrites Surfaces. In ASME 2009 Heat Transfer Summer Conference collocated with the InterPACK09 and 3rd Energy Sustainability Conferences (847-855). American Society of Mechanical Engineers.

El-Genk, M. S., and Parker, J. L., (2004a), "Pool Boiling in Saturated and Subcooled HFE-7100 Dielectric Fluid From a Porous Graphite Surface," Proceeding 9th Intersociety Conference on Thermal Phenomena, 1, 655-662.

El-Genk, M. S., and Parker, J. L., (2004b), "Pool Boiling in Saturated and Subcooled FC-72 Dielectric Fluid From a Porous Graphite Surface," Proceeding ASME International Mechanical Engineering Congress (IMECE-2004), Paper IMECE2004-59905.

El-Genk, M. S., & Parker, J. L. (2005). Enhanced boiling of HFE-7100 dielectric liquid on porous graphite. Energy Conversion and Management, 46(15), 2455-2481.

El-Genk, M. S., & Parker, J. L. (2008). Nucleate boiling of FC-72 and HFE-7100 on porous graphite at different orientations and liquid subcooling. Energy conversion and management, 49(4), 733-750.

El-Genk, M. S., (2012), "Nucleate Boiling Enhancements on Porous Graphite and Micro-porous and Macro-Finned Copper," Heat Transfer Engineering, 33(3), 175-204, 2012

El-Genk, M. S., and Saber, H. H., (2006), "Composite Spreader for Submersion Cooling of a Computer Chip with Non-Uniform Heat Dissipation," Proceeding Thermal and Thermomechanical Phenomena in Electronic Systems, and 10th intersociety conference (ITHERM 2006), 591-598.

El-Genk, M. S., and Saber, H. H., Parker, J. L., (2005), "Efficient Spreaders for Cooling High-Power Computer Chips," Applied Thermal Engineering, 27, 1072-1088.

El-Genk, M. S., Saber, H. H., & Parker, J. (2005, January). Thermal analyses of composite copper/porous graphite spreaders for immersion cooling applications. In ASME 2005 Pacific Rim Technical Conference and Exhibition on Integration and Packaging of MEMS, NEMS, and Electronic Systems collocated with the ASME 2005 Heat Transfer Summer Conference (305-314). American Society of Mechanical Engineers.

El-Genk, M. S., & Saber, H. H. (2008). Composite spreader for cooling computer chip with non-uniform heat dissipation. Components and Packaging Technologies, IEEE Transactions on, 31(1), 165-172.

El-Genk, M., & Ali, A. F. (2013). Saturation Boiling on MPC: Effects of Thickness, Inclination Angle, Transient Bubble Growth, and Nucleation Site Density, *Multiphase Science and Technology, 25*(2-4).

El-Genk, M. S., Suszko, A., & Ali, A. F. (2013, November). Effects of surface roughness and inclination angle on nucleate boiling of PF-5060 dielectric liquid on copper. In ASME 2013 International Mechanical Engineering Congress and Exposition, American Society of Mechanical Engineers, V08CT09A034-V08CT09A034.

Estes, K. A., & Mudawar, I. (1995). Comparison of two-phase electronic cooling using free jets and sprays. Journal of Electronic Packaging, 117(4), 323-332.

Fritz, W. (1935). Berechnung des maximalvolume von dampfblasen. Phys. Z., 36, 379-388.

Gao, Z., Zhang, Y., Fu, Y., Yuen, M. M., & Liu, J. (2013). Thermal chemical vapor deposition grown graphene heat spreader for thermal management of hot spots. Carbon, 61, 342-348.

Ghosh, S., Calizo, I., Teweldebrhan, D., Pokatilov, E. P., Nika, D. L., Balandin, A. A., ... & Lau, C. N. (2008). Extremely high thermal conductivity of graphene: Prospects for thermal management applications in nanoelectronic circuits. Applied Physics Letters, 92(15), 151911-151911.

Gorenflo, D., Chandra, U., Kotthoff, S., and Luke, A., (2004), "Influence of Thermophysical Properties on Pool Boiling Heat Transfer of Refrigerants," Int. J. Refrigeration, 27, 492–502.

Griffith, P. (1957). The correlation of nucleate boiling burn-out data. Cambridge, Mass.: MIT Division of Industrial Cooperation.

Hall, D. D., & Mudawar, I. (1999). Ultra-high critical heat flux (CHF) for subcooled water flow boiling—II: high-CHF database and design equations. International Journal of Heat and Mass Transfer, 42(8), 1429-1456.

Haramura, Y., & Katto, Y. (1983). A new hydrodynamic model of critical heat flux, applicable widely to both pool and forced convection boiling on submerged bodies in saturated liquids. International Journal of Heat and Mass Transfer, 26(3), 389-399.

Hendricks, T. J., Krishnan, S., Choi, C., Chang, C. H., & Paul, B. (2010). Enhancement of pool-boiling heat transfer using nanostructured surfaces on aluminum and copper. International Journal of Heat and Mass Transfer, 53(15), 3357-3365.

Hibiki, T., & Ishii, M. (2003). Active nucleation site density in boiling systems. International Journal of Heat and Mass Transfer, 46(14), 2587-2601.

Honda, H., Takamastu, H., & Wei, J. J. (2002). Enhanced boiling of FC-72 on silicon chips with micro-pin-fins and submicron-scale roughness. Journal of heat transfer, 124(2), 383-390.

Honda, H., & Wei, J. (2003). Advances in enhanced boiling heat transfer from electronic components. JSME International Journal Series B, 46(4), 479-490.

Hong, K. T., Imadojemu, H., & Webb, R. L. (1994). Effects of oxidation and surface roughness on contact angle. Experimental Thermal and Fluid Science, 8(4), 279-285.

Hosseini, R., Gholaminejad, A., & Jahandar, H. (2011). Roughness Effects on Nucleate Pool Boiling of R-113 on Horizontal Circular Copper Surfaces. World Academy of Science, Engineering and Technology, 55, 679-684.

Hosseini, R., Gholaminejad, A., Nabil, M., & Samadinia, M. H. (2011, January). Concerning the effect of surface material on nucleate boiling heat transfer of R-113. In ASME/JSME 2011 8th Thermal Engineering Joint Conference, American Society of Mechanical Engineers, T10238-T10238.

Howard, A. H., & Mudawar, I. (1999). Orientation effects on pool boiling critical heat flux (CHF) and modeling of CHF for near-vertical surfaces. International journal of heat and mass transfer, 42(9), 1665-1688.

Hsu, Y. Y. (1962). On the size range of active nucleation cavities on a heating surface. Journal of Heat Transfer, 84(3), 207-213.

Hsu, C. C., & Chen, P. H. (2012). Surface wettability effects on critical heat flux of boiling heat transfer using nanoparticle coatings. International Journal of Heat and Mass Transfer, 55(13), 3713-3719.

Hsu, C. C., Su, T. W., & Chen, P. H. (2012). Pool boiling of nanoparticle-modified surface with interlaced wettability. Nanoscale research letters, 7(1), 1-7.

Hutter, C., Kenning, D. B. R., Sefiane, K., Karayiannis, T. G., Lin, H., Cummins, G., & Walton, A. J. (2010). Experimental pool boiling investigations of FC-72 on silicon with artificial cavities and integrated temperature microsensors. Experimental Thermal and Fluid Science, 34(4), 422-433.

Im, Y., Dietz, C., Lee, S. S., & Joshi, Y. (2012). Flower-like CuO nanostructures for enhanced boiling. Nanoscale and Microscale Thermophysical Engineering, 16(3), 145-153.

Intel Corporation, (2015), www.intel.com

ITRS, International Technology Roadmap for Semiconductors, (2013).

Ivey, H. J. (1967). Relationships between bubble frequency, departure diameter and rise velocity in nucleate boiling. International Journal of Heat and Mass Transfer, 10(8), 1023-1040.

Jabardo, J. M. S., Ribatski, G., & Stelute, E. (2009). Roughness and surface material effects on nucleate boiling heat transfer from cylindrical surfaces to refrigerants R-134a and R-123. Experimental Thermal and Fluid Science, 33(4), 579-590.

Jabardo, J. (2010). An Overview of Surface Roughness Effects on Nucleate Boiling Heat Transfer. Open Transport Phenomena Journal, 2, 24-34.

Jakob, M., & Fritz, W. (1931). Versuche über den Verdampfungsvorgang. Forschung im Ingenieurwesen, 2(12), 435-447.

Jensen, M. K., & Memmel, G. J. (1986). Evaluation of bubble departure diameter correlations. In Proceedings of the Eighth International Heat Transfer Conference (4), 1907-1912.

Jones, B. J., & Garimella, S. V. (2007, January). Effects of surface roughness on the pool boiling of water. In ASME/JSME 2007 Thermal Engineering Heat Transfer Summer Conference collocated with the ASME 2007 InterPACK Conference, American Society of Mechanical Engineers, 219-227.

Jones, B. J., McHale, J. P., & Garimella, S. V. (2009). The influence of surface roughness on nucleate pool boiling heat transfer. Journal of Heat Transfer, 131(12), 121009.

Kandlikar, S. G., & Steinke, M. E. (2002). Contact angles and interface behavior during rapid evaporation of liquid on a heated surface. International Journal of Heat and Mass Transfer, 45(18), 3771-3780.

Kandlikar, S. G., & Bapat, A. V. (2007). Evaluation of jet impingement, spray and microchannel chip cooling options for high heat flux removal. Heat Transfer Engineering, 28(11), 911-923.

Kang, M. G. (2000). Effect of surface roughness on pool boiling heat transfer. International journal of heat and mass transfer, 43(22), 4073-4085.

Khan, N., Toh, K. C., & Pinjala, D. (2008). Boiling heat transfer enhancement using micro-machined porous channels for electronics cooling. Heat Transfer Engineering, 29(4), 366-374.

Kim, J. (2007). Spray cooling heat transfer: the state of the art. International Journal of Heat and Fluid Flow, 28(4), 753-767.

Kim, S. J., Bang, I. C., Buongiorno, J., & Hu, L. W. (2007). Surface wettability change during pool boiling of nanofluids and its effect on critical heat flux. International Journal of Heat and Mass Transfer, 50(19), 4105-4116.

Kim, S. Y., Paek, J. W., & Kang, B. H. (2003). Thermal performance of aluminum-foam heat sinks by forced air cooling. Components and Packaging Technologies, IEEE Transactions on, 26(1), 262-267.

Kim, J., & Kim, M. H. (2006). On the departure behaviors of bubble at nucleate pool boiling. International journal of multiphase flow, 32(10), 1269-1286.

Klein, C. A., & Holland, M. G. (1964). Thermal conductivity of pyrolytic graphite at low temperatures. I. Turbostratic structures. Physical Review, 136(2A), A575.

Kline, S. J., and McClintock, F. A., (1952), "Describing Uncertainties in Single-Sample Experiments," ASME Mechanical Engineering, 75, 3-8.

Kocamustafaogullari, G., & Ishii, M. (1983). Interfacial area and nucleation site density in boiling systems. International Journal of Heat and Mass Transfer, 26(9), 1377-1387.

Koide, M., Fukuzono, K., Yoshimura, H., Sato, T., Abe, K., & Fujisaki, H. (2006). High-performance flip-chip BGA technology based on thin-core and coreless package substrate. In *2006 Electronic Components and Technology Conference*, 23-29.

Kou, H. S., Lee, J. J., & Chen, C. W. (2008). Optimum thermal performance of microchannel heat sink by adjusting channel width and height. International Communications in Heat and Mass Transfer, 35(5), 577-582.

Kozitskii, V. I. (1972). Heat transfer coefficients for boiling of n-butane on surfaces of various roughness. Chemical and Petroleum Engineering, 8(1), 23-24.

Kurihara, H. M., & Myers, J. E. (1960). The effects of superheat and surface roughness on boiling coefficients. AIChE Journal, 6(1), 83-91.

Kutateladze, S. S. (1952). Heat transfer in condensation and boiling. State Scientific and Technical Publishers of Literature on Machinery.

Kutateladze, S. S., & Gogonin, I. I. (1979). Growth rate and detachment diameter of a vapor bubble in free convection boiling of a saturated liquid. Teplofizika Vysokikh Temperatur, 17, 792-797.

Lasance, C. J., & Simons, R. E. (2005). Advances in high-performance cooling for electronics. Electronics Cooling, 11(4).

Li, X., Cai, W., Colombo, L., & Ruoff, R. S. (2009). Evolution of graphene growth on Ni and Cu by carbon isotope labeling. *Nano letters*, *9*(12), 4268-4272.

Lide, D. R. (Ed.). (2004). *CRC handbook of chemistry and physics*. CRC press.

Lorenz, J. J., Mikic, B. B., & Rohsenow, W. M. (1972). The effects of surface conditions on boiling characteristics. Cambridge, Mass.: MIT Engineering Projects Laboratory.

Luke, A. (2006). Preparation, measurement and analysis of the microstructure of evaporator surfaces. International journal of thermal sciences, 45(3), 237-256.

Mahajan, R., Chiu, C. P., & Chrysler, G. (2006). Cooling a microprocessor chip. *Proceedings of the IEEE*, *94*(8), 1476-1486.

Marcinichen, Jackson Braz, Jonathan Albert Olivier, and John Richard Thome. (2012) On-chip two-phase cooling of datacenters: Cooling system and energy recovery evaluation, *Applied Thermal Engineering* (41), 36-51.

McHale, J. P., & Garimella, S. V. (2008, January). Measurements of bubble nucleation characteristics in pool boiling of a wetting liquid on smooth and roughened surfaces. In ASME 2008 Heat Transfer Summer Conference collocated with the Fluids Engineering, Energy Sustainability, and 3rd Energy Nanotechnology Conferences (619-629). American Society of Mechanical Engineers.

McHale, J. P., & Garimella, S. V. (2010). Bubble nucleation characteristics in pool boiling of a wetting liquid on smooth and rough surfaces. International Journal of Multiphase Flow, 36(4), 249-260.

McHale, J. P., & Garimella, S. V. (2013). Nucleate boiling from smooth and rough surfaces–Part 1: Fabrication and characterization of an optically transparent heater–sensor substrate with controlled surface roughness. Experimental Thermal and Fluid Science, 44, 456-467.

McHale, J. P., & Garimella, S. V. (2013). Nucleate boiling from smooth and rough surfaces–Part 2: analysis of surface roughness effects on nucleate boiling. Experimental Thermal and Fluid Science, 44, 439-455.

Mikic, B. B., & Rohsenow, W. M. (1969). A new correlation of pool-boiling data including the effect of heating surface characteristics. Journal of Heat Transfer, 91(2), 245-250.

Mikic, B. B., Rohsenow, W. M., & Griffith, P. (1970). On bubble growth rates. International Journal of Heat and Mass Transfer, 13(4), 657-666.

Miller, W. J., Gebhart, B., & Wright, N. T. (1990). Effects of boiling history on a microconfigured surface in a dielectric liquid. International communications in heat and mass transfer, 17(4), 389-398.

Mudawar, I., & Bowers, M. B. (1999). Ultra-high critical heat flux (CHF) for subcooled water flow boiling—I: CHF data and parametric effects for small diameter tubes. International Journal of Heat and Mass Transfer, 42(8), 1405-1428.

Mudawar, I., Howard, A. H., & Gersey, C. O. (1997). An analytical model for near-saturated pool boiling critical heat flux on vertical surfaces. International journal of heat and mass transfer, 40(10), 2327-2339.

Nimkar, N. K., Bhavnani, S. H., and Jaeger, R. C., (2006). “Benchmark Heat Transfer Date for Microstructured Surfaces for Immersion-Cooled Microelectronics,” IEEE Trans. On Components and Packaging Tech., 29(1), 89-97.

Nimkar, N. D., Bhavnani, S. H., & Jaeger, R. C. (2006). Effect of nucleation site spacing on the pool boiling characteristics of a structured surface. International journal of heat and mass transfer, 49(17), 2829-2839.

Nishikawa, K., Fujita, Y., Ohta, H., and Hidaka, S., (1982). Effects of System Pressure and Surface Roughness on Nucleate Boiling Heat Transfer, (Memoirs of the Faculty of Engineering, Vol. 42), Kyushu University, Fukuoka, Kyushu, Japan, 95–111.

Nishikawa, K., Fujita, Y., Uchida, S., and Ohta, H., (1984). “Effect of Surface Configuration on Nucleate Boiling Heat Transfer,” International. Journal of. Heat and Mass Transfer, 27, 1559-1571.

Nvidia Corporation, (2015), www.nvidia.com

O'Hanley, H., Coyle, C., Buongiorno, J., McKrell, T., Hu, L. W., Rubner, M., & Cohen, R. (2013). Separate effects of surface roughness, wettability, and porosity on the boiling critical heat flux. Applied Physics Letters, 103(2), 024102.

Olivier, J. A., Marcinichen, J. B., & Thome, J. R. (2010). Two-phase cooling of datacenters: reduction in energy costs and improved efficiencies. In 13th Brazilian Congress of Thermal Sciences and Engineering—ENCIT2010, Uberlandia, MG, Brazil.

Olivier, J. A., Marcinichen, J. B., Bruch, A., & Thome, J. (2011). Green Cooling of High Performance Microprocessors: Parametric Study Between Flow Boiling and Water Cooling. Journal of Thermal Science and Engineering Applications, 3(4), 041003.

Parker, J. L., & El-Genk, M. S. (2006). Effect of surface orientation on nucleate boiling of FC-72 on porous graphite. Journal of Heat Transfer, 128(11), 1159-1175.

Parker, J. L., & El-Genk, M. S. (2009). Saturation boiling of HFE-7100 dielectric liquid on copper surfaces with corner pins at different inclinations. Journal of Enhanced Heat Transfer, 16(2), 103-122.

Pastukhov, V. G., Maidanik, Y. F., Vershinin, C. V., & Korukov, M. A. (2003). Miniature loop heat pipes for electronics cooling. Applied Thermal Engineering, 23(9), 1125-1135.

Pavlova, A., & Amitay, M. (2006). Electronic cooling using synthetic jet impingement. Journal of heat transfer, 128(9), 897-907.

Phan, H. T., Caney, N., Marty, P., Colasson, S., & Gavillet, J. (2009). Surface wettability control by nanocoating: the effects on pool boiling heat transfer and nucleation mechanism. International Journal of Heat and Mass Transfer, 52(23), 5459-5471.

Phan, H. T., Caney, N., Marty, P., Colasson, S., & Gavillet, J. (2010). A model to predict the effect of contact angle on the bubble departure diameter during heterogeneous boiling. International Communications in Heat and Mass Transfer, 37(8), 964-969.

Pioro, I. L., Rohsenow, W., & Doerffer, S. S. (2004). Nucleate pool-boiling heat transfer. I: review of parametric effects of boiling surface. International Journal of Heat and Mass Transfer, 47(23), 5033-5044.

Priarone, A. (2005). Effect of surface orientation on nucleate boiling and critical heat flux of dielectric fluids. International journal of thermal sciences, 44(9), 822-831.

Rainey, K. N., and You, S. M., (2000). “Pool Boiling Heat Transfer from Plain and Microporous, Square Pin-Finned Surfaces in Saturated FC-72,” ASME J. Heat Transfer, 122, 509-516.

Rainey, K. N., & You, S. M. (2001). Effects of heater size and orientation on pool boiling heat transfer from microporous coated surfaces. International Journal of Heat and Mass Transfer, 44(14), 2589-2599.

Ramaswamy, C., Joshi, Y., Nakayama, W., & Johnson, W. B. (2002). High-speed visualization of boiling from an enhanced structure. International journal of heat and mass transfer, 45(24), 4761-4771.

Ramaswamy, C., Joshi, Y., Nakayama, W., & Johnson, W. B. (2003). Effects of varying geometrical parameters on boiling from microfabricated enhanced structures. Journal of Heat Transfer, 125(1), 103-109.

Reed, S. J., & Mudawar, I. (1999). Elimination of boiling incipience temperature drop in highly wetting fluids using spherical contact with a flat surface. International journal of heat and mass transfer, 42(13), 2439-2454.

Revellin, R., Quiben, J. M., Bonjour, J., & Thome, J. R. (2008). Effect of local hot spots on the maximum dissipation rates during flow boiling in a microchannel. Components and Packaging Technologies, IEEE Transactions on, 31(2), 407-416.

Ribatski, G., & Jabardo, J. M. S. (2003). Experimental study of nucleate boiling of halocarbon refrigerants on cylindrical surfaces. International journal of heat and mass transfer, 46(23), 4439-4451.

Rini, D. P., Chen, R. H., & Chow, L. C. (2001). Bubble behavior and heat transfer mechanism in FC-72 pool boiling. Experimental heat transfer, 14(1), 27-44.

Rohsenow, W.M., (1952). “A method of correlating heat transfer data for surface boiling of liquids,” Transactions of the ASME, 74, 969–976.

Roll, J. B., & Myers, J. E. (1964). The effect of surface tension on factors in boiling heat transfer. AIChE Journal, 10(4), 530-534.

Ruckenstein, E. (1961). A physical model for nucleate boiling heat transfer from a horizontal surface. Buletinul Institutului Politehnic Bucuresti (Romania) Changed to Bul. Inst. Politeh.'Gheorghe Gheorghiu-Dej'Bucuresti, 23.

Saeidi, D., & Alemrajabi, A. A. (2013). Experimental investigation of pool boiling heat transfer and critical heat flux of nanostructured surfaces. International Journal of Heat and Mass Transfer, 60, 440-449.

Sauer Jr, H. J., Medrow, R. A., & Sinnarwalla, A. M. (1975). Effects of surface condition on nucleate boiling of refrigerant-11. ASHRAE Transactions, 81(part 2), 274-281.

Schmidt, R. (2004). Challenges in electronic cooling—opportunities for enhanced thermal management techniques—microprocessor liquid cooled minichannel heat sink. Heat Transfer Engineering, 25(3), 3-12.

Semenov, O., Vassighi, A., & Sachdev, M. (2006). Impact of self-heating effect on long-term reliability and performance degradation in CMOS circuits. *Device and Materials Reliability, IEEE Transactions on*, *6*(1), 17-27.

Shooshtari, A., Kahn, J., Bar-Cohen, A., Dessiatoun, S., Ohadi, M., Getz, M., & Norley, J. (2006, May). The impact of a thermal spreader on the temperature distribution in a plasma display panel. In Thermal and Thermomechanical Phenomena in Electronics Systems, 2006. ITHERM'06. The Tenth Intersociety Conference on (395-401). IEEE.

Slack, G. A. (1962). Anisotropic thermal conductivity of pyrolytic graphite. Physical Review, 127(3), 694.

Smalc, M., Shives, G., Chen, G., Guggari, S., Norley, J., & Reynolds, R. A. (2005, January). Thermal performance of natural graphite heat spreaders. In ASME 2005 Pacific Rim Technical Conference and Exhibition on Integration and Packaging of MEMS, NEMS, and Electronic Systems collocated with the ASME 2005 Heat Transfer Summer Conference, American Society of Mechanical Engineers, 79-89.

Sriraman, S. R., & Banerjee, D. (2007, January). Pool boiling studies on nano-structured surfaces. In ASME 2007 International Mechanical Engineering Congress and Exposition American Society of Mechanical Engineers, 317-324.

Takata, Y., Hidaka, S., Cao, J. M., Nakamura, T., Yamamoto, H., Masuda, M., & Ito, T. (2005). Effect of surface wettability on boiling and evaporation. Energy, 30(2), 209-220.

Taylor, R. (1966). The thermal conductivity of pyrolytic graphite. Philosophical Magazine, 13(121), 157-166.

Tilton, D. E., & Tilton, C. L. (1993). U.S. Patent No. 5,220,804. Washington, DC: U.S. Patent and Trademark Office.

Tong, X. C. (2011). Advanced materials for thermal management of electronic packaging (Vol. 30). Springer Science & Business Media.

Tsang, D. K. L., Marsden, B. J., Fok, S. L., & Hall, G. (2005). Graphite thermal expansion relationship for different temperature ranges. *Carbon*, *43*(14), 2902-2906

Tuma, P. E. (2010, February). The merits of open bath immersion cooling of datacom equipment. In Semiconductor Thermal Measurement and Management Symposium, 2010. SEMI-THERM 2010. 26th Annual IEEE, 123-131.

Ujereh, S., Fisher, T., & Mudawar, I. (2007). Effects of carbon nanotube arrays on nucleate pool boiling. International Journal of Heat and Mass Transfer, 50(19), 4023-4038.

Vishnev, I. P., Filatov, I. A., Vinokur, Ya. G., Gorokhov, V. V., and Svalov, G. G., (1976), "Study of Heat Transfer in Boiling of Helium on Surfaces with Various Orientations," Heat Transfer-Soviet Research, 8, 104-108.

Wang, C. H., & Dhir, V. K. (1993). Effect of surface wettability on active nucleation site density during pool boiling of water on a vertical surface. Journal of Heat Transfer, 115(3), 659-669.

Wei, J. J., & Honda, H. (2003). Effects of fin geometry on boiling heat transfer from silicon chips with micro-pin-fins immersed in FC-72. International Journal of Heat and Mass Transfer, 46(21), 4059-4070.

Wei, J. (2008). Challenges in cooling design of CPU packages for high-performance servers. Heat Transfer Engineering, 29(2), 178-187.

Wenzel, R. N. (1949). Surface roughness and contact angle. The Journal of Physical Chemistry, 53(9), 1466-1467.

Wright, N., & Gebhart, B. (1989). Enhanced boiling on microconfigured surfaces. Journal of Electronic Packaging, 111(2), 112-120.

Wu, E., Sune, J., Lai, W., Nowak, E., McKenna, J., Vayshenker, A., & Harmon, D. (2002). Interplay of voltage and temperature acceleration of oxide breakdown for ultra-thin gate oxides. Solid-State Electronics, 46(11), 1787-1798.

Wu, W., Bostanci, H., Chow, L. C., Hong, Y., Su, M., & Kizito, J. P. (2010). Nucleate boiling heat transfer enhancement for water and FC-72 on titanium oxide and silicon oxide surfaces. International Journal of Heat and Mass Transfer, 53(9), 1773-1777.

Xiong, Y., Smalc, M., Norley, J., Chang, J., & Mayer, H. (2008, May). Thermal tests and analysis of thin graphite heat spreader for hot spot reduction in handheld devices. In Thermal and Thermomechanical Phenomena in Electronic Systems, 2008. ITHERM 2008. 11th Intersociety Conference, IEEE, 583-590.

Xu, G., Guenin, B., & Vogel, M. (2004, June). Extension of air cooling for high power processors. In Thermal and Thermomechanical Phenomena in Electronic Systems, 2004. ITHERM'04. The Ninth Intersociety Conference, IEEE, 186-193.

Yang, S. R., & Kim, R. H. (1988). A mathematical model of the pool boiling nucleation site density in terms of the surface characteristics. International journal of heat and mass transfer, 31(6), 1127-1135.

You, S. M., Simon, T. W., Bar-Cohen, A., and Hong, Y. S., 1995, "Effects of Dissolved Gas Content on Pool Boiling of a Highly Wetting Fluid," ASME J. Heat Transfer, 117, 687- 692.

Yu, C. K., Lu, D. C., & Cheng, T. C. (2006). Pool boiling heat transfer on artificial micro-cavity surfaces in dielectric fluid FC-72. Journal of Micromechanics and Microengineering, 16(10), 2092.

Zhang, H. Y., Pinjala, D., & Teo, P. S. (2003, December). Thermal management of high power dissipation electronic packages: From air cooling to liquid cooling. In Electronics Packaging Technology, 2003 5th Conference (EPTC 2003), IEEE, 620-625.

Zuber, N., (1959). "Hydrodynamic Aspects of Boiling Heat Transfer," Ph.D. Dissertation, University of California, Los Angeles, CA.

Zuber, N., (1963). "Nucleate Boiling. The Region of Isolated Bubbles and the Similarity with Natural Convection," International Journal of Heat and Mass Transfer, 6, 53-76.

Zweben, C. (2006). Thermal materials solve power electronics challenges. Power Electronics Technology, 32(2), 40-47.

Appendix A – Sample Uncertainty Calculations

A.1 Experimental Uncertainties

This appendix provides sample calculations from the methodology described in Chapter 3 used to estimate the uncertainties in the experimental measurements of the performed pool boiling experiments over the course of this research. These include the uncertainties in the measurements of the applied heat flux, recorded temperatures, and the subsequent heat transfer coefficient.

Table A.1 provides a list of raw experimental parameters and variables that were recorded during one experiment for the saturation nucleate boiling of PF-5060 on a rough Cu surface.

Table A.1 A sample of the raw data from the LabVIEW program used to control the pool nucleate boiling experiments. The red values are used in the sample calculations.

Current I (A)	Voltage V (V)	Power P (W)	T_w (°C)	T_b (°C)	ΔT_{sat} (K)	q (W)	h_{NB} (W/cm^{2}K)
0.54413	9.46605	5.15077	58.88358	51.23399	7.48358	5.20333	0.6802103
0.76069	13.2597	10.08649	60.4679	51.17167	9.0679	10.18941	1.0960798
0.92629	16.08044	14.89514	61.95414	51.28174	10.55414	15.04713	1.4099106
1.0797	18.53149	20.00842	64.21285	51.3808	12.81285	20.21259	1.5751645

The manufacturer stated systematic and random uncertainties in the measurements for the power provided to the heating element by the DC power supply are 0.05% ± 5mV for the applied voltage and 0.15% ± 5mA for the supplied electrical current, respectively (Agilent, 2000). The manufacturer stated systematic uncertainty in the thermocouples temperature measurements is ± 0.2 K (Omega, 2004).

The power removed by the boiling surface was the product of the current and the voltage drop across the heating element, less the estimated losses. The uncertainty in the power measurement, derived from Equations (3.1) – (3.3) is:

$$\frac{\Delta P}{P} = \left[\left(\frac{\Delta V}{V}\right)^2 + \left(\frac{\Delta I}{I}\right)^2\right]^{1/2} \qquad (A.1)$$

As an example, in Table A1, when the applied surface heat flux q was 10.18941 W/cm^2, the measured input voltage and current were 13.2597 V and 0.76069 A (Table A.1), respectively. The corresponding uncertainty in the applied power was estimated using Equation A.1 as:

$$\frac{\Delta P}{P}=\left[\left(\frac{0.0005V+0.005}{V}\right)^2+\left(\frac{0.0015I+0.005}{I}\right)^2\right]^{1/2} \qquad \text{(A.2)}$$

$$\frac{\Delta P}{P}=\left[\left(\frac{0.01163}{13.2597}\right)^2+\left(\frac{0.006141}{0.76069}\right)^2\right]^{1/2}=0.00812\ or\ 0.81\% \qquad \text{(A.3)}$$

For the experiments, the uncertainty of the surface heat flux q, is expressed as a function of the uncertainty of applied power (Equation (A.2) – (A.3), the estimated side heat losses, ε (3%, Chapter 3), and the uncertainty of the surface area, 10 mm ± 2% as:

$$\frac{\Delta q}{q}=\left[\left(\frac{\Delta P}{P}(1-\varepsilon)\right)^2+\left(\frac{\Delta A}{A}\right)^2\right]^{1/2} \qquad \text{(A.4)}$$

Thus, the estimated uncertainty in the heat flux from Equation (A.4) is:

$$\frac{\Delta q}{q}=\left[(0.00812(1-0.97))^2+\left(\frac{0.02}{10}\right)^2\right]^{1/2}=0.0311\ or\ 3.11\% \qquad \text{(A.5)}$$

Based off of the uncertainties in surface heat flux and the measured temperatures, the uncertainty in the heat transfer coefficient, h_{NB}, is:

$$\frac{\Delta h_{NB}}{h_{NB}}=\left[\left(\frac{\Delta q}{q}\right)^2+\left(\frac{\Delta(T_w-T_b)}{(T_w-T_b)}\right)^2\right]^{1/2} \qquad \text{(A.6)}$$

From Equation (A.6), in the $\Delta(T_w-T_b)$ term, there is an uncertainty in both the T_w and T_b term, and is that of the manufacturer stated systematic uncertainty in the thermocouples temperature measurements of ± 0.2 K (Omega, 2004).Therefore, Equation (A.6) may be rewritten as:

$$\frac{\Delta h_{NB}}{h_{NB}}=\left[\left(\frac{\Delta q}{q}\right)^2+\left(\frac{(\Delta T_w^2+\Delta T_b^2)^{1/2}}{(T_w-T_b)}\right)^2\right]^{1/2} \qquad \text{(A.6)}$$

Using the obtained values from Equation (A.4), and relevant values from Table A.1, the estimated uncertainty in the heat transfer coefficient, h_{NB}, is:

$$\frac{\Delta h_{NB}}{h_{NB}} = \left[(0.0311)^2 + \left(\frac{(0.2^2 + 0.2^2)^{1/2}}{9.0679}\right)^2\right]^{1/2} = 0.0435 \text{ or } 4.35\% \quad \text{(A.7)}$$

Table A.2 provides the estimated uncertainties for the values listed in Table A.1, which covered the majority of the boiling curve. From Table A.2, it can be seen that the estimated uncertainties were relatively consistent throughout the entirety of the experiments, and slightly decreased as the input power increased.

Table A.2. The calculated uncertainties of the q and h_{NB} and Equations (A.1) – (A.7), for the experiments from a sample list of values provided in Table A.1.

Current I (A)	Voltage V (V)	Power P (W)	Estimated Error in q (%)	Estimated Error in h_{NB} (%)
0.54413	9.46605	5.15077	3.19	4.88
0.76069	13.2597	10.08649	3.11	4.35
0.92629	16.08044	14.89514	3.09	4.07
1.0797	18.53149	20.00842	3.07	3.78

The maximum nucleate boiling heat transfer coefficient, h_{MNB}, typically occurred at powers >15 W. Therefore, based off Table A.2, the uncertainty of the h_{MNB} was typically ~4%.

A.2 Dimple Bubble Growth Measurements Uncertainties

This appendix provides sample calculations from the methodology described in Chapter 3 used to estimate the uncertainties of the dimple bubble departure diameter in the course of this research. Unlike the spherical bubble measurements of the rough Cu surfaces were departure diameter measurements and associated uncertainties were obtained directly, the departure diameter of the dimple required conversion of the measured volume of an ellipsoid to that of an equivalent sphere, and subsequent diameter.

The volume of an ellipsoid is

$$V = 4\pi abc \tag{A.8}$$

where a is half the length of the major axis, and b and c are half the lengths of the minor axes. For the dimple bubble measurements, the a and b axes were measured, and c was assumed to equal b. The equivalent spherical departure diameter was obtained from equating the volume of a sphere to Equation (A.8) as:

$$D_d^* = (8ab^2)^{1/3} \tag{A.9}$$

The uncertainty is from this expression is:

$$\frac{\Delta D_d^*}{D_d^*} = \left[\left(\frac{1}{3}\frac{\Delta a}{a}\right)^2 + \left(\frac{2}{3}\frac{\Delta b}{b}\right)^2\right]^{1/2} \tag{A.10}$$

The uncertainties were calculated using the raw pixel measurements, and later converted to metric units. Table A.3 lists sample pixel measurements of a bubble just before departure on the three dimpled surfaces investigated in this research.

Table A.3. Sample pixel measurements of the dimple bubble ellipsoid just before departure for the dimpled surfaces investigated in this research.

Dimple surface Φ_d (µm)	a (px)	b (px)	Aspect Ratio (a/b)
300	25	22	1.14
400	28	24	1.16
500	35	30	1.16

For each measurement of a and b, the associated uncertainty was ± 2 pixels, and was related to the image pixel resolution. Using the values provided in Table A.3 in Equation (A.10), the estimated uncertainties for these particular sets of dimpled bubble measurements just before departure are:

$$\frac{\Delta D_d^*}{D_d^*}(\Phi_d = 300\ \mu m) = \left[\left(\frac{1}{3}\frac{2}{25}\right)^2 + \left(\frac{2}{3}\frac{2}{22}\right)^2\right]^{1/2} = 0.066\ or\ {\sim}6.6\% \tag{A.11}$$

$$\frac{\Delta D_d^*}{D_d^*}(\Phi_d = 400\ \mu m) = \left[\left(\frac{1}{3}\frac{2}{28}\right)^2 + \left(\frac{2}{3}\frac{2}{24}\right)^2\right]^{1/2} = 0.0604\ or\ {\sim}6\%$$

$$\frac{\Delta D_d^*}{D_d^*}(\Phi_d = 500\ \mu m) = \left[\left(\frac{1}{3}\frac{2}{35}\right)^2 + \left(\frac{2}{3}\frac{2}{30}\right)^2\right]^{1/2} = 0.0483\ or\ {\sim}4.8\%$$

Because each individual set of measurements resulted in a slightly different uncertainties, and the final departure diameters were based off the correlated transient growth measurements plus half an additional frame (Equations X – X), a conservative maximum aspect ratio of 1.2 was assumed for all measurements, from which the corresponding a and b values were obtained (Equation (A.9)). The final uncertainties were calculated to be ~6.7%, ~6.2%, ~4.9%, for the 300, 400, and 500 µm dimpled surfaces, respectively, and were verified by the very similar uncertainties of the individual sets of measurements such as those presented in Equation (A.11).

Note that in Table A.3, the conversions from pixel to metric units varied for the difference surfaces relative sizes between each $\Phi_{d.}$ Therefore the final values of the uncertainty provided in Table 3.1 are based off the the conversion to metric units specific for each dimpled surface, and was different for each Φ_d based off the camera focusing distance at the time of image capture.

Appendix B – List of Developed Correlations

This appendix provides a list of experimentally and computationally correlations obtained in this research for the pool nucleate boiling of PF-5060 on rough, dimpled, and composite heat spreaders, along with applicable ranges, for quick reference.

The maximum saturation nucleate boiling heat transfer coefficient on rough Cu surfaces:

$$h_{MNB}(Ra,\theta) = (1 - 1.73 \times 10^{-7}\theta^{2.9})1.63Ra^{0.227} \tag{B.1}$$

Applicable range : For Ra = 0.039 – 1.79 μm, $\theta = 0^o – 180^o$, ΔT_{sub} = 0 K

The Critical Heat Flux on rough Cu surfaces:

$$CHF(Ra,\theta,\Delta T_{sub}) = (0.193Ra^{0.078})(1 - 2.86\ \times\ 10^{-7}\theta^{2.83}) \times \ldots$$

$$\{1 + (0.022 + 8.47 \times 10^{-8}\theta^{2.36})\Delta T_{sub}\}(h_{fg}\sqrt{\rho_g}[\sigma(\rho_l - \rho_g)]^{0.25}) \tag{B.2}$$

Applicable range : Ra = 0.039 – 1.79 μm, $\theta = 0^o – 180^o$, ΔT_{sub} = 0 – 30 K

The natural convection heat transfer coefficient on rough Cu surfaces:

$$h_{NC}(\theta) = 0.038(1 - 1.57 \times 10^{-6}\theta^{2.32})\ \Delta T_b^{0.2} \tag{B.3}$$

Applicable range : Ra = 0.039 – 1.79 μm, $\theta = 0^o – 180^o$, ΔT_{sub} = 0 – 30 K

Bubble transient growth rate on smooth and rough Cu surfaces:

$$\mathrm{D_b}(\mu\mathrm{m}) = 234 + 81\sqrt{\mathrm{t_b}}\ \text{(smooth Cu)} \tag{B.4a}$$

$$\mathrm{D_b}(\mu\mathrm{m}) = 206 + 48\sqrt{\mathrm{t_b}}\ \text{(rough Cu)} \tag{B.4b}$$

Applicable range : Ra = 0.039 – 1.79 μm, $\theta = 0^o$, ΔT_{sub} = 0 K

The maximum nucleate boiling heat transfer coefficient on dimpled Cu surfaces:

$$h_{MNB}(\Phi_{\mathrm{d}},\theta) = h_{MNB}(\Phi_{\mathrm{d}},0^o)(1 - 2.505 \times 10^{-7}\theta^{2.84}) \tag{B.5}$$

Applicable range: Φ_{d} = 300 – 500 μm, P/D = 2.0, $\theta = 0^o – 180^o$, ΔT_{sub} = 0 K

$$h_{MNB}(\Phi_{\mathrm{d}}, 0^{o}, \Delta T_{sub}) = h_{MNB}(\Phi_{\mathrm{d}}, 0^{o}, 0\ K)(1 - 0.078\Delta T_{sub}^{0.52}) \tag{B.6}$$

Applicable range: Φ_d = 300 – 500 μm, P/D = 2.0, θ = 0^o, ΔT_{sub} = 0 – 30 K

The Critical Heat Flux on dimpled Cu surfaces:

$$\mathrm{CHF_{sat}}(\Phi_{\mathrm{d}}, \theta) = \mathrm{CHF_{sat}}(\Phi_{\mathrm{d}}, 0^{\mathrm{o}})(1 - 1.157 \times 10^{-7}\theta^{3}) \tag{B.7}$$

Applicable range: Φ_d = 300 – 500 μm, P/D = 2.0, θ = 0^o – 180^o, ΔT_{sub} = 0 K

$$CHF(\Phi_{\mathrm{d}}, 0^{o}, \Delta T_{sub}) = CHF_{sat}(\Phi_{\mathrm{d}}, 0^{o}, 0\ K)(1 + 0.0183\Delta T_{sub}) \tag{B.8}$$

Applicable range: Φ_d = 300 – 500 μm, P/D = 2.0, θ = 0^o, ΔT_{sub} = 0 – 30 K

The natural convection heat transfer coefficient on dimpled Cu surfaces:

$$h_{NC}(0^{o}) = 0.044\ \Delta T_{b}^{0.2} \tag{B.9}$$

Applicable range: Φ_d = 300 – 500 μm, P/D = 2.0, θ = 0^o, ΔT_{sub} = 0 – 30 K

Bubble transient growth rate on dimpled Cu surfaces:

$$\mathrm{D_b^*}(\mu\mathrm{m}) = 273 + 43\sqrt{\mathrm{t_b}}\ (\Phi_\mathrm{d} = 300\ \mu\mathrm{m}) \tag{B.10a}$$

$$\mathrm{D_b^*}(\mu\mathrm{m}) = 322 + 64\sqrt{\mathrm{t_b}}\ (\Phi_\mathrm{d} = 400\ \mu\mathrm{m}) \tag{B.10b}$$

$$\mathrm{D_b^*}(\mu\mathrm{m}) = 361 + 80\sqrt{\mathrm{t_b}}\ (\Phi_\mathrm{d} = 500\ \mu\mathrm{m}) \tag{B.10c}$$

Applicable range: Φ_d = 300 – 500 μm, P/D = 2.0, θ = 0^o, ΔT_{sub} = 0 K

Appendix C – List of Publications

El-Genk, Mohamed S., Arthur Suszko, and Amir F. Ali. "Effects of surface roughness and inclination angle on nucleate boiling of PF-5060 dielectric liquid on copper." ASME 2013 International Mechanical Engineering Congress and Exposition. American Society of Mechanical Engineers, (2013).

El-Genk, Mohamed S., and Arthur Suszko. "Saturation nucleate boiling and correlations for PF-5060 dielectric liquid on inclined rough copper surfaces." Journal of Heat Transfer 136.8 (2014), 081503.

El-Genk, Mohamed S., and Arthur Suszko. "Saturation and subcooled CHF correlations for PF-5060 dielectric liquid on inclined rough Copper surfaces." Multiphase Science and Technology 26.2 (2014).

Suszko, Arthur, and Mohamed S. El-Genk. "Dielectric liquids natural convection on small rough Cu surfaces at different orientations." International Journal of Heat and Mass Transfer 81 (2015), 289-296.

Suszko, Arthur, and Mohamed S. El-Genk. “A composite Cu / HOPG heat spreader for immersion cooling of high power chips”, Proceedings of the ASME 2015 International Technical Conference and Exhibition, InterPACKICNMM2015-48678 (2015)

Suszko, Arthur, and Mohamed S. El-Genk. “Transient Growth of Bubbles in Saturation Boiling of PF-5060 Dielectric Liquid on Rough Surfaces”, Proceedings of the 1st Thermal and Fluid Engineering Summer Conference, Paper #TFESC-12541 (2015)

El-Genk, M. S., A. Suszko, and K. Kato, Saturation Nucleate Boiling of PF-5060 on Inclined Dimpled Surfaces. Proceedings 1st Thermal and Fluid Engineering Summer Conference, TFESC, 2015. Paper # TFESC-12561 (2015)

Suszko, A. and M.S. El-Genk, “Saturation Boiling of PF-5060 on Rough Cu Surfaces: Bubbles Transient Growth, Departure Diameter and Detachment Frequency,” *Int. J. Heat and Mass Transfer* (submitted for review, March 2015)

Suszko, A. and M.S. El-Genk, “Thermally Anisotropic Composite Heat Spreaders for Enhanced Thermal Management of High-Powered Microprocessors,” *Int. J. Thermal Sciences* (submitted for review, July 2015)